



HAL
open science

Caractérisation et applications des écoulements de polymères en films minces nanoimprimés

Etienne Rognin

► **To cite this version:**

Etienne Rognin. Caractérisation et applications des écoulements de polymères en films minces nanoimprimés. Autre. Université de Grenoble, 2013. Français. NNT : 2013GRENI037 . tel-01124100

HAL Id: tel-01124100

<https://theses.hal.science/tel-01124100v1>

Submitted on 6 Mar 2015

HAL is a multi-disciplinary open access archive for the deposit and dissemination of scientific research documents, whether they are published or not. The documents may come from teaching and research institutions in France or abroad, or from public or private research centers.

L'archive ouverte pluridisciplinaire **HAL**, est destinée au dépôt et à la diffusion de documents scientifiques de niveau recherche, publiés ou non, émanant des établissements d'enseignement et de recherche français ou étrangers, des laboratoires publics ou privés.

THÈSE

Pour obtenir le grade de

DOCTEUR DE L'UNIVERSITÉ DE GRENOBLE

Spécialité : **Mécanique des fluides, procédés, énergétique.**

Arrêté ministériel : 7 août 2006

Présentée par

Étienne ROGNIN

Thèse dirigée par **Laurent DAVOUST** et
co-encadrée par **Stefan LANDIS**

préparée au sein du **CEA** (Commissariat à l'Énergie Atomique et aux
Énergies Alternatives) / **DOPT** (Département d'Optronique) / **LCE** (Laboratoire
des Composants pour l'Éclairage),
du **LEGI** (Laboratoire des Écoulements Géophysiques et Industriels)
et du **SIMaP** (Science et Ingénierie des Matériaux et Procédés),
dans l'**École Doctorale IMEP2** (Ingénierie, matériaux, mécanique,
énergétique, environnement, procédés, production)

Characterization and applications of flowing nanoimprinted thin polymer films

Thèse soutenue publiquement le **4 février 2013**,
devant le jury composé de :

M. Didier CHAUSSY

Professeur, LGPP (Grenoble), Président

Mme. Véronique BARDINAL

Chargée de Recherche HDR, LAAS (Toulouse), Rapporteur

M. Pierre GILORMINI

Professeur, PIMM, ENSAM (Paris), Rapporteur

M. Arne SCHLEUNITZ

Ingénieur Recherche, Micro Resist Technology GmbH (Berlin), Examineur

M. Laurent DAVOUST

Professeur, SIMAP (Grenoble), Directeur de la thèse

M. Stefan LANDIS

Expert Senior, CEA (Grenoble), Co-encadrant de la thèse



Caractérisation et applications des écoulements de polymères en films minces nanoimprimés

Résumé. Cette thèse présente des résultats théoriques et expérimentaux portant sur des écoulements à l'échelle nanoscopique de polymères fondus. L'étude analytique et numérique de l'écoulement d'un film de polymère, préalablement nanostructuré par nanoimpression puis recuit au dessus de sa température de transition vitreuse, a permis de dégager différentes dynamiques de nivellement selon la topographie initiale du film. Certaines ont été appliquées à l'élaboration d'éléments optiques par recuit de nanostructures complexes. Une méthode de mesure de la viscosité Newtonienne et du temps terminal de relaxation d'un polymère déposé en film mince a également pu être développée. Enfin, un travail exploratoire portant sur un procédé de nanoimpression sans épaisseur résiduelle par démouillage est présenté. L'accent a porté sur le calcul précis de la pression de disjonction dans un milieu stratifié en utilisant la théorie moderne de Lifshitz basée sur les propriétés optiques des matériaux en interaction.

Mots clés. Lithographie par nanoimpression, polymères en couche mince, films ultra-minces, nanorhéologie, fluage, démouillage, pression de disjonction.

Characterization and applications of flowing nanoimprinted thin polymer films

Abstract. This thesis presents theoretical and experimental work on nanoscale flows of polymer melts. Different leveling dynamics emerge from the analytical and numerical study of the reflow of a polymer film that is first nanoimprinted and then annealed above its glass transition temperature, depending on the initial topography of the film. These concepts were applied to the manufacturing of optical devices from the reflow of complex nanostructures. A method to measure the Newtonian viscosity and the terminal relaxation time of a thin polymer film was also developed. Finally, an exploratory work on a residual-layer-free nanoimprint process based on dewetting is presented. Emphasis was put on the accurate computation of the disjoining pressure in stratified media with the modern Lifshitz theory based on the optical properties of the interacting materials.

Keywords. Nanoimprint lithography, thin polymer films, ultra-thin films, nanorheology, reflow, dewetting, disjoining pressure.

Remerciements

Cette thèse a été co-dirigée de manière très complémentaire par Laurent Davoust au LEGI puis au SIMaP et Stefan Landis au CEA. Laurent, j'ai eu beaucoup de plaisir à travailler avec toi. Malgré mes visites peu fréquentes au début, tu as pu apporter le recul nécessaire et tu m'as fait confiance en me suivant dans des voies qui n'étaient pas gagnées d'avance: pour tout cela, merci! Stefan, nous avons passé de nombreuses heures à résoudre des problèmes en salle blanche ou à discuter au bureau. Par ton exigence et ta disponibilité, tu as su faire en sorte que je donne le meilleur de moi-même, le tout dans une ambiance très amicale: pour tout cela, merci!

Je remercie mon jury de soutenance, présidé par Didier Chaussy, qui a évalué mon travail. Merci à mes rapporteurs, Véronique Bardinal et Pierre Gilormini, qui ont eu l'audace et la patience d'éplucher cet épais manuscrit dans les moindres détails. Merci à Arne Schleunitz d'avoir eu la gentillesse de venir d'outre-Rhin, et dont l'expertise et la vision des technologies de nanoimpression ont été précieuses pour le jugement de mon travail. Merci à Emilie Ortiga pour la relecture attentive du manuscrit.

J'ai pu aborder sereinement nombre de problèmes durant ma thèse grâce à l'enseignement que j'ai reçu à l'École Centrale Paris, associant le pragmatisme de l'ingénieur à la rigueur du scientifique. Je ne peux citer tous les professeurs qui ont contribué à me faire aimer la mécanique des fluides, la thermique et la physique, mais je les remercie de tout cœur.

Cette thèse a été financée par le Département d'optronique du CEA Grenoble. Je tiens à remercier pour leur confiance les directeurs successifs de ce département, Xavier Hugon – dont je remercie au passage la participation dans son propre rôle pour le mythique film “les dix commandements du thésard” – et Bruno Mourey. Merci à Bernard André de m'avoir accueilli dans le Laboratoire des Composants pour l'Éclairage. Merci à toute la dream-team de nanoimprint et associés: Nico, Marion, Yann, Roselyne (qui a permis la réalisation d'un certain nombre d'images de ce manuscrit). Merci à Hubert pour nos discussions de mécanique et de rhéologie, merci pour la seule journée où nous avons pu être dans le même bureau, ça vallait le coup d'essayer, merci de m'avoir initié au rugby lors d'une matinée d'automne mémorable, même si j'avoue ne toujours pas y jouer. Continue à être scandaleux! Merci à Vincent pour ta bonne humeur indéfectible, les séances de brainstorming endiablées et ces petits-déjeuners gargantuesques de la Napa Valley.

Les amitiés nouées au CEA dépassent largement les frontières des labos ou des domaines d'expertise. Je voudrais remercier mes compagnons de la première heure,

Clément, Johann, Marine, Cyrille, Anthony, Frédérique, Audrey, Amélie, Matteo, Fabien, Benoit et Paul de l'ILL. Merci André de m'avoir initié à Gnuplot. Merci aux collègues de l'AITAP, on a bien rigolé. Mais aussi Marie, Marion, Antoine, Tiphaine, Jean-Claude, Daivid, Paul, Boris, Matthieu et Hélène. Il y a eu H1 (trop rarement), H2 (tous les mardi) et H3 (surtout). Mais avant tout il y a eu ce fameux film des thésards, ces soirées, ces ukulélés, cette journée moustache, ces vins, ces sorties en montagne...

Merci aussi à tous mes amis venus me soutenir lors de mon grand oral, en particulier les amis de l'école de communauté et ma famille, et ceux qui ne pouvaient se déplacer mais qui m'ont soutenu d'une manière ou d'une autre.

Je ne peux terminer sans évoquer le souvenir d'êtres chers qui ont rejoint l'éternité pendant que j'effectuais ma thèse. Je n'en citerai que deux. D'abord Marion, camarade de promotion et venue faire comme moi son stage de fin d'études au CEA de Grenoble. Merci pour le témoignage de ta vie, ta fraîcheur et ta simplicité. Prie pour nous, Marion. Et puis mon grand-père Maurice, qui n'est pas étranger à ma vocation scientifique. Cher grand-père, l'univers n'a enfin plus de secret pour toi.

Pour finir, merci à Élise qui a accepté un pari un peu fou, celui de marcher sur l'eau avec moi, en devenant mon épouse. Merci de m'avoir soutenu pour cette thèse, mon "bébé", que je te dédie.

Caractérisation et applications des écoulements de polymères en films minces nanoimprimés: un aperçu

Introduction

La nanofabrication

Ces dernières décennies, les nanotechnologies ont ouvert des perspectives nouvelles dans de nombreux domaines, comme les télécommunications, l'énergie, les matériaux ou la santé. La fabrication à l'échelle moléculaire a incité les chercheurs et les ingénieurs à aborder les problèmes sous un angle nouveau.

Pour les applications demandant la structuration de surfaces, deux tendances semblent se dégager à l'heure actuelle: d'un côté la nécessité d'obtenir des résolutions de plus en plus fines. C'est le cas par exemple des substrats pour la spectroscopie Raman comportant des motifs métalliques nanométriques.¹ D'un autre côté, des structures de tailles micrométriques, mais de formes complexes tridimensionnelles, comme les réseaux de microlentilles à la surface de capteurs d'images.² Pour répondre à ces nouveaux besoins, des techniques de nanostructuration à bas coût pour de larges surfaces doivent être développées.

La nanoimpression

Les techniques de lithographie classiques reposent sur le principe suivant (figure 1a): (i) une résine sensible aux photons (lithographie visible ou UV) ou aux électrons (lithographie électronique) est couchée sur le substrat à structurer. (ii) Cette couche est exposée à un flux d'énergie non-uniforme, ce qui induit un contraste chimique dans la couche. (iii) La résine est sélectivement retirée. Elle forme ainsi un masque pour la gravure du substrat sous-jacent. Les lithographies classiques en tant que technologies dominantes de l'industrie des semi-conducteurs ont été poussées à un

¹Z. Tian, B. Ren, D. Wu, *Journal of Physical Chemistry B* 106, 37 (2002), pp. 9463–9483.

²C. Fesenmaier, Y. Huo, P. Catrysse, *Optics Express* 16, 25 (2008), pp. 20457–20470.

niveau de performance très élevé. Cependant, le coût des équipements et des procédés cantonne ces technologies aux étapes de structuration à forte valeur ajoutée.

La nanoimpression est une technique de lithographie qui se différencie de l'approche précédente par le fait que la structuration est donnée par un contraste topographique plutôt qu'un contraste chimique. Plusieurs variantes existent à l'heure actuelle, la première étant la nanoimpression dite *thermique*. Elle fut développée par Chou et al.³ Les principales étapes sont (figure 1b): (i) un polymère thermo-plastique est déposé sur le substrat. (ii) un moule nanostructuré est mis en pression contre cette couche. L'ensemble est porté à une température supérieure à la température de transition vitreuse du polymère qui devient alors visqueux et est mis en forme par le moule. (iii) L'ensemble est refroidi. (iv) Le système est démoulé.

Les avantages de la nanoimpression sont nombreux. Nous pouvons citer pour commencer un coût d'équipement réduit du fait de la simplicité du procédé, et une bonne performance en matière de résolution (limitée cependant par la résolution du moule). Mais surtout, la nanoimpression se distingue par la possibilité qu'elle offre de structurer directement (c'est à dire sans étape de gravure) des matériaux fonctionnels, et de mouler des formes multi-niveaux ou analogiques (par opposition à la structuration binaire de la lithographie classique).

Problématiques abordées dans la thèse

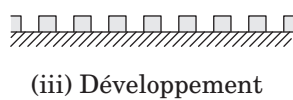
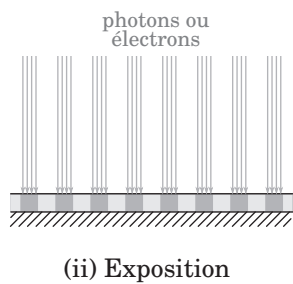
La nanoimpression développée depuis maintenant deux décennies est un procédé en voie d'industrialisation. De nombreux problèmes d'ordre industriels mobilisent d'importants efforts de recherches. Parmi ceux-ci, nous pouvons citer l'alignement submicronique du moule sur le substrat, l'uniformité du pressage et de l'épaisseur résiduelle, le débit d'impression des machines, etc.

Cependant, des phénomènes d'ordres plus fondamentaux restent à étudier afin de comprendre et d'exploiter toutes les potentialités de l'impression aux petites échelles. Le travail effectué dans cette thèse a porté sur une meilleure compréhension des écoulements à l'échelle nanoscopique de polymères fondus. L'étude analytique et numérique de l'écoulement d'un film de polymère, préalablement nanostructuré par nanoimpression puis recuit au dessus de sa température de transition vitreuse, a permis de dégager différentes dynamiques de nivellement selon la topographie initiale du film. Certaines ont été appliquées à l'élaboration d'éléments optiques par recuit de nanostructures complexes. Une méthode de mesure de la viscosité Newtonienne et du temps terminal de relaxation d'un polymère déposé en film mince a également pu être développée.

Pour finir, nous nous sommes intéressés au démouillage de films ultra-minces. Ce phénomène permet d'envisager un procédé d'impression sans épaisseur résiduelle. En plus de réalisations expérimentales, notre travail a porté sur le calcul précis de la pression de disjonction dans un milieu stratifié en utilisant la théorie moderne de Lifshitz basée sur les propriétés optiques des matériaux en interaction.

³S. Y. Chou, P. R. Krauss, and P. J. Renstrom. Applied Physics Letters 67, 3114–3116 (1995).

(a) Lithographie classique



(b) Nanoimpression thermique

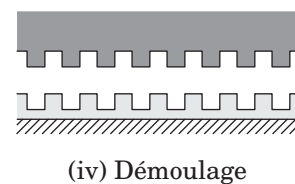
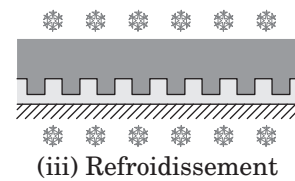
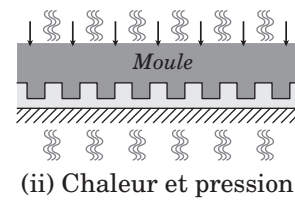
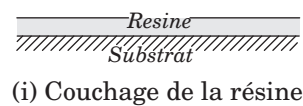


Figure 1 – Étapes principales (schéma en coupe) de procédés de lithographie: **(a)** lithographie optique ou électronique, comparée à **(b)** la nanoimpression thermique.

Mécanique des fluides pour la nanoimpression

Écoulements à surface libre

Afin d'étudier la dynamique des écoulements de polymères fondus aux petites échelles, nous nous sommes concentrés sur des écoulements à surface libre. Le substrat sous-jacent constitue le support imperméable (et indéformable) de l'écoulement. L'interface entre le fluide et l'air constitue la deuxième condition aux limites. Nous verrons à la fin de cette partie quelles sont les forces qui gouvernent l'écoulement.

Caractériser des écoulements à de si petites échelles n'est pas aisé. Des techniques performantes ont été développées dans le cadre de la microfluidique. On peut citer par exemple la micro-PTV (Particle Tracking Velocimetry) ou la micro-PIV (Particle Image Velocimetry), pour lesquelles des traceurs physiques (billes) ou chimiques (solutés fluorescents) entraînés par l'écoulement sont suivis par des procédés d'imagerie plus ou moins complexes. Cependant dans le cadre de nos systèmes, ces techniques ne sont pas applicables car trop invasives. En effet, la taille des traceurs (quelques dizaines de nanomètres) deviendrait commensurable à l'échelle du domaine fluide, ou alors un traceur chimique modifierait sensiblement les propriétés rhéologiques ou surfaciques des matériaux dont on veut caractériser l'écoulement.

La méthode de caractérisation choisie dans notre cas repose quant à elle sur le suivi de l'interface libre. Si le mouvement de l'interface est mesuré, alors avec un modèle adapté, nous pouvons remonter au champ de vitesses dans le fluide et à d'autres grandeurs intéressantes. Certains groupes exploitent un suivi de l'interface en temps réel, c'est-à-dire effectuent des mesures en continu au cours de l'écoulement. Leurs méthodes reposent par exemple soit sur de la scattérométrie, de la diffusion de rayons x, ou alors sur des mesures AFM sur plaque chauffante. De telles mises en œuvre expérimentales sont extrêmement délicates ou alors coûteuses, et ne s'appliquent que pour des topographies de surfaces particulières (motifs périodiques pour les méthodes optiques).

Nous avons pour notre part choisi d'exploiter une propriété des polymères qui est l'existence d'une température de transition vitreuse, c'est-à-dire une température en dessous de laquelle le matériau n'est plus visqueux mais solide. Notre méthode de caractérisation consiste donc en une succession de trempes et de recuits des films, afin d'accéder à un échantillonnage en temps de notre écoulement. Une fois le matériau refroidi à température ambiante, nous pouvons alors utiliser les moyens de caractérisation bien maîtrisés du laboratoire (microscopie optique, électronique, profilométrie, AFM, etc.).

Nivellement et instabilité: deux phénomènes observés

Que se passe-t-il lors d'un recuit d'un film de polymère nanostructuré? Quelques expériences préliminaires peuvent nous montrer que deux évolutions de topographie sont possibles. La figure 2 montre un exemple de motif imprimé (le moule est un réseau de lignes dont la largeur est modulée spatialement) soumis à un recuit. Dans le premier cas (figure b), l'épaisseur résiduelle est forte (90% de l'épaisseur moyenne)

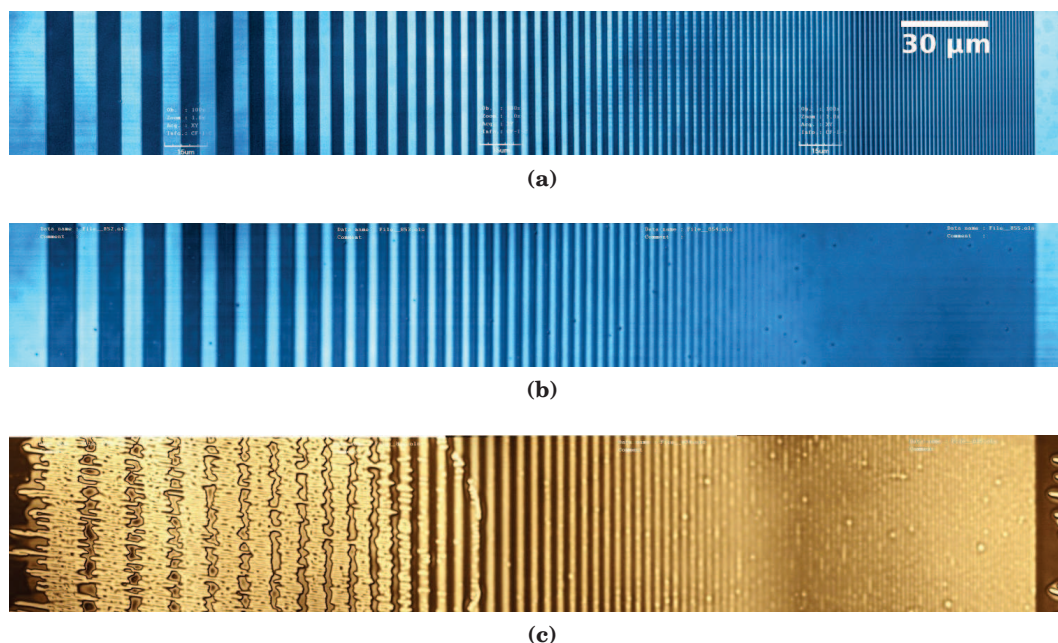


Figure 2 – Film de polymère nanostructuré vu au microscope optique. **(a)** Impression originale; **(b)** motif après recuit lorsque l'épaisseur résiduelle est forte; **(c)** motif après recuit lorsque l'épaisseur résiduelle est faible.

et est représentée par les parties sombres. On assiste à une disparition des motifs, les lignes les plus fines ayant totalement flué tandis que les lignes de largeur intermédiaire s'estompent progressivement.

Dans le deuxième cas, l'épaisseur résiduelle est faible (10% de l'épaisseur moyenne) et cette fois représentée par les parties claires de l'image (la différence de couleur par rapport au premier cas est due à la différence d'épaisseur de polymère). On retrouve l'effacement des motifs fins à droite, en revanche, une forte instabilité s'est développée à gauche au niveau des motifs les plus larges. Il s'agit du démouillage du film, c'est-à-dire sa fragmentation en gouttelettes isolées sur le substrat.

Nous pouvons voir sur cet exemple simple qu'il y a une compétition entre le démouillage du film et son nivellement. Dans la suite, nous allons rentrer plus en détails dans la physique de ces phénomènes.

Échelles du problème

Les écoulements de liquides visqueux à l'échelle de la nanoimpression sont différents de ceux dont nous pouvons faire l'expérience à l'échelle humaine. La réduction des échelles de longueur joue en effet sur deux niveaux:

1. Les forces et leurs effets qui sont habituellement négligeables à l'échelle macroscopique deviennent prépondérants aux petites échelles. C'est le cas par exemple des forces de surface en raison de l'inflation du rapport surface sur volume. C'est aussi le cas des forces intermoléculaires à longue portée, appelées aussi

forces de van der Waals, dont le rayon d'action est de l'ordre de la centaine de nanomètre. La condition aux limites de non glissement à une interface imperméable, habituelle en mécanique des fluides macroscopique, peut elle aussi être remise en cause.

2. À cause du confinement de la matière, c'est-à-dire lorsque l'échelle du volume fluide devient commensurable à la taille moléculaire du constituant, certaines propriétés du fluide peuvent dépendre de sa géométrie. C'est le cas par exemple de la viscosité, de la température de transition vitreuse, de la conductivité thermique, etc. Ce phénomène, quoique d'importance cruciale pour la nanoimpression, n'a pas été étudié dans cette thèse. Il a fait l'objet d'une thèse précédente au laboratoire.⁴

Au-delà même de la prise en considération de ces effets de réduction d'échelle, une question reste ouverte: peut-on légitimement représenter la matière par une approche continue lorsque le volume de fluide est composé de quelques centaines de molécules, voire une dizaine si l'on considère une section transversale d'un film nanométrique? Dans notre étude, nous avons observé le comportement de films dont les parties les plus fines étaient de l'ordre de 5 nm (après pressage), à comparer avec une taille moléculaire de 1 nm (polystyrène 30 kg/mol). Il est apparu qu'une approche fondée sur l'échelle locale des milieux continus était suffisamment prédictive et efficace pour modéliser nos systèmes. Nous avons donc privilégié cette approche aux dépens de celle fondée sur la dynamique moléculaire, plus fastidieuse et restrictive quant à la géométrie du système étudié.

Équation de Navier-Stokes. Pour un fluide visqueux, la quantité de mouvement (dans une modélisation eulérienne) obéit à l'équation de Navier-Stokes:

$$\rho \left(\frac{\partial \mathbf{v}}{\partial t} + (\mathbf{v} \cdot \nabla) \mathbf{v} \right) = -\nabla p + \nabla \cdot \mathbb{T} + \mathbf{f}, \quad (1)$$

où ρ est la masse volumique, \mathbf{v} le champ de vitesses, t le temps, p le champ de pression, \mathbb{T} le tenseur des contraintes visqueuse et éventuellement \mathbf{f} la somme des forces d'action à distance. Voyons maintenant comment évolue l'équation de Navier-Stokes avec la réduction des échelles de longueur.

Intéressons-nous aux termes de gauche de l'équation (1). Pour un écoulement faiblement transitoire (par exemple sans vibration acoustique) et à faible nombre de Reynolds,⁵ ces termes sont négligeables devant le tenseur des contraintes visqueuses. Ici, à cause de la réduction d'échelle (autour du micron) et de vitesse (un micron par seconde), et de l'utilisation de polymères très visqueux (100 Pa.s), le Reynolds est de 10^{-14} . Nous pouvons en conclure que les termes inertiels sont négligeables et pouvons réécrire l'équation sous la forme suivante, appelée *équation de Stokes*:

$$\nabla p = \nabla \cdot \mathbb{T} + \mathbf{f}. \quad (2)$$

⁴T. Leveder, 2009.

⁵Nombre connu des mécaniciens des fluides, défini par $Re = \frac{\rho V \ell}{\eta}$, où V et ℓ sont une vitesse et une longueur caractéristique, et η la viscosité Newtonienne du fluide.

Intéressons-nous maintenant aux conditions aux limites. À l'interface libre, sous une approche d'interface infiniment fine (modèle de Gibbs), le saut de pression (pression de Laplace) s'écrit:

$$p_{\text{int}} - p_{\text{ext}} = \gamma\kappa, \quad (3)$$

où γ est la tension de surface et κ la courbure locale de l'interface. Lorsque la tension de surface n'est pas homogène, un effet *Marangoni* peut se produire: l'interface tire vers les régions à plus forte tension. Dans notre cas, nous n'en observons pas, pour deux raisons majeures: vues les conditions extrêmes de pureté chimique de nos polymères,⁶ il y a peu de chance de trouver des éléments adsorbés à l'interface. Deuxièmement, la tension de surface étant sensible à la température, il pourrait y avoir un effet Marangoni thermique. Or une analyse en ordre de grandeur de la thermique montre clairement que le film est homogène en température tout au long de son cycle.

Une dernière condition aux limites à vérifier est l'hypothèse de non-glissement à l'interface avec le substrat. Bien qu'il n'existe pas de consensus dans la littérature, une longueur de glissement de quelques nanomètres à quelques dizaines de nanomètres peut être observée pour une interface atomiquement plane comme les substrats de silicium. Cependant, pour les géométries que nous avons choisies, nous n'avons pas observé de glissement.

Pour finir, il faut dresser l'inventaire des forces d'action à distance, représentées par le terme \mathbf{f} dans l'équation (1). À l'échelle macroscopique, ce terme est généralement la gravité ou une force électromagnétique. Pour les écoulements microscopiques, l'influence de la gravité peut être comparée à celle de la tension de surface par le nombre de Bond:

$$\text{Bo} = \frac{\rho g \ell^2}{\gamma}, \quad (4)$$

où g est l'accélération de la pesanteur et ℓ une longueur caractéristique. Dans notre cas, $\text{Bo} \sim 10^{-3}$, ce qui signifie que la gravité ne joue aucun rôle moteur dans l'écoulement.

Nous avons vu qu'une autre force peut intervenir aux échelles nanométriques: les interactions à longue portée de van der Waals. Ces forces intermoléculaires sont d'origine électromagnétique. Leur effet à l'échelle des milieux continus se traduit, dans le cas des films ultra-minces, par l'existence d'une pression de disjonction fortement dépendante de l'épaisseur. Dans le cadre de la théorie d'Hamaker, cette pression notée Π , s'exprime comme:

$$\Pi(h) = -\frac{A}{6\pi h^3}, \quad (5)$$

où A est appelée constante d'Hamaker (de l'ordre de 10^{-20} J) et h l'épaisseur du film.

Rhéologie. Le dernier aspect fondamental des écoulements de polymères fondus est la rhéologie, c'est-à-dire le comportement à la contrainte du fluide (le terme $\nabla \cdot \mathbf{T}$

⁶Quoiqu'une analyse chimique permettrait de quantifier cette pureté, nous pouvons le vérifier indirectement en mesurant la température de transition vitreuse du polymère. L'expérience montre que cette température est très sensible aux adjonctions d'impuretés.

dans l'équation de Stokes). Lorsque la sollicitation du polymère est assez lente (plus lente que le temps de relaxation du matériau), le fluide peut être traité comme un fluide Newtonien. La divergence du tenseur des contraintes s'écrit alors:⁷

$$\nabla \cdot \mathbb{T} = \eta \nabla^2 \mathbf{v}, \quad (6)$$

où η est un paramètre appelé *viscosité Newtonienne*. La viscosité est en général dépendante de la température, et pour les polymères fondus cette dépendance est extrême: une augmentation de 10°C peut diviser la viscosité par 10. C'est pourquoi la température est un paramètre important en nanoimpression, tout comme la fine connaissance de la viscosité du matériau en fonction de celle-ci.

Si maintenant la sollicitation du matériau est plus rapide, un comportement viscoélastique est observé. Si le taux de déformation est toutefois faible en amplitude, une théorie dite de *viscoélasticité linéaire* peut être employée. On y exprime les données de l'écoulement dans le domaine fréquentiel et la divergence du tenseur des contraintes prend la forme:

$$\nabla \cdot \mathbb{T}(\omega) = \eta(\omega) \nabla^2 \mathbf{v}(\omega), \quad (7)$$

où $\eta(\omega)$ est une viscosité complexe dépendante de la fréquence ω . Par exemple, pour une fréquence proche de l'inverse du temps terminal de relaxation du polymère, la viscosité complexe peut s'écrire:

$$\eta(\omega) = \frac{\eta_0}{1 - i\omega\tau_t}, \quad (8)$$

où η_0 est la viscosité à fréquence nulle (ou viscosité Newtonienne comme nous l'avons vu), et τ_t le temps terminal de relaxation. L'équation (8) est appelée *modèle de Maxwell* à un mode.

Écoulements pour une épaisseur résiduelle importante

Dans cette partie nous allons nous intéresser au fluage d'un motif dont l'épaisseur résiduelle est importante. La particularité topographique d'un tel motif est que son amplitude (ou profondeur) est faible par rapport à l'épaisseur moyenne du film, ce que nous allons exploiter grâce à la théorie des ondes capillaires.

Théorie des ondes capillaires

La théorie des ondes capillaires est un modèle physique permettant de décrire l'évolution d'une interface libre de liquide soumise à une petite déformation. À notre échelle, nous pouvons spontanément penser aux rides causées à la surface d'un lac par le vent ou un jet de pierre. Nous avons adapté cette théorie à l'effacement d'un motif nanométrique.

La figure 3 montre la géométrie d'une zone d'intérêt de fluide, supposée périodique dans les dimensions horizontales. La hauteur locale et instantanée de fluide

⁷En supposant le fluide incompressible.

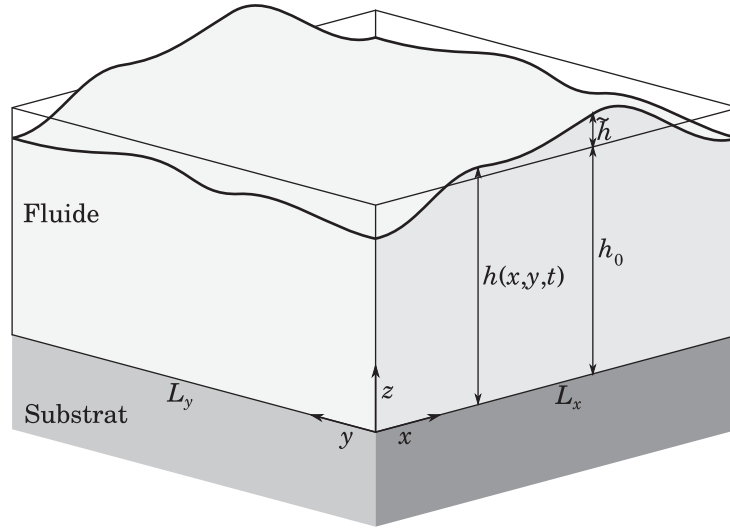


Figure 3 – Géométrie et symboles pour la théorie des ondes capillaires.

est désignée par $h(x, y, t)$. L'amplitude de déformation de l'interface est définie par $\tilde{h} = h - h_0$, où h_0 est l'épaisseur moyenne du film. Avec l'hypothèse $\tilde{h} \ll h_0$, appelée *hypothèse des petites perturbations*, nous pouvons approximer la pression à la hauteur h par celle en h_0 :

$$p(h) \approx p(h_0), \quad (9)$$

et linéariser la pression de disjonction:

$$\Pi(h) \approx \Pi(h_0) + \frac{\partial \Pi}{\partial h}(h_0) \times \tilde{h}. \quad (10)$$

Avec l'hypothèse additionnelle des faibles pentes ($|\nabla h| \ll 1$), la pression de Laplace peut aussi être linéarisée:

$$\Delta p \approx -\gamma \nabla^2 h. \quad (11)$$

Voyons maintenant comment exploiter ces conditions aux limites pour résoudre l'écoulement. La première étape est d'exprimer les équations de bilan de masse et de quantité de mouvement dans le système de coordonnées (\mathbf{k}, z, ω) . Autrement dit, la topographie de la surface libre est décomposée en ondes planes (ondes *capillaires* de vecteur d'onde \mathbf{k}), et la dynamique de l'écoulement est étudiée dans le domaine fréquentiel (ω), ce qui nous permettra de prendre en compte des écoulement viscoélastiques (cf. équation 8). Ce procédé nous permet de transformer les équations aux dérivées partielles en équations algébriques. Le détail des calculs n'est pas reporté ici. Le résultat prend la forme d'une relation de dispersion, c'est à dire une condition nécessaire qui relie la fréquence de l'onde ω à son vecteur d'onde \mathbf{k} *via* les différents paramètres physiques et géométriques. Cette relation de dispersion s'exprime par:

$$\frac{i\omega\eta(\omega)h_0}{\gamma} = f(kh_0, \text{Ha}), \quad (12)$$

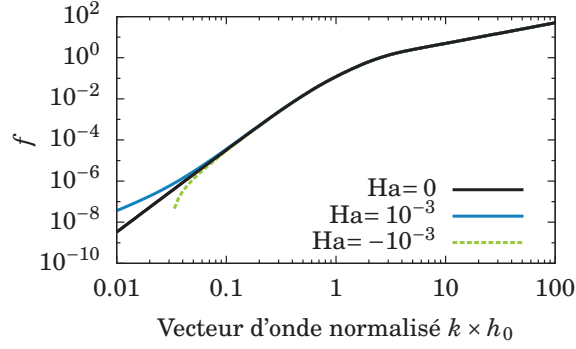


Figure 4 – Fonction f pour différentes valeurs du nombre d’Hamaker.

où f est une fonction sans dimension du vecteur d’onde normalisé $k \times h_0$ (avec $k = \sqrt{\mathbf{k} \cdot \mathbf{k}}$) et d’un nombre sans dimension, Ha , appelé dans cette thèse *nombre d’Hamaker*, défini par:

$$Ha = \frac{h_0^2 \frac{\partial \Pi}{\partial h}(h_0)}{\gamma}. \quad (13)$$

Le nombre d’Hamaker permet de quantifier l’influence des forces à longue portée par rapport à celle de la tension de surface. La fonction f a une expression analytique assez complexe non reportée ici, mais elle est tracée sur la figure 4. En cas d’un nombre d’Hamaker négatif, il y a croissance exponentielle de l’onde capillaire pour les fréquences spatiales plus petites qu’une fréquence critique (divergence de la ligne pointillée montrée sur la figure 4): c’est le démouillage spinodal. Nous reviendrons sur ce phénomène.

Noyau de nivellement. La difficulté du problème revient maintenant à résoudre l’équation de dispersion, c’est-à-dire exprimer ω comme fonction explicite de k . C’est chose aisée lorsque la fonction rhéologique $\eta(\omega)$ prend une forme simple. Nous allons voir brièvement deux cas:

CAS NEWTONIEN La viscosité ne dépend pas de la fréquence. On montre que l’évolution topographique de la surface se met sous la forme:

$$\hat{h}(k, t) = \hat{h}(k, 0) \times \underbrace{\exp\left(-\frac{f(kh_0, Ha)}{Ca}\right)}_{\text{Noyau de nivellement}}, \quad (14)$$

où Ca est un *nombre de capillarité* défini par:

$$Ca = \frac{\eta h_0}{\gamma t}. \quad (15)$$

L’exponentielle est appelée *noyau de nivellement*. Ce noyau joue le rôle d’un filtre linéaire pour la topographie. En cas de nombre d’Hamaker positif ou nul, ce filtre peut même être qualifié de passe-bas. La figure 5a montre la forme du noyau pour différentes valeurs de Ca .

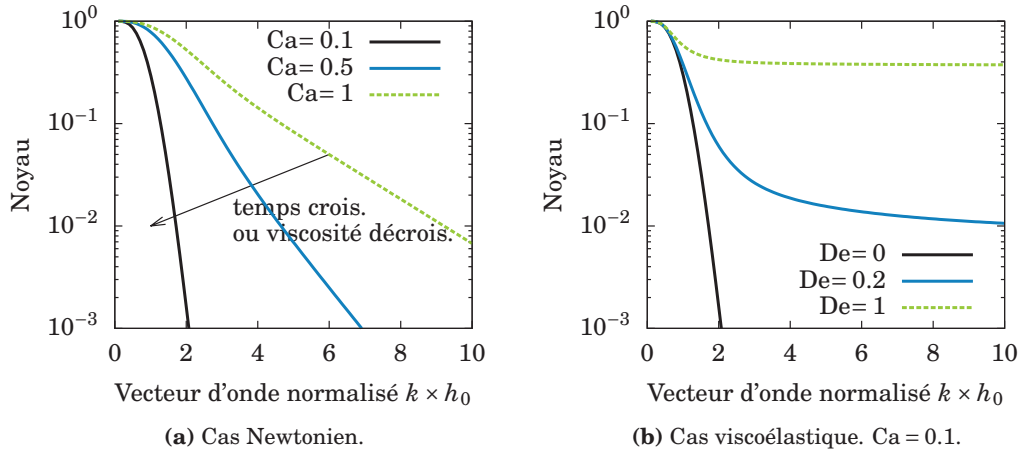


Figure 5 – Noyaux de nivellements pour différents paramètres.

CAS VISCOÉLASTIQUE MONOMODE La viscosité dépend de la fréquence par la relation (8) que nous rappelons ici:

$$\eta(\omega) = \frac{\eta_0}{1 - i\omega\tau_t}. \quad (16)$$

L'évolution topographique est alors:

$$\hat{h}(k, t) = \hat{h}(k, 0) \times \underbrace{\exp\left(-\frac{1}{\frac{Ca}{f} + De}\right)}_{\text{Noyau de nivellement}}, \quad (17)$$

avec un nombre sans dimension supplémentaire, le nombre de Deborah, défini par:

$$De = \frac{\tau_t}{t}. \quad (18)$$

Ce nombre rapporte le temps de relaxation au temps de l'expérience: si le temps d'expérience est trop long, le caractère élastique devient négligeable. Le noyau de nivellement est reporté figure 5b. La particularité de ce noyau est qu'au lieu de tendre vers zéro pour les hautes fréquences, il montre une asymptote horizontale vers la valeur $\exp(-1/De)$. Nous reviendrons sur l'importance de cette propriété pour la rhéométrie des films minces par fluage de nanostructures.

Application à la nanorhéologie

De nombreuses méthodes ont été développées pour mesurer les propriétés rhéologiques de fluides. On en trouvera de nombreuses références dans le corps de cette thèse. Le tableau 1 en rapporte les principales ainsi que leurs inconvénients pour la mesure de propriétés de films minces.

Table 1 – Méthodes connues de rhéométrie appliquées aux films minces.

methode	Limites ou inconvénients
Méthodes macroscopiques (bulk)	Grand volume de fluide requis. Seules les propriétés macroscopiques sont mesurées
Démouillage (nucléation et croissance des trous)	Difficultés théoriques de la ligne de contact. Contrainte forte sur le choix des matériaux.
Pointe AFM immergée	Connaissance de la forme exacte de la pointe requise. Dérive en température des équipements
Diffraction rayons X (dynamique de surface)	Méthode couteuse. Traitement numérique délicat. Motifs périodiques requis.

Présentation de la méthode. La phénoménologie du nivellement que nous avons présentée dans la sous-section précédente nous a permis de développer dans cette thèse une méthode de nanorhéologie pour les films de polymère. Cette méthode est basée sur le concept de noyau de nivellement: si nous pouvons mesurer expérimentalement ce noyau, alors nous pouvons accéder aux propriétés rhéologiques de film. Il y a deux façons de procéder:

1. Le noyau est mesuré comme une fonction du temps, à une longueur d'onde donnée. Cela demande de suivre l'évolution de motifs périodiques, à l'instar de travaux déjà effectués au laboratoire.⁸ C'est une méthode efficace mais qui demande de nombreuses trempes et mesures d'échantillons pour être précise.
2. Le noyau est mesuré comme une fonction des longueurs d'ondes, en comparant la topographie à deux temps donnés. Cette méthode n'avait jamais été exploitée auparavant et c'est celle que nous avons retenue. Le développement de motifs adaptés, riches d'un point de vue spectral (c'est-à-dire présentant à la fois des petites et des grandes longueurs d'onde), techniquement réalisables en lithographie, a été nécessaire. Ces motifs ont fait l'objet d'un dépôt de brevet.⁹ Leur développement est détaillé dans le corps de cette thèse.

La figure 6 présente le déroulement de la méthode: (i) le matériau est déposé en couche mince, (ii) le motif est imprimé par nanoimpression, (iii) la topographie initiale est mesurée par AFM, (iv) un fluage à température donnée, pendant un temps donné, suivi d'une trempe, est effectué, (v) la topographie fluée est mesurée par AFM.

Voyons maintenant deux réalisations expérimentales de cette méthode.

Cas Newtonien. La viscosité d'un film de polystyrène 30 kg/mol d'environ 150 nm d'épaisseur a pu être mesurée à 120°C à l'aide de la méthode que nous venons de décrire. La figure 7a rapporte les deux mesures AFM qui ont été effectuées. Ces mesures sont transformées en termes de fréquences spatiales à l'aide d'un algorithme

⁸Thèse de T. Leveder, 2009.

⁹EP 2011/0161960, US 2012/0095705.

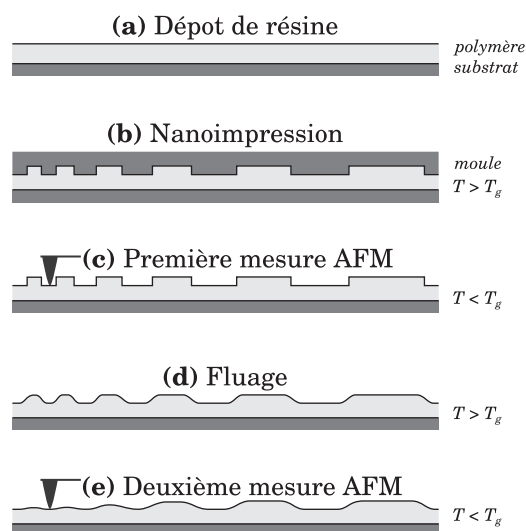
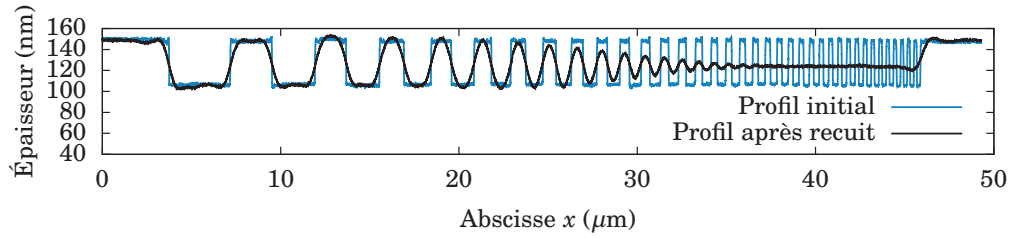


Figure 6 – Méthode de nanorhéologie développée dans cette thèse.

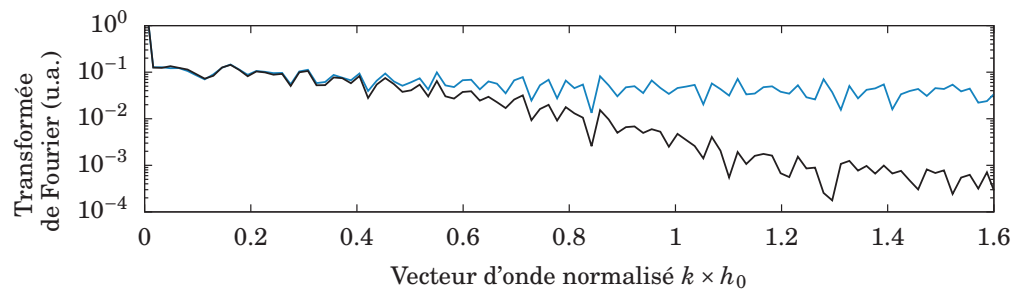
standard de transformée de Fourier (figure 7b). Nous pouvons constater que le spectre du motif recuit voit ses hautes fréquences largement diminuées, ce qui confirme le caractère passe-bas du fluage. En faisant le rapport du spectre flué sur le spectre initial, nous obtenons le noyau de nivellement expérimental, représenté sur la figure 7c. Il ne reste plus qu'à ajuster le modèle Newtonien par la méthode des moindres carrés en prenant le nombre de capillarité (équation 15) comme paramètre d'optimisation. Le résultat est ici $Ca = 0.062 \pm 0.001$. L'épaisseur moyenne est mesurée par ellipsométrie, le temps est un paramètre d'expérience, et la valeur de la tension de surface est prise dans la littérature: nous pouvons donc en déduire la viscosité recherchée, ici $1.0 \pm 0.2 \times 10^6$ Pa·s. Une discussion sur la précision de la mesure est développée dans ce manuscrit.

Nous pouvons répéter la méthode à différentes températures et obtenir la variation de la viscosité Newtonienne en fonction de la température. Le résultat est porté sur la figure 8. Comme attendu pour un polymère, la viscosité diminue avec la température. Cette variation a été largement étudiée et se nomme *loi WLF*. Les paramètres de cette loi ont été mesurés par différents groupes et les courbes résultantes sont également tracées. Nous trouvons un bon accord entre nos mesures et les tendances publiées. Nous remarquons également que même dans le cas d'un film de 150 nm, la viscosité macroscopique est retrouvée, et nous ne mettons donc pas en évidence un changement de propriété dû au confinement de la matière.

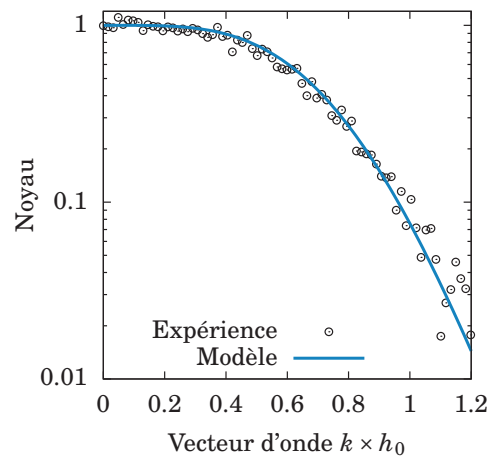
Cas viscoélastique. L'idée maintenant est d'étudier plus finement ce qu'il advient des hautes fréquences spatiales lors d'un recuit. Nous avons vu que dans le cas d'un modèle de Maxwell à un mode, le noyau de nivellement comporte une asymptote horizontale, ou du moins une inflexion de la courbe vers cette asymptote (figure 5b page xv), traduisant le caractère élastique – le caractère visqueux étant mis en évi-



(a) Mesures AFM du film avant et après recuit.



(b) Transformée de Fourier des mesures de la figure a.



(c) Noyau de nivellement de l'expérience, points expérimentaux et modèle Newtonien déduit par optimisation.

Figure 7 – Mesure de viscosité Newtonienne d'un film de polystyrène 30 kg/mol à 120°C.

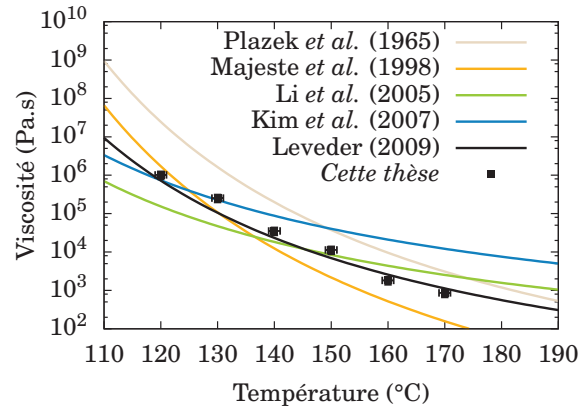


Figure 8 – Mesure de viscosité à différentes températures pour le polystyrène 30 kg/mol et comparaison avec les modèles publiés.

dence par les basses fréquences. Comme les hautes fréquences fluent plus vite que les basses fréquences, nous devons effectuer des temps de recuit plus courts pour mettre en évidence cette élasticité.

Une réalisation expérimentale est présentée sur la figure 9. Nous pouvons voir sur les mesures AFM de la figure 9a qu’un fluage court (ici 30 s) atténue les motifs haute fréquence sans les niveler complètement. Une fois encore, le noyau de nivellement présenté figure 9c est obtenu par le ratio des transformées de Fourier (figure 9b). Un modèle de nivellement viscoélastique en supposant un fluide de Maxwell à un mode (équation 17) est ajusté aux points expérimentaux. Il y a cette fois-ci deux paramètres d’ajustement: le nombre de capillarité comme dans le cas visqueux, et le nombre de Deborah (équation 18). Ce dernier nous permet de mesurer le temps de relaxation du fluide, ici nous trouvons $\tau_t = 10 \pm 2$ s.

Afin de mettre en évidence le caractère élastique du fluage, un modèle purement visqueux est également tracé, et nous constatons qu’il serait incapable de décrire correctement le fluage des hautes fréquences spatiales.

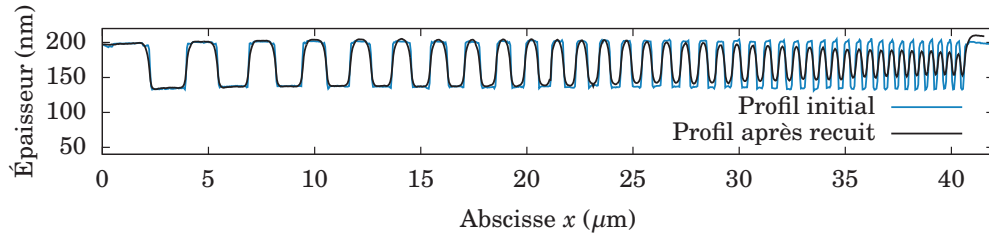
La méthode de mesure peut être répétée à plusieurs températures afin d’étudier la thermo-dépendance du temps de relaxation. C’est le sens de la figure 10. En ce qui concerne la viscosité basse fréquence (η_0 de l’équation (8)) tracée sur la figure 10a, nous retrouvons sans difficulté la viscosité Newtonienne mesurée précédemment avec des temps de fluage longs.

Intéressons-nous maintenant au temps de relaxation. Dans la modélisation la plus simple des polymères dits *linéaires* (chaque molécule est un filament), le temps de relaxation le plus long, appelé temps terminal, est le rapport de la viscosité basse fréquence par un module de cisaillement élastique:

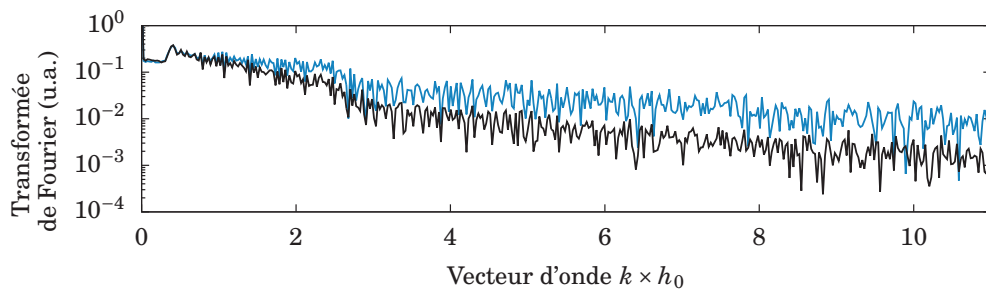
$$\tau_t(T) = \frac{\eta_0(T)}{G_e(T)}, \quad (19)$$

avec

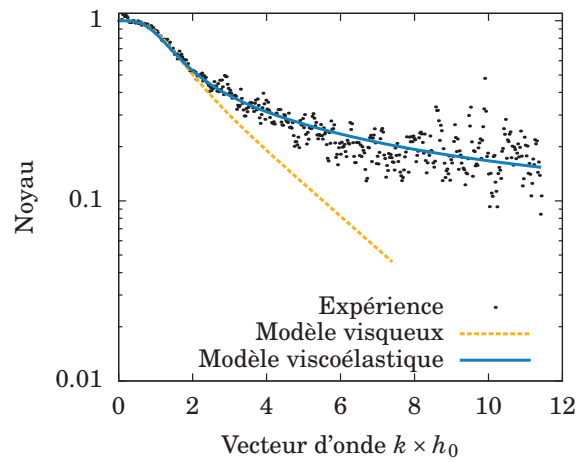
$$G_e(T) = \frac{\rho(T)RT}{M_e}, \quad (20)$$



(a) Mesures AFM du film avant et après recuit.



(b) Transformée de Fourier des mesures de la figure a.



(c) Noyau de nivellement de l'expérience, points expérimentaux et modèle viscoélastique de Maxwell à un mode, déduit par optimisation.

Figure 9 – Mesure de viscoélasticité d'un film de polystyrène 130 kg/mol de 200 nm d'épaisseur à 140°C.

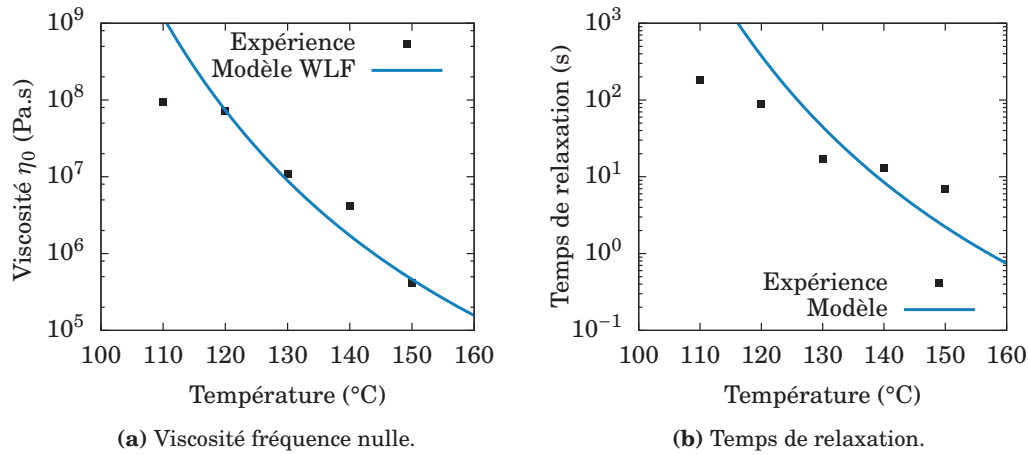


Figure 10 – Mesure de viscoélasticité en fonction de la température, pour un modèle de Maxwell à un mode.

où ρ est la masse volumique, R la constante des gaz parfaits et M_e une masse molaire dite d'*enchevêtrement*, dépendante du matériau. Bien que le module G_e dépende de la température, cette dépendance est de l'ordre de quelques pourcents sur 100 °C (la diminution de la masse volumique compense en partie le facteur T). En comparaison avec les variations de plusieurs ordres de grandeur de la viscosité, nous pouvons dire que G_e est quasi-constant, et donc que la thermo-dépendance du temps de relaxation est la même que celle de la viscosité. Pour notre matériau, nous trouvons $G_e \approx 0.2$ MPa. La courbe de la figure 10b est donc la même que celle de la figure 10a au facteur G_e près, et il est remarquable que ce modèle simple décrive, au moins en ordre de grandeur, les temps de relaxation mesurés.

En conclusion de cette partie, nous avons développé une méthode de rhéologie d'un film mince de polymère. Cette méthode, basée sur le fluage d'un motif nanoimprimé, utilise des équipements courants de salle blanche. Elle permet de mesurer une très large gamme de viscosité. Elle peut également donner accès au temps de relaxation du matériau, ce qui jusqu'alors n'était possible qu'au moyen de méthodes macroscopiques. Or le temps de relaxation est une donnée importante pour les procédés de nanoimpression, afin par exemple d'éviter une relaxation élastique des motifs lors du démoulage.

Écoulements pour une épaisseur résiduelle faible

Considérons maintenant des écoulements dont l'épaisseur résiduelle est faible. Dans le cas d'un fluage de motifs, l'hypothèse de faible perturbation de l'interface n'est plus vérifiée, et la théorie des ondes capillaires ne peut plus être appliquée. Nous allons nous servir d'une autre théorie, couramment utilisée en nanoimpression et en

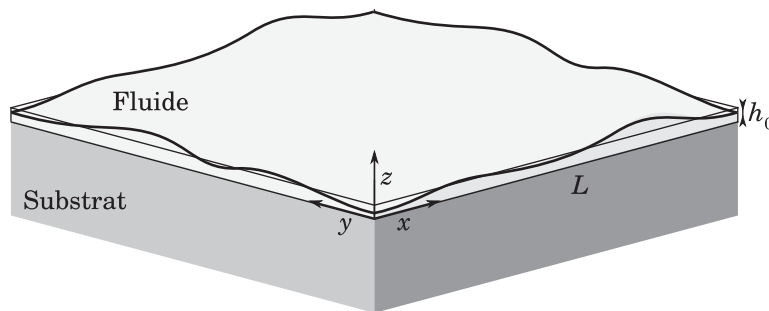


Figure 11 – Géométrie en théorie de la lubrification.

microfluidique: la théorie de la lubrification.¹⁰

Théorie de la lubrification

Le point de départ de la théorie de lubrification est le concept de film mince: une dimension du domaine fluide, l'épaisseur moyenne notée h_0 , est beaucoup plus faible que les autres dimensions, d'ordre de grandeur L (figure 11). La théorie de lubrification est à la mécanique des fluides ce que la théorie des plaques est à la mécanique des solides. Sous cette hypothèse géométrique, le rapport $\varepsilon = h_0/L$ est très inférieur à l'unité. Un développement asymptotique au premier ordre en ε des équations de Stokes et du bilan de masse peut être fait.

Le résultat principal est que le gradient de pression est horizontal, donc que l'écoulement est principalement parallèle au substrat. Précisément, nous trouvons que la variation locale d'épaisseur h est donnée par l'équation dite de *Reynolds*:

$$\frac{\partial h}{\partial t} = \nabla \cdot \underbrace{\left(\frac{h^3}{3\eta} \nabla p \right)}_{\text{flux}}, \quad (21)$$

où ∇p est le gradient de pression et η la viscosité (nous considérons un écoulement Newtonien). Dans cette équation, l'accroissement de l'épaisseur est donné par la divergence d'un flux. Ce flux est proportionnel au gradient de pression, mais il est une fonction non-linéaire de l'épaisseur. Cette non-linéarité rend impossible la résolution analytique de l'écoulement comme nous avons pu le faire précédemment avec la théorie des ondes capillaires. Cependant cette équation qui ne porte que sur l'interface et non le volume de fluide, est rapidement résolue numériquement, en particulier pour les écoulements bi-dimensionnels. Dans ce but, nous avons développé un code de calcul par une méthode de volumes finis.

Nous considérons par la suite que la viscosité est constante (elle ne dépend pas de l'épaisseur, aussi faible soit-elle) et que les forces de van der Waals sont négligeables. Nous pouvons avoir une première approche de la non-linéarité de l'équation (21)

¹⁰A. Oron, S. H. Davis, and S. G. Bankoff. *Reviews of Modern Physics* 69, 931 (1997);
R. V. Craster and O. K. Matar. *Reviews of Modern Physics* 81, 1131 (2009).

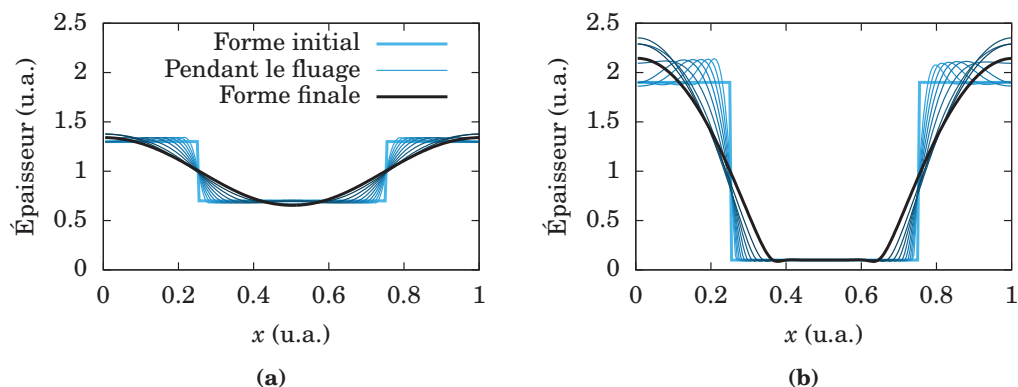


Figure 12 – Calcul numérique d’un fluage de deux créneaux sur le même temps; **(a)** l’épaisseur résiduelle est forte; **(b)** l’épaisseur résiduelle est faible.

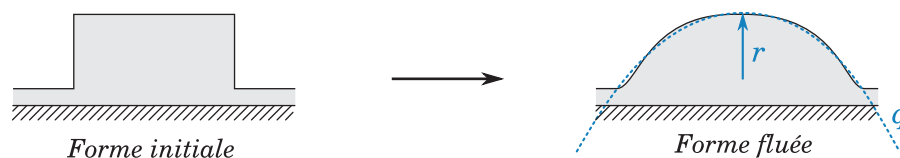


Figure 13 – Principe de fabrication d’une micro-lentille asphérique par fluage.

en comparant le fluage d’un créneau dans deux cas: avec une épaisseur résiduelle forte et une épaisseur résiduelle faible. Les résultats numériques sont présentés sur la figure 12. Nous voyons que dans le premier cas, le créneau se transforme progressivement en sinusoïde. Nous retrouvons les résultats de la théorie des ondes capillaires où le fluage est un filtrage passe-bas pour la topographie: les harmoniques (hautes fréquences spatiales) fluent beaucoup plus vite et il ne reste que le fondamental de motif. Dans le second cas où l’épaisseur résiduelle est faible, nous trouvons un comportement différent: le haut du motif a flué, tandis que le fond a peu évolué. Nous obtenons une forme qui n’est pas symétrique par rapport à la ligne d’épaisseur moyenne. Dans la sous-section suivante, nous allons voir comment exploiter ce phénomène.

Fabrication de formes complexes par fluage

L’idée de départ est la fabrication de formes complexes, par exemple des formes comportant des pentes et des courbures, à partir de motifs simples (créneaux ou multi-niveaux) que l’on fait fluer. La forme de départ joue bien entendu un rôle capital pour la forme finale. L’originalité de notre approche est la suivante: nous venons de voir que l’épaisseur résiduelle, lorsqu’elle est faible, est également un paramètre important pour la forme finale obtenue. La présence d’une épaisseur résiduelle en nanoimpression nous permet ainsi de tirer partie d’une particularité du procédé généralement considérée comme un défaut.

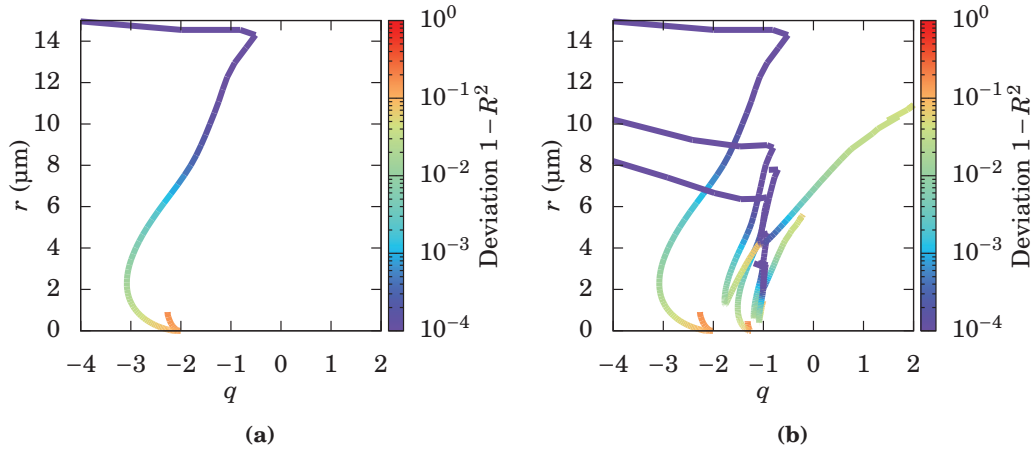


Figure 14 – Paramètres de lentilles couverts par des fluages de créneaux. **(a)** Fluage d'un créneau. **(b)** Hauteur, largeur et épaisseur résiduelle du créneau variables. Le coefficient de corrélation R^2 est d'autant plus proche de 1 que la forme approche celle d'une conique.

Illustrons ce concept par un exemple: la fabrication de micro-lentilles asphériques dont le principe est reporté sur la figure 13. Un créneau est flué et on peut comparer la forme finale à une conique:

$$h(x) = \frac{\frac{x^2}{r}}{1 + \sqrt{1 - (1+q)\frac{x^2}{r^2}}}, \quad (22)$$

avec r le rayon de courbure au sommet et q l'indice de conique ($q < -1$ pour une hyperbole, $q = -1$ pour une parabole, $q > -1$ pour une ellipse, et $q = 0$ pour un cercle). Lorsque $q \neq 0$, la lentille est dite *asphérique* (il y a bien entendu d'autres formes d'asphéricité que les coniques).

Au cours de son fluage, le créneau va parcourir différentes formes de coniques, avec une corrélation plus ou moins bonne. Ceci est illustré par la figure 14a. Le fluage démarre en bas du diagramme. La corrélation est très mauvaise. Après un rapide coude, la corrélation s'améliore, la forme ressemble de plus en plus à une conique. Le rayon de courbure augmente car le fluage aplati le motif. Puis il y a une dernière branche en haut du diagramme où l'indice de conique diminue fortement: la forme est devenue une sinusoïde fortement aplatie.

Il ne reste plus qu'à faire varier les paramètres de la forme initiale: hauteur, largeur et épaisseur résiduelle, comme représenté sur la figure 14b. Nous pouvons ainsi avoir accès au domaine des r et q accessibles grâce à cette technique de fabrication, pour une certaine tolérance de corrélation donnée.

Démouillage des films ultra-minces

Nous allons maintenant aborder un autre aspect des écoulements à faible épaisseur résiduelle. Comme nous l'avons vu au début de ce chapitre avec la figure 2c, le démouillage, c'est-à-dire la rupture de continuité du film, peut se produire pour des épaisseurs suffisamment faibles. Il peut y avoir démouillage si la pression de disjonction augmente lorsque l'épaisseur du film diminue: si cette pression n'est pas contre-balançée par la tension de surface, il y a alors un écoulement qui se crée des zones minces vers les zones épaisses, finissant par dénuder le substrat sous-jacent. Il s'agit du *démouillage spinodal*.

Si le démouillage spinodal est possible en théorie, il se peut qu'il ne soit jamais observé expérimentalement, ou alors que d'autres formes de démouillage interviennent bien avant (comme la nucléation de trous au niveau des poussières ou des zones d'hétérogénéité). En effet, si nous considérons un film plan soumis à la pression de disjonction (et à la tension de surface), nous pouvons à l'aide de la théorie des ondes capillaires, extraire un temps caractéristique de démouillage, de la forme:

$$\tau_d = \frac{12\eta\gamma}{h^3 \frac{\partial \Pi}{\partial h}^2}, \quad (23)$$

où nous rappelons que η désigne la viscosité, γ la tension de surface, h l'épaisseur du film et $\Pi(h)$ la pression de disjonction. Nous y reconnaissons les termes opposés au démouillage: la viscosité et la tension de surface. Comme le facteur $\partial \Pi / \partial h$ est généralement en $1/h^4$, le temps caractéristique varie comme h^5 . Ainsi si un film de 10 nm démouille en une seconde, un film de 100 nm du même matériau mettra plus d'une journée pour démouiller à la même température.

Le démouillage de films de polystyrène sur substrats de silicium est un sujet largement étudié aujourd'hui. Certains auteurs rapportent par ailleurs une augmentation du démouillage si le substrat est recouvert d'une couche d'oxyde de silicium.¹¹ Néanmoins, très peu d'études ont été publiées concernant le démouillage confiné, c'est-à-dire le démouillage du film lorsque celui-ci est pris en étau entre le substrat et le moule. Or ce phénomène intervient couramment en nanoimpression.¹² La figure 15 en rapporte quelques images. L'image 15a en microscopie optique montre un ensemble de motifs (réseaux) imprimé dans un film de polystyrène sur un substrat de silicium recouvert d'une couche d'oxyde. Des digitations, appelées instabilités de Saffman-Taylor, se sont formées en dehors des motifs pendant l'impression. L'image 15b en est un grossissement. De tels défauts en nanoimpression ont déjà fait l'objet d'études.¹³ Cependant, les images c-f sont plus intéressantes en ce qui nous concerne: nous avons pu observer pour la première fois des digitations dans

¹¹R. Seemann, S. Herminghaus, C. Neto, S. Schlagowski, D. Podzimek, R. Konrad, H. Mantz, and K. Jacobs. *Journal of Physics: Condensed Matter* 17, S267–S290 (2005).

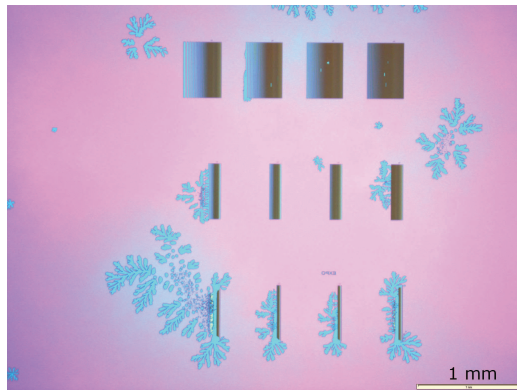
H. Zhao, Y. J. Wang, and O. K. C. Tsui. *Langmuir* 21, 5817–5824 (2005).

¹²S. Y. Chou, L. Zhuang, and L. Guo. *Applied Physics Letters* 75, 1004–1006 (1999).

S. Harkema, E. Schäffer, M. D. Morariu, and U. Steiner. *Langmuir* 19, 9714–9718 (2003).

S. Landis, N. Chaix, C. Gourgon, and T. Leveder. *Nanotechnology* 19, 125305 (2008).

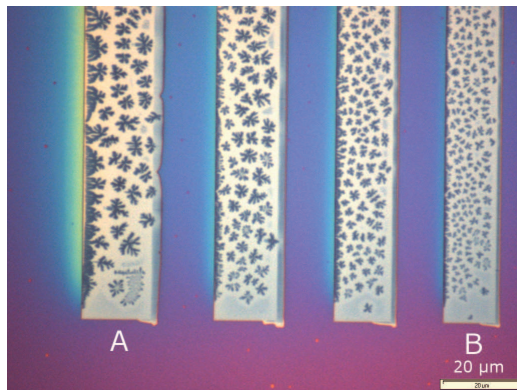
¹³H. Schift, L. J. Heyderman, M. A. d. Maur, and J. Gobrecht. *Nanotechnology* 12, 173–177 (2001).



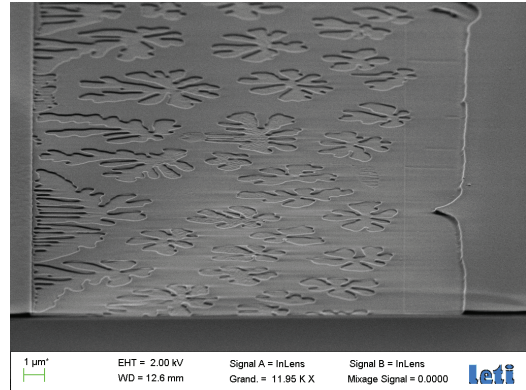
(a) Motifs imprimés dans le polystyrène.



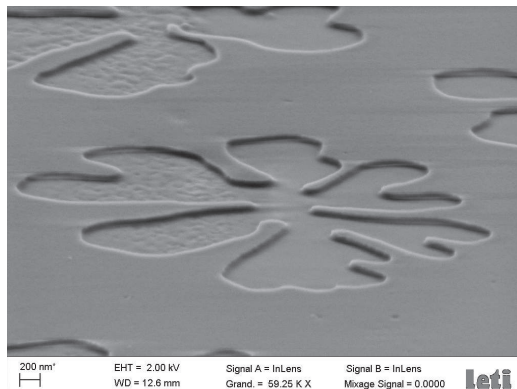
(b) Grossissement d'une instabilité en dehors du motif.



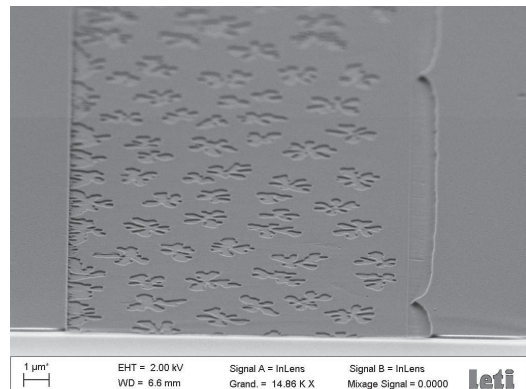
(c) Digitations formées dans l'épaisseur résiduelle.



(d) Grossissement (MEB) de l'épaisseur résiduelle (tranchée A).



(e) Grossissement (MEB) d'une digitation dans l'épaisseur résiduelle.



(f) Grossissement (MEB) de l'épaisseur résiduelle (tranchée B).

Figure 15 – Instabilité de Saffman-Taylor dans un film de polystyrène confiné. Conditions d'impression: température 180°C, pression 13 bar.

l'épaisseur résiduelle. La taille caractéristique de ces formes est de l'ordre du micron, soit beaucoup plus petite que les instabilités observées en dehors des motifs. De façon étonnante et encore inexpliquée, les instabilités sont plus grandes là où l'épaisseur résiduelle s'étend sur une grande largeur (tranchée A), et deviennent de plus en plus petites à mesure que cette largeur diminue (tranchée B). Dans cette configuration expérimentale, aucune instabilité n'a été observée dans des tranchées plus petites que 5 μm .

Théorie de Lifshitz des forces à longue portée. Le contrôle du démouillage pendant l'impression a deux intérêts technologiques majeurs:

1. Nous pouvons minimiser le démouillage si nous le considérons comme source de défektivité. C'est le cas par exemple du démouillage en dehors des motifs imprimés (digitations, ponts capillaires...).
2. Nous pouvons maximiser le démouillage au niveau de l'épaisseur résiduelle. Nous pouvons ainsi tenter d'obtenir un procédé de nanoimpression pour lequel l'épaisseur résiduelle est absente ou négligeable.

Nous nous sommes intéressés à la seconde application. Nous avons voulu étudier l'influence d'une couche d'oxyde de silicium pour le démouillage confiné. Jusqu'à présent, nous avons employé la théorie d'Hamaker pour exprimer la pression de disjonction dans un film mince. Pour une configuration simple à deux interfaces (par exemple un film supporté par un substrat), la pression dite *non-retardée*¹⁴ est donnée par l'équation (5) que nous rappelons ici:

$$\Pi(h) = -\frac{A}{6\pi h^3}. \quad (24)$$

La difficulté se concentre sur l'appréciation de la constante A , et en réalité la théorie d'Hamaker ne donne pas de méthode satisfaisante pour la calculer.

Revenons un instant sur l'origine des forces à longue portée. Van der Waals les a découvertes en travaillant sur les gaz à la fin du XIX^e siècle, et London en a déterminé la nature en 1930. Les molécules électriquement neutres s'attirent mutuellement à cause de la fluctuation de leur nuage électronique, ce qui attribue un moment dipolaire instantané à chaque molécule. Même si ce moment dipolaire est nul en moyenne, l'énergie d'interaction d'une paire de dipôles prend une valeur finie, qui dépend de la polarisabilité du milieu. Pour obtenir l'interaction résultante entre deux objets macroscopiques, il reste néanmoins à sommer ces interactions moléculaires. Or la théorie d'Hamaker les somme paire à paire, en négligeant les interactions plus complexes (réflexion sur un troisième dipôle, etc.).

Pour étudier nos systèmes, nous avons préféré utiliser la théorie moderne de Lifshitz. Cette théorie donne un moyen pratique de calculer la pression de disjonction à partir des propriétés optiques des matériaux.¹⁵ Nous pouvons l'aborder de

¹⁴Il s'agit de l'expression asymptotique de la pression pour un film infiniment mince. L'expression pour un film d'épaisseur finie est en réalité plus complexe.

¹⁵J. N. Israelachvili. Academic Press Inc, 2nd revised edition edition (1991), Chap. 11. V. A. Parsegian. Cambridge University Press (2005).

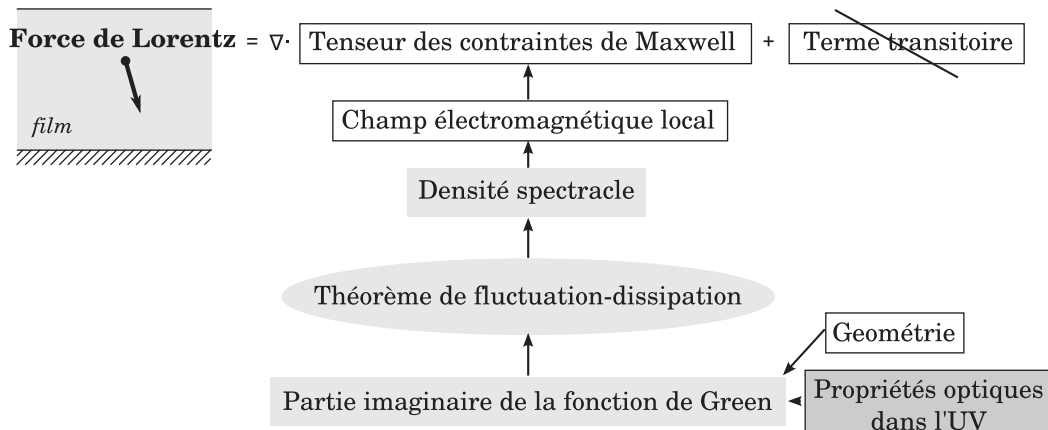


Figure 16 – Les forces à longue portée dans le cadre de la théorie de Lifshitz.

manière très schématique par le diagramme de la figure 16. Le point de départ est le calcul de la force de Lorentz par unité de volume. Cette force peut être exprimée comme la somme de deux termes: la divergence d'un tenseur, appelé *tenseur des contraintes de Maxwell*, et un terme transitoire dépendant du vecteur de Poynting, qui n'intervient pas ici.¹⁶ Le tenseur de Maxwell dépend uniquement du champ électromagnétique local. Comme nous l'avons vu, ce champ est fluctuant (dipôles fluctuants), et la physique statistique peut nous donner la densité spectrale de ce champ via le théorème de fluctuation-dissipation. Ce théorème fait intervenir la partie imaginaire de la fonction de Green du champ électromagnétique, qui dépend elle-même de la géométrie et des propriétés optiques du système (propagation du champ électromagnétique et réflexions sur les interfaces). Le problème de sommation des interactions, simplifié dans le cas de la théorie d'Hamaker, est donc ici rigoureusement pris en compte par le calcul des fonctions de Green.

Influence d'une couche d'oxyde. Revenons au problème qui nous intéresse: nous voulons savoir si l'ajout d'une couche d'oxyde de silicium sur le substrat permet de favoriser significativement le démouillage de l'épaisseur résiduelle pendant le procédé d'impression. À l'aide de la théorie de Lifshitz, nous avons donc calculé la pression de disjonction dans le film de polystyrène, afin d'obtenir le temps caractéristique de démouillage donné par l'équation (23) page xxv. Le système calculé est représenté par la figure 17a. Nous fixons une épaisseur pour la couche d'oxyde et calculons le temps de démouillage en fonction de l'épaisseur de polystyrène.

Le résultat du calcul pour plusieurs couches d'oxyde est tracé figure 17b. Deux groupes se distinguent sur ce graphe: un premier groupe rassemblant le silicium nu et le silicium recouvert de sa couche d'oxyde natif. Pour ces deux systèmes, le temps de démouillage diverge en dessous d'une vingtaine de nanomètres, c'est-à-dire que le démouillage spinodal ne se produit plus pour des couches de polystyrène trop fines.

¹⁶J. D. Jackson. John Wiley & Sons (1998).

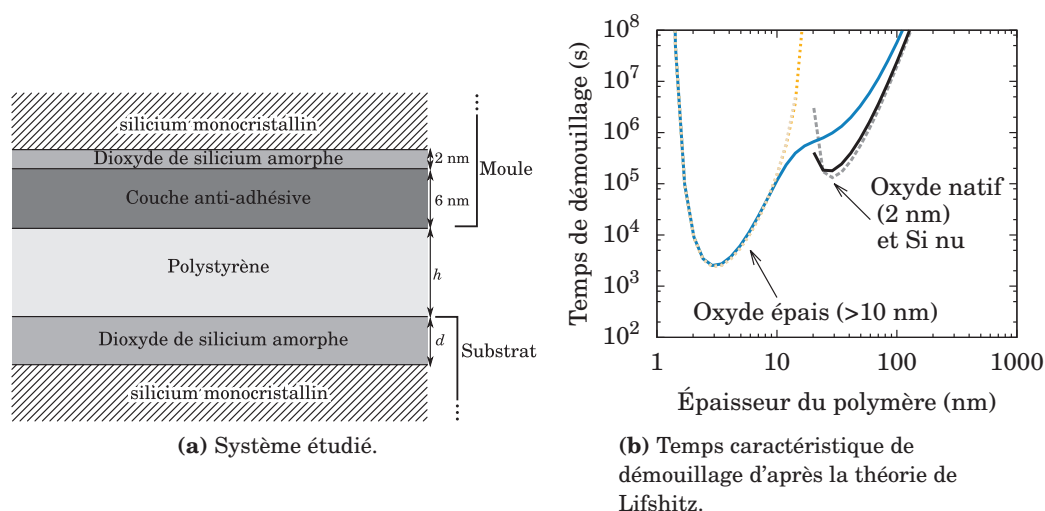


Figure 17 – Effet d'une couche d'oxyde de silicium sur la modélisation du démouillage pendant un procédé de nanoimpression à 180°C.

En revanche, le deuxième groupe, formé des épaisseurs d'oxyde les plus importantes, autorise un démouillage confiné des films ultra-minces. Il n'y a cependant pas de différence notable entre les épaisseurs d'oxyde, la limite étant donnée par une épaisseur de 11 nm (ligne continue commune aux deux groupes).

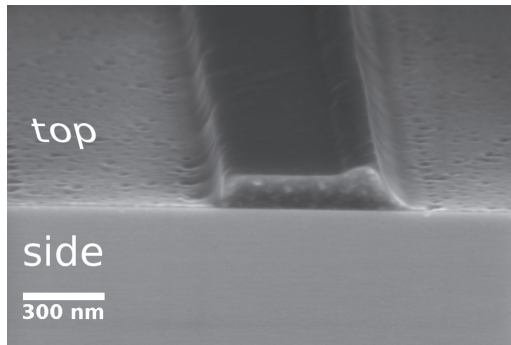
Ce calcul nous enseigne qu'une couche d'oxyde plus importante que l'oxyde natif pourrait avoir une influence favorable sur le démouillage en configuration confinée. Nous avons mené une série d'expérience afin de confirmer cette propriété.

Une couche de polystyrène (30 kg/mol) a été déposée sur différents substrats de 200 mm de diamètre. Ici nous n'en retiendrons que deux: un substrat standard, recouvert d'une couche d'oxyde natif de 2 nm, un autre substrat sur lequel une couche d'oxyde de 53 nm¹⁷ a été formée. Nous avons utilisé un moule comprenant des lignes de 147 nm de profondeur et de largeurs allant de 100 nm à 30 μ m. Les impressions ont été réalisées à 13 bar et 180°C pendant 15 min.

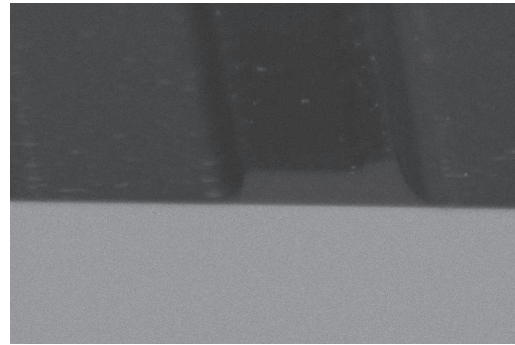
La figure 18 montre les résultats des impressions. Pour chaque échantillon, deux images en microscopie électronique sont présentées:¹⁸ celle de gauche est un contraste topographique de la surface (électrons secondaires), celle de droite est un contraste chimique (électrons rétrodiffusés, insensibles au chargement électrique de la surface). Sur les images de droite, chaque nuance de gris représente un matériau en fonction du numéro atomique de ses constituants. Par exemple, nous voyons sur la figure 18d de bas en haut: le silicium en gris clair, l'oxyde en gris moyen, et le polymère en gris foncé. Cette propriété est intéressante pour localiser les zones de démouillage. Sur la figure 18b, nous pouvons voir que l'épaisseur résiduelle est tou-

¹⁷Les épaisseurs sont mesurées par ellipsométrie.

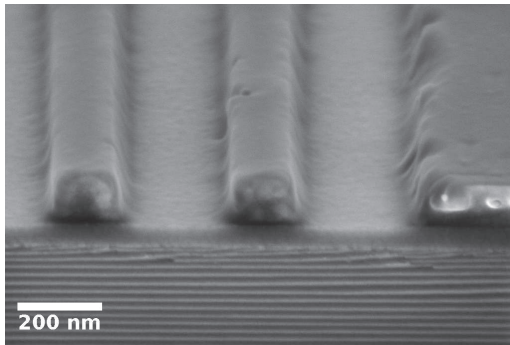
¹⁸*Nota bene*: il s'agit de vues en coupe inclinées, c'est-à-dire que sur la moitié haute de l'image, nous voyons le dessus de l'échantillon, tandis que sur la moitié basse nous voyons la coupe.



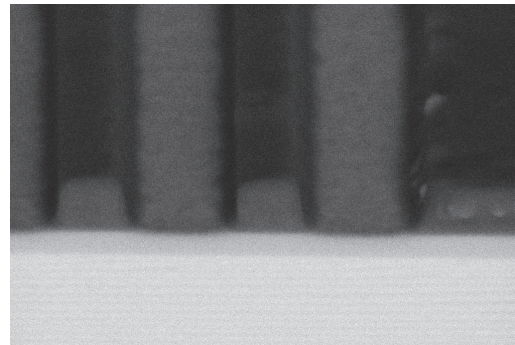
(a) Oxyde natif (2 nm), contraste topographique.



(b) Oxyde natif (2 nm), contraste chimique.



(c) Oxyde 53 nm, contraste topographique.



(d) Oxyde 53 nm, contraste chimique.

Figure 18 – Vues au microscopie électronique à balayage (coupe inclinée) de deux impressions: (a)&(b) une sur substrat standard; (c)&(d) l'autre sur substrat recouvert d'une couche de 53 nm d'oxyde.

jours présente, mais est parsemée de trous. En revanche, sur l'image 18d nous voyons que l'épaisseur résiduelle est rapportée en gris clair, ce qui suggère le démouillage du polymère dans cette zone. Néanmoins, la quantité de polymère restante n'a pu être précisément estimée.

Finalement, cette série d'expériences permet de confirmer l'influence positive d'une couche d'oxyde épaisse sur le démouillage de l'épaisseur résiduelle pendant l'impression. D'autres expériences seraient néanmoins nécessaires pour étudier plus finement la dynamique du démouillage en configuration confinée, et en présence d'autres matériaux.

Conclusion et perspectives

Cette thèse s'est attachée à mieux comprendre les écoulements de polymères fondus pour les procédés de nanoimpression. En ce qui concerne le fluage de nanostructures, nous avons tiré partie de deux modélisations suivant l'importance de l'épaisseur résiduelle. Le premier modèle présenté dans ce chapitre est une adaptation de la théorie des ondes capillaires pour les fortes épaisseurs résiduelles. Il s'agit à notre connaissance de la première application de cette théorie au fluage de motifs. Un des avantages décisifs de cette modélisation est, outre le fait de fournir des solutions analytiques (ou semi-analytiques) des écoulements, de pouvoir appréhender des fluides viscoélastiques. Le second modèle, courant en nanoimpression, est basé sur la théorie de lubrification. Nous avons pu reparcourir certains points clés de cette modélisation, comme la différence de vitesse de fluage en fonction de l'épaisseur locale.

Nous avons développé une méthode innovante de nanorhéologie des polymères en couche mince. Cette méthode, basée sur le fluage de motifs particuliers brevetés, permet d'accéder *in situ* à la viscosité et au temps de relaxation du matériau, qui sont des données clés pour les procédés de nanoimpression. Une application de cette méthode aux films ultra-minces (moins de 50 nm) serait une perspective intéressante pour étudier la variation des propriétés rhéologiques due au confinement de la matière.

Nous avons également appliqué le fluage à la fabrication de nanostructures complexes. Les modélisations simples de fluage que nous avons développées nous permettent d'envisager une optimisation rapide du motif initial afin d'approcher au mieux la forme désirée par fluage. Ceci a par exemple été appliqué à la fabrication de micolentilles asphériques. Cependant, pour les motifs à fort rapport de forme, une modélisation numérique complète est nécessaire. Il pourrait aussi être intéressant d'exploiter d'autres forces d'écoulement, comme des forces électrostatiques ou acoustiques.

Enfin nous nous sommes intéressés au démouillage de films ultra-minces dans le but de développer un procédé de nanoimpression sans épaisseur résiduelle. Nous avons appliqué la théorie de Lifshitz au calcul de la pression de disjonction dans le film de polymère. Cette théorie permet de prendre rigoureusement en compte l'influence d'un empilement de couches à proximité du fluide. Nous avons introduit le concept d'ingénierie de pression de disjonction par ajout de couches dédiées sur le moule ou le substrat. Il reste néanmoins beaucoup à faire, tant sur le plan théorique qu'expérimental, afin de maîtriser parfaitement le démouillage pour un procédé de nanoimpression sans épaisseur résiduelle.

Characterization and applications
of flowing nanoimprinted
thin polymer films

Edited on July 15, 2013 by Étienne Rognin
(etienne.rognin@centraliens.net).

This document was typeset by LYX document processor
(lyx.org) on $\text{L}\text{A}\text{T}\text{E}\text{X}$. Vector graphics were made with
Inkscape (inkscape.org), plots with Gnuplot
(gnuplot.info). These softwares are released under Open
Source licenses.

The original pdf version of this document contains useful
hyperlinks.

Contents

List of Symbols	xli
1 Introduction	1
1.1 Manufacturing at the nanoscale	1
1.2 Nanoimprint lithography	2
1.2.1 Nanoimprint processes	2
1.2.2 Features and advantages of NIL	4
1.2.3 Challenges	5
1.2.4 Issues addressed in this work	7
1.2.5 Equipments	8
1.3 Reading guideline	11
I Fluid mechanics for nanoimprint	15
2 Fluid mechanics at the nanoscale	17
2.1 Scales of the problem	18
2.1.1 Intermolecular forces	18
2.1.2 The continuum hypothesis	19
2.1.3 Scaling laws and nanoscale effects	21
2.2 Fundamental equations	23
2.2.1 Incompressible continuity equation	23
2.2.2 The Stokes equation	24
2.2.3 Energy transport	25
2.2.4 The isothermal hypothesis	26
2.2.5 Boundary conditions	27
2.2.6 Driving forces	29
2.3 Conclusion	30
3 Polymer melts rheology	35
3.1 Introduction	35
3.2 Basic properties of polymers	35
3.2.1 Molecular weight	35
3.2.2 Dimensions	36
3.2.3 Glass transition temperature	37

3.2.4	Density	38
3.2.5	Surface tension	39
3.2.6	Polymers used in this thesis	39
3.3	Bulk viscosity and viscoelasticity	39
3.3.1	Linear theory of viscoelastic fluids	39
3.3.2	Shear-thinning	42
3.3.3	Zero-shear viscosity: the WLF law	42
3.3.4	Linear viscoelasticity of polymers: the theory of reptation	45
3.4	Thin films properties	46
3.4.1	Thickness-dependent glass transition temperature	46
3.4.2	Thickness-dependent viscosity	47
II Creeping flows and applications		53
4	The supported thin film equations of creeping flow	55
4.1	Fundamental hypotheses	55
4.2	Lubrication theory: long wave approximation	57
4.2.1	The Reynolds equation	57
4.2.2	Smoothing or not smoothing	58
4.2.3	Governing dimensionless numbers	58
4.2.4	Some effects of non-linearity	61
4.3	Capillary wave theory: small deformation approximation	64
4.3.1	Dispersion relation	65
4.3.2	Viscous flows	66
4.3.3	Viscoelastic flows	68
4.4	Shear thinning criteria	70
4.4.1	Streamlines	70
4.4.2	Shear rate for a sinusoid	70
4.4.3	Shear rate in a nanoimprinted film	72
4.5	Comparison with full Stokes equation	74
4.5.1	Leveling delay	75
4.5.2	Kernel function	76
4.6	Conclusion	77
5	Partial reflow with residual layer for complex shapes manufacturing	81
5.1	General purposes	81
5.2	Reflow with a large residual layer	82
5.2.1	Reflow of spatially modulated isodense patterns	83
5.2.2	Reflow of non-isodense patterns	85
5.2.3	Reflow of 3D shapes	86
5.2.4	Elastic reflow	90
5.3	Reflow with a thin residual layer	91
5.3.1	Concept	91
5.3.2	Aspherical lens	91

5.3.3	Inverse reflow programing	94
5.4	Conclusion	94
6	Characterization of annealed nanoimprinted patterns applied to [...]	
	rheology	97
6.1	Introduction	97
6.1.1	State of the art	97
6.1.2	Overview of our method	98
6.2	Reflow of spatially modulated patterns	100
6.2.1	Model	100
6.2.2	Pattern design	101
6.2.3	Mold fabrication	101
6.3	Experimental viscosity measurements	102
6.3.1	Experiments	102
6.3.2	Results and discussion	104
6.4	Experimental viscoelastic measurements	106
6.4.1	Models	108
6.4.2	Single temperature example	108
6.4.3	Temperature dependence	111
6.4.4	Maxwell versus reptation model	111
6.5	Conclusion and outlooks	111
III	Tuned instabilities	117
7	Disjoining pressure and the modern theory of van der Waals forces	119
7.1	Studied geometries	119
7.2	Long-range van der Waals forces	120
7.2.1	Pair interaction between molecules	120
7.2.2	Hamaker's theory	121
7.2.3	Lifshitz' theory and the fluctuating sources	122
7.3	Dielectric functions	123
7.3.1	Macroscopic optical properties of materials	123
7.3.2	Experimental measurements and temperature dependence	125
7.4	Computation of van der Waals forces	126
7.4.1	Maxwell stress tensor	126
7.4.2	The issue of oscillating distribution	128
7.4.3	Integration in the complex plane	130
7.5	Exact solution for planar geometry	132
7.5.1	Retarded regime	132
7.5.2	Comparison with literature values	133
7.5.3	Anisothermal force and temperature dependence	133
7.6	Approximation for long-wave topology	134
7.7	Conclusion and open problems	134

8 Dewetting dynamics	139
8.1 Main concepts	139
8.2 Supported dewetting	142
8.2.1 Morphology	142
8.2.2 Growth rate in capillary wave theory	144
8.2.3 Dewetting structured film	145
8.3 Confined dewetting	147
8.3.1 State of the art	147
8.3.2 Evolution of the dewetted area.	148
8.3.3 Conclusion	148
9 Towards tuned dewetting for residual-layer-free nanoimprint	153
9.1 Disjoining pressure engineering	153
9.1.1 Disjoining pressure in stratified media	153
9.1.2 Role of silicon oxide	154
9.2 Supported dewetting experiments of the residual layer	158
9.2.1 Concept	158
9.2.2 Manufacturing of metallic nanostructures	158
9.2.3 Conclusion and outlooks	160
9.3 Dewetting experiments of the residual layer during imprint	161
9.3.1 Residual-layer-free nanoimprint: state of the art	161
9.3.2 Complete filling with silicone oxide layers: experiments	161
9.3.3 Other materials: simulations	168
9.3.4 Conclusion and outlooks	168
IV Conclusion and appendices	171
10 Conclusion	173
A Mathematical treatments for the supported thin film equations of creeping flow	177
A.1 Fourier transform	177
A.1.1 Fourier transform of an integrable function	177
A.2 Lubrication theory	178
A.2.1 Derivation of the Reynolds equation	178
A.2.2 Harmonics generation in lubrication theory	180
A.3 Capillary wave theory	181
A.3.1 Derivation of the dispersion relation	181
A.3.2 Solving integral dispersion relation	183
A.3.3 Streamlines	184
A.3.4 Shear rate	185
A.3.5 Reflow of spatially modulated patterns	187

B Numerical integration of the lubrication equation	189
B.1 Numerical scheme	189
B.2 Octave/Matlab Script	190
B.3 Inverse reflow programing	192
B.3.1 Cost function	192
B.3.2 Main script	194
C Flow simulation and rheological properties fitting in capillary wave theory	197
C.1 Main concept	197
C.2 Preliminary functions	197
C.2.1 Assumptions on geometry signals	197
C.2.2 rfft: Fast Fourier transform of a real signal	198
C.2.3 irfft: inverse of rfft	198
C.2.4 wavevector	198
C.2.5 f	199
C.3 Simulating a 2D flow	199
C.4 Simulating a 3D flow	200
C.5 Fitting rheological properties	201
C.5.1 Viscoelastic single mode Maxwell model	201
C.5.2 Cost function for a reptation model	202
D Numerical computation of the disjoining pressure	203
D.1 Optical data	203
D.2 Disjoining pressure formula	203
D.3 Matlab/Octave scripts	204
D.3.1 Dielectric functions from spectroscopic data	204
D.3.2 Green function for a simple set of 3 media	205
D.3.3 Green function for 5 media	205
D.3.4 Main function	207

List of Symbols

ϵ_0	permittivity of free space ($\text{N}\cdot\text{V}^{-2}$), page 124
\hbar	reduced Planck constant ($\text{J}\cdot\text{s}$), page 125
B	magnetic field ($\text{V}\cdot\text{s}\cdot\text{m}^{-2}$), page 124
E	electric field ($\text{V}\cdot\text{m}^{-1}$), page 124
μ_0	permeability of free space ($\text{s}^2\cdot\text{V}^2\cdot\text{N}^{-1}\cdot\text{m}^{-2}$), page 124
ξ_n	Matsubara frequency of order n (s^{-1}), page 128
A	Hamaker constant (J), page 30
k_B	Boltzmann constant ($\text{J}\cdot\text{K}^{-1}$), page 125
q	Conic paramter (with r), page 89
r	Conic paramter (with q), page 89
Bi	Biot number, page 26
Bo	Bond number, page 29
Br	Brinkman number, page 25
Ca	Capillary number, page 57
Cy	Cauchy number, page 24
De	Deborah number, page 66
Ha	Hamaker number, page 57
Kn	Knudsen number, page 20
Re	Reynolds number, page 24
β	Navier slip length (m), page 28
c_1, c_2	Coefficients for the WLF model (c_2 in K), page 42

c_p	Heat capacity ($\text{J}\cdot\text{kg}^{-1}\cdot\text{K}^{-1}$), page 25
η	Viscosity ($\text{Pa}\cdot\text{s}$), page 24
η_0	Zero-shear viscosity ($\text{Pa}\cdot\text{s}$), page 40
\mathbf{f}	Body force ($\text{N}\cdot\text{m}^{-3}$), page 24
γ	Surface tension or energy ($\text{N}\cdot\text{m}^{-1}$ or $\text{J}\cdot\text{m}^{-2}$), page 26
G	Elastic shear modulus (Pa), page 25
g	Gravity acceleration ($\text{m}\cdot\text{s}^{-2}$), page 29
$\dot{\gamma}$	Shear strain rate (s^{-1}), page 38
$\dot{\gamma}_0$	Critical shear rate (shear thinning) (s^{-1}), page 40
G_e	Plateau modulus (Pa), page 43
H	Heat transfer coefficient per unit of surface ($\text{W}\cdot\text{m}^{-2}\cdot\text{K}^{-1}$), page 26
h	Local film thickness (m), page 28
h_0	Mean film thickness (m), page 28
κ	Curvature (m^{-1}), page 27
k	Wavevector (m^{-1}), page 55
ℓ	Typical length (m), page 20
Λ	Mean free path (m), page 20
λ_e	Critical elastic wavelength (m), page 66
ℓ_{cap}	Capillary length (m), page 29
ℓ_e	Effective elementary length (m), page 35
M_e	Average molecular mass between entanglements ($\text{kg}\cdot\text{mol}^{-1}$), page 43
M_w	Molecular weight ($\text{kg}\cdot\text{mol}^{-1}$), page 34
N	Degree of polymerization, page 34
∇	Gradient (m^{-1}), page 30
$\nabla\cdot$	Divergence operator (m^{-1}), page 23
p	Pressure field (Pa), page 24
Pe	Péclet number, page 25

Π	Disjoining pressure (Pa), page 30
ρ	Density ($\text{kg}\cdot\text{m}^{-3}$), page 24
R	Gas constant ($\text{J}\cdot\text{K}^{-1}\cdot\text{mol}^{-1}$), page 43
R_{EE}	End-to-end distance (polymer size) (m), page 34
R_G	Radius of gyration (m), page 35
\mathbb{T}	Viscous stress tensor (Pa), page 24
T	Temperature (K or $^{\circ}\text{C}$), page 25
t	Time (s), page 65
τ_C	Rouse relaxation time of a polymer (s), page 44
τ_d	Characteristic time of thermal diffusion (s), page 26
τ_t	Terminal relaxation time of a polymer (s), page 43
T_g	Glass transition temperature (K or $^{\circ}\text{C}$), page 35
T_s	Reference temperature for the WLF model (K), page 42
\mathbf{v}	Velocity ($\text{m}\cdot\text{s}^{-1}$), page 23

Chapter 1

Introduction

1.1 Manufacturing at the nanoscale

Over the past few decades, nanotechnologies have opened new opportunities in various fields such as information technologies, energy, chemistry or biology. Manufacturing at the molecular level motivates scientists and engineers to face problems from new points of view.

Smaller and smaller. In information technologies, the miniaturization of optical devices has created a new need for micro and nano optical components. For instance, micro-lenses array can be created at the surface of an imaging sensor in order to bring new functions at the pixel level (Völkel *et al.*, 2003; Vaillant *et al.*, 2007; Fesenmaier *et al.*, 2008). In a different field, *labs on chip* are systems that perform many tasks of biological analysis along a functionalized surface of small extent, with tiny amounts of fluid. The applications for health are extremely promising (Becker and Locascio, 2002; Cho *et al.*, 2003; Stone *et al.*, 2004; Mills *et al.*, 2005; Craighead, 2006). Nevertheless their widespread distribution requires the control of a process to manufacture microfluidic channels and nanoscale functions at low cost.

Surface nanopatterning as a performance booster. It has been demonstrated that appropriate surface nanopatterning can enhance the efficiency of solar cells (Zeng *et al.*, 2006; Bermel *et al.*, 2007), or promote photon extraction of LED and OLED (Schnitzer *et al.*, 1993; Matterson *et al.*, 2001; Möller and Forrest, 2002; Green *et al.*, 2001). In sensors applications, substrates for Raman spectroscopy with specific metallic nanostructures on their surface enable a phenomenon called Surface Enhanced Raman Scattering (SERS). Thanks to this effect, molecules can be detected even in extremely small concentration (Moskovits, 1985; Tian *et al.*, 2002; Li *et al.*, 2011). In biology, cell growth substrates, for instance, benefit from new properties of patterned surfaces for tissue engineering, drug testing, or even neuronal computing. On a substrate patterned with nanopillars, cell colonies do not spread randomly but gather at certain places of the pattern, forming organized lines, arrays and clusters (Kleinfeld *et al.*, 1988; Chen *et al.*, 1997; Lehnert *et al.*, 2004).

These applications based on large surfaces require low cost, high throughput and high resolution patterning techniques. Nanoimprint lithography is a promising technology for such purposes. This manufacturing technology is the framework of the present thesis.

1.2 Nanoimprint lithography

1.2.1 Nanoimprint processes

NanoImprint Lithography (NIL) is a patterning technique in which a topography is replicated by pressing a mold (master) into a material. The difference in hardness between the mold and the imprinted material enables the displacement (or flow) and the shaping of the latter. It can be realized by heating the material at a temperature where it becomes relatively viscous, or starting from a viscous material, by hardening the molded shape with a curing process, or a combination of both. Extensive reviews on NIL were published by Guo (2004, 2007); Schiff (2008); Schiff and Kristensen (2010); Landis (2010), to cite only a few.

The particularity of NIL that distinguishes it from other molding techniques such as injection, is that the characteristic dimensions of the imprinted patterns scale down from several micrometers to a few nanometers. At such scales, the patterning techniques usually employed are the optical photo-lithography or the electron-beam lithography. The principle of these techniques, here called classical lithography, is outlined on figure 1.1a on the facing page. (i) A photo-sensitive or electron-sensitive resist is coated on a substrate. (ii) The film is exposed selectively to an energy beam, which can be light going through a mask or a deflected electron beam. A chemical reaction in the exposed areas changes the chemical properties of the resist. (iii) A chemical cleaning called development reveals the patterning of the film.

Classical lithography, as the driving technology in the semiconductor industry, has achieved great resolutions and complex manufacturing capabilities. Nevertheless, the cost of equipments and processes prevents this technology from spreading outside high value-added patterning steps. In particular, it makes this technology less relevant for the applications cited in the previous section.

Thermal NIL. Thermal NIL was first developed by Chou *et al.* (1995, 1996a,b). Figure 1.1b presents the main steps of thermal NIL:

1. A thin thermoplastic resist film is coated on a substrate.
2. A patterned mold is pressed against the film and the whole system is heated at a temperature at which the resist is viscous and can flow. The cavities of the mold are filled by capillary forces and pressure applied by the mold.
3. The film is cooled down to room temperature at which the resist recovers its solid-like mechanical behavior.
4. The system is demolded.

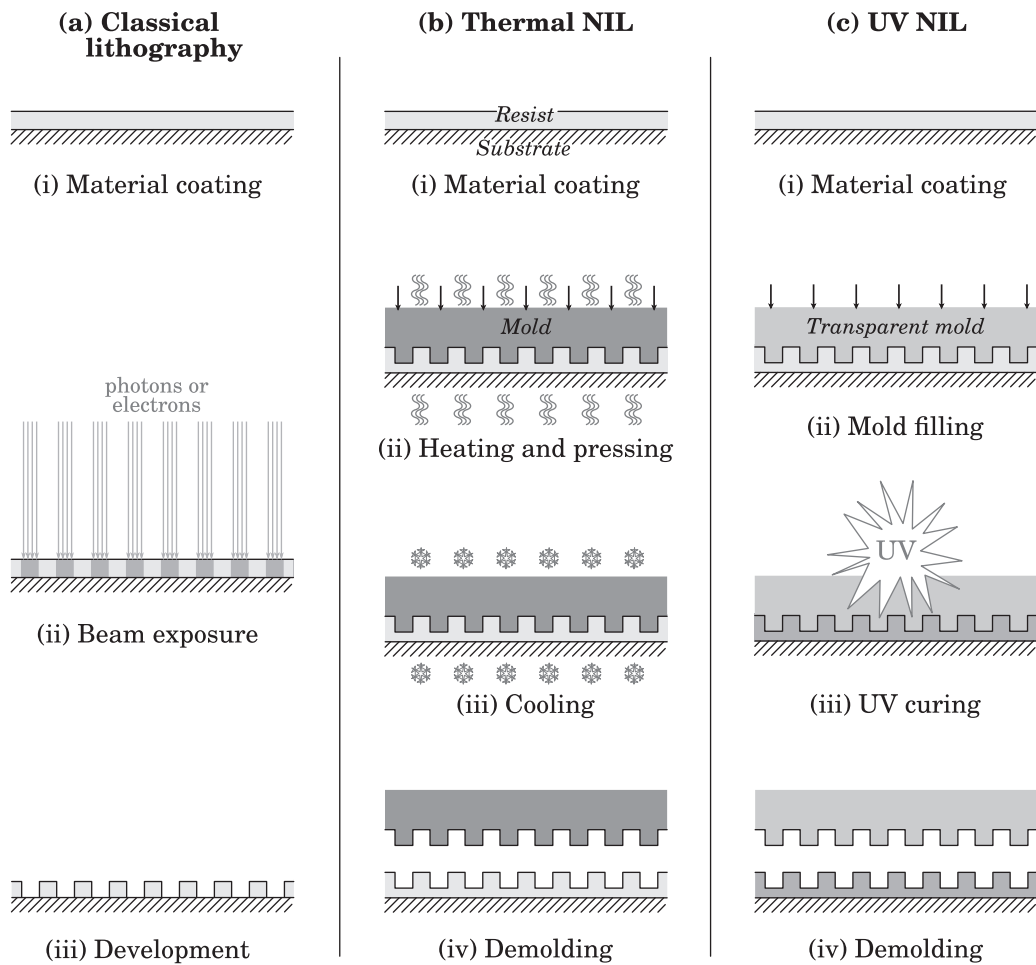


Figure 1.1 – Main steps (cross-section scheme) of lithography processes in (a) Classical lithography, compared with (b) Thermal NIL, and (c) UV NIL.

UV NIL. This technique was first developed by Haisma *et al.* (1996) from Philips Research Laboratories. Similarly to thermal NIL, this technique consists in molding a thin resist film. But the change in mechanical properties of the resist is not given by temperature, but by an ultraviolet light (UV) assisted chemical reaction. The steps of UV NIL are the following (see Fig. 1.1c):

1. A thin UV-curable resist film is coated on a substrate. The material is usually viscous at room temperature.
2. A UV-transparent patterned mold is pressed against the resist.
3. The patterned film is cured by UV exposure. The molecules of the resist cross-link with covalent bonds: they form a hard three-dimensional network.
4. The system is demolded.

Other NIL processes. Many variants of NIL have been proposed, but the aim here is not to list them exhaustively. For instance, in order to enhance the throughput or to pattern large surfaces, several techniques have been developed:

FAST-NIL (Fig. 1.2a) is similar to thermal NIL, but is based on the idea that only the thin resist layer needs to be heated, and not the whole imprint system. The flow of the resist (or even of the substrate) is enabled by a very localized heating, which speeds up the thermal cycles considerably. The required energy is transferred either by thermal resistances embedded in the mold (Tormen *et al.*, 2008), ultra-sonic waves (Mekaru *et al.*, 2007; Mayer *et al.*, 2012), or a laser pulse through a transparent mold (Chou *et al.*, 2002; Xia *et al.*, 2003). These promising techniques are challenged by physical issues in nanoscale and high temperature gradient heat transfer, and out-of-equilibrium phenomena.

STEP AND REPEAT (Fig. 1.2b) is a process where the mold is smaller than the surface to be patterned. The imprint (thermal or UV) process is performed at a location and the mold is moved to the next area. Alignment and stitching are the general issues encountered in this process.

ROLL TO PLATE (Fig. 1.2c) makes use of a cylindrical mold that rolls over the resist layer.

ROLL TO ROLL (Fig. 1.2d) is a process to nanopattern a rolled-up film.

1.2.2 Features and advantages of NIL

The principle of NIL is simple, and thus relatively low-cost. It does not require expensive optical systems or light sources, as in the case of optical lithography. In fact, even if the mold is expensive to produce, the expense is offset by the capability to produce as many imprints as needed.

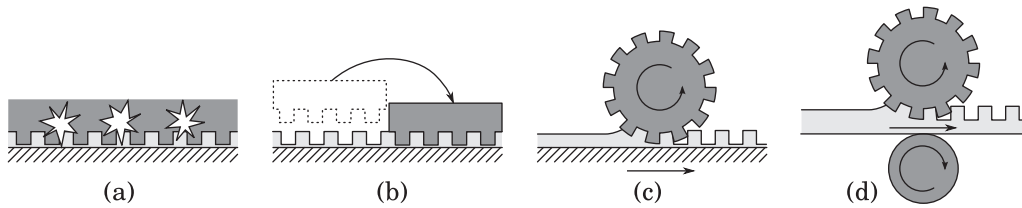


Figure 1.2 – Some variants of nanoimprint processes for high throughput or large surface applications: **(a)** Fast-NIL (local heating of the resist); **(b)** Step and repeat; **(c)** Roll to plate; **(d)** Roll to roll.

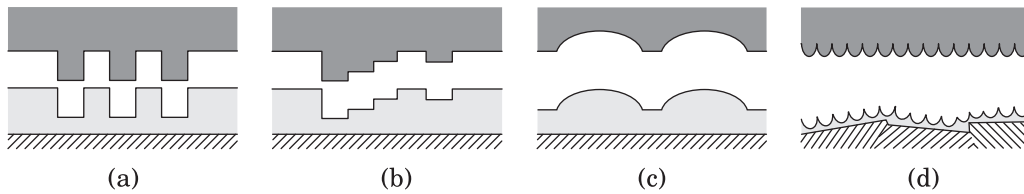


Figure 1.3 – Various types of nanoimprint molds: **(a)** 2D classical mold **(b)** 3D multi-level mold **(c)** 3D smooth mold **(d)** Soft mold.

The resolution is not limited by a chemical reaction resolution or a beam size. It is rather limited by the resolution of the mold itself, and by how intimate the molding of the material is. In fact, it has been demonstrated by Hua *et al.* (2004) that the topography of a single 2-nm molecule could be reproduced.

Another advantage of NIL is the variety of topographies that can be molded. Several types are presented in figure 1.3. In addition to the classical two-dimensional (2D) shapes (Fig. 1.3a), three-dimensional (3D) multi-level (Fig. 1.3b) or smooth (Fig. 1.3c) patterns can be replicated. Besides, when making use of a bendable mold, non-planar substrates such as polycrystalline materials or rounded surfaces can be patterned (Fig. 1.3d).

Many materials are available for NIL, and their cost is usually lower than high-resolution photoresists. Moreover, functional materials such as high-index optical, or conductor polymers can be directly patterned.

1.2.3 Challenges

In spite of the many advantages listed above, NIL has encountered challenges that are as serious as they are exciting. Here again, the purpose is not to refer to them thoroughly, but to draw the general issues encountered in this technology.

Issues specific to thermal NIL. When needed, alignment is a major challenge in thermal NIL. Alignment is the ability to place the patterning of a layer aligned with respect to a previously patterned underlying stack. It requires transparent molds in the short wavelengths, where silicon molds generally used are opaque. Since the

system is heated for enabling flow of the resist, thermal expansion also plays against precision displacement and mechanical contact. Thermal expansion of silicon is of the order of $1 \mu\text{m}/\text{m}/\text{K}$, which represents an expansion of $30 \mu\text{m}$ for a 200-mm wafer heated from room temperature to a standard imprint temperature of 170°C . Or equivalently, for the same wafer, a misalignment of 200 nm is induced by a temperature difference of only one degree Celsius.

Moreover, heating the wafer may damage the previously made structures. If the thermal cycle is too long, dopants can migrate from their original place, or structures can reflow.

Issues specific to UV NIL. For UV NIL, the fast process cycles are penalized by mold cleaning steps and reduced mold lifetime. Indeed, the UV-assisted chemical reaction happening at the interface between the mold and the UV-resist tend to damage the anti-sticking coatings of the mold.

A hot topic in UV NIL is also the pattern fidelity of the molding. The cross-linking reactions induce a shrinkage of the resist which is highly anisotropic and heterogeneous. An important effort is put in the development of low-shrinkage materials and the numerical prediction of the phenomenon.

General challenges. NIL in general is also confronted with the following challenges. Because NIL is a patterning technique that requires mechanical contact, the amount of defects in the shaping process, called *defectivity*, is pointed out as a major issue. Defects may come from various phenomena. The most spectacular one (because visible to the naked eye) is particle contamination. If a particle gets trapped between the mold and the resist, it will induce a severe deformation of the mold during imprint, and the patterning defect may spread far from the actual particle location. Nevertheless, defectivity by particle contamination is likely to be eliminated with more advanced automatic equipments and foup¹ handling.

Other types of defectivity are ill mold filling and capillary defects. They originate from uncontrolled fluid flows during imprint. The driving force of the flow is indeed not always the pressure applied by the mold, which is a process parameter, but may be capillary phenomena. Capillary defects may create unwanted patterns such as viscous fingering, holes, etc. Friction and propagating cracks occurring during demolding can also damage the imprinted patterns, in particular high aspect ratio² features.

Finally, other challenges involve the residual layer. The residual layer is the resist layer left under the protrusions of the mold. This aspect is a characteristic difference between NIL and classical lithography where unwanted resist is completely washed away at the development step (Fig. 1.1). Figure 1.4 on the facing page is an illustration of a residual layer issue. In this example, NIL is used to create a lithographic mask, in other words, the imprinted pattern is to be transferred into the underlying substrate. Usually, the residual layer is removed (or opened) with a Reactive Ion

¹Foup means Front Opening Universal Pod.

²Height over width of the feature.

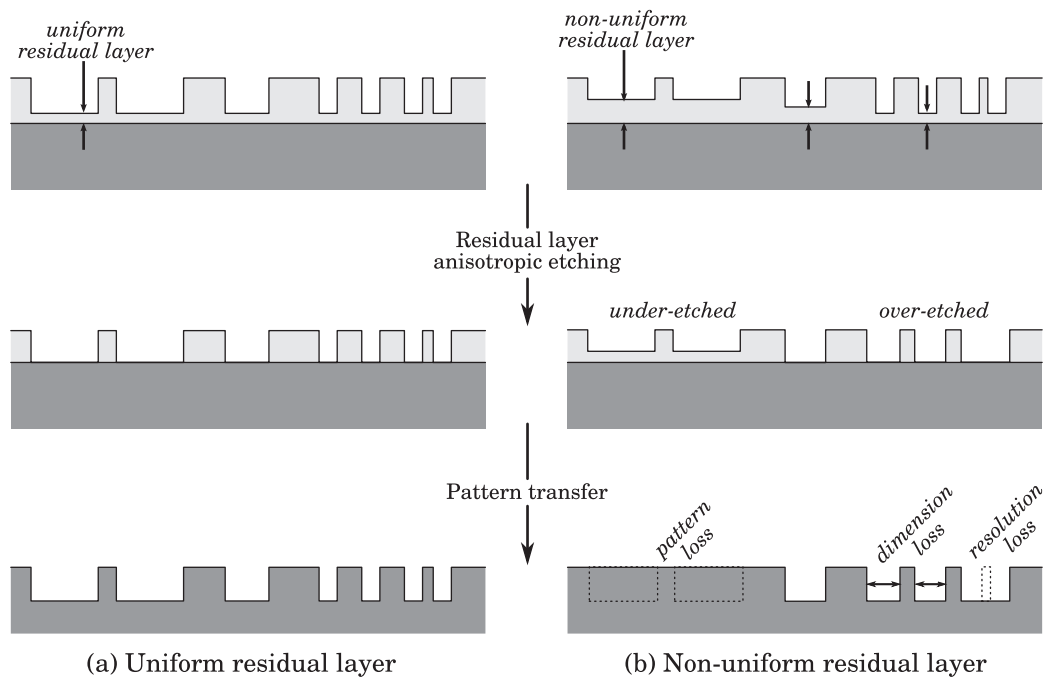


Figure 1.4 – Pattern transfer from a nanoimprinted mask with (a) a uniform residual layer and (b) a non-uniform residual layer.

Etching (RIE) process that is highly anisotropic for that purpose. In an ideal case, the residual layer is uniform (Fig. 1.4a), and the RIE reduces the resist thickness vertically without damaging the patterns horizontally. Nevertheless, in a realistic case, the residual may not be uniform (Fig. 1.4b). Indeed, narrow protrusions of the mold displace the resist more easily than larger ones. Where the residual layer is thicker, the RIE may not open this layer at all, whereas where it is thinner, the RIE may begin to attack the resist on the sidewalls. The resulting transferred pattern may then be quite different from the original master.

Important efforts have been put in the control and simulation of the residual layer. This is a multi-scale, highly-coupled problem between fluid and solid mechanics.

1.2.4 Issues addressed in this work

This thesis presents theoretical and experimental work on nanoscale flows of polymer melts occurring in the framework of nanoimprint lithography. Developments in microfluidics have brought a good understanding of capillary driven flows. However, at the nanoscale, in other words for polymer films thinner than about a hundred nanometers, other effects must be considered, such as disjoining pressure arising from the long-range van der Waals interactions, or even the deviation of material properties (viscosity, glass transition temperature) from their bulk value. A better understanding of these effects is an important step in the development of nanoimprint technology.

Reflow of a nanoimprinted pattern. Reflow of nanostructures is a common and growing manufacturing technique, especially in optical applications where smooth and curved topographies are needed. This technique is mainly empirical, and the available models are limited to few geometries and mechanical behavior laws. In this work, we apply versatile and efficient modeling tools to the reflow of a polymer film that is first nanoimprinted and then annealed above its glass transition temperature. Depending on the initial topography of the film, different leveling dynamics emerge from this analytical and numerical study. Several concepts of reflow, for instance based on the material viscoelasticity, or the thickness of the residual layer, can be developed. These concepts are applied to the manufacturing of optical devices from the reflow of complex nanostructures.

Nanoscale polymer characterization. An accurate knowledge of the mechanical properties of polymers at the nanoscale is a key step towards realistic simulations of NIL processes. Relevant physical inputs such as the material viscosity or the elastic relaxation time are required to produce consistent NIL models. However, a general, low-cost and fast method is still lacking to measure *in situ* the mechanical properties of polymer melts. In this work, we develop such a method based on the leveling of an especially designed nanoimprinted pattern. The Newtonian viscosity and the terminal relaxation time of coated polymer films can be measured in a standard NIL environment.

Dewetting of ultra-thin films. For very thin films, disjoining pressure becomes the driving force, and can lead to the breakup of the residual layer and the growth of dry areas on the substrate, a phenomenon referred to as spinodal dewetting. The current understanding of this phenomenon is limited to several ideal cases, and not appropriate to NIL where topographies and flows are complex.

If unwanted, dewetting can be a severely damaging phenomenon, and the ability to control its dynamics would be a key factor to reduce mold filling defectivity in NIL. On the other hand, a controlled dewetting of the residual layer could open a new route towards residual-layer-free NIL processes. In this work, an exploratory work is carried out in that matter. Emphasis is put on the accurate computation of the disjoining pressure in stratified media with the modern Lifshitz theory based on the optical properties of the interacting materials. The dewetting of the residual layer is studied in two configurations: during the imprint and after the imprint during an annealing step. The disjoining pressure can be tuned by the materials of the substrate or of the mold in order to promote the dewetting of the residual layer.

1.2.5 Equipments

For this thesis, experiments were carried out in the clean rooms of CEA Grenoble. Advanced pre-production tools could be used. Nevertheless, the drawback is that little customization freedom is left to the user.

Substrates, molds and materials. For substrates we use standard 200-mm (8") silicon wafers, that are monocrystalline silicon disks of 750 μm of thickness and 200 mm of diameter. A thin (2 nm) native oxide layer covers the wafer. The molds are made of the same wafers and are manufactured by e-beam lithography. The surface of the molds is coated with a fluorinated silane anti-sticking layer.

The materials mainly used in this work are thermoplastic polymers. They are diluted in a solvent (toluene or anisole) and cast by a rotating process called *spin-coating*. Any remaining solvent is expelled by a short annealing. The thickness of the coated layer depends on the rotation speed and the polymer concentration. With this technique, highly uniform (variation of the order of the nanometer over the full wafer) films from several nanometers to several micrometers can be manufactured.

Thermal nanoimprint tool. The imprints were made with a commercial tool EVG 520HE from EV Group, pictured in figure 1.5a. It consists in a press enclosed in a vacuum chamber. Figure 1.5b represents the stack of a standard imprint process in this equipment. The vise is composed of two heating and cooling systems, on each side of the press. On each side, a hard steel plate transfers the pressure of the press to a soft PTFE layer that can absorb roughness or small defects. This soft layer is wrapped in a multi-purpose clean room wipe in order to limit contamination. The mold and the coated wafer are finally sandwiched in the middle of this stack.

The process is controlled by software with feed-back from pressure and temperature sensors. The user can for instance control the vacuum in the chamber, the temperature of the bottom and top plate (in the limit of the thermal inertia of the system), the force (in Newtons) applied by the screw, up to 40 kN (about a weight of 4000 kg, or a pressure of 13 bar on the wafer). Figure 1.6 displays a record of an imprint monitoring.

Characterization. Characterization of flows at the macroscale is usually done by optical methods, such as Particle Tracking Velocimetry (PTV), or Particle Image Velocimetry (PIV). The velocity field of the flow can be extracted from images correlation of moving tracers. These methods cannot be used at the micro and nanoscale because of limitations due to the diffraction of light. In fact, a down-scale approach of PIV consists in following submicron fluorescent beads as embedded tracers in the material. Nevertheless, the numerous results reported for this technique (Tretheway and Meinhart, 2002; Oppong *et al.*, 2006; Joseph and Tabeling, 2005) make use of tracers of 50-nm to 500-nm typical diameter, which is comparable to the thickness of our polymer films. Although 25-nm fluorescent tracers are now available (for the smallest), this size of bead still makes the method highly invasive for sub-100-nm film flows.

The general method followed in this work is based on the characterization of the free interface of the flow. Indeed, if the motion of the free interface is known, with use of an appropriate model, we can extract some information about the flow inside the fluid. This is called an *inverse* method. Several techniques have been developed to monitor the free interface at the nanoscale in real-time. They will be extensively reviewed in the beginning of chapter 6. In this work, we preferred to benefit from

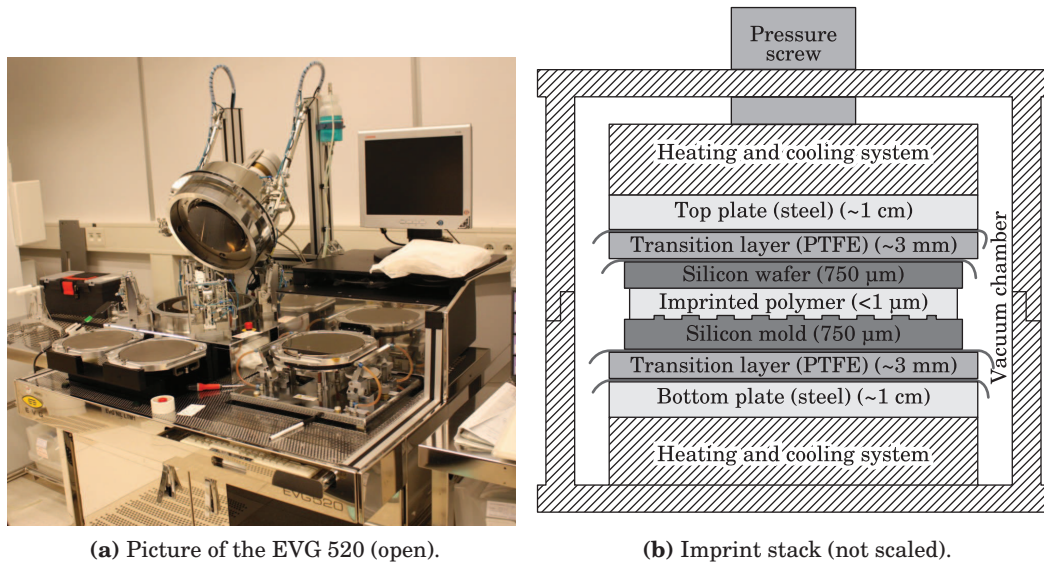


Figure 1.5 – Thermal NIL equipment.

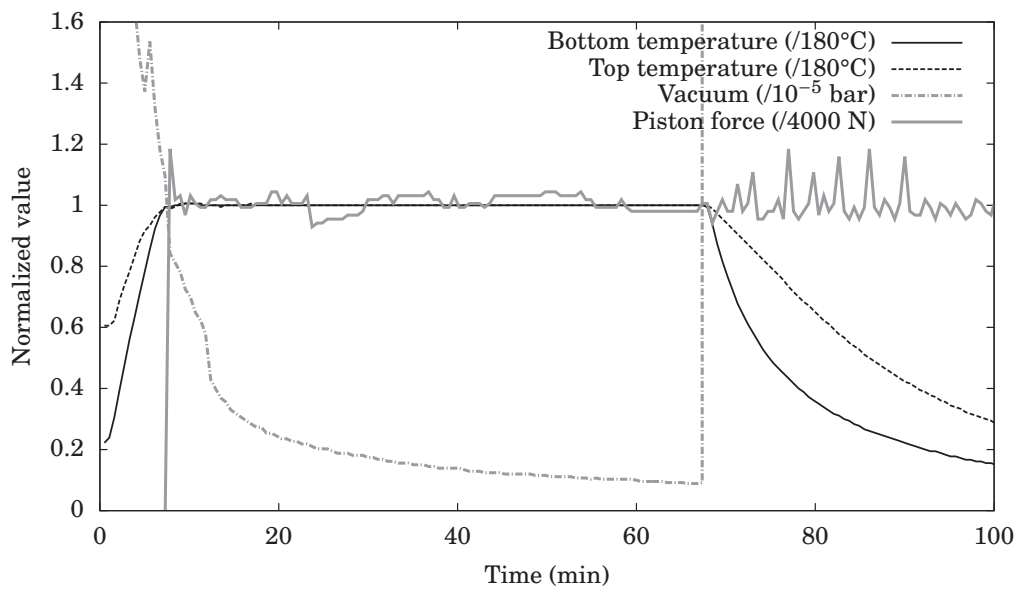


Figure 1.6 – Monitoring of a standard imprint process. 0–8 min heating and vacuum step; 8 min–68 min, imprint step; 68 min–100 min, cooling step; after 100 min, force releasing and demolding.

the fact that polymers we used have a solid-like behavior at room temperature. By a quench (rapid cooling) of the resist, we can then observe a frozen state of the flow. This allows the observation of the free interface to be made by common microscopy techniques, such as optical and confocal microscopy (resolution down to 200 nm), scanning electron microscopy (a few nanometers) or atomic force microscopy (less than a nanometer in height, a few nanometers in lateral dimensions). Flows occurring during the imprint process could only be characterized after cooling and demolding.

1.3 Reading guideline

In addition to this introductory chapter, this manuscript is divided into four parts:

Fluid mechanics for nanoimprint. This part gathers two didactic chapters. Chapter 2 is devoted to nanoscale fluid mechanics. The fundamental equations are derived from scaling discussions. Chapter 3 presents polymer melts rheology. Basic properties are reviewed, as well as thin film properties that are specific to the nanoimprint field. As these two chapters are mainly intended for non-specialists of the field, experienced readers would rapidly move on to the next part.

Creeping flows and applications. Chapter 4 presents two theories of nanoscale free surface flows. The commonly used lubrication theory is reviewed. Nevertheless, it was found that another model based on capillary wave theory is more appropriate in some cases. Results that are special achievements of this thesis, for instance on non-linearity, viscoelasticity, or shear thinning, are also discussed. Chapter 5 is completely dedicated to the applications of patterned films reflow. Various concepts of reflow are exposed, many of which are illustrated by experimental implementations. Chapter 6 presents the reflow of specially designed nanopatterns for characterizing polymer properties. Viscosity and viscoelasticity can be extracted with the method presented there.

Tuned instabilities. This part addresses the problem of thin polymer film stability. Chapter 7 presents the Lifshitz theory for computing the contribution of long-range van der Waals forces to the disjoining pressure in a thin film. Readers who are not familiar with van der Waals forces or electrostatics may find this chapter rather cumbersome. However, a thorough comprehension is not necessary for to follow this part, and chapter 7 can be skipped in a first approach. Chapter 8 is a review of the dewetting dynamics of thin polymer films. In addition, new observations of dewetting patterns under confinement are reported. Chapter 9 is a presentation of exploratory work on a residual-layer-free nanoimprint process based on dewetting phenomena. Both theoretical calculations and experimental implementations are investigated.

Conclusion and appendices. Chapter 10 is the closing chapter of this thesis. It contains a summary of work developed in this thesis. The following appendices report

the mathematical developments used throughout the manuscript. Commented source codes of several numerical tools are also reported.

References

- H. Becker and L. E. Locascio. Polymer microfluidic devices. *Talanta* **56**, 267–287 (2002).
- P. Bermel, C. Luo, L. Zeng, L. C. Kimerling, and J. D. Joannopoulos. Improving thin-film crystalline silicon solar cell efficiencies with photonic crystals. *Optics Express* **15**, 16986–17000 (2007).
- C. S. Chen, M. Mrksich, S. Huang, G. M. Whitesides, and D. E. Ingber. Geometric control of cell life and death. *Science* **276**, 1425–1428 (1997).
- S. K. Cho, H. Moon, and C.-J. Kim. Creating, transporting, cutting, and merging liquid droplets by electrowetting-based actuation for digital microfluidic circuits. *Journal of Microelectromechanical Systems* **12**, 70 – 80 (2003).
- S. Y. Chou, P. R. Krauss, and P. J. Renstrom. Imprint of sub-25 nm vias and trenches in polymers. *Applied Physics Letters* **67**, 3114–3116 (1995).
- S. Y. Chou, P. R. Krauss, and P. J. Renstrom. Imprint lithography with 25-nanometer resolution. *Science* **272**, 85–87 (1996)a.
- S. Y. Chou, P. R. Krauss, and P. J. Renstrom. Nanoimprint lithography. *Journal of Vacuum Science and Technology B: Microelectronics and Nanometer Structures* **14**, 4129–4133 (1996)b.
- S. Y. Chou, C. Keimel, and J. Gu. Ultrafast and direct imprint of nanostructures in silicon. *Nature* **417**, 835–837 (2002).
- H. Craighead. Future lab-on-a-chip technologies for interrogating individual molecules. *Nature* **442**, 387–393 (2006).
- C. C. Fesenmaier, Y. Huo, and P. B. Catrysse. Optical confinement methods for continued scaling of CMOS image sensor pixels. *Optics Express* **16**, 20457–20470 (2008).
- M. A. Green, J. Zhao, A. Wang, P. J. Reece, and M. Gal. Efficient silicon light-emitting diodes. *Nature* **412**, 805–808 (2001).
- L. J. Guo. Nanoimprint lithography: Methods and material requirements. *Advanced Materials* **19**, 495–513 (2007).
- L. J. Guo. Recent progress in nanoimprint technology and its applications. *Journal of Physics D: Applied Physics* **37**, R123–R141 (2004).
- J. Haisma, M. Verheijen, K. v. d. Heuvel, and J. v. d. Berg. Mold-assisted nanolithography: A process for reliable pattern replication. *Journal of Vacuum Science and Technology B: Microelectronics and Nanometer Structures* **14**, 4124–4128 (1996).
- F. Hua, Y. Sun, A. Gaur, M. A. Meitl, L. Bilhaut, L. Rotkina, J. Wang, P. Geil, M. Shim, J. A. Rogers, and A. Shim. Polymer imprint lithography with molecular-scale resolution. *Nano Letters* **4**, 2467–2471 (2004).

- P. Joseph and P. Tabeling. Direct measurement of the apparent slip length. *Physical Review E* **71**, 035303 (2005).
- D. Kleinfeld, K. H. Kahler, and P. E. Hockberger. Controlled outgrowth of dissociated neurons on patterned substrates. *The Journal of Neuroscience* **8**, 4098–4120 (1988).
- S. Landis. NanoImprint lithography. In *Nano Lithography*, pages 87–168. Wiley-ISTE, 1 edition (2010).
- D. Lehnert, B. Wehrle-Haller, C. David, U. Weiland, C. Ballestrem, B. A. Imhof, and M. Bastmeyer. Cell behaviour on micropatterned substrata: limits of extracellular matrix geometry for spreading and adhesion. *Journal of Cell Science* **117**, 41–52 (2004).
- W.-D. Li, F. Ding, J. Hu, and S. Y. Chou. Three-dimensional cavity nanoantenna coupled plasmonic nanodots for ultrahigh and uniform surface-enhanced raman scattering over large area. *Optics Express* **19**, 3925–3936 (2011).
- B. J. Matterson, J. M. Lupton, A. F. Safonov, M. G. Salt, W. L. Barnes, and I. D. W. Samuel. Increased efficiency and controlled light output from a microstructured light-emitting diode. *Advanced Materials* **13**, 123–127 (2001).
- A. Mayer, K. Dhima, S. Möllenbeck, S. Wang, and H.-C. Scheer. A novel tool for frequency assisted thermal nanoimprint (T-NIL). pages 83520N–83520N (2012).
- H. Mekar, H. Goto, and M. Takahashi. Development of ultrasonic micro hot embossing technology. *Microelectronic Engineering* **84**, 1282–1287 (2007).
- C. Mills, E. Martinez, F. Bessueille, G. Villanueva, J. Bausells, J. Samitier, and A. Errachid. Production of structures for microfluidics using polymer imprint techniques. *Microelectronic Engineering* **78-79**, 695–700 (2005).
- M. Moskovits. Surface-enhanced spectroscopy. *Reviews of Modern Physics* **57**, 783–826 (1985).
- S. Möller and S. R. Forrest. Improved light out-coupling in organic light emitting diodes employing ordered microlens arrays. *Journal of Applied Physics* **91**, 3324–3327 (2002).
- F. K. Opong, L. Rubatat, B. J. Frisken, A. E. Bailey, and J. R. de Bruyn. Microrheology and structure of a yield-stress polymer gel. *Physical Review E* **73**, 041405 (2006).
- H. Schiff. Nanoimprint lithography: An old story in modern times? a review. *Journal of Vacuum Science & Technology B: Microelectronics and Nanometer Structures* **26**, 458–480 (2008).
- H. Schiff and A. Kristensen. Nanoimprint lithography – patterning of resists using molding. In *Handbook of Nanotechnology*, pages 239–278. Bhushan, Bharat, springer edition (2010).
- I. Schnitzer, E. Yablonovitch, C. Caneau, T. J. Gmitter, and A. Scherer. 30% external quantum efficiency from surface textured, thin-film light-emitting diodes. *Applied Physics Letters* **63**, 2174–2176 (1993).
- H. Stone, A. Stroock, and A. Ajdari. Engineering flows in small devices. *Annual Review of Fluid Mechanics* **36**, 381–411 (2004).

- Z.-Q. Tian, B. Ren, and D.-Y. Wu. Surface-enhanced raman scattering: from noble to transition metals and from rough surfaces to ordered nanostructures. *The Journal of Physical Chemistry B* **106**, 9463–9483 (2002).
- M. Tormen, R. Malureanu, R. H. Pedersen, L. Lorenzen, K. H. Rasmussen, C. J. Lüscher, A. Kristensen, and O. Hansen. Fast thermal nanoimprint lithography by a stamp with integrated heater. *Microelectronic Engineering* **85**, 1229–1232 (2008).
- D. C. Tretheway and C. D. Meinhart. Apparent fluid slip at hydrophobic microchannel walls. *Physics of Fluids* **14**, L9–L12 (2002).
- J. Vaillant, A. Crocherie, F. Hirigoyen, A. Cadien, and J. Pond. Uniform illumination and rigorous electromagnetic simulations applied to CMOS image sensors. *Optics Express* **15**, 5494–5503 (2007).
- R. Völkel, M. Eisner, and K. Weible. Miniaturized imaging systems. *Microelectronic Engineering* **67-68**, 461–472 (2003).
- Q. Xia, C. Keimel, H. Ge, Z. Yu, W. Wu, and S. Y. Chou. Ultrafast patterning of nanostructures in polymers using laser assisted nanoimprint lithography. *Applied Physics Letters* **83**, 4417–4419 (2003).
- L. Zeng, Y. Yi, C. Hong, J. Liu, N. Feng, X. Duan, L. C. Kimerling, and B. A. Alamariu. Efficiency enhancement in si solar cells by textured photonic crystal back reflector. *Applied Physics Letters* **89**, 111111–111111–3 (2006).

Part I

Fluid mechanics for nanoimprint

Chapter 2

Fluid mechanics at the nanoscale

If, in some cataclysm, all of scientific knowledge were to be destroyed, and only one sentence passed on to the next generations of creatures, what statement would contain the most information in the fewest words? I believe it is the atomic hypothesis (or atomic fact, or whatever you wish to call it), that all things are made of atoms—little particles that move around in perpetual motion, attracting each other when they are little distance apart, but repelling upon being squeezed into one another. In that one sentence, you will see, there is an enormous amount of information about the world, if just a little imagination and thinking are applied. (Feynman *et al.*, 1963, p. 1-2)

All things are made of atoms—Right from the beginning of his famous *Lectures on Physics*, Feynman emphasizes the role of atoms in our current understanding of matter and how it behaves. In classical fluid mechanics, phenomena are described from a macroscopic point of view, and matter is thought as a continuous medium, which is the common experience we have in our everyday life. However, when dealing with smaller and smaller fluid objects, the atomic nature of matter cannot be ignored anymore.

A lot of results can still be derived from continuum mechanics, but with care and awareness of hypotheses and limitations. Do nanoimprint flows fall in this category? It turned out that the continuum hypothesis could fairly account for what we observed in the experiments reported in this thesis. That is why, from a heuristic point of view, we can say that continuum mechanics is relevant to nanoimprint processes, at least at the (both time and length) scales of the phenomena we studied in this thesis. This chapter aims at detailing the physical justifications of the continuum hypothesis, and what the fundamental equations consequently are.

2.1 Scales of the problem

2.1.1 Intermolecular forces

From a microscopic point of view, as depicted by Feynman's words, a fluid is a batch of molecules (each molecule is made of atoms). In a gas, molecules are rather far apart from one another (≈ 3 nm for air at room temperature) and collide like billiards balls. Whereas in a liquid, the intermolecular distance is of the order of the molecular size itself (several angstroms), molecules are rather densely packed and slide on one another. We will consider hereafter only liquids.

What are the properties of molecules in a liquid? First, the position of molecules is rather random at long range, although there is some correlation at very short range, that is in the neighborhood of the molecule (Barker and Henderson, 1976). Second, molecules are constantly moving. The average displacement of molecules is a *flow* or a mass flux, and the fluctuating motion is heat. The forces acting between molecules are called *intermolecular forces*. They are responsible for the macroscopic properties of the fluid. They originate from the many-body electromagnetic interactions between charges (electron clouds and nuclei) of different molecules as well as inside molecules themselves. Computation of such forces, especially in a liquid of macromolecules, is a very complex quantum issue. In spite of their common electromagnetic origin, intermolecular forces are separated in categories depending on their strength and range, that is why we talk about forces in the plural. A comprehensive review of intermolecular forces can be found in the book by Israelachvili (1991). Table 2.1 summarizes the intermolecular forces encountered in our case, and we will develop some of them below.

Note the microscopic origin of viscosity. An interesting macroscopic property of fluids is viscosity. If a liquid is given some motion, for example a glass of water stirred with a spoon, and then is put to rest, after some time the motion vanishes due to viscosity. Viscosity is responsible for the irreversible dissipation of momentum. But at the molecular level, mechanical interactions are reversible. Through the enormous amount of collisions, molecules that have a specific ordered velocity will fall back in a more probable distribution (Villani, 2001).

Molecular dynamics. If we know the forces between molecules, then it is possible to simulate the flow at the molecular level by computing the position and velocity of each molecule, given by Newton's laws. This is the field of *Molecular Dynamics* simulations (MD) and its variants. Some aspects of nanoimprint process (Hsu *et al.*, 2005; Kang *et al.*, 2007; Woo *et al.*, 2009; Yao *et al.*, 2010; Chandross and Grest, 2011; He *et al.*, 2012, to name a few) or polymer dynamics (Baschnagel and Varnik, 2005; Barrat *et al.*, 2010; Solar *et al.*, 2012) have been studied with MD. However, MD suffers from severe limitations in our case. As an example, let us take a $10 \times 10 \times 10$ cube of $30 \text{ kg}\cdot\text{mol}^{-1}$ polystyrene molecules, which represents roughly a 37 nm-edge cube. The MD set is a 1000-body problem containing approximately 10^8 degrees of freedom. First, the intermolecular forces are not exactly known (because of the many-body

Table 2.1 – Intermolecular forces in liquids.

Interaction	Range (nm)	Macroscopic effects
covalent bonds	short (0.03 – 0.1)	molecular structure
core repulsion	short (0.1 – 0.4)	(in)compressibility, viscosity, elasticity
van der Waals, dispersion forces between molecules	short (0.1 – 1)	surface energy, viscosity, elasticity
hydrophobic interactions	short (0.1 – 1)	surface energy, dewetting
van der Waals, dispersion forces between large objects	long (1 – 100)	adhesion, spinodal dewetting, molecular assemblies
configurational entropy, steric repulsion in polymer	long (chain length)	viscosity, elasticity

quantum problem involved). An approximate pair potential (that is, the potential between two isolated molecules, often the Lennard-Jones potential) is used instead. A cut-off distance is also usually introduced in the potential, in order to reduce the correlation between molecules, so that long-range forces are discarded. And finally, MD describes the dynamics at short times, at the scale of molecular vibrations, and in a small volume, thus it is rather difficult to model the imprint and reflow of a full pattern over several minutes.

An intermediate modeling of fluids between molecular dynamics and continuum mechanics is the *Lattice Boltzmann Method* (LBM). The goal of this method is to compute the local statistical distribution of velocity, and not individual motions of molecules as in MD, nor average quantities as in continuum mechanics. The velocity distribution evolves in time by modeling the statistics of collisions. LBM is powerful when dealing with complex flows such as multiphase flows, wetting dynamics, or complex boundary conditions. A recent review of LBM applied to microfluidics can be found in Zhang (2011) (see also Attar and Körner, 2009 for wetting dynamics; Malaspinas *et al.*, 2010 for polymer flows).

2.1.2 The continuum hypothesis

We want to model our system in terms of average quantities, like mass, momentum, or heat—we saw that the flow is the average transport of mass, where high spatial and temporal fluctuations are filtered out. In order to do so, we have to define a volume and a time of integration. They are as small as possible, but large enough for the volume to blur the molecular aspect of matter (Fig. 2.1a) and for the time to get rid of fluctuations at equilibrium¹. Those dimensions are actually the resolution of

¹Local thermodynamic equilibrium is necessary to define macroscopic quantities like temperature or pressure.

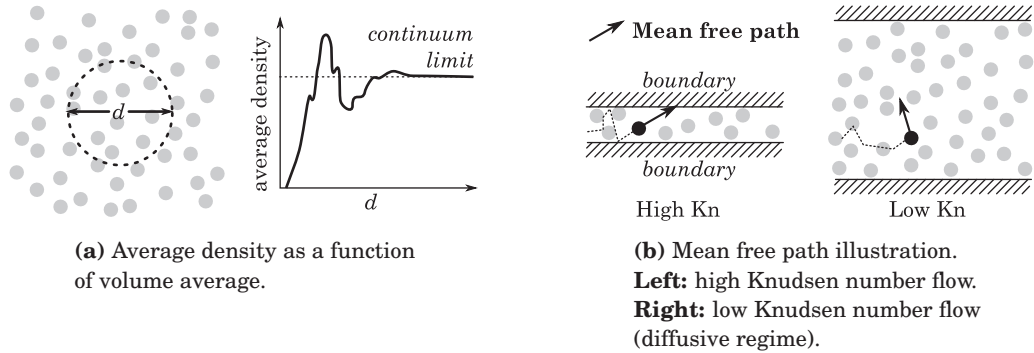


Figure 2.1 – Limits of continuum hypothesis. Gray dots represent molecules.

continuum mechanics, and regarding fluids, the volume of integration is known as a *fluid particle* (Bruus, 2008). How do they compare with the scales of our systems?

We will take care of the time scales later, for now we will focus on length scales. At the microscopic scale, for the transport of each quantity (mass, momentum, heat), it is possible to define a carrier, either real (when some particle is the carrier) or virtual. Then we have to compare the mean free path of the carrier Λ to the finest dimension of our system ℓ , with use of the *Knudsen number* Kn :

$$Kn = \frac{\Lambda}{\ell}. \quad (2.1)$$

Continuum fluid dynamics is a macroscopic description of the fluid in the limit $Kn \rightarrow 0$ (Fig. 2.1b). For a molecule of air at room temperature, the mean free path is roughly 100nm. In liquids, as molecules are quite densely packed, the mean free path is rather of the order of intermolecular distance (several angstroms, as we saw earlier). Then in our systems, for polymer films of several nanometers, the Knudsen number for mass and momentum, where carriers are the molecules themselves, is $Kn \sim 0.1$. It is clear that we are in a borderline situation. Nevertheless, a molecular modeling was not necessary to model our observations, that is why a continuum approach is still relevant in our case.

Now, let us look into heat transport—a thorough introduction to nanoscale heat transfer can be found in the book by Carminati *et al.* (2010). The carrier of heat in opaque condensed matter is a virtual particle called *phonon*. In crystal lattice, phonons scatter on defects, grain boundaries, by mutual collision or other mechanisms. Still, in a monocrystalline material such as a silicon wafer, the mean free path of phonons can be rather large, a few hundred nanometers at room temperature. This is quite commensurable with the finest protrusions of our nanoimprint molds. So the macroscopic description of heat diffusion is unlikely to apply in the patterns of the mold. However, in the polymer melt, the mean free path is again of the order of intermolecular distance. So, as in the case of mass and momentum transport, the Knudsen number is about 0.1. Here again, heat transfer is a borderline case. However, we will study only systems in thermal equilibrium.

Returning to the time average, the situation in our case is much simpler. We have to compare the mean time between collisions of the carrier to our time resolution. If we are interested in small time scales, smaller than the mean time between collisions, then we are in the field of out-of-equilibrium physics. For a molecule of air at room temperature, the mean time between collisions 0.2ns. For phonon, an order of magnitude of the mean time between collisions is the mean free path over the sound velocity, and for silicon this yields 0.1ns. And for liquids it is expected to be even smaller. This is far less than our time resolution in classical thermal imprint, where it is several seconds at best. Note that this may not be the case when using ultra-fast imprint or laser pulse annealing.

2.1.3 Scaling laws and nanoscale effects

Flows at the micro and nanoscales are different from what we can experience at our human scale. Small bugs can grab drops of water between their claws without any container, and some species can even walk on the surface of water. At even smaller scale, other phenomena appear. When the problem scales down to a few hundreds of molecular sizes (see figure 2.2), even if matter can be seen as a continuous medium, physical effects of two kinds come into play (Squires and Quake, 2005):

SCALING EFFECTS Forces and effects that are commonly negligible at the macroscale become prominent at the nanoscale. Because the ratio of surface over volume increases in the sample, surface forces, such as surface tension, are likely to become the driving forces. Other forces, such as long-range van der Waals forces that are not usually taken into account at the macroscale, are no longer negligible when the size of the flow compares with the range of the forces (a hundred nanometers). Slippage may also occur between the liquid and a solid interface: at a few nanometers, the usual no-slip boundary condition for the flow may not hold.

CONFINEMENT EFFECTS Volume properties (mechanical properties, viscosity, fusion temperature, glass transition temperature, heat diffusion...) of the material depend on its size. We will see in the next chapter that the viscosity of a polymer film is a thickness-dependent property, when the thickness reduces to several molecular lengths.

Note on the term *confinement*: when the dimensions of the material reduce to several molecular lengths, we talk about *confinement effects*. However, we will also use the expression *confined film*, which means that the polymer film is sandwiched between the substrate and the overlaying mold, as opposed to a *supported film* that is a coated polymer film with a free interface.

Another feature of tracking flows at the nanoscale is that we can observe processes that would be extremely slow at the macroscale. For example, glaciers appear solid to our common experience, but it is known that some of them slowly deform and flow. Figure 2.3a is a picture of the Aletsch glacier in the Swiss canton of Valais. It flows at a velocity at its center of about 200 m per year, that is 6 $\mu\text{m/s}$. Such a velocity

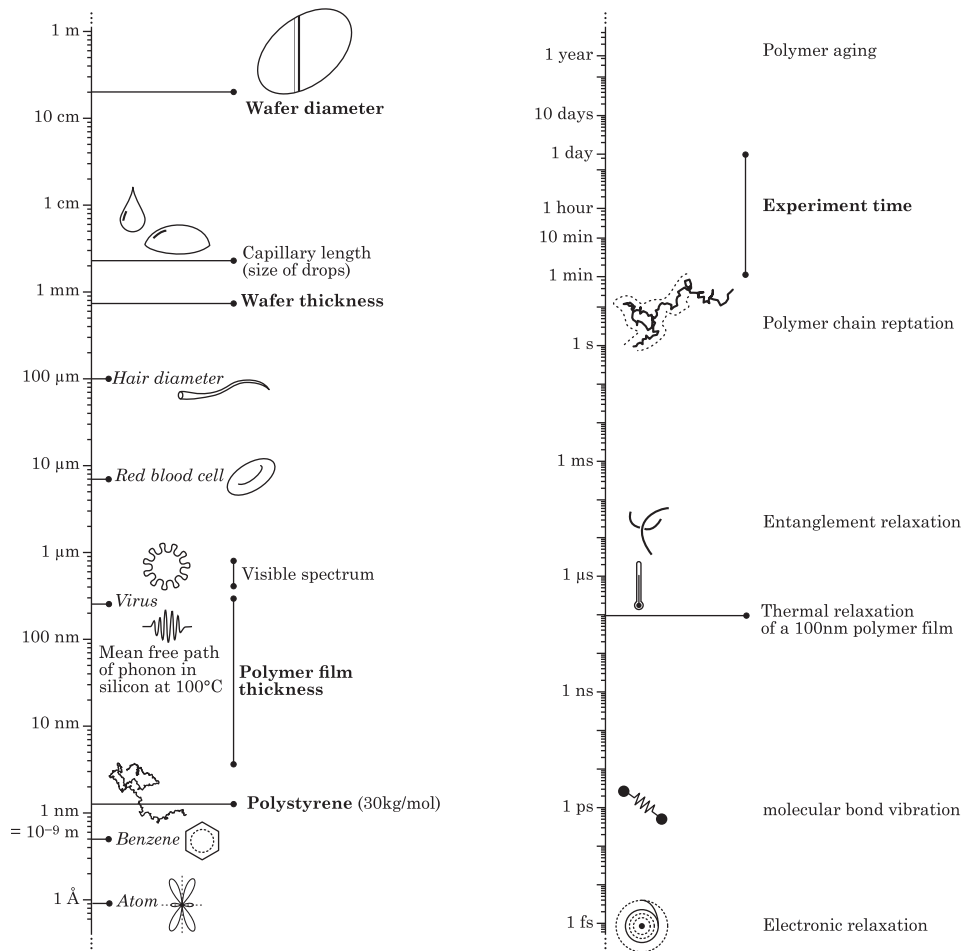


Figure 2.2 – Length scales and time scales in nanoimprint.



(a) The Aletsch glacier in the Swiss canton of Valais. (Credit: Dirk Beyer under Creative Commons)



(b) Pitch Drop Experiment. (Credit: John Mainstone, University of Queensland under Creative Commons)

Figure 2.3 – Slow flows at macroscale.

is quite high at the microscale. Another fascinating example is the *Pitch Drop Experiment*, an experiment that is claimed to be one of the world's longest experiments (Edgeworth *et al.*, 1984). It was started by Professor Parnell in 1927 at the University of Queensland (Australia) and is still on today. It consists of a funnel filled with pitch, an extremely viscous kind of bitumen (see figure 2.3b). While the same funnel filled with water would empty within a few seconds, only eight drops of pitch have fallen since the beginning of the experiment. Pitch viscosity was assessed to be about 10^8 Pa·s, in other words, 100 billion times more viscous than water. In chapter 6, we will see how we can characterize viscosities of this order of magnitude with nanoscale flows of only several minutes.

2.2 Fundamental equations

In the previous section, we gave some arguments for using continuum mechanics, although the dimensions of our systems approach the molecular size. We now review the well known equation of fluid mechanics. With scaling arguments, we will find what the driving terms are. We consider a chemically pure fluid.

2.2.1 Incompressible continuity equation

When the velocities are much lower than the velocity of sound in the fluid, then the fluid can be considered as incompressible. Moreover, in thermal equilibrium, the

density of the fluid is homogeneous, and the incompressible continuity equation is:

$$\nabla \cdot \mathbf{v} = 0, \quad (2.2)$$

where $\nabla \cdot$ is the divergence of the velocity field \mathbf{v} .

2.2.2 The Stokes equation

In the continuum approach, the transport of momentum is classically described by the Navier-Stokes equation:

$$\rho \left(\frac{\partial \mathbf{v}}{\partial t} + (\mathbf{v} \cdot \nabla) \mathbf{v} \right) = -\nabla p + \nabla \cdot \mathbb{T} + \mathbf{f}, \quad (2.3)$$

where ρ is the fluid density, p the pressure field, \mathbb{T} the viscous stress tensor, and \mathbf{f} any external body force field.

A source of beauty and diversity of fluid mechanics lies in the non-linearity of the term $\rho(\mathbf{v} \cdot \nabla)\mathbf{v}$ in equation (2.3). It is also the source of its mathematical difficulty. In two dimensions, it has been proven that smooth and globally defined solutions exist for a given Navier-Stokes problem, nevertheless, in three dimension, it is one of the famous one-million-dollar problem of the Clay Mathematics Institute! However, with decreasing size of the fluid domain, decreasing velocities, and increasing fluid viscosity, this non-linear term can be neglected.²

For a simple Newtonian fluid of viscosity η , the viscous term $\nabla \cdot \mathbb{T}$ is reduced to $\eta \nabla^2 \mathbf{v}$. The comparison between the inertial terms (left hand side of equation 2.3) and the viscous term is then given by the *Reynolds number*:

$$\text{Re} = \frac{\rho V \ell}{\eta}, \quad (2.4)$$

where V is a characteristic velocity, and ℓ a characteristic length³ of the fluid domain. By taking $\rho \sim 10^3 \text{ kg}\cdot\text{m}^{-3}$, $V \sim 10^{-9} \text{ m}\cdot\text{s}^{-1}$, $\ell \sim 10^{-6} \text{ m}$ and $\eta = 10^2 \text{ Pa}\cdot\text{s}$ ⁴, we get $\text{Re} \sim 10^{-14}$. Therefore, in our case, the viscous term prevails and the inertial term can be neglected. Our systems can be described by the *Stokes equation*:

$$\nabla p = \nabla \cdot \mathbb{T} + \mathbf{f}. \quad (2.5)$$

Note on high frequency case. If a time-dependent boundary condition is applied on the fluid, then the time derivative of inertial term is not necessarily negligible, and the following time-dependent Stokes equation has to be used:

$$\rho \frac{\partial \mathbf{v}}{\partial t} = -\nabla p + \nabla \cdot \mathbb{T} + \mathbf{f}. \quad (2.6)$$

This can happen when dealing with acoustic waves, ultra-fast imprint, etc. At high enough frequencies, the viscoelastic nature of the fluid appears (we will see this in

²But don't worry, non-linearity will come back with boundary conditions!

³This time, the largest dimension.

⁴Order of viscosity of polystyrene $30 \text{ kg}\cdot\text{mol}^{-1}$ at 180°C .

detail in chapter 3). Then we have to compare the inertial term to the elastic term through the *Cauchy number*:

$$\text{Cy} = \frac{\rho\omega^2\ell^2}{G}, \quad (2.7)$$

where ω is the driving frequency and G the elastic shear modulus. For instance, if we assume a characteristic time of $1\mu\text{s}$ ($\omega \sim 10^6\text{s}^{-1}$, ultra-fast imprint), $\rho \sim 10^3\text{kg}\cdot\text{m}^{-3}$, $G \sim 1\text{MPa}$ then the flow is still driven by elasticity below $\ell \sim 32\mu\text{m}$, but above, inertial effects occur.

2.2.3 Energy transport

Heat transport in an opaque fluid free of internal heat source, is described by the equation:

$$\underbrace{\frac{\partial}{\partial t}\rho c_p T}_{\text{variation of internal energy}} + \underbrace{\nabla \cdot \rho c_p T \mathbf{v}}_{\text{heat convection}} = \underbrace{K\nabla^2 T}_{\text{heat conduction}} + \underbrace{\mathbb{T} : \nabla \mathbf{v}}_{\text{viscous dissipation}} - \underbrace{\left(\frac{\partial \ln \rho}{\partial \ln T}\right)_p \frac{\partial p}{\partial t}}_{\text{enthalpic contribution}}, \quad (2.8)$$

where c_p is the heat capacity at constant pressure, T is the temperature, and K is the thermal conductivity, assuming c_p and K are constant.⁵ Whether heat transfer is driven by conduction (heat exchange without mass flux, $K\nabla^2 T$ term) or convection (transport of hot matter, $\nabla \cdot \rho c_p T \mathbf{v}$ term) is given by the *Péclet number*:

$$\text{Pe} = \frac{c_p \rho \ell V}{K}, \quad (2.9)$$

where ℓ is again a characteristic length, and V a characteristic velocity. The inequality $\text{Pe} \ll 1$ means that heat transfer by conduction is much faster than heat transfer by convection. For polystyrene, we have roughly $c_p \approx 2\text{kJ}\cdot\text{kg}^{-1}\cdot\text{K}^{-1}$ and $K \approx 0.2\text{W}\cdot\text{m}^{-1}\cdot\text{K}^{-1}$, which yields, assuming the same values for ρ , ℓ and V as for the Reynolds number computation, a Péclet number: $\text{Pe} \sim 10^{-8}$. Therefore, in our polymer films, heat transfer will be driven by conduction.

Now we can ask if heat produced by viscous dissipation ($\mathbb{T} : \nabla \mathbf{v}$) is significant compared to heat brought by conduction. The comparison is made with use of the *Brinkman number*:⁶

$$\text{Br} = \frac{\eta V^2}{KT}, \quad (2.10)$$

where T is the temperature of the substrate. By taking $\eta \sim 10^8\text{Pa}\cdot\text{s}$, $T \sim 400\text{K}$, K and V as above, we get: $\text{Br} \sim 10^{-12}$, which means that heat generated by viscous

⁵In fact, for polystyrene, their variation between T_g and $T_g + 100$ is less than 10%, which has to be compared to the factor 10^6 for viscosity.

⁶In a one-dimensional approach, if we imagine a film of thickness ℓ , with the boundary conditions $T(0) = T(\ell) = T_0$, then the temperature profile $T(z)$ at long times would be:

$$\frac{T(z)}{T_0} = 1 + \text{Br} \times \left(\frac{z}{\ell} - \frac{z^2}{\ell^2} \right)$$

shear is negligible. This is caused by the extremely low characteristic speed that counterbalances high viscosity. It may not be generally the case, such as in polymer extrusion where velocities and shear are much higher.

Finally let us consider the enthalpic term $-(\partial \ln \rho / \partial \ln T)_p \partial p / \partial t$. For an ideal gas, $-(\partial \ln \rho / \partial \ln T)_p = 1$, and we know that heat is produced by compressing the gas ($\partial p / \partial t > 0$). For polystyrene at 500 K, it is of the order of 3 (we will see an expression of $\rho(T)$ in the next chapter), which is not far from unity. Regarding the pressure, it can be given by the Laplace pressure (which we will introduce below): γ / ℓ with γ the surface tension. Besides, we will see in chapter 4 that the characteristic leveling time for high frequency shapes is of the order of $\eta \ell / \gamma$. The comparison of the enthalpic term with the conduction term yields:⁷

$$\frac{\gamma^2}{KT\eta} \sim 10^{-7}, \quad (2.11)$$

with $\gamma \sim 0.03 \text{ N}\cdot\text{m}^{-1}$, $T = 500 \text{ K}$ and $\eta \sim 10^2 \text{ Pa}\cdot\text{s}$, which means that heat produced by variation of pressure will immediately dissipate through thermal conduction in the fluid.

With the scaling discussion we presented so far, we can deduce that heat transfers in our fluids at the small scale and in solids at the macroscale are quite similar. It is of diffusive nature, and the equation of heat can be recast as follows:

$$\frac{\partial}{\partial t} \rho c_p T = K \nabla^2 T. \quad (2.12)$$

2.2.4 The isothermal hypothesis

Now, if we consider a flat thin film of thickness ℓ , and if we assume that temperature is homogeneous at one boundary of the film, then from equation (2.12), the characteristic time τ_d of thermal diffusion in the film is:

$$\tau_d = \frac{\rho c_p \ell^2}{K}. \quad (2.13)$$

For a 100 nm-thick polystyrene film, $\tau_d \sim 0.1 \mu\text{s}$, whereas for a 750 μm -thick silicon⁸ wafer, $\tau_d \sim 10 \text{ ms}$. This characteristic time has to be compared to the characteristic time of heat transfer at boundaries. This ratio is called the *Biot number*:

$$\text{Bi} = \frac{H\ell}{K}, \quad (2.14)$$

where H is the heat transfer coefficient per unit of surface related to the (linearized) transfer phenomenon. In the limit $\text{Bi} \rightarrow 0$ corresponding to an infinitely fast conduction, the temperature inside the material can be considered as homogeneous. The temperature variations are then imposed by boundary conditions.

⁷To our knowledge, the dimensionless quantity does not have a traditional name.

⁸For silicon: $K = 148 \text{ W}\cdot\text{m}^{-1}\cdot\text{K}^{-1}$, $c_p = 700 \text{ J}\cdot\text{kg}^{-1}\cdot\text{K}^{-1}$, and $\rho = 2330 \text{ kg}\cdot\text{m}^{-3}$.

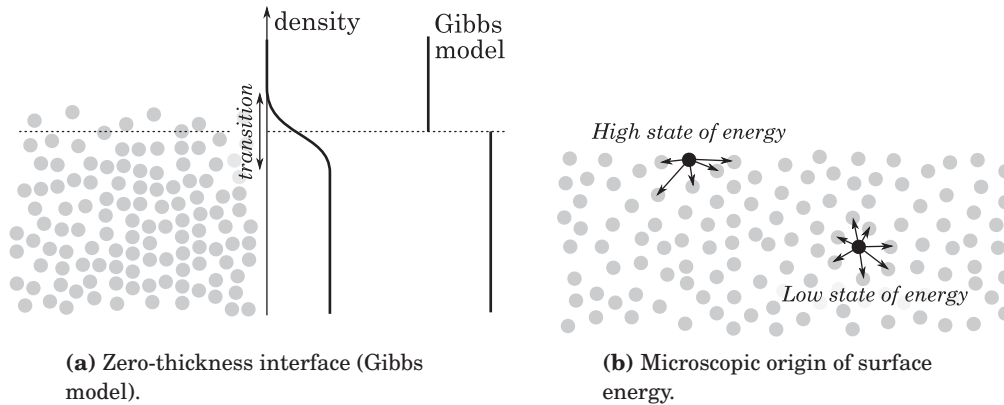


Figure 2.4 – Gibbs interface and surface energy.

If we assume that a silicon wafer is put on a chuck with a thermal contact of the order $H \sim 100 \text{ W}\cdot\text{m}^{-2}\cdot\text{K}^{-1}$, then $\text{Bi} = 10^{-3}$, and consequently the temperature is homogeneous inside the wafer. In case of an exchange by free convection and radiation between the polymer film and air at room temperature, H is of the same order of magnitude,⁹ $H \sim 6 \text{ W}\cdot\text{m}^{-2}\cdot\text{K}^{-1}$ (Taine and Petit, 1993). Consequently, $\text{Bi} = 10^{-6}$, which means that the temperatures inside both the polymer film and the wafer are homogeneous.

This is why we will consider that temperature in our films is homogeneous, an assumption that we call the *isothermal hypothesis*.

2.2.5 Boundary conditions

Now that we have reviewed the equations governing the inside of the fluid, let us focus on the boundary conditions. First, we need to define what an interface is. Figure 2.4a is a sketch of what a real (frozen) interface looks like: there is a transition zone between one medium (the fluid) and the other (here, vacuum). If we extend the bulk density of each medium up to a mathematical surface (dotted line), we define what is called a Gibbs interface that has a zero thickness. The difference between the real transition and the virtual step creates excess quantities that come into play for the modeling of the system. Although we deal with nanoscale flows, this model is still relevant because the transition zone doesn't exceed the molecular length in our case.

Surface tension. One consequence of surface excess quantity is surface tension. Molecules that are at the free surface have less interacting neighbors (see figure 2.4b): they are in a higher state of energy. The fluid tends to minimize this excess energy by minimizing the extent of the free surface. The resulting effect is a pressure jump

⁹For radiative transfer, it is given by the linearized Stefan-Boltzmann law: $H = 4\sigma T_{ext}^3$ with $\sigma = 5.67 \times 10^{-8}$ SI units.

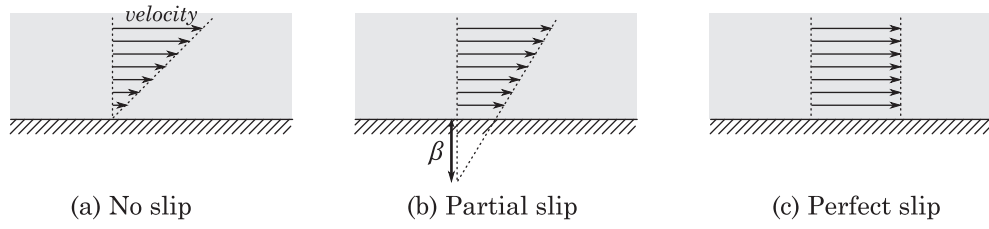


Figure 2.5 – Couette flow with various slip conditions. β is the slip length.

at the interface, called the *Laplace pressure*:

$$P_{\text{inside}} - P_{\text{outside}} = \gamma \kappa, \quad (2.15)$$

with γ the *surface tension* or interfacial energy, and κ the local curvature of the interface.

If surface tension is not homogeneous on the surface, then a force called the *Marangoni effect* appears tangentially to the interface. We will not consider it in our case, because of the isothermal hypothesis (surface tension depends on temperature) and because there is no chemical gradient (adsorbed substances alter surface tension).

Slip length. For macroscopic flows, the classical boundary condition for the velocity on an impermeable solid is the *no-slip* condition: the fluid velocity of the fluid equals that of the solid. If the solid is at rest, then the fluid velocity is zero at the boundary. However, for nanoscopic flows, a slip can occur between the fluid and the solid (Bocquet and Barrat, 2007). This phenomenon is often modeled by a so-called *Navier slip* condition (Navier, 1822). The tangential velocity is proportional to the shear stress at the interface. For Newtonian fluids, this leads to the condition:

$$v_{\parallel} = \beta \frac{\partial v_{\parallel}}{\partial z}, \quad (2.16)$$

with v_{\parallel} the tangential velocity, β the slip length, and $\frac{\partial v_{\parallel}}{\partial z}$ the normal derivative of the tangential velocity. The slip length β is illustrated in figure 2.5. In this figure, the velocity field of a Couette flow is shown with three different slip conditions. With a no-slip condition, the velocity vanishes at the solid interface (figure 2.5a). With a partial slip condition, the velocity is finite at the interface, and virtually vanishes at a distance β from the interface (figure 2.5b). With a perfect slip condition, we get a plug flow (figure 2.5c). Typical dimensions of the slip length range from several nanometers to several micrometers (Neto *et al.*, 2005). Nevertheless, we could not see any effect of a non-zero slip length in our experiments.

Surface roughness. Interfaces are not perfectly flat, as depicted in figure 2.6a. Roughness can be quantified by the root mean square deviation of the interface, ex-

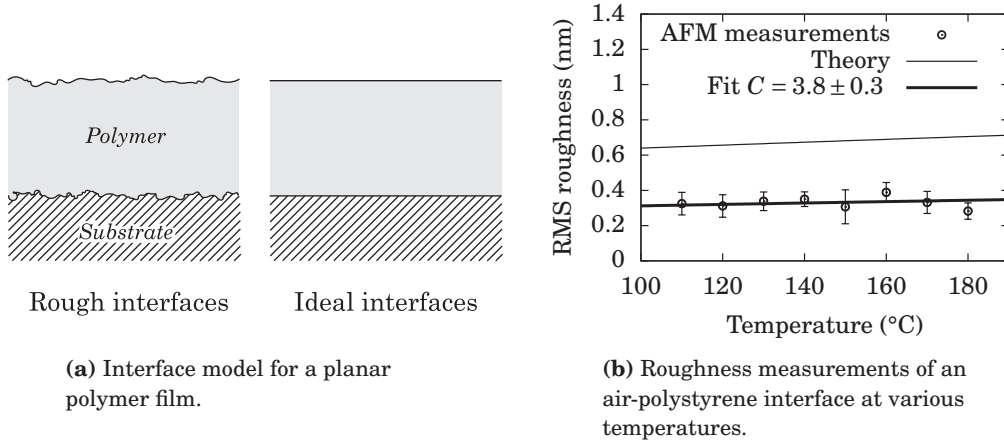


Figure 2.6 – Roughness of interfaces.

pressed as follows:

$$\langle h \rangle_{\text{RMS}} = \sqrt{\frac{1}{L} \int_0^L (h(x) - h_0)^2 dx}, \quad (2.17)$$

where $h(x)$ is the local position of the interface and h_0 its mean value. For a free interface, thermal motion causes the roughening of the interface. According to statistical physics (Mecke, 2001), the thermal roughening at temperature T should be:

$$\langle h \rangle_{\text{RMS}} = \sqrt{C \frac{k_B T}{2\pi\gamma}}, \quad \text{with } C = \ln \frac{2\pi\ell_{\text{cap}}}{a}, \quad (2.18)$$

where k_B is the Boltzmann constant, γ the surface tension, ℓ_{cap} the capillary length as we will see below, of the order of the millimeter, and a the molecular size.

Several polystyrene samples were heated at a definite temperature and then rapidly quenched at room temperature. An AFM measurement of each sample could give the roughness of the interface. Results are reported on figure 2.6b. A typical roughness of 0.3 nm is found. We could think that the surface should be more rough with increasing temperature because the Brownian motion gets stronger. However, this difference is weak, and actually falls inside the measurement uncertainty. The roughness of a silicon wafer is 0.16 nm. Compared with the dimensions of the flow (about ten to several hundreds of nanometers), interfaces can be modeled by (locally) flat interfaces.

2.2.6 Driving forces

The flow is driven by forces acting as boundary conditions, such as surface tension, or by body forces (noted \mathbf{f} in the Stokes equation 2.5). From a top down approach, one might wonder whether gravity as a body force plays a role in microscale flows. A

typical result of microfluidics is that it does not. If we compute the ratio of the gravity force over surface tension, we get the *Bond number*:

$$\text{Bo} = \frac{\rho g \ell^2}{\gamma}, \quad (2.19)$$

where g is the gravity acceleration. With $\ell \sim 100 \mu\text{m}$, we get $\text{Bo} \sim 10^{-3}$, hence negligible gravity. In fact, it is useful to compute what is called the *capillary length* ℓ_{cap} , given by:

$$\ell_{\text{cap}} = \sqrt{\frac{\gamma}{\rho g}}. \quad (2.20)$$

Gravity plays a role only at length scales greater than the capillary length. In our case, $\ell_{\text{cap}} \sim 2 \text{mm}$.

The force field \mathbf{f} could be an electrodynamic force. Treatments of thin film flows under electric field have been done by Schäffer *et al.* (2000, 2001); Wu *et al.* (2010). Although this is an interesting issue, we chose to apply no electrodynamic field and to focus on the classical nanoimprint process.

The last forces of interest are the *van der Waals forces*. If we go back to intermolecular forces of table 2.1 on page 19, we see that there are long-range dispersion forces between ensembles of molecules. In a thin film, it is assumed that van der Waals force \mathbf{f} can be expressed by the gradient of a pressure, $\mathbf{f} = -\nabla\Pi$, with Π called the *disjoining pressure*. This concept was first introduced by Derjaguin (1936). His idea was to sum all the interactions at play in the film and express the result as a pressure difference between the film and a bulk of the same material (Fig. 2.7). The computation of Π is a delicate issue, to which chapter 7 is devoted. Here we begin with the common expression for a film of thickness h :

$$\Pi(h) = -\frac{A}{6\pi h^3}, \quad (2.21)$$

where A is the Hamaker constant that depends on the materials (both film and surrounding materials). A typical order of magnitude for A is $10 \times 10^{-21} \text{J}$, which gives a pressure of 1 bar for a film thickness of 3 nm. The interesting property of A is that it can be either positive or negative. A negative Hamaker constant means that pressure in thinner parts of the film is higher, which can lead to the rupture of the film. This process is called *spinodal dewetting*. For flows with a free interface, we will see in chapter 4 a proper way to quantify the competition between surface tension and van der Waals forces, through the dimensionless *Hamaker number*.

2.3 Conclusion

In this chapter, we saw that continuum mechanics can be relevant to model flows at sub-micron scales, provided that scaled-down equations and specific driving forces are used. Table 2.2 on the next page collects the values of hydrodynamic and thermal dimensionless numbers for thermal nanoimprint.

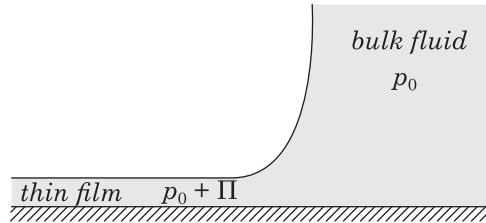


Figure 2.7 – Concept of disjoining pressure (Π).

Table 2.2 – Hydrodynamic and thermal dimensionless numbers in classical thermal nanoimprint.

Number	Symbol	Meaning	Eq.	Value	Consequence
Knudsen	Kn	$\frac{\text{mean free path}}{\text{typical length}}$	(2.1)	10^{-1}	continuum hypothesis
Reynolds	Re	$\frac{\text{inertial forces}}{\text{viscous forces}}$	(2.4)	10^{-14}	negligible inertia
Cauchy	Cy	$\frac{\text{inertial forces}}{\text{elastic forces}}$	(2.7)	10^{-21}	negligible inertia
Péclet	Pe	$\frac{\text{heat convection}}{\text{heat diffusion}}$	(2.9)	10^{-8}	negligible convection
Brinkman	Br	$\frac{\text{viscous heat}}{\text{heat diffusion}}$	(2.10)	10^{-12}	negligible viscous heat
Biot	Bi	$\frac{\text{surface heat transfer}}{\text{diffusion}}$	(2.14)	10^{-3}	homogeneous temp.
Bond	Bo	$\frac{\text{gravity}}{\text{surface tension}}$	(2.19)	10^{-3}	negligible gravity
Hamaker	Ha	$\frac{\text{van der Waals forces}}{\text{surface tension}}$	(4.11)	$< 10^{-2}$	see chapter 4

References

- E. Attar and C. Körner. Lattice boltzmann method for dynamic wetting problems. *Journal of Colloid and Interface Science* **335**, 84–93 (2009).
- J. A. Barker and D. Henderson. What is "liquid"? understanding the states of matter. *Reviews of Modern Physics* **48**, 587 (1976).
- J.-L. Barrat, J. Baschnagel, and A. Lyulin. Molecular dynamics simulations of glassy polymers. *Soft Matter* **6**, 3430 (2010).
- J. Baschnagel and F. Varnik. Computer simulations of supercooled polymer melts in the bulk and in confined geometry. *Journal of Physics: Condensed Matter* **17**, R851–R953 (2005).
- L. Bocquet and J.-L. Barrat. Flow boundary conditions from nano- to micro-scales. *Soft Matter* **3**, 685–693 (2007).
- H. Bruus. *Theoretical microfluidics*, volume 18. Oxford University Press, USA (2008).
- R. Carminati, P. Chantrenne, S. Dilhaire, S. Gomez, N. Trannoy, and G. Tessier. *Microscale and Nanoscale Heat Transfer*. Springer, softcover reprint of hardcover 1st ed. 2007 edition (2010).
- M. Chandross and G. S. Grest. Molecular scale modeling of polymer imprint nanolithography. *Langmuir* **28**, 1049–1055 (2011).
- B. Derjaguin. Range of action of surface forces. *Nature* **138**, 330–331 (1936).
- R. Edgeworth, B. J. Dalton, and T. Parnell. The pitch drop experiment. *European Journal of Physics* **5**, 198–200 (1984).
- R. P. Feynman, R. B. Leighton, M. L. Sands, and M. A. Gottlieb. *The Feynman lectures on physics*. Pearson/Addison-Wesley (1963).
- Y. He, T. Sun, Y. Yuan, J. Zhang, and Y. Yan. Molecular dynamics study of the nanoimprint process on bi-crystal al thin films with twin boundaries. *Microelectronic Engineering* **95**, 116–120 (2012).
- Q. Hsu, C. Wu, and T. Fang. Studies on nanoimprint process parameters of copper by molecular dynamics analysis. *Computational Materials Science* **34**, 314–322 (2005).
- J. N. Israelachvili. *Intermolecular and Surface Forces*. Academic Press Inc, 2nd revised edition edition (1991).
- J.-H. Kang, K.-S. Kim, and K.-W. Kim. Molecular dynamics study of pattern transfer in nanoimprint lithography. *Tribology Letters* **25**, 93–102 (2007).
- O. Malaspinas, N. Fiétier, and M. Deville. Lattice boltzmann method for the simulation of viscoelastic fluid flows. *Journal of Non-Newtonian Fluid Mechanics* **165**, 1637–1653 (2010).
- K. Mecke. Thermal fluctuations of thin liquid films. *Journal of Physics Condensed Matter* **13**, 4615–4636 (2001).
- C. L. M. H. Navier. *Mémoire sur les lois du mouvement des fluides: lu à l'Académie Royale des Sciences ; le 18 mars 1822* (1822).

- C. Neto, D. R. Evans, E. Bonaccorso, H.-J. Butt, and V. S. J. Craig. Boundary slip in newtonian liquids: a review of experimental studies. *Reports on Progress in Physics* **68**, 2859–2897 (2005).
- E. Schäffer, T. Thurn-Albrecht, T. P. Russell, and U. Steiner. Electrohydrodynamic instabilities in polymer films. *Europhysics Letters (EPL)* **53**, 518–524 (2001).
- E. Schäffer, T. Thurn-Albrecht, T. P. Russell, and U. Steiner. Electrically induced structure formation and pattern transfer. *Nature* **403**, 874–877 (2000).
- M. Solar, H. Meyer, C. Gauthier, C. Fond, O. Benzerara, R. Schirrer, and J. Baschnagel. Mechanical behavior of linear amorphous polymers: Comparison between molecular dynamics and finite-element simulations. *Physical Review E* **85**, 021808 (2012).
- T. M. Squires and S. R. Quake. Microfluidics: Fluid physics at the nanoliter scale. *Reviews of Modern Physics* **77**, 977 (2005).
- J. Taine and J.-P. Petit. *Heat transfer*. Prentice Hall (1993).
- C. Villani. Limites hydrodynamiques de l'équation de boltzmann. *Séminaire Bourbaki* **53**, 893 (2001).
- Y. S. Woo, D. E. Lee, and W. I. Lee. Molecular dynamic studies on deformation of polymer resist during thermal nano imprint lithographic process. *Tribology Letters* **36**, 209–222 (2009).
- N. Wu, M. E. Kavousanakis, and W. B. Russel. Coarsening in the electrohydrodynamic patterning of thin polymer films. *Physical Review E* **81**, 026306 (2010).
- C. H. Yao, C. H. Chang, C. W. Hsieh, and C. K. Sung. Effects of mold shape and sidewall roughness on nanoimprint by molecular dynamics simulation. *Microelectronic Engineering* **87**, 864–868 (2010).
- J. Zhang. Lattice boltzmann method for microfluidics: models and applications. *Microfluidics and Nanofluidics* **10**, 1–28 (2011).

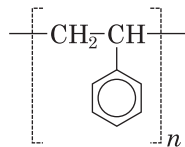
Chapter 3

Polymer melts rheology

3.1 Introduction

Polymers are large molecules made of repeating elementary units joined together by covalent bonds, forming chains. For some polymers called *branched polymers*, branches are grafted to the main chain. However, in this thesis, we study only *linear polymers*, in other words, polymers made of a single chain.

Many kinds of polymers are commonly employed in nanoimprint. The family of polymer mainly used in this thesis is polystyrene (PS), of the chemical diagram:



PS is a standard polymer that has been extensively studied both theoretically and experimentally.

In the next sections, we will see how polymers (and polystyrene in particular) are characterized in term of molecular weights, dimensions, mechanical and energy properties.

3.2 Basic properties of polymers

3.2.1 Molecular weight

In a real synthesized polymer, the degree of polymerization of each molecule, that is the number of repeating unit making a chain, is not exactly the same. Consequently, all the molecules are not of the same molecular weight, but there is instead a distribution around an average molecular weight. There are commonly two types of averages:

1. The *number-average* molecular weight:

$$M_n = \frac{\sum N_i \times M_i}{\sum N_i}, \quad (3.1)$$

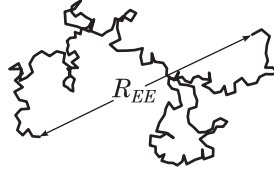


Figure 3.1 – An example of a random walk chain. R_{EE} is the end-to-end distance.

with N_i the number of molecules of molecular weight M_i .

2. The *weight-average* molecular weight:

$$M_w = \frac{\sum N_i \times M_i^2}{\sum N_i \times M_i}. \quad (3.2)$$

In this thesis, as well as the majority of literature, M_w is employed to characterize the molecular weight of a material.

One quantity characterizing the distribution around the average molecular weight is the PolyDispersity Index (PDI) defined by:

$$\text{PDI} = \frac{M_w}{M_n}. \quad (3.3)$$

The PDI has a value equal or greater than unity¹. The closer it is to 1 (*monodisperse* material), the more narrow is the distribution. The PDI is one of the parameters that have a significant impact on the material properties, especially on viscosity. It should be noted that the variations of basics properties for large PDI are far from being fully understood (Bicerano, 2002).

3.2.2 Dimensions

The shape of polymer chains has been well modeled by *random walk* topology (Fig. 3.1). In this theory, the orientations of the bonds between each repeating unit are completely uncorrelated (random). If there is no additional constraint, the mean distance from one end of the chain to the other end, called the *end-to-end distance*, is:

$$R_{EE} = \ell \sqrt{N}, \quad (3.4)$$

with ℓ the length of a repeating unit and N the degree of polymerization. Now, if we constrain the orientation of the bonds into a certain solid angle, the expression

¹This property comes from the double inequality:

$$(\sum N_i M_i)^2 \leq \sum N_i^2 M_i^2 \leq (\sum N_i) (\sum N_i M_i^2).$$

remains, but with an effective elementary length ℓ_e in place of ℓ . Moreover, if the chain cannot cross itself, the theory yields (Jones, 2002):

$$R_{EE} = \ell_e N^\delta, \quad (3.5)$$

with $\delta > 0.5$. For polystyrene, we used in this thesis the following empirical formula (in SI units) as a function of the molecular weight (Zhou and Yan, 1996; Leveder, 2009):

$$R_{EE}(M_w) = 6.598 \times 10^{-11} M_w^{0.5106}. \quad (3.6)$$

In some cases, the radius of gyration R_G is preferred to characterize the size of polymers. It is defined as the mean distance of each element from the center of gravity of the chain. It is however straightforward to move from one quantity to the other by use of the property: $R_G^2 = R_{EE}^2/6$.

3.2.3 Glass transition temperature

Glass is an amorphous state of solid matter. When glass is heated above a temperature called the *glass transition temperature*, noted T_g , it becomes viscous and can flow. A phase transition from a glassy state to a fluid state is characterized by discontinuity in the thermal expansion coefficient or specific heat,² and a continuous change in volume or viscosity. On the contrary, a freezing or crystallization transition leads to discontinuity in these latter properties—for instance, there is discontinuity in volume and viscosity between solid ice and liquid water at 0°C.

For polystyrene, $T_g \approx 100^\circ\text{C}$. The practical aspect of the glass transition temperature is that it is the temperature above which the material has to be heated in order to be shaped by injection molding or imprint. The higher the temperature is above T_g , the less viscous the polymer becomes. The dependence of viscosity on temperature will be discussed in section 3.3.3. The understanding of T_g at the molecular level is an issue beyond the scope of this thesis. Recent advances in that field are reported in the review by Berthier and Biroli (2011).

Dependence on the molecular weight. The glass transition temperature depends weakly on molecular weight, except for very small M_w . The common expression for this dependence was first proposed by Fox and Flory (1950), as a function of M_n : $T_g = T_g^\infty - K_g/M_n$ with T_g^∞ the glass transition temperature for infinite M_n and K_g a fitting parameter. We can write this expression as a function of M_w :

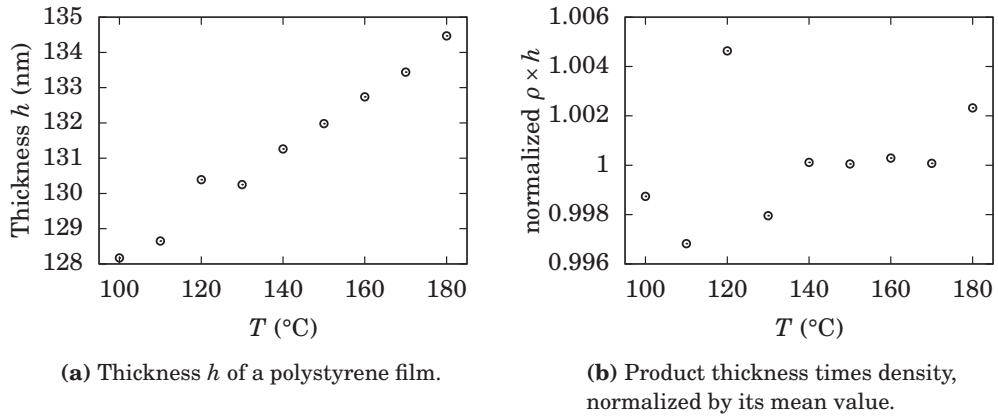
$$T_g(M_w) = T_g^\infty - \frac{K_g \times \text{PDI}}{M_w}. \quad (3.7)$$

Table 3.1 gives the parameters of the latter equation for polystyrene from various authors. It yields T_g

²These discontinuities are used to actually measure T_g , for example by ellipsometry or differential scanning calorimetry.

Table 3.1 – Parameters of the Fox-Flory correction for polystyrene.

Reference	T_g^∞ (K)	K_g (kg·mol ⁻¹)
Fox and Flory (1950)	373	170
Bicerano (2002)	382	200
Singh <i>et al.</i> (2004)	366	113
Kim <i>et al.</i> (2007b)	382	100

**Figure 3.2** – Experimental test of the temperature dependence of density (Eq. 3.8) for polystyrene 30 kg·mol⁻¹.

3.2.4 Density

Regarding the density of polystyrene for $T > T_g$, the work of Fox and Loshaek (1955a) is frequently cited. They accounted for the thermal and molar dependence with the following empirical formula (in S.I. units):

$$\frac{1}{\rho} = 7.67 \times 10^{-4} + 5.5 \times 10^{-7} T + 6.43 \times 10^{-8} \frac{T}{M_w}. \quad (3.8)$$

This expression yields, for polystyrene 30 kg·mol⁻¹ at T_g : $\rho = 1028 \text{ kg}\cdot\text{m}^{-3}$.

The temperature dependence of equation 3.8 can be experimentally checked by ellipsometry measurements, as reported on figure 3.2. The thickness of a polystyrene film ($M_w = 30 \text{ kg}\cdot\text{mol}^{-1}$) can be measured at various temperatures (Fig. 3.2a). Given the large difference in thermal expansion between the silicon wafer ($\approx 3 \times 10^{-6} \text{ K}^{-1}$) and the polystyrene film ($\approx 6 \times 10^{-4} \text{ K}^{-1}$), we can assume that the film expands only along its thickness. Then the product of the thickness by density (mass of polymer per unit of surface) should be a constant. This is verified by figure 3.2b, where the product $h \times \rho$ is a constant within 0.5%.

Table 3.2 – Polymers used in this thesis.

Polymer	Short name	M_w^a (kg·mol ⁻¹)	PDI ^a	R_{EE}^b (nm)	T_g^c (K)	γ^d (mN·m ⁻¹)
Polystyrene	PS 30k	30	1.06	1.3	373 ± 1	32 ± 3
Polystyrene	PS 130k	130	1.06	3.0	375 ± 1	32 ± 3

^aSupplier data.^bFrom Eq. (3.6).^cMeasured from previous studies by Leveder (2009).^dSee Sec. 3.2.5.

3.2.5 Surface tension

The surface tension of polystyrene melts varies with both molecular weight and temperature. In a review by Dee and Sauer (1998), a power law of $M_n^{2/3}$ and a linear decrease with temperature is reported. However, this variation is small—in contrast with the variation of viscosity—for entangled polystyrene and for the range of temperature investigated in this thesis (120°C to 180°C). Typical values (extrapolated for our molecular weights from tabulated data by Bicerano, 2002) are $\gamma_{@120^\circ\text{C}} = 33.3 \text{ mN}\cdot\text{m}^{-1}$ and $\gamma_{@180^\circ\text{C}} = 29.0 \text{ mN}\cdot\text{m}^{-1}$ for PS 30k, and $\gamma_{@120^\circ\text{C}} = 34.8 \text{ mN}\cdot\text{m}^{-1}$ and $\gamma_{@180^\circ\text{C}} = 30.4 \text{ mN}\cdot\text{m}^{-1}$ for PS 130k. As we do not know the exact thermal dependency, it is reasonable to take a constant value $\gamma = 32 \pm 3 \text{ mN}\cdot\text{m}^{-1}$ for both molecular weights.

3.2.6 Polymers used in this thesis

Commercially available polystyrene from Sigma-Aldrich was used for this thesis. Table 3.2 summarizes the properties of the material we used.

3.3 Bulk viscosity and viscoelasticity

3.3.1 Linear theory of viscoelastic fluids

From the previous chapter, we saw that one of the terms in the equation of motion is the divergence of the viscous stress tensor, written $\nabla \cdot \mathbb{T}$. The closure of the momentum equation by an expression of stresses as a function of strains or strain rates is an issue dealt with by a devoted scientific field called *rheology*. An extensive study of rheological models for polymers as well as experimental results can be found in the book by Ferry (1980). Here we report only basic ideas we will need for the following chapters.

A simple shear is a deformation of a material element where one face slides parallel to the opposite one (figure 3.3 on the next page). At small shear strains, a solid may behave like an ideal Hooke's spring: the stress σ_t is proportional to the strain γ , and the coefficient of proportionality is called the *shear modulus*:

$$\sigma_t = G\gamma. \quad (3.9)$$

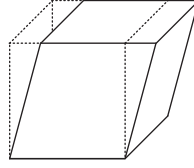


Figure 3.3 – Schematic of a simple shear strain.

On the other hand, at small strain rates, a fluid may behave like an ideal Newton's fluid. The stress is proportional to the strain rate, and in the case of an incompressible fluid, it takes the form:

$$\sigma_t = \eta \dot{\gamma}, \quad (3.10)$$

where η is called the *dynamic viscosity*.

Now, at both small strains and strain rates, a realistic fluid material, such as a polymer melt, stores a part of the mechanical energy and dissipates the remaining part into heat (see equation 2.8 on page 25). If a stress is instantaneously applied on such material, it flows but also store some elastic energy. If the stress stops, the elastic energy is relaxed by shape deformation, which can be harmful for nanoimprinted patterns for example. Another way to consider viscoelastic fluids is the following: if an oscillating shear stress of frequency ω is applied on the fluid, the strain is not in quadrature phase ($+\pi/2$), as it would be for a Newtonian fluid. It is neither in phase, like a Hookean spring. In fact, both the phase and the proportionality coefficient depend on the frequency of the oscillation. We can define a complex viscosity, written $\eta(\omega)$ (note: in references, it is also written η^*):

$$\sigma_t(\omega) = \eta(\omega) \dot{\gamma}(\omega). \quad (3.11)$$

Transposed in the time domain, the stress would be a convolution of the history of strain rate with a viscosity kernel. Note: in literature, the complex shear modulus $G(\omega)$ is more commonly employed than the complex viscosity. However, it is straightforward to move from one expression to another with the relation $G(\omega) = -i\omega\eta(\omega)$.³




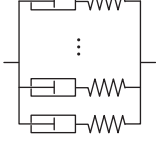
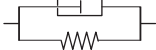
For example, the shear behavior can be modeled by a spring of elasticity G put serially with a dashpot of viscosity η . For a stress σ_t , the total strain is the sum of the elastic strain σ_t/G plus the viscous strain $-\sigma_t/i\omega\eta$. If we note $\tau = \eta/G$ the relaxation time, we get: $\sigma_t/\gamma = -i\omega\eta/(1 - i\omega\tau)$. In terms of strain rates, we finally get:

$$\eta(\omega) = \frac{\eta}{1 - i\omega\tau}. \quad (3.12)$$

This viscoelastic model is called the *Maxwell model*. Table 3.3 summarizes the most common linear models used in literature. Specific models for polymers are presented below in paragraph 3.3.4.

³Note that the sign of the $i\omega$ factor depends on the sign convention for the Fourier transform.

Table 3.3 – Summary of most common linear rheology models.

Name	Diagram	$\eta(\omega)$
Hookean solid		$\frac{G}{-i\omega}$
Newtonian fluid		η
Maxwell monomode		$\frac{\eta}{1 - i\omega\tau}$
Maxwell multimode		$\sum \frac{\eta_n}{1 - i\omega\tau_n}$
Continuous spectrum	-	$\int \frac{\eta(x)}{1 - i\omega\tau(x)} dx$
Kelvin-Voigt		$\eta + i\frac{G}{\omega}$
Cole-Cole	-	$\frac{\eta}{1 + (-i\omega\tau)^\beta} \quad \beta \in]0, 1]$

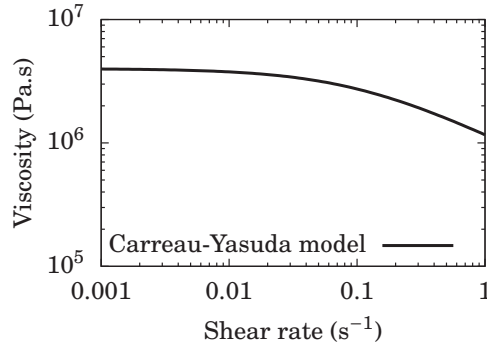


Figure 3.4 – Shear thinning behavior of polystyrene.

With linear viscoelasticity, the divergence of viscous stress tensor in frequency domain can be recast in the handy form:⁴

$$\nabla \cdot \mathbb{T} = \eta(\omega) \nabla^2 \mathbf{v}(\omega),$$

where $\nabla^2 \mathbf{v}$ is the Laplacian of the velocity field.

3.3.2 Shear-thinning

For a finite (and especially large) strain rate, the linear relation of equation (3.11) does not always hold, and non-linear stress-strain relations such as power laws or Carreau-Yasuda models are required (Carreau, 1972; Yasuda *et al.*, 1981). The critical strain rate at which non-linear behaviors appear is an intrinsic property of the material and usually depends on temperature. A critical shear rate can be estimated for PS 130k with a shear-rate-dependent viscosity model plotted on figure 3.4, which is the following Carreau-Yasuda function:

$$\eta(\dot{\gamma}) = \eta_0 \left(1 + \left(\frac{\dot{\gamma}}{\dot{\gamma}_0} \right)^a \right)^{\frac{n-1}{a}}, \quad (3.13)$$

where η_0 is the zero-shear viscosity, a and n are fitting parameters of the model (for PS 130k, $a = 0.93$ and $n = 0.49$), and $\dot{\gamma}_0$ the critical shear rate ($\dot{\gamma}_0 = 0.1 \text{ s}^{-1}$ at 140°C). Below $\dot{\gamma}_0$, the viscosity is weakly dependent on the shear rate: it is the linear regime. Above $\dot{\gamma}_0$, the viscosity decreases with increasing shear rate: it is the shear thinning regime.

3.3.3 Zero-shear viscosity: the WLF law

In this subsection, we present the standard laws for the thermal and molecular weight dependence of zero-shear viscosity. The zero-shear viscosity is the viscosity for vanishing shear strain. A remarkable property is that there are no cross terms

⁴Again, for incompressible fluids.

between the mass dependence and the temperature dependence, in other words, those two variables can be studied separately, provided that we use the relative temperature $T - T_g(M_w)$. In the following section, we will see that viscosity also depends on the thickness of the film, for thicknesses of a few molecular lengths.

Dependence on molecular weight. Contrary to the glass transition temperature, viscosity depends strongly on the molecular weight. Two regimes separated by a critical mass M_c are reported: for $M_w < M_c$, viscosity is proportional to M_w , and for $M_w > M_c$, viscosity is proportional to $M_w^{3.4}$ (Fox and Loshaek, 1955b; Colby *et al.*, 1987). The value 3.4 of the exponent is rather independent of the material (Bicerano, 2002) and can be explained by the *theory of reptation* (Jones, 2002). However, the critical molecular weight M_c is an intrinsic property of a polymer and depends on the repeating unit. For polystyrene, the commonly accepted value is $M_c \approx 31 - 38 \text{ kg}\cdot\text{mol}^{-1}$.

Dependence on temperature. In the previous section, we saw that the glass transition temperature was the key parameter for the viscous properties of polymers. In the range $T_g < T < 1.2T_g$ (in K)—that is, for polystyrene, between about 100°C and 180°C—the polymer is in a highly viscous, *rubbery* state. Empirical formulas can be found in the book by Bicerano (2002, p. 506) for temperatures greater than $1.2T_g$. Still, as we didn't reach temperatures greater than about 180°C in our processes, we will now focus on viscosity models for $T < 1.2T_g$.

The starting point is the common concept of free volume (Jones, 2002). In this theory, the motion of the chains is made possible by the space (free volume) left between the molecules. The free volume f is assumed to expand linearly with temperature, so that at a given temperature and for a given molecular weight, it is:

$$f(T, M_w) = f_g + \alpha_f (T - T_g(M_w)), \quad (3.14)$$

with f_g the free volume at T_g , and α_f the expansion coefficient of the free volume.

In early works, Vogel (1921), Fox and Flory (1948) and Doolittle (1951) proposed a relationship for viscosity of the form $\eta(T) = A \exp(B/f(T, M_w))$, where A is a function of M_w and B is assumed to be constant. It can be recast in what is now called the *Vogel-Fulcher model*:

$$\eta(T, M_w) = A(M_w) \exp\left(\frac{B}{\alpha_f (T - T_\infty(M_w))}\right), \quad (3.15)$$

with $T_\infty(M_w) = T_g(M_w) - f_g/\alpha_f$, and where viscosity diverges for $T \rightarrow T_\infty$. With the molecular-weight dependence seen in the previous paragraph, we can write:

$$\eta(T, M_w) = A_c \left(\frac{M_w}{M_c}\right)^a \exp\left(\frac{B}{\alpha_f (T - T_\infty(M_w))}\right), \quad (3.16)$$

with $a = 1$ for $M_w < M_c$ and $a = 3.4$ for $M_w > M_c$. In a recent review, Kim *et al.* (2007b) gathered an important amount of published experimental measurements of polystyrene viscosity, for various molecular weights and temperatures. The fitted values are reported on table 3.4 as well as results from other authors.

Table 3.4 – Parameters of the Vogel-Fulcher model for polystyrene.

Reference	B/α_f	M_c	$T_\infty(M_c)$	A_c
	(K)	(kg·mol ⁻¹)	(°C)	(Pa·s)
Kim <i>et al.</i> (2007b)	2083	38	48 ^a	7.1×10^{-5} ^b
Majeste <i>et al.</i> (1998)	1620 ± 50	35	48 ^c	3.1×10^{-4} ^c
Plazek (1965)	1442 ^d	Not available	52 ^e	1.8×10^{-2} ^f

^aComputed from value given in table II and formula (6)

^bComputed from Eq. (18) and (19).

^cComputed from value at 3.5 kg/mol.

^dComputed from $\alpha_f = f_g/c_2 = 5.9\text{K}^{-1}$ and $B = 0.85$.

^eComputed from $T_\infty = T_g - c_2$, not M_w -dependent.

^fAssuming $M_c = 35$ kg/mol.

Table 3.5 – Parameters of the WLF model for polystyrene.

Reference	T_s	c_1	c_2	$\eta_s@35\text{kg}\cdot\text{mol}^{-1}$
	(°C)		(K)	(Pa·s)
Williams <i>et al.</i> (1955)	$T_g + 50$	8.8	101.6	not available
Plazek (1965)	T_g	13.3	47.5	not available
Li <i>et al.</i> (2005) ^a	150	7.88	111.3	9.8×10^3 ^b
Leveder (2009)	$T_g + 50$	11.0 ± 0.2	101 ± 1	8.1×10^3
<i>Measured in this thesis</i> (Chap. 6)	$T_g + 50$	12.6 ± 0.1	101 ± 1	$1.1 \pm 0.2 \times 10^4$

^aBulk values.

^bComputed from the viscosity at $123\text{kg}\cdot\text{mol}^{-1}$

Another formally equivalent way to express the thermal dependence of viscosity at a given molecular weight is as follows. Williams, Landel, and Ferry (1955) proposed an expression for the normalized viscosity, now called the *WLF model*:

$$\frac{\eta(T)}{\eta_s} = \exp\left(-c_1 \frac{T - T_s}{c_2 + T - T_s}\right), \quad (3.17)$$

where T_s is an arbitrary reference temperature, $\eta_s = \eta(T_s)$, and c_1 and c_2 are fitting parameters depending on T_s and on the material. It should be noted that T_s must be defined relatively to $T_g(M_w)$, for example $T_s = T_g + 50\text{K}$, in order to keep the correct M_w dependence. Values of c_1 and c_2 from literature are reported in table 3.5. The relations between the Vogel-Fulcher and the WLF parameters are:

$$c_1 = \frac{B}{\alpha_f(T_s - T_\infty)} \quad \text{and} \quad c_2 = T_s - T_\infty. \quad (3.18)$$

3.3.4 Linear viscoelasticity of polymers: the theory of reptation

We briefly mentioned that the reptation motion of polymer chains was responsible for the 3.4 exponent in the M_w dependence of viscosity (for $M_w > M_c$). Reptation is a type of motion where a chain can move only inside a virtual tube that accounts for the restrictive presence of the other chains. It was proposed for polymer motion by Edwards (1967), de Gennes (1971) and Doi and Edwards (1978) [for a review, see Doi and Takimoto (2003)]. Above T_g , the molecular entanglement of polymer chains gives to the material the particular property to behave like an elastic solid for short time scales and a viscous fluid for long time scales. On the basis of that theory, if we assume a simple Maxwell model for viscoelasticity (see table 3.3) it is possible to show that the shear modulus G_e , called the *plateau modulus*, is given by:

$$G_e = \frac{\rho RT}{M_e}, \quad (3.19)$$

where ρ is the density, R is the gas constant, T the temperature and M_e the average molecular mass between entanglements (Jones, 2002). Unfortunately, M_e is not precisely known, but an accepted order of magnitude is $M_e \approx \frac{1}{2}M_c$. The associated relaxation time is called the *terminal relaxation time*, and is:

$$\tau_t = \frac{\eta_0}{G_e}, \quad (3.20)$$

where η_0 is the zero-shear viscosity. The terminal time is of really practical importance. For reflow experiment, formally it is the time needed to reach a steady state flow under constant stress, in other words, it is during this time that elastic effects are present. For imprint processes, it is the time needed for internal stresses to relax. In chapter 6, we will present a method to measure an order of magnitude of the terminal time.

Because ρ decreases with temperature, the product $\rho \times T$ depends weakly on T . With use of Eq. (3.8), we get: $G_e(T_g) = 0.21 \text{ MPa}$ and $G_e(T_g + 100) = 0.24 \text{ MPa}$ for polystyrene $30 \text{ kg}\cdot\text{mol}^{-1}$. As a consequence, τ follows approximately the same dependence on temperature that we saw previously for viscosity.

Plazek and O'Rourke (1971) measured the viscoelastic properties of polystyrene for molecular weights ranging from $1.1 \text{ kg}\cdot\text{mol}^{-1}$ to $800 \text{ kg}\cdot\text{mol}^{-1}$. In their experiments, a torque is applied on a polystyrene cylinder whose creep relaxation is measured. For molecular weight above M_e , a shear modulus of a few MPa is found. Moreover, there is no dependence on temperature above $T_g + 10^\circ\text{C}$.

In a recent review, Majeste *et al.* (1998) proposed a more complex rheological model for polystyrene. In the entangled regime, they added the contributions of different relaxation mechanisms. However, for low shear frequencies, the following term prevails:

$$\eta(\omega) = \frac{\rho RT}{M_e} \int_0^1 \frac{\tau(x)}{1 - i\omega\tau(x)} dx, \quad \tau(x) = \begin{cases} \frac{Nx^4}{16} \tau_C & \text{for } 0 < x < \frac{2v}{\sqrt{N}} \\ \left(x - \frac{v}{\sqrt{N}}\right)^2 \tau_C & \text{for } \frac{2v}{\sqrt{N}} < x < 1 \end{cases} \quad (3.21)$$

with

$$\tau_C = \frac{\zeta_0 R_{EE}^2 N_e^2 N^2}{\pi^2 k_B T}, \quad (3.22)$$

where ζ_0 is the monomeric friction coefficient, R_{EE} the radius of gyration, N is the degree of polymerization, N_e is the average number of repeat units between entanglement, k_B the Boltzmann constant and ν an adjustable parameter. It is a Maxwell model with a continuous spectrum, accounting for the different relaxation times in the reptation process as well as tube length fluctuations. If $\nu = 0$, it corresponds to a pure reptation. In this case, we have a simple relation between η_0 and τ_C , in the limit $\omega \rightarrow 0$:

$$\eta_0 = \frac{G_e \tau_C}{3}, \quad (3.23)$$

and the model can be recast in:

$$\eta(\omega) = \int_0^1 \frac{3\eta_0 x^2}{1 - i\omega\tau_C x^2} dx. \quad (3.24)$$

The latter model is then a 2-parameters model (like the Maxwell model) if we set $\nu = 0$. A variable ν can be introduced as an additional fitting parameter.

For classical thermal nanoimprint, time scales of reptation are enough to have a fair understanding of the polymer behavior. However, for ultra-fast imprints, it could be relevant to take into account faster relaxation processes (Majeste *et al.*, 1998).

3.4 Thin films properties

When the dimensions of the material go down to a few molecular lengths, effects of the granular consistency of matter appear. The variation of mechanical properties are important for process modeling, as thicknesses of a few nanometers are commonly reached in nanoimprint processes. In this section, we focus on the properties of thin polymer films. For a review in different configurations, such as polymers in nanopores or composite materials, see the work of Alcoutlabi and McKenna (2005).

3.4.1 Thickness-dependent glass transition temperature

With the development of miniaturization of polymer films, many authors have reported a variable T_g with variable thicknesses of supported films. Keddie *et al.* (1994) made the first quantitative analysis and proposed a phenomenological law for T_g as a function of thickness h :

$$T_g(h) = T_g^{\text{bulk}} \left[1 - \left(\frac{\xi}{h} \right)^\delta \right], \quad (3.25)$$

with T_g^{bulk} the glass transition temperature of the bulk, $\xi = 3.2 \pm 0.6$ nm a characteristic length and $\delta = 1.8 \pm 0.2$ an adjustable parameter. The authors reported a very weak dependence for ξ on molecular weight, in particular much weaker than that of the chain length R_{EE} ($\sim \sqrt{M_w}$, see Eq. (3.6) on page 37). Later works supported these observations (Fukao and Miyamoto, 2000; Ellison and Torkelson, 2003; Merabia

et al., 2004; Yang *et al.*, 2010, 2011; and for a review of earlier works, see Forrest and Dalnoki-Veress, 2001). Contrary to others, Singh *et al.* (2004) found a M_w -dependence for ξ , of the order of R_{EE} . Herminghaus *et al.* (2001); Kim *et al.* (2001b,a) proposed another model of the form:

$$T_g(h) = \frac{T_g^{\text{bulk}}}{1 + \frac{\xi}{h}}, \quad (3.26)$$

where ξ is of the order of the monomer length (7 – 10 Å).

Several models have been proposed to explain this reduction of T_g : 2-, 3-layers or continuous gradient of mobility or relaxation times, anisotropy of chain conformation, etc. The fundamental understanding of this variation in T_g is beyond the scope of this thesis. However, from a practical point of view, we note that the role of the free surface and of the underlying substrate were rapidly emphasized. Carrying out experiments on free standing films, a linear variations for thickness below a critical thickness h_c was found (de Gennes, 2000; Dalnoki-Veress *et al.*, 2001; Frick *et al.*, 2003):

$$T_g(h) = T_g^{\text{bulk}} + \alpha(h - h_c) \quad \text{for } h < h_c, \quad (3.27)$$

where this time h_c is strongly dependent on M_w . On the other hand, Sharp and Forrest (2003) found no reduction of T_g for metal-coated films, and if the coating is removed, the reduction of T_g is recovered, showing the importance of the free interface.

We notice that there were also contradicting reports of increase in T_g by Wallace *et al.* (1995) for supported films, or no M_w dependence for free standing films by Ge *et al.* (2000).

3.4.2 Thickness-dependent viscosity

What is important from a process point of view is the rheological behavior of the polymer and its variation with h (and possibly M_w). Is viscosity reduced in thin films? Does this reduction hold when the film is confined by the mold? Is the WLF model still relevant?

Using X-ray photon correlation spectroscopy, Kim *et al.* (2003, 2007a); Li *et al.* (2005); Yang *et al.* (2009) studied the variation of viscosity with film thickness. Masson and Green (2002); Bodiguel and Fretigny (2006, 2007) measured the viscosity of thin polystyrene films by monitoring the nucleation and growth of dewetting holes. Similarly to the reduction of T_g , the former proposed a law of the form:

$$\eta(h) = \eta^{\text{bulk}} \left[1 - K \left(\frac{\xi}{h} \right)^\delta \right], \quad (3.28)$$

with $\xi = 3.2\text{nm}$, $\delta = 1.8$ (same values reported by Keddie *et al.* (1994)), and a fitting parameter $K = 35$. Nevertheless, neither the dependence on molecular weight nor the dependence on temperature was studied and the authors were skeptical about the use of a WLF model for thin films. On the other hand, Bodiguel and Fretigny (2006, 2007) developed a model where viscosity varies inside the film. They performed

their experiments on liquid substrate and assumed a z -dependent viscosity near the interface:

$$\frac{\eta(z)}{\eta^{\text{bulk}}} = 1 - \exp\left[-\left(\frac{z}{R_G}\right)^\beta\right], \quad 0 < z < \frac{h}{2}, \quad (3.29)$$

where β is a fitting parameter. The length scale here is the dimension of a chain (equivalently R_G or R_{EE}). The observed viscosity is then the mean viscosity over the whole thickness of the film:

$$\eta(h) = \eta^{\text{bulk}} \frac{2}{h} \int_0^{h/2} \left(1 - \exp\left[-\left(\frac{z}{R_G}\right)^\beta\right]\right) dz. \quad (3.30)$$

They confirmed that a Vogel-Fulcher law fairly describes the temperature dependence, with bulk values for B/α_f and T_∞ (see Eq. (3.15) on page 43), but with h -dependent A .

Leveder (2009); Leveder *et al.* (2010) showed that it is possible to model the thickness dependence of viscosity with use of an *extended WLF model* (xWLF) built as follows. The length scale of the phenomenon is R_{EE} , and we define the normalized thickness h^* by:

$$h^*(M_w) = \frac{h}{R_{EE}(M_w)}. \quad (3.31)$$

The glass transition temperature is assumed to be a function of h^* with the expression reported by Singh *et al.* (2004):⁵

$$T_g(h^*, M_w) = T_g^{\text{bulk}}(M_w) \left(1 - \alpha \left(\frac{1}{h^*(M_w)}\right)^\delta\right), \quad (3.32)$$

with $\alpha = 0.968$, $\delta = 1.78$ and T_g^{bulk} is the molecular-weight-dependent T_g for bulk material. Now, if we define the reference temperature $T_s(h^*, M_w) = T_g(h^*, M_w) + \text{constant}$, then the xWLF model is:

$$\frac{\eta(T, h^*, M_w)}{\eta_s^{\text{bulk}}(M_w)} = \exp\left(-c_1^{\text{bulk}} \frac{T - T_s(h^*, M_w)}{c_2^{\text{bulk}} + T - T_s(h^*, M_w)}\right). \quad (3.33)$$

The strength of Leveder's approach is that the reduction of η with h is recovered with no fitting parameter, provided that an expression of $T_g(h^*)$ is known. This idea was also suggested by Yang *et al.* (2009) who were able to describe their observation of reduced viscosity by inserting Herminghaus *et al.* (2001) expression for thickness-dependent T_g (Eq. 3.26) in a Vogel-Fulcher model.

In addition, Leveder measured $T_g(h^*)$ for a confined film, that is, a film sandwiched between two silicon plates. T_g was found to increase with decreasing h^* and the behavior is well modeled by Eq. (3.32) with the parameters: $\alpha = -0.968$ and

⁵From our point of view, an interesting feature in Singh's ellipsometry experiments is that multiple angles were used in order to decorrelate the variations of specific volume and those of the optical index with temperature, resulting in a more accurate assessment of T_g .

$\delta = 1.41$. By inserting this $T_g(h^*)$ function into the xWLF model, viscosity increases with decreasing thickness. This increased viscosity was experimentally measured by nanoimprint experiments, and data were consistent with the xWLF model presented above (Leveder, 2009, p. 173).

References

- M. Alcoutlabi and G. B. McKenna. Effects of confinement on material behaviour at the nanometre size scale. *Journal of Physics: Condensed Matter* **17**, R461–R524 (2005).
- L. Berthier and G. Biroli. Theoretical perspective on the glass transition and amorphous materials. *Reviews of Modern Physics* **83**, 587–645 (2011).
- J. Bicerano. *Prediction of polymer properties*. CRC Press (2002).
- H. Bodiguel and C. Fretigny. Reduced viscosity in thin polymer films. *Physical Review Letters* **97**, 266105 (2006).
- H. Bodiguel and C. Fretigny. Viscoelastic properties of ultrathin polystyrene films. *Macromolecules* **40**, 7291–7298 (2007).
- P. J. Carreau. Rheological equations from molecular network theories. *Transactions of the Society of Rheology* **16**, 99–127 (1972).
- R. H. Colby, L. J. Fetters, and W. W. Graessley. The melt viscosity-molecular weight relationship for linear polymers. *Macromolecules* **20**, 2226–2237 (1987).
- K. Dalnoki-Veress, J. A. Forrest, C. Murray, C. Gigault, and J. R. Dutcher. Molecular weight dependence of reductions in the glass transition temperature of thin, freely standing polymer films. *Physical Review E* **63**, 031801 (2001).
- P. G. de Gennes. Reptation of a polymer chain in the presence of fixed obstacles. *The Journal of Chemical Physics* **55**, 572–579 (1971).
- P. de Gennes. Glass transitions in thin polymer films. *The European Physical Journal E: Soft Matter and Biological Physics* **2**, 201–205 (2000).
- G. T. Dee and B. B. Sauer. The surface tension of polymer liquids. *Advances in Physics* **47**, 161 (1998).
- M. Doi and S. F. Edwards. Dynamics of concentrated polymer systems. part 1. Brownian motion in the equilibrium state. *Journal of the Chemical Society, Faraday Transactions 2* **74**, 1789 (1978).
- M. Doi and J.-i. Takimoto. Molecular modelling of entanglement. *Philosophical Transactions of the Royal Society of London. Series A: Mathematical, Physical and Engineering Sciences* **361**, 641–652 (2003).
- A. K. Doolittle. Studies in newtonian flow. II. the dependence of the viscosity of liquids on Free-Space. *Journal of Applied Physics* **22**, 1471–1475 (1951).
- S. F. Edwards. The statistical mechanics of polymerized material. *Proceedings of the Physical Society* **92**, 9–16 (1967).

- C. J. Ellison and J. M. Torkelson. The distribution of glass-transition temperatures in nanoscopically confined glass formers. *Nat Mater* **2**, 695–700 (2003).
- J. D. Ferry. *Viscoelastic Properties of Polymers*. John Wiley & sons (1980).
- J. A. Forrest and K. Dalnoki-Veress. The glass transition in thin polymer films. *Advances in Colloid and Interface Science* **94**, 167–195 (2001).
- T. G. Fox and S. Loshaek. Influence of molecular weight and degree of crosslinking on the specific volume and glass temperature of polymers. *Journal of Polymer Science* **15**, 371–390 (1955)a.
- T. G. Fox and S. Loshaek. Isothermal viscosity-molecular weight dependence for long polymer chains. *Journal of Applied Physics* **26**, 1080–1082 (1955)b.
- T. G. Fox and P. J. Flory. Viscosity-molecular weight and viscosity-temperature relationships for polystyrene and polyisobutylene. *J. Am. Chem. Soc.* **70**, 2384–2395 (1948).
- T. G. Fox and P. J. Flory. Second-Order transition temperatures and related properties of polystyrene. i. influence of molecular weight. *Journal of Applied Physics* **21**, 581–591 (1950).
- B. Frick, K. Dalnoki-Veress, J. Forrest, J. Dutcher, C. Murray, and A. Higgins. First inelastic neutron scattering studies on thin free standing polymer films. *The European Physical Journal E: Soft Matter and Biological Physics* **12**, 93–96 (2003).
- K. Fukao and Y. Miyamoto. Glass transitions and dynamics in thin polymer films: Dielectric relaxation of thin films of polystyrene. *Physical Review E* **61**, 1743 (2000).
- S. Ge, Y. Pu, W. Zhang, M. Rafailovich, J. Sokolov, C. Buenviaje, R. Buckmaster, and R. M. Overney. Shear modulation force microscopy study of near surface glass transition temperatures. *Physical Review Letters* **85**, 2340 (2000).
- S. Herminghaus, K. Jacobs, and R. Seemann. The glass transition of thin polymer films: some questions, and a possible answer. *The European Physical Journal E: Soft Matter and Biological Physics* **5**, 531–538 (2001).
- R. A. L. Jones. *Soft Condensed Matter*. Oxford University Press (2002).
- J. L. Keddie, R. A. L. Jones, and R. A. Cory. Size-Dependent depression of the glass transition temperature in polymer films. *Europhysics Letters (EPL)* **27**, 59–64 (1994).
- H. Kim, A. Rühm, L. B. Lurio, J. K. Basu, J. Lal, D. Lumma, S. G. J. Mochrie, and S. K. Sinha. Surface dynamics of polymer films. *Physical Review Letters* **90**, 068302 (2003).
- H. Kim, Z. Jiang, H. Lee, Y. J. Lee, X. Jiao, C. Li, L. Lurio, M. Rafailovich, and S. Sinha. Hydrodynamic surface fluctuations of polymer films by coherent x-ray scattering. *Thin Solid Films* **515**, 5536–5540 (2007)a.
- J. H. Kim, J. Jang, D. Lee, and W. Zin. Thickness and composition dependence of the glass transition temperature in thin homogeneous polymer blend films. *Macromolecules* **35**, 311–313 (2001)a.
- J. H. Kim, J. Jang, and W. Zin. Thickness dependence of the glass transition temperature in thin polymer films. *Langmuir* **17**, 2703–2710 (2001)b.

- S. H. Kim, F. Teymour, and J. A. Debling. A unifying approach for melt rheology of linear polystyrene. *Journal of Applied Polymer Science* **103**, 2597–2607 (2007)b.
- T. Leveder. Etude et caractérisation de films polymère ultra-minces dans le cadre de la lithographie par nanoimpression. PhD thesis, Institut Polytechnique de Grenoble (2009).
- T. Leveder, S. Landis, N. Chaix, and L. Davoust. Thin polymer films viscosity measurements from nanopatterning method. *Journal of Vacuum Science & Technology B: Microelectronics and Nanometer Structures* **28**, 1251 (2010).
- C. Li, T. Koga, C. Li, J. Jiang, S. Sharma, S. Narayanan, L. B. Lurio, X. Hu, X. Jiao, S. K. Sinha, S. Billet, D. Sosnowik, H. Kim, J. C. Sokolov, and M. H. Rafailovich. Viscosity measurements of very thin polymer films. *Macromolecules* **38**, 5144–5151 (2005).
- J. Majeste, J. Montfort, A. Allal, and G. Marin. Viscoelasticity of low molecular weight polymers and the transition to the entangled regime. *Rheologica Acta* **37**, 486–499 (1998).
- J. Masson and P. F. Green. Viscosity of entangled polystyrene thin film melts: Film thickness dependence. *Physical Review E* **65**, 031806 (2002).
- S. Merabia, P. Sotta, and D. Long. Heterogeneous nature of the dynamics and glass transition in thin polymer films. *The European Physical Journal E: Soft Matter and Biological Physics* **15**, 189–210 (2004).
- D. Plazek and V. O'Rourke. Viscoelastic behavior of low molecular weight polystyrene. *Journal of Polymer Science Part A-2: Polymer Physics* **9**, 209–243 (1971).
- D. J. Plazek. Temperature dependence of the viscoelastic behavior of polystyrene. *The Journal of Physical Chemistry* **69**, 3480–3487 (1965).
- J. S. Sharp and J. A. Forrest. Free surfaces cause reductions in the glass transition temperature of thin polystyrene films. *Physical Review Letters* **91**, 235701 (2003).
- L. Singh, P. J. Ludovice, and C. L. Henderson. Influence of molecular weight and film thickness on the glass transition temperature and coefficient of thermal expansion of supported ultrathin polymer films. *Thin Solid Films* **449**, 231–241 (2004).
- H. Vogel. The law of the relation between the viscosity of liquids and the temperature. *Physik Zeitschrift* **22**, 645–646 (1921).
- W. E. Wallace, J. H. van Zanten, and W. L. Wu. Influence of an impenetrable interface on a polymer glass-transition temperature. *Physical Review E* **52**, R3329–R3332 (1995).
- M. L. Williams, R. F. Landel, and J. D. Ferry. The temperature dependence of relaxation mechanisms in amorphous polymers and other glass-forming liquids. *Journal of the American Chemical Society* **77**, 3701–3707 (1955).
- Z. Yang, D. Peng, A. Clough, C. Lam, and O. Tsui. Is the dynamics of polystyrene films consistent with their glass transition temperature? *The European Physical Journal - Special Topics* **189**, 155–164 (2010).
- Z. Yang, C. Lam, E. DiMasi, N. Bouet, J. Jordan-Sweet, and O. K. C. Tsui. Method to measure the viscosity of nanometer liquid films from the surface fluctuations. *Applied Physics Letters* **94**, 251906 (2009).

- Z. Yang, A. Clough, C. Lam, and O. K. C. Tsui. Glass transition dynamics and surface mobility of entangled polystyrene films at equilibrium. *Macromolecules* (2011).
- K. Yasuda, R. Armstrong, and R. Cohen. Shear flow properties of concentrated solutions of linear and star branched polystyrenes. *Rheologica Acta* **20**, 163–178 (1981).
- Z. Zhou and D. Yan. Configurational-conformational statistics of stereoirregular polystyrene. *Macromolecular Theory and Simulations* **5**, 939–945 (1996).

Part II

Creeping flows and applications

Chapter 4

The supported thin film equations of creeping flow

One straightforward way to simulate the flow is to numerically solve the Stokes equation in the fluid domain with appropriate boundary conditions. Nowadays this can be done in reasonable time with a desktop computer for usual patterns (up to several micrometers), and we will see some implementation in the last section of this chapter. Sometimes, for particularly harsh topologies, numerical computation cannot be avoided. However, the simulation at the wafer scale is still a matter of heavy scientific computing, and above all, the physical understanding of capillary phenomena can only be comprehended by working through the equations. After how much time is an annealed pattern leveled by surface tension? What is the characteristic period of dewetting? What is the influence of viscosity? It is possible to answer these questions with the asymptotic (in other words, approximate) models presented below, based on lubrication theory and capillary wave theory.

Although the theoretical developments can be found in numerous books (see for example Bruus, 2008), they are reported here for a didactic purpose, along with fundamental hypotheses specific to nanoimprint processes. In both cases, the approach is the same: we start from the transient Stokes equation describing the flow at low Reynolds number, presented in chapter 2. Then, depending on geometrical assumptions, an asymptotic model for the time-dependent thickness of the film is found. In the capillary wave theory, an analytical solution can be expressed as a function of rheological properties. But first, let us see the fundamental hypotheses common for both models.

4.1 Fundamental hypotheses

We consider a fluid film supported by a flat impermeable solid substrate at rest (Fig. 4.1 on the next page). We assume that the shape of the film is periodic in both directions x and y , and we consider only an elementary unit of dimensions $L_x \times L_y$. The mean thickness over this surface is h_0 . With mass conservation and isothermal hypothesis, h_0 does not depend on time. The instantaneous local thick-

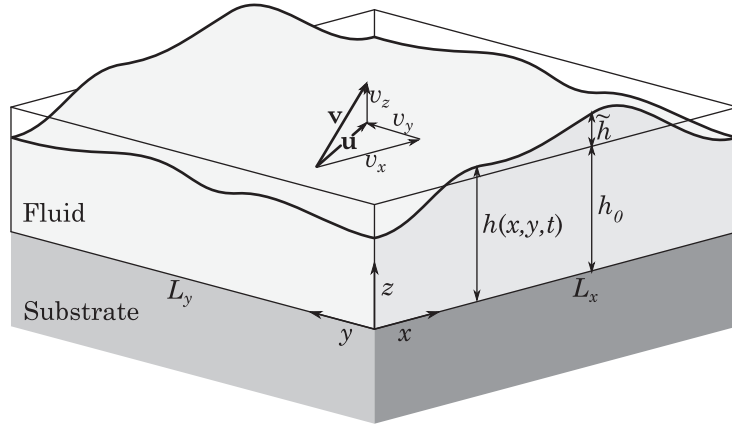


Figure 4.1 – Geometry and symbols.

ness of the film is written $h(x, y, t)$, and its variation relative to the mean thickness is $\tilde{h}(x, y, t) = h(x, y, t) - h_0$. The origin for the height z is taken at the surface of the solid. The horizontal part of the velocity field $\mathbf{v} = (v_x, v_y, v_z)$ is the vector $\mathbf{u} = (v_x, v_y)$. For readability, we write f' the z -derivative of a function f (not to be confused with the real part of a quantity).

In chapter 2, we already went through fundamental considerations, and argued that the Stokes equation (Eq. 2.5) is relevant for modeling flows at the nanoscale. We also saw that the boundary conditions are:

1. For the liquid-substrate interface at rest: impermeability,

$$v_z = 0, \quad (4.1)$$

and Navier slip,

$$\mathbf{u}(z = 0) = \beta \mathbf{u}'(z = 0), \quad (4.2)$$

with β the slip length. The value $\beta = 0$ implies a classical no-slip boundary condition.

2. For the free liquid surface: Laplace pressure depends on the local curvature of the interface, κ , that can be written:

$$\kappa = \nabla_H \cdot \left(\frac{\nabla_H h}{\sqrt{1 + (\nabla_H h)^2}} \right), \quad (4.3)$$

where ∇_H is the horizontal differential operator $\left(\frac{\partial}{\partial x}, \frac{\partial}{\partial y} \right)$. With the hypothesis of small slopes, $|\nabla h|^2 \ll 1$, the curvature is $\kappa \approx \nabla^2 h$. We will discuss this approximation in section 4.5.

We saw in chapter 2 that van der Waals forces could be present as a force field, $\mathbf{f} = -\nabla \Pi$, with Π called the disjoining pressure. If Π depends only on $h(x, y)$ (and

not on z), then it is equivalent to take the disjoining pressure into account either as a field $-\nabla\Pi$ inside the fluid domain, or as a pressure $\Pi(h)$ at the free interface. For simplicity in computation, the latter option is preferred, and finally the normal boundary condition at the free interface is the sum of the Laplace pressure and the disjoining pressure:

$$p(z = h(x, y)) - \sigma_{zz} = -\gamma\nabla^2 h + \Pi(h). \quad (4.4)$$

Moreover, since there is no tangential stress externally applied upon the liquid surface, the last boundary condition writes as:

$$\sigma_t(z = h(x, y)) = 0. \quad (4.5)$$

Regarding the assumption on the disjoining pressure, we will see in chapter 7 that Π is a function of $h(x, y)$ only, provided that the global shape of the deformed interface is large compared to the thickness of the film. If it is not the case, in other words if the wavelength of the deformation is high, we can ask whether the disjoining pressure is enhanced compared to a flat interface. If the deformation is small in amplitude, results from computations of Casimir forces between corrugated plates show that the force is rather weaker. In that case, Laplace pressure is more likely to be the driving force of the flow. As we will consider only films in either the first configuration (long waves) or the second one (small amplitudes), then the assumption $\Pi = \Pi(h)$ is rather relevant.

4.2 Lubrication theory: long wave approximation

The starting point for lubrication theory is the concept of *thin film*, in other words, one dimension of the fluid domain called *thickness* is much smaller than the other dimensions. It is the counterpart of plate theory in solid mechanics. Lubrication theory was first developed by Reynolds (1886). It was originally intended to model the flow of a lubricant between moving parts of a mechanism, hence its name. An extensive study of lubrication theory applied to capillary driven thin film flows can be found in the seminal review by Oron *et al.* (1997), later completed by Craster and Matar (2009).

4.2.1 The Reynolds equation

If L is the horizontal extension of the fluid domain, let $\varepsilon = 2\pi h_0/L$ be the lubrication ratio. In terms of wavevector, if $k = 2\pi/L$, then $\varepsilon = k \times h_0$. In lubrication theory, $\varepsilon \ll 1$, equivalently $L \gg h_0$, or even $k \ll 1/h_0$, this is why this theory is also sometimes called *long wave approximation*. A detailed mathematical treatment of the path from the Stokes equation to the Reynolds equation can be found in Cimatti (1983); Bayada and Chambat (1986). Here we report the main concepts.

If we assume $\varepsilon \ll 1$, then it is possible to develop the continuity and Stokes equations according to a regular perturbation in powers of ε . The first order term can then

be computed. This is carried out in appendix A. The main result of lubrication theory is that pressure does not depend on height, it is only a function of (x, y) . The velocity field is therefore mainly parallel to the substrate, except for normal motion responsible for the height variation of the free interface. From a mass balance, we find that the local temporal variation of the thickness is the divergence of a flux. This flux is proportional to the local pressure gradient and is a rather complicated function of the thickness:

$$\frac{\partial h}{\partial t} = \nabla_H \cdot \left(\frac{h^2(h + 3\beta)}{3\eta(h)} \nabla_H p \right), \quad (4.6)$$

where ∇_H is the horizontal differential operator—for readability, the suffix H is not written hereafter— p is the local pressure, and $\eta(h)$ is the (possibly thickness-dependent) fluid viscosity. The equation above is called the *Reynolds equation* for supported thin films.

Let us now focus on the pressure field. As already mentioned above, it is given by the Laplace pressure and the disjoining pressure. With the result that p does not depend on z , it is consistent to disregard the normal viscous stress, σ_{zz} , so that the pressure field takes the form:

$$p(x, y) = -\gamma \nabla^2 h + \Pi(h). \quad (4.7)$$

If we assume that surface tension does not depend on thickness, with use of the Reynolds equation (4.6), we get:

$$\frac{\partial h}{\partial t} + \nabla \cdot \left[\frac{h^2(h + 3\beta)}{3\eta(h)} \left(\gamma \nabla^3 h - \frac{\partial \Pi}{\partial h} \nabla h \right) \right] = 0, \quad (4.8)$$

with the writing convention $\nabla^3 = \nabla(\nabla^2)$. We now see that the flux is a sum of two terms, one driven by surface tension and the other one driven by the disjoining pressure. Depending on the sign of $\partial \Pi / \partial h$, those two terms will compete or collaborate. This equation has been extensively considered in literature to model the spinodal dewetting of thin films, or the leveling of patterns.

4.2.2 Smoothing or not smoothing

The effect of surface tension is to reduce the free interface of the film to a minimum state of energy, in other words, to minimize the surface area. That is why under annealing, sharp edges tend to smooth and protrusions are leveled. However, the smoothing may not occur because of the disjoining pressure. Figure 4.2 on the facing page shows two Atomic Force Microscopy (AFM) measurements of a nanoimprinted polystyrene film. The initial profile is made of lines of various wavelength. After annealing, the area of smaller wavelength (right area) is leveled to a large extent, whereas the large wavelengths (left area) lead to the dewetting of the film.

4.2.3 Governing dimensionless numbers

The linear stability analysis below will give us the characteristic time of the leveling.

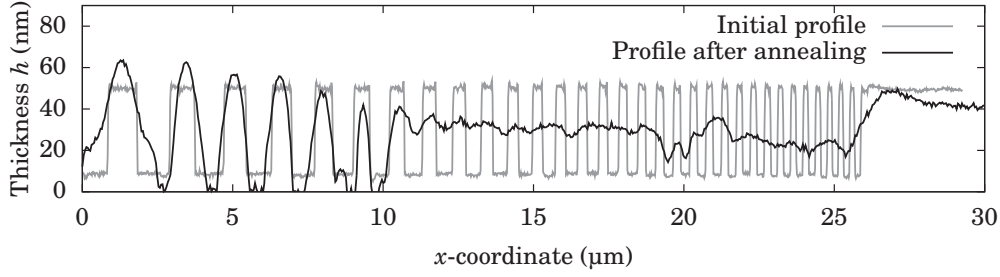


Figure 4.2 – AFM profiles of a nanoimprinted polystyrene film, before and after annealing.

Linear stability analysis. We assume an invariance of the geometry along the y -axis, which implies a 2D flow. We study the evolution of a small deformation of the surface: $h(t) = h_0 + \tilde{h}(t) \cos(k \times x)$ with $\tilde{h} \ll h_0$. We also assume $\beta \ll h_0$ (no-slip boundary condition) and $\eta = \eta(h_0)$ (constant viscosity). Keeping only the first order terms in \tilde{h} , equation (4.8) yields:

$$\frac{\partial \tilde{h}}{\partial t} + \frac{1 + \frac{\text{Ha}}{\varepsilon^2}}{\tau} \tilde{h}(t) = 0, \quad (4.9)$$

with $\varepsilon = k \times h_0$ as defined above, τ the characteristic time:

$$\tau = \frac{3\eta}{\gamma h_0^3 k^4}, \quad (4.10)$$

and Ha the dimensionless *Hamaker number*:

$$\text{Ha} = \frac{h_0^2 \frac{\partial \Pi}{\partial h}(h_0)}{\gamma}. \quad (4.11)$$

Note that Ha may be either positive or negative, depending on the sign of $\frac{\partial \Pi}{\partial h}$. The Hamaker number quantifies the ratio of the disjoining pressure over the Laplace pressure. If $|\text{Ha}| \ll \varepsilon^2$, the Laplace pressure prevails and the van der Waals forces can be neglected. We will see that it is often the case in our experimental setup. In that case, the small perturbation \tilde{h} exponentially decreases with the characteristic time τ , and we can define a *capillary number* of the experiment:

$$\text{Ca} = \frac{\tau}{t} = \frac{3\eta}{\gamma h_0^3 k^4 t}. \quad (4.12)$$

The capillary number quantifies the effect of viscous forces versus surface tension. If $\text{Ca} \gg 1$, the viscous stress overcomes the surface tension drive, and almost no flow is observed.

Let us go back to the Hamaker number. If we now assume that $|\text{Ha}| \sim \varepsilon^2$, then the disjoining pressure may be taken into account. Moreover, if $\text{Ha} < 0$, then the film is known to be unstable, as we saw on figure 4.2, and in our case, the small perturbation

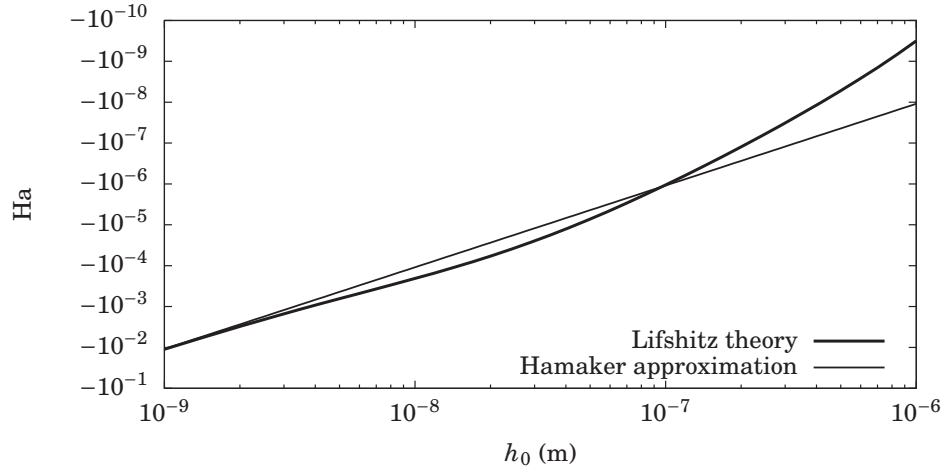


Figure 4.3 – Hamaker number for a supported polystyrene film on silicon oxide substrate. The thick line is the result of the Lifshitz theory, the thin line is the Hamaker approximation: $Ha = A/(2\pi h_0^2 \gamma)$ with $A = -2.2 \times 10^{-21}$ J fitted from the Lifshitz theory.

\tilde{h} exponentially increases if $Ha < -\varepsilon^2$. We leave the question of how fast the increase is to chapter 8. For now, we only discuss whether the disjoining pressure is significant for the flow.

How can we compute Ha ? We will see this issue in detail in chapter 7, but for now we can obtain an order of magnitude of Ha by making use of the Hamaker theory for the disjoining pressure (Israelachvili, 1991). In this theory, $\Pi(h)$ is of the form:

$$\Pi(h) = \frac{-A}{6\pi h^3}, \quad (4.13)$$

with A the *Hamaker constant*, typically ranging from ± 1 to $\pm 10 \times 10^{-21}$ J. The unit of the Hamaker constant is sometimes the zepta Joule: $1 \text{ zJ} = 10^{-21}$ J. Thus, from equation (4.11), the Hamaker number is given by:

$$Ha = \frac{A}{2\pi h_0^2 \gamma}. \quad (4.14)$$

Figure 4.3 is a plot of the negative Hamaker number for a supported polystyrene film on a silicon oxide substrate (unstable film). The Hamaker number defined by equation (4.11) is computed from the full Lifshitz theory (Chap. 7), and compared to the Hamaker number approximated by equation (4.14). The result is that, first, the Hamaker approximation gives a fairly good order of magnitude of Ha , at least for films below 100 nm. Second, Ha is small, mainly because of the strength of van der Waals forces compared to surface tension of our materials, so that in our experimental setup, Ha is very unlikely to exceed unity.

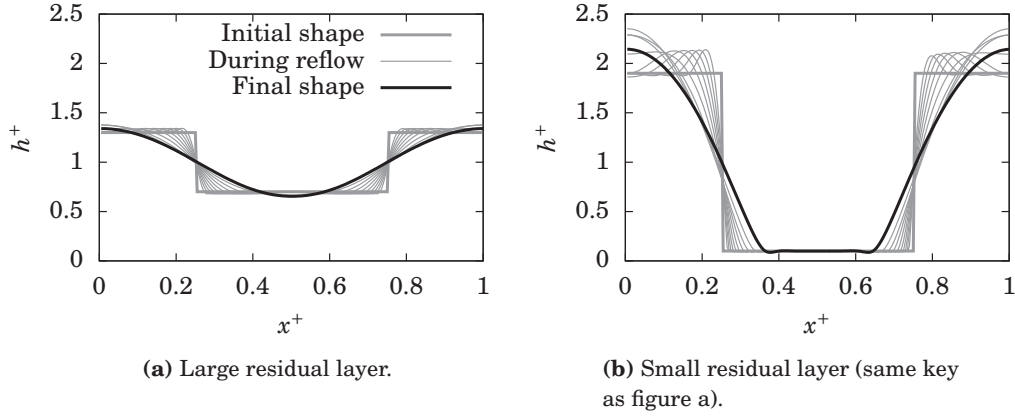


Figure 4.4 – Simulated reflow of a square profile ($x^+ = \frac{x}{L}$, $h^+ = \frac{h}{h_0}$) during $t^+ = \frac{t}{\tau} = 0.1$.

4.2.4 Some effects of non-linearity

We developed a finite-volume method to solve the non-linear lubrication equation. Details are reported in appendix B on page 189. For now, we assume a constant viscosity and surface tension and neglect disjoining pressure. In addition, we assume a 2D flow, as in the previous subsection. In terms of dimensionless quantities: $t^+ = t/\tau$ (Eq. 4.10), $x^+ = x/L$ and $h^+ = h/h_0$, equation (4.8) can be recast in:

$$\frac{\partial h^+}{\partial t^+} + \frac{1}{(2\pi)^4} \times \frac{\partial}{\partial x^+} \left(h^{+3} \frac{\partial^3 h^+}{\partial x^{+3}} \right) = 0. \quad (4.15)$$

Two-tier reflow. One of the effects of non-linearity in equation (4.15) is what we call in this thesis *two-tier reflow*. We already saw that the time evolution of the thickness is caused by the divergence of a flux. If we try to analyze the non-linearity at least qualitatively, we can say that this flux is of the order of the thickness to the power of three (h^{+3}). So, in thin areas ($h^+ < 1$), the flow is largely hindered by the substrate, whereas in thicker areas ($h^+ > 1$) the flow is made easier. The resulting effect is that protrusions are deformed and flow faster at the top than at the bottom.

This effect is particularly amplified if thin areas (residual layer) are much thinner than the mean thickness of the film, as we can see in figure 4.4. We simulated the reflow of a square profile during $t^+ = 0.1$, for two initial topologies. The first one is a square profile with a rather large (relative) residual layer (Fig. 4.4a). After $t^+ = 0.1$, we can see that the shape is almost sinusoidal. The second topology is a square profile with this time a thin residual layer (Fig. 4.4b). In this case, after the same time of reflow, the top of the protrusions are rounded, but the bottom shows little evolution. For practical applications, such as for microlens arrays (see chapter 5 on page 81), it may be interesting to have the top of the features smoothed while the bottom is still sharp.

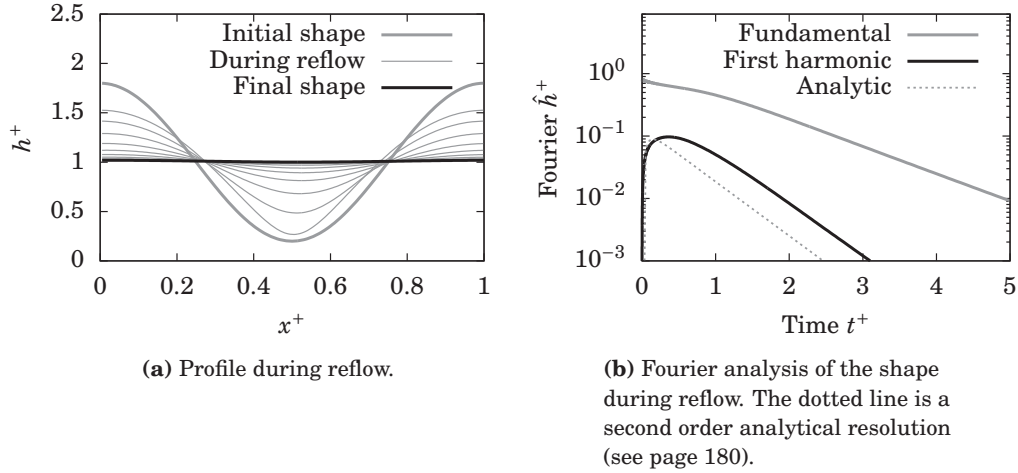
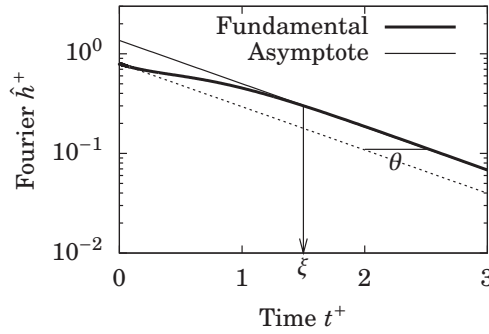


Figure 4.5 – Simulated reflow of a sinusoidal profile during $t^+ = 5$.

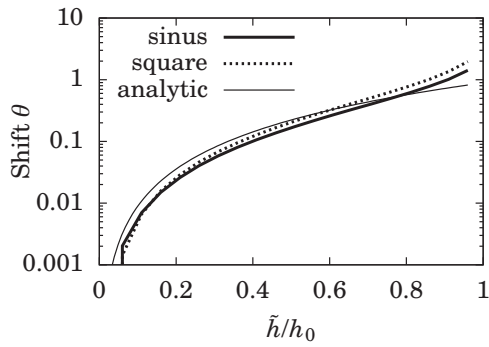
Generation of high order modes. Let us follow the reflow of a sinusoidal shape, as depicted in figure 4.5. Before the reflow, the shape is formed by a single mode, called the fundamental, of half amplitude $\tilde{h}^+ = 0.8$. Because of two-tier reflow, the bottom of the sinusoid flows more slowly than the top (Fig. 4.5a). the sinusoid is distorted, and clearly other modes of high order (*harmonics*) appear at the beginning of the reflow. However, at long times, these harmonics vanish and a pure sinusoid is recovered, until the film becomes flat. If we perform a Fourier analysis of the shape during the reflow, we can extract the amplitude of the fundamental and the harmonics. On figure 4.5b, the fundamental starts at \tilde{h}^+ and decrease with time. A straight line in this semi-log plot means that the decrease is exponential, and for the fundamental at long time it is $\exp(-t^+)$.

Is it possible to extract information about harmonics by working on the lubrication equation (4.15)? First, we recall that the characteristic time depends on the wavevector to the power of four (Eq. 4.10). So, the first harmonic ($2 \times$ fundamental) should decrease much faster, as $\exp(-16t^+)$. In addition, it turns out that for a small amplitude of the fundamental, the problem is weakly non-linear, and we can extract some information about how fast the first harmonic increases. This treatment is done in appendix A, section A.2.2 on page 180. This increase is in $\exp(14t^+)$, which is rapidly hindered by the $\exp(-16t^+)$ decrease. Maximum amplitude is about $0.14\tilde{h}^{+2}$ and is reached at $t^+ = \ln 8/18 \approx 0.1$. The solution is plotted on figure 4.5b (dotted line, “Analytic”). Although it does not perfectly fit the simulated harmonic,¹ it gives a correct order of magnitude of the maximum amplitude, and the $\exp(-16t^+)$ decrease is recovered.

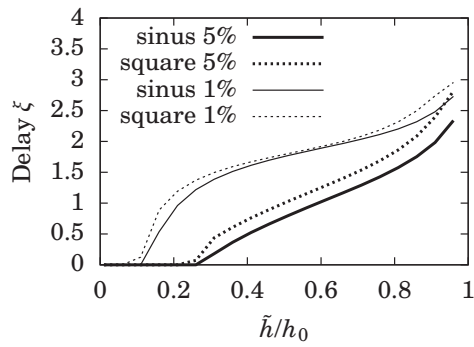
¹The fit is much better for $h^+ < 0.4$, but for the purpose of this section, we study highly non-linear cases.



(a) Evolution of the fundamental of a sinusoidal profile ($\tilde{h}^+ = 0.8$). Definition of the shift θ and the delay ξ .



(b) Shift factor.



(c) Delay.

Figure 4.6 – Delay of the linear regime for a square and a sinusoidal profile.

Delay. Let us go back to the fundamental mode of the shape. We found with the linear stability analysis above that for long times it exponentially decreases in $\exp(-t^+)$. Now, until this asymptotic regime is reached, the variation of the fundamental mode is not trivial, as we can see on figure 4.6a on the preceding page, and of course depends on the full initial shape. This aspect was studied by Keunings and Bousfield (1987). It can be of practical interest to know the time after which the asymptotic regime is reached, in other words the time after which the lubrication equation can be linearized. We can describe the long-time asymptote by $\exp(-t^+ + \theta)$ where θ is a shift factor. Figure 4.6b shows simulated values of θ for two initial shapes (sinusoid and square profiles), along with the function $\frac{57}{64}\tilde{h}^{+2}$ obtained from the mathematical development of section A.2.2 on page 180. There are no significant differences between a square and a sinusoidal shape. Besides, the analytic shift fairly accounts for computed value over a large range of amplitude \tilde{h}^+ .

We also define the time ξ , called *delay*, beyond which the amplitude of the fundamental is closer than a definite distance to its linear asymptote. Figure 4.6c reports the delay for criteria of 5% and 1%. Here again, no significant difference is found between the two topologies. Remarkably, there is no delay below $\tilde{h}^+ = 0.25$ for the 5% criterion. This means that, for this degree of accuracy, if we consider for example a 100 nm polymer film, the reflow of patterns that are up to 50 nm deep can be modeled by a linear approach. In other words, the linear description is very robust, and we will take advantage of this property in chapter 6.

4.3 Capillary wave theory: small deformation approximation

On the one hand, the Reynolds equation is efficient to model the flow whose free interface is highly deformed in amplitude ($\tilde{h} \sim h_0$), but on the other hand, the lubrication hypothesis sets the wavelength of the shape still large compared to the thickness ($L \gg h_0$). With this limitation, the Reynolds equation cannot be used when the wavelength of the interface is of same order of magnitude as the thickness or less, such as in the case of thick films or when accounting for the behavior of high frequency harmonics of the free interface. The aim of this section is to solve the equations of the flow regardless of the lubrication hypothesis, but in the limit of small deformed interface ($\tilde{h} \ll h_0$).

Watching ripples caused by a stone or by the wind blowing on the water's surface is a common experience. The waves can travel (sometimes over thousands of kilometers) thanks to gravity and inertia and their phase speed depends on their wavelength. Regarding capillary waves at the microscopic scale, the picture is the same, except that the driving forces are different. First quantitative developments applied to thin films come from the paint industry. Orchard (1963) derived the conditions for brush marks to relax before the paint dries. More recent developments in microfluidics were done by Jäckle (1998); Henle and Levine (2007).

4.3.1 Dispersion relation

In the frequency domain, we recall the linear Stokes equation for small Cauchy numbers (see Eq. 2.5 on page 24):

$$\nabla p(\omega) = \eta(\omega) \nabla^2 \mathbf{v}(\omega). \quad (4.16)$$

We describe below a method to solve the flow from a linear perturbation method. We begin with transforming the flat coordinates (x, y) into the Fourier domain $\mathbf{k} = (k_x, k_y)$, the height coordinate z is left in the real space. For example, the velocity field becomes: $\mathbf{v}(x, y, z) \rightarrow \hat{\mathbf{v}}(k_x, k_y, z)$. Each variable depends then on k_x, k_y, z and ω , but for simplicity most of these dependences are not written. Under this transformation, we have for the continuity equation:

$$\mathbf{k} \cdot \hat{\mathbf{u}} = i \hat{v}'_z, \quad (4.17)$$

and for the equation of motion:

$$\frac{i \hat{p}}{\eta(\omega)} \mathbf{k} = -k^2 \hat{\mathbf{u}} + \hat{\mathbf{u}}'', \quad (4.18)$$

$$\frac{\hat{p}'}{\eta(\omega)} = -k^2 \hat{v}_z + \hat{v}''_z, \quad (4.19)$$

where $k = \sqrt{\mathbf{k}^2}$. We now focus on boundary conditions. At the bottom of the fluid, we have the Navier slip and non-penetration boundary condition:

$$\hat{\mathbf{u}}(z=0) = \beta \hat{\mathbf{u}}'(z=0), \quad (4.20)$$

$$\hat{v}_z(z=0) = 0, \quad (4.21)$$

According to the normal component of the jump momentum balance (JMB), the pressure at the liquid interface is again given by the sum of two contributions: surface tension and the van der Waals forces (disjoining pressure), *linearized* in h_0 :

$$\hat{p}(z=h_0) - \hat{\sigma}_{zz} = \left(\gamma k^2 + \frac{\partial \Pi}{\partial h}(h_0) \right) \hat{h}(\mathbf{k}, \omega). \quad (4.22)$$

Moreover, as no external shear stress is supposed to apply along the interface, we can write the tangential component of the JMB as:

$$\eta(\omega) (i \hat{v}_z \mathbf{k} + \hat{\mathbf{u}}')_{z=h_0} = \mathbf{0}. \quad (4.23)$$

In addition, as a linearized kinematic condition at the fluid-air interface, the vertical velocity equals the growth rate of the thickness:

$$-i \omega \hat{h}(\mathbf{k}, \omega) = \hat{v}_z(h_0). \quad (4.24)$$

Finally, we say that there is no stress applied on the material at the time before the reflow ($t < 0$), in other words there is no residual elastic stress caused by the imprint.

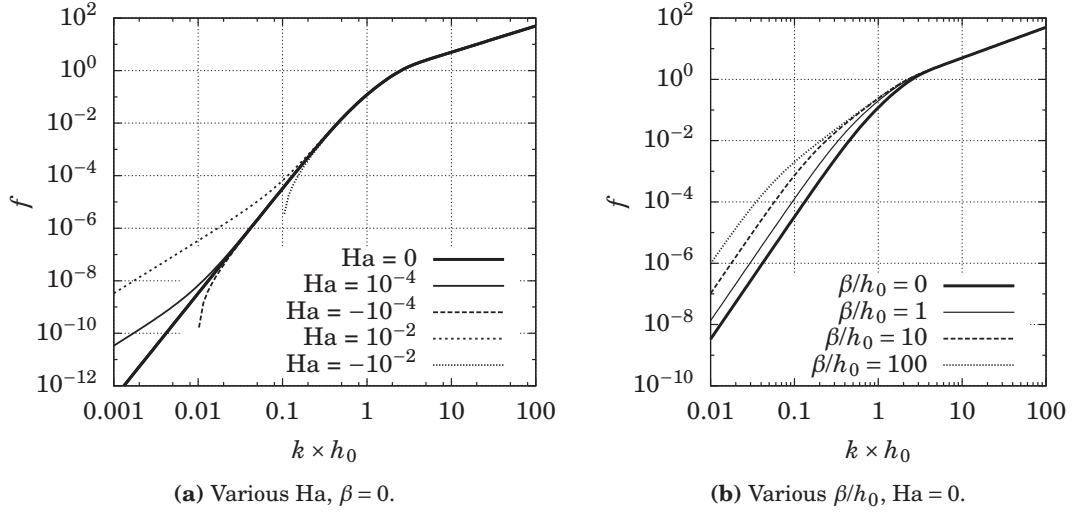


Figure 4.7 – Function $f(kh_0, \text{Ha}, \beta)$, plotted for various Hamaker numbers and slip lengths.

All the elements are set to solve the equation of motion. This calculation is carried out in appendix A, section A.3. We finally get the *dispersion relation* between the wavevector k and the complex frequency ω :

$$\frac{i\omega\eta(\omega)h_0}{\gamma} = f(kh_0, \text{Ha}, \beta). \quad (4.25)$$

where f is a dimensionless function of the normalized wavevector kh_0 , of the dimensionless Hamaker number as defined above (Eq. 4.11), and of the slip length β :

$$f(kh_0, \text{Ha}, \beta) = \frac{kh_0 \sinh \cosh kh_0 - k^2 h_0^2 + 2kh_0 k \beta \sinh^2 kh_0}{2 \cosh^2 kh_0 + 2k^2 h_0^2 + 4k\beta(kh_0 + \sinh \cosh kh_0)} \left(1 + \frac{\text{Ha}}{k^2 h_0^2} \right). \quad (4.26)$$

Plots of f for various values of β/h_0 and Ha are reported in figure 4.7.

The problem is now to find an explicit expression of ω as a function of k .

4.3.2 Viscous flows

If the material is a Newtonian fluid ($\eta(\omega) = \text{constant}$), the relation dispersion has only one root on the imaginary axis, which means that all the modes are purely damped (i.e. they do not propagate). The decay time $\tau(k)$ for each mode of wavevector k is:

$$i\omega = \frac{1}{\tau(k)} = \frac{\gamma f(kh_0, \text{Ha}, \beta)}{\eta h_0}. \quad (4.27)$$

From this result, we can write the evolution of the thickness back in the time domain. Each spatial mode follows an exponential decrease with a wavevector-dependent char-

acteristic time:²

$$\hat{h}(\mathbf{k}, t) = \hat{h}(\mathbf{k}, 0) \times \exp\left(-\frac{t}{\tau(k)}\right). \quad (4.28)$$

Here again, as in lubrication theory, we see that a negative Hamaker number can cause instability in the film, provided that the term $\text{Ha}/k^2 h_0^2$ is smaller than -1 . If this occurs, the decay time τ becomes negative: it is a growth characteristic time. Features whose wavevectors are smaller than $k_c = \sqrt{|\text{Ha}|}/h_0$ tend to grow exponentially, leading to the rupture of the film.

Finally returning to figure 4.7b, we see that a large relative slip length, β/h_0 , leads to a larger value of f for small wavevectors (large shapes). Consequently, the reflow is indeed faster (lower τ) if slip occurs at the interface with the substrate. We will see in section 4.4.1 below, that the flow at the bottom interface is negligible for high wavevectors, that is why slip has no influence in the range $kh_0 > 1$.

Kernel function. The latter equation (4.28) shows that, for $\text{Ha} \geq 0$, the reflow of the film is equivalent to a low-pass Fourier spatial filter. The exponential decrease $\exp(-t/\tau(k))$ is called the *kernel function* of the reflow, and is given by the physical parameters of the problem. Equation (4.28) can be recast in:

$$\hat{h}(\mathbf{k}, t) = \hat{h}(\mathbf{k}, 0) \times \exp\left(-\frac{f(kh_0, \text{Ha}, \beta)}{\text{Ca}}\right), \quad (4.29)$$

with the capillary number Ca defined by:

$$\text{Ca} = \frac{\eta h_0}{\gamma t}. \quad (4.30)$$

Note that this definition differs from Eq. (4.12) since this capillary number does not depend on the wavevector k .

When the slip as well as van der Waals forces are not significant, the decay time has two known asymptotic regimes. It is therefore important to take both regimes into account with the full dispersion relation (4.25) if we want to describe a wide range of spatial frequencies.

Thin film regime. When $kh_0 \ll 1$, we have $\tau_k \sim 3\eta/\gamma h_0^3 k^4$ and the result of lubrication theory that we saw in the previous section is recovered (see Eq. 4.10). This

²We have:

$$h(\mathbf{k}, t) = \int \frac{d\omega}{2\pi} \hat{h}(\mathbf{k}, \omega) \exp(-i\omega t),$$

$$h(\mathbf{k}, 0) = \int \frac{d\omega}{2\pi} \hat{h}(\mathbf{k}, \omega).$$

Equation (4.27) gives:

$$h(\mathbf{k}, t) = \int \frac{d\omega}{2\pi} \hat{h}(\mathbf{k}, \omega) \underbrace{\exp\left(-\frac{t}{\tau(k)}\right)}_{\text{not } \omega\text{-dependent}} = h(\mathbf{k}, 0) \exp\left(-\frac{t}{\tau(k)}\right).$$

scaling of the decay time regarding both k and h_0 was experimentally verified by Lev-eder *et al.* (2010). In order to predict the flow, the power law for the thickness requires h_0 to be measured with great accuracy. Thin films with slip boundary condition were theoretically studied by Kargupta *et al.* (2003).

Thick film regime. On the other hand, when $kh_0 \gg 1$, we find $\tau_k \sim 2\eta/\gamma k$ which is the dispersion relation for bulk flows reported by Harden *et al.* (1991); Hamdorf and Johannsmann (2000). Note that in that case with $h_0 \rightarrow \infty$, the decay time does not depend on the thickness of the film. We will take advantage of this property in chapter 5 to predict the reflow of patterns made in a film without a uniform thickness.

4.3.3 Viscoelastic flows

The great advantage of capillary wave theory is the fact that it allows us to use any linear viscoelastic function as an input in the dispersion relation. What happens when the fluid is viscoelastic? From a physical point of view, we saw in chapter 3 that viscoelastic effects appear for high frequency shear rates, or equivalently at small time scales. Precisely, for supported films, the higher the wavevector of the shape, the faster the decay. Thus viscoelastic effects are likely to appear during the reflow of smallest features.

If the material is a viscoelastic Maxwell fluid, the frequency-dependent viscosity is:

$$\eta(\omega) = \frac{\eta_0}{1 - i\omega\tau_t}, \quad (4.31)$$

with η_0 the zero-frequency viscosity and τ_t the relaxation time of the material (terminal time for a polymer melt). From the dispersion relation we get:

$$\tau(k) = \frac{\eta h_0}{\gamma f(kh_0)} + \tau_t, \quad (4.32)$$

and we can express the theoretical damping function with:

$$\hat{h}(k, t) = \hat{h}(k, 0) \times \exp\left(-\frac{1}{\frac{\text{Ca}}{f} + \text{De}}\right), \quad (4.33)$$

where the dimensionless parameters are the capillary number as defined above in equation (4.30), and the Deborah number:

$$\text{De} = \frac{\tau_t}{t}. \quad (4.34)$$

Since function $f(kh_0)$ vanishes for small k (large shapes), De is negligible compared to the Ca/f factor, thus the material behaves like a Newtonian fluid. However for large k (details, sharp edges, and so on), the kernel tends towards an horizontal asymptote of value $\exp(-1/\text{De})$. All high frequencies have then approximately the same damping dynamics (Fig 4.8a on the facing page, $kh_0 > 4$). The critical wavelength λ_e below

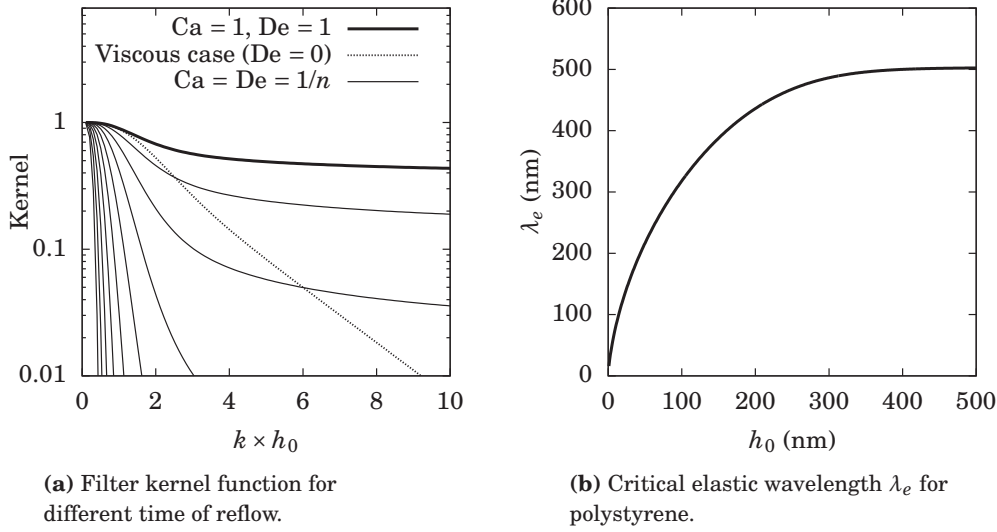


Figure 4.8 – Viscoelastic flow.

which elastic behavior may appear is when De and Ca/f are comparable in size, in other words, for:

$$f\left(\frac{2\pi h_0}{\lambda_e}\right) = \frac{\eta_0 h_0}{\gamma \tau_t}. \quad (4.35)$$

The asymptotic expressions are:

$$\lambda_e \sim \begin{cases} \pi \frac{\gamma}{G_e} & \text{thick film regime,} \\ 2\pi \left(\frac{\gamma h_0^3}{3G_e}\right)^{\frac{1}{4}} & \text{thin film regime,} \end{cases} \quad (4.36)$$

where $G_e = \eta_0/\tau_t$ is the plateau modulus already encountered in chapter 3. This is an interesting result: the critical wavelength depends neither on time nor on temperature. For polystyrene, λ_e is plotted on figure 4.8b.

Although λ_e does not depend on time, we have to keep in mind that after a certain time of reflow, all features smaller than λ_e will have completely vanished and eventually no elastic effect will be observed. This time is of course of the order of τ_t , but say, for our measurement instruments, a mode will be considered as flattened for a relative decrease of 95%. For the λ_e -mode, this leads to $t \sim 6\tau_t$. So reflow experiments with an elastic effect should be shorter than $6\tau_t$.

Reptation model. Reversing the dispersion relation is not always straightforward. For example, in a reptation model, the viscoelastic function is given by an integral. From equation (3.24) on page 46 and the dispersion relation (4.25), we get:

$$\int_0^1 \frac{3x^2}{\frac{\tau}{t} - Dex^2} dx = \frac{f}{Ca}, \quad (4.37)$$

where Ca is the capillary number relative to the zero-shear viscosity and De is the Deborah number relative to the characteristic time of reptation: $De = \tau_C/t$. The numerical computation of τ as a function of k is presented in appendix A, section A.3.2 on page 183. We will use this method in chapter 6.

4.4 Shear thinning criteria

In this section, we consider a Newtonian fluid, and a no-slip boundary condition at the solid interface. We address the issue of shear thinning. We saw in the previous chapter that the linear stress-strain rate relation holds only for small strain rates. The theory developed in this chapter give us tools to compute the shear rate in a supported flowing film and eventually assess whether shear thinning occurs.

4.4.1 Streamlines

Before we investigate shear rate in a flowing film, let us consider streamlines. Streamlines are curves drawn at a given time, that are tangent to the velocity vectors. The method to plot such curves is presented in appendix A, section A.3.3. With streamlines, we can see the influence of an obstacle (here, the underlying substrate) on the flow. Figure 4.9 on the next page gathers plots of streamlines and shear rate in flowing sinusoidal films. Three cases are studied:

1. Thin film regime (Fig. 4.9a bottom, $kh_0 = 0.5$): the streamlines are deeply influenced by the bottom interface, the flow is almost parallel to the substrate in a large area.
2. Intermediate (Fig. 4.9a middle, $kh_0 = 3$): streamlines begins to stretched vertically. The substrate has still an influence on the bottom streamlines.
3. Thick film regime (Fig. 4.9a top, $kh_0 = 10$): the substrate has no influence on the streamlines, there is almost no flow in the bottom area of the film.

4.4.2 Shear rate for a sinusoid

We want to compare the maximum shear rate in the film, $|\dot{\gamma}|_{\max}$, to a critical shear rate, $\dot{\gamma}_0$, above which non-linear rheology takes place. The linear rheology hypothesis holds for:

$$|\dot{\gamma}|_{\max} < \dot{\gamma}_0. \quad (4.38)$$

We consider a sinusoidal profile: $h(x) = h_0 + \tilde{h} \cos kx$ with $kh_0 \ll 1$. For now, \tilde{h} may be large, that is, of the order of h_0 . In lubrication theory, it is possible to compute the shear rate in the film, given the free surface $h(x)$. This mathematical development is reported in appendix A, section A.3.4 on page 185. The results for the maximum shear rate are:

1. $\dot{\gamma}_{\max}$ is located on the bottom interface.

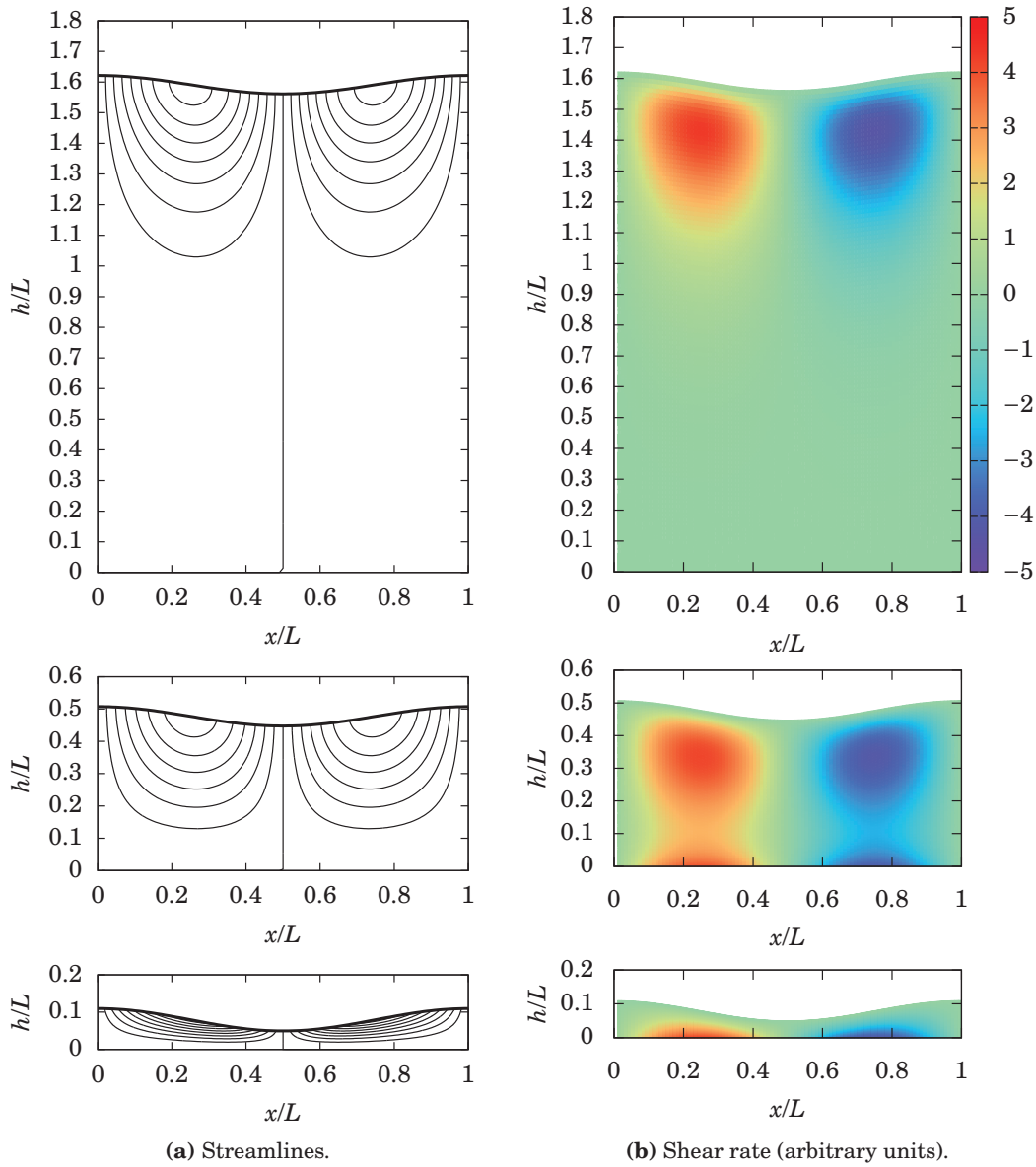


Figure 4.9 – Streamlines and shear rate for a sinusoidal film with various thickness (from top to bottom: $kh_0 = 10, 3, 0.5$) in capillary wave theory.

2. $\dot{\gamma}_{\max}$ is weakly non-linear in \tilde{h} .
3. The non-linearity can be accounted for by an upper bound for $\dot{\gamma}_{\max}$:

$$\dot{\gamma}_{\max} < 1.3 \frac{\gamma \tilde{h} k^3 h_0}{\eta}. \quad (4.39)$$

In particular, the factor 1.3 tends towards unity in the limit $\tilde{h} \rightarrow 0$.

If we assume now that $\tilde{h} \ll h_0$, but kh_0 is unconstrained, developments of capillary wave theory can be used (see section A.3.4). Figure 4.9b on the previous page shows the shear rate inside a sinusoidal film of various thickness (various kh_0). In the thin film regime (Fig. 4.9b bottom, $kh_0 = 0.5$), the shear rate is concentrated near the substrate. In the thick film regime (Fig. 4.9b top, $kh_0 = 10$), the shear rate is located near the free interface. For the intermediate case (Fig. 4.9b middle, $kh_0 = 3$), a mix of the two regimes is found.

In addition to these particular examples, we used capillary wave theory to compute the maximum shear rate for a sinusoidal film of various kh_0 . It turns out that the maximum shear rate can be expressed by:

$$\dot{\gamma}_{\max} = \frac{\gamma}{\eta} \tilde{h} k^2 \dot{\Gamma}(kh_0), \quad (4.40)$$

where $\dot{\Gamma}(kh_0)$ is a dimensionless function of the normalized wavevector kh_0 (see equation A.72 on page 186). Figure 4.10 shows $\dot{\Gamma}$ computed at various kh_0 . Obviously, $\dot{\Gamma}$ has two asymptotic regimes. When $kh_0 \rightarrow 0$ (thin film regime), then the maximum shear rate is reached at the bottom interface, and lubrication theory gives $\dot{\Gamma}(kh_0) = kh_0$ (Eq. 4.39). When $kh_0 \rightarrow \infty$ (thick film regime), the maximum shear rate is reached just under the free surface (at $kz \approx kh_0 - 1$) and yields $\dot{\Gamma} = e^{-1}$. In the latter case, the maximum shear rate does not depend on the thickness anymore but only on the wavevector, as we saw for the viscous characteristic time of reflow. Between the two asymptotic regimes, there is a transition zone that has a non-trivial evolution (see Fig. 4.9b middle). The maximum is $\dot{\Gamma} = 0.46$ at $kh_0 = 1.2$. From equation (4.40) it is possible to define the following criterion for the Newtonian behavior:

$$\tilde{h} k^2 < 2.17 \frac{\dot{\gamma}_0 \eta}{\gamma}. \quad (4.41)$$

An interesting property of polymers is that the product $\dot{\gamma}_0 \eta$ depends weakly on temperature (in the range T_g to $T_g + 100^\circ\text{C}$), exactly as we saw in the previous section for the plateau modulus of viscoelastic flows (section 4.3.3 on page 68). Consequently, the shear thinning threshold is only a function of the topography.

4.4.3 Shear rate in a nanoimprinted film

In the previous paragraph, we saw that it is possible to define a Newtonian behavior criterion as a function of the material parameters and the wavevector of the sinusoidal profile. However, it is not possible to extend this approach to crenelated profiles, more commonly used in nanoimprint. Indeed, the maximum shear rate is found

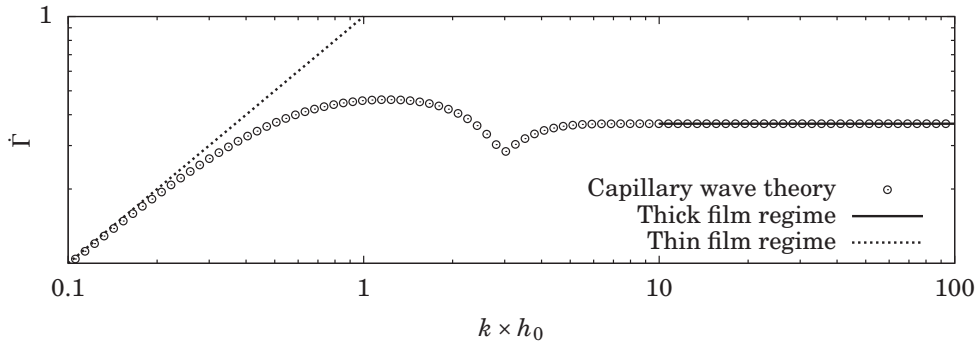


Figure 4.10 – Maximum shear rate factor $\dot{\Gamma}$ as a function of the normalized wavevector kh_0 .

to become infinite as the shape tends toward a perfect square signal, even if the approximate Laplace pressure γk^2 is replaced by the exact pressure (Fourier transform of the curvature, Eq. 4.3). The reason is the following. The Fourier series of our square film is:

$$h(x) = h_0 + \frac{4\tilde{h}}{\pi} \sum_{n=0}^{\infty} \frac{(-1)^n \cos[(2n+1)kx]}{2n+1}, \quad (4.42)$$

which means that each mode mk (odd m) has a relative amplitude of $1/m$. Now, if we go back to the case of a sinusoidal profile, we find a wavevector dependence for the maximum shear rate of k^2 (Eq. 4.41). So for a given mode mk of the square profile, the maximum shear rate is proportional to $m^2/m = m$, which grows to infinity with m . So the maximum shear rate is driven by the highest order of the shape.

Obviously, for realistic nanoimprinted profiles, the maximum shear rate is finite, for two main reasons. First, from an experimental point of view, nanoimprinted profiles are not perfectly sharp. Second, from a theoretical point of view, wavelengths smaller than the molecular length cannot be described by a continuum approach. In fact, we can compute the shear rate (in capillary wave theory) in a realistic film from an AFM measurement. The shear rate is normalized in the following way (see equation A.70 on page 186):

$$\dot{\gamma}^+ = \dot{\gamma} \frac{\eta}{\gamma} \quad (\text{in m}^{-1}), \quad (4.43)$$

and the criterion for the Newtonian behavior reduces to:

$$|\dot{\gamma}^+| < \frac{\dot{\gamma}_0 \eta}{\gamma}. \quad (4.44)$$

This equation has to be compared to what we found in the case of a sinusoidal shape (equation 4.41). Here again, like in the sinusoidal case, the shear thinning threshold does not depend on temperature.

Figure 4.11 on the next page shows an example of shear rate computation for an annealed nanoimprinted film. The free interface was measured by AFM at room temperature. Figure 4.11a is a map of the normalized shear rate $|\dot{\gamma}^+|$ (in log scale). $\dot{\gamma}^+$

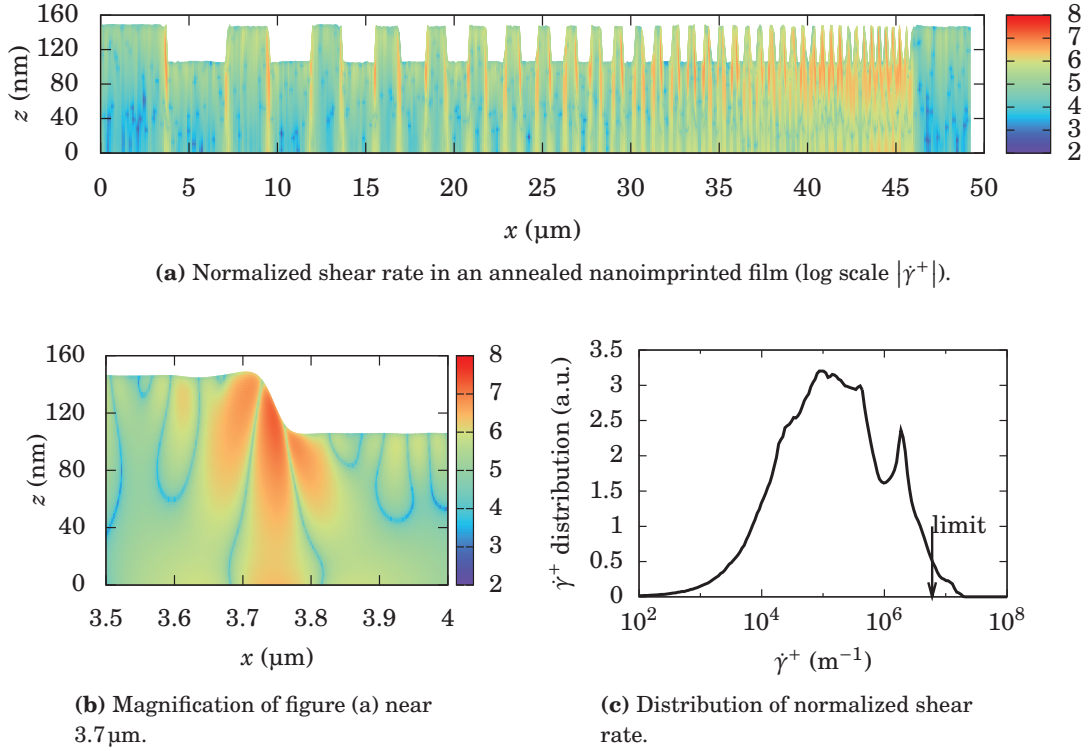


Figure 4.11 – Shear rate computation in an annealed nanoimprinted film.

is higher near the walls of the lines (Fig. 4.11b). The computation gives $\dot{\gamma}_{\max}^+ = 1.9 \times 10^7 \text{ m}^{-1}$. This value has to be compared to $\dot{\gamma}_0 \eta / \gamma \sim 6 \times 10^6 \text{ m}^{-1}$. Obviously, the shear thinning threshold is likely to be crossed. However, from this simple comparison, we cannot say whether the effect is significant. If we consider the distribution of $\dot{\gamma}^+$, as plotted on figure 4.11c, we can compute that more than 98% of the film stays under the threshold. That is why, in this particular example, we can say that the film will keep a Newtonian behavior to a large extent.

4.5 Comparison with full Stokes equation

In capillary wave theory, there are two main assumptions: small deformations, $\tilde{h} \ll h_0$, and small slopes, $\tilde{h} \ll \lambda$. In lubrication theory, small slopes are assumed as well. In section 4.2.4, we saw the effect of high deformation, but still under the assumption of small slopes. What happens when this assumption is not valid any more? What are the legitimate domains of our asymptotic models? To investigate these questions, we used a numerical tool developed in our group for surface tension driven flows, called *NanoNem* (Teyssedre and Gilormini, 2012).

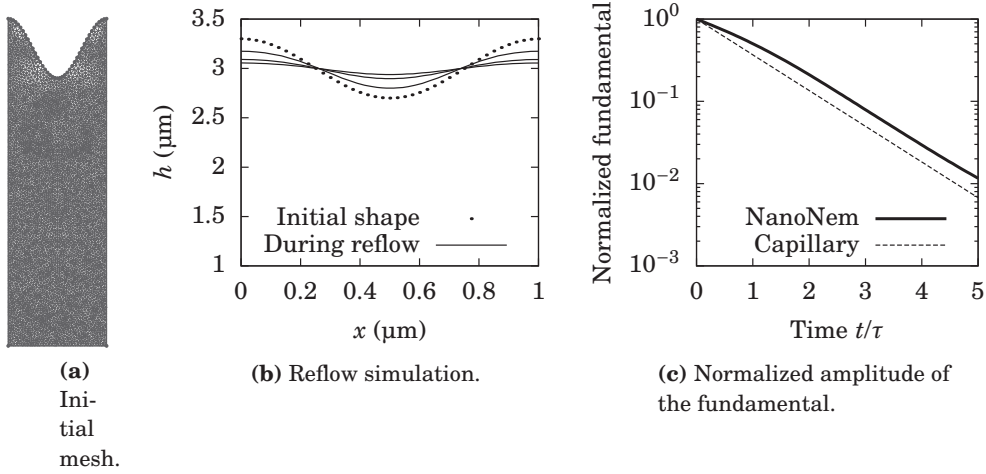
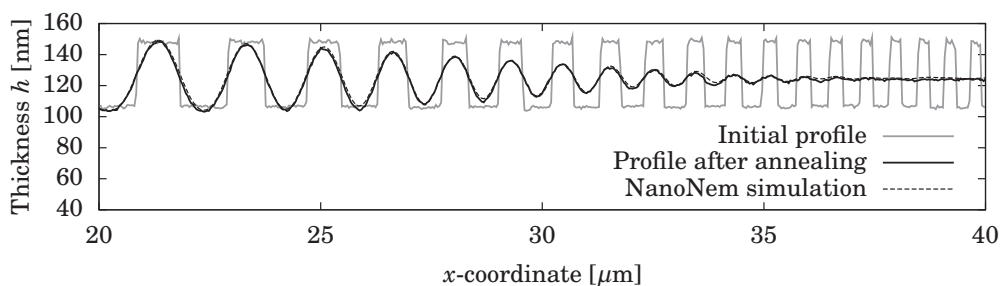


Figure 4.12 – Leveling delay for high aspect ratios.

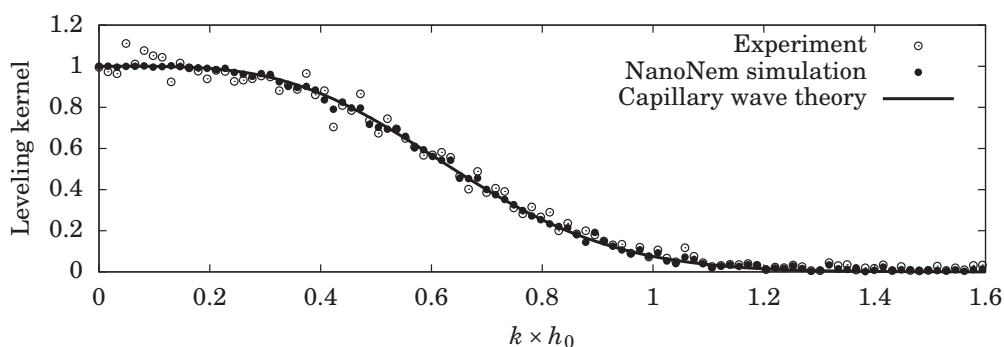
4.5.1 Leveling delay

Let us begin with an example. We consider a film with a sinusoidal shape, as depicted on figure 4.12a on this page. The deformation of the interface, \tilde{h} , is relatively small, compared to the mean thickness, h_0 : $\tilde{h}/h_0 = 0.1$. However, the maximum slope is rather important, and is of the order of unity. The reflow of this pattern was simulated in NanoNem, using the mesh of figure 4.12a. The result is shown on figure 4.12b (not in 1:1 ratio). For each time step, we can compute the first order term of the spatial Fourier transform of the pattern. Figure 4.12c presents the evolution of this term during reflow, normalized by its initial value. The simulated data is plotted along with the decreasing exponential function from capillary wave theory (see Eq. 4.28 on page 67). We can note two observations:

1. It takes more time for the pattern to flow in the simulation than the expected dynamics in capillary wave theory. This can be understood by the following remark. Where the slope is not small, then Laplace pressure is not any more proportional to the second derivative of the thickness, h'' , but to the exact expression of the local curvature, $h'' \times (1 + h'^2)^{-3/2}$. The exact expression is smaller than its approximation by h'' . The result is that in capillary wave theory, the Laplace pressure is always overestimated. Hence a faster dynamics is found in this case than the one found in the complete simulation.
2. After some time, the simulation exhibits an asymptotic regime parallel to the capillary wave dynamics. It is the same situation as in section 4.2.4 where we studied the leveling delay in lubrication theory. During reflow, the pattern height decreases, therefore the slopes also decrease and finally the requirements for capillary wave regime are reached. Note that the agreement between the asymptotic regime of the simulation and capillary wave dynamics is also a way to validate the numerical tool (Gilormini and Teysse, 2012).



(a) AFM measurements and NanoNem simulation of an annealed film.



(b) Kernel function (leveling rate).

Figure 4.13 – Reflow experiment (polystyrene $30 \text{ kg}\cdot\text{mol}^{-1}$ at 120°C during 5 min) and comparison with NanoNem simulation and capillary wave theory.

Other simulations need to be carried out in order to quantify the impact of large slopes on the leveling dynamics, as we did in section 4.2.4 for large deformations.

4.5.2 Kernel function

In the previous paragraph, we considered the reflow of a single spatial frequency. We can also simulate the reflow of a complex pattern to see the global effects of large slopes. Figure 4.13 is a reflow experiment of a spatially modulated pattern where large slopes are encountered at the walls of the initial pattern. The polymer film is patterned with a thermal nanoimprint process and the shape of the film is measured by atomic force microscopy (AFM) before and after annealing. We will see this experiment in more detail in chapter 6. For now, we focus on the pattern leveling. In a previous section, we saw that the reflow in capillary wave theory is mathematically equivalent to a low-pass spatial filter (see Eq. 4.28 on page 67). Here, we can see this effect on figure 4.13a: smallest features (right side) have completely disappeared, while larger patterns (left side) have only been rounded. The simulation of this reflow process with NanoNem fits the measurement data very well.

We can compute the Fourier transforms of the initial and annealed profiles. The ratio of these transforms gives the kernel function of the reflow (see Eq. 4.29), plotted

on figure 4.13b. We can notice that the smooth kernel function of capillary wave theory fits the experimental data very well—again, we will see the consequences in detail in chapter 6. Besides, the NanoNem simulation fits the experimental data as well. Nevertheless, this simulation alone cannot account for the scatter between the experimental data and capillary wave modeling. In other words, in spite of large slopes at some localized parts of the initial pattern, capillary wave theory is relevant to model this reflow experiment.

4.6 Conclusion

In this chapter, we saw how we can model the flow of a supported liquid film by making use of asymptotic models. As a conclusion, table 4.1 on the following page shows the various topographies that can describe a patterned film, along with the corresponding relevant model. The next two chapters are devoted to various implementations of supported flowing films.

Table 4.1 – Supported film topography and corresponding relevant model.

Deformation ratio	Aspect ratio	Diagram	Solving method	Distinctive features
$\frac{\tilde{h}}{h_0} \ll 1$	$\frac{\tilde{h}}{\lambda} \ll 1$		Capillary Wave Theory	<ul style="list-style-type: none"> – No mesh (Fourier transform) – Viscoelastic – 3D
	$\frac{\tilde{h}}{\lambda} \gtrsim 1$		Full Stokes (NanoNem)	<ul style="list-style-type: none"> – Mesh of fluid domain and interface – Complex boundary conditions – Not yet 3D
$\frac{\tilde{h}}{h_0} \sim 1$	$\frac{\tilde{h}}{\lambda} \gtrsim 1$			
	$\frac{\tilde{h}}{\lambda} \ll 1$		Lubrication Theory	<ul style="list-style-type: none"> – Mesh of interface only

References

- G. Bayada and M. Chambat. The transition between the stokes equations and the reynolds equation: A mathematical proof. *Applied Mathematics & Optimization* **14**, 73–93 (1986).
- H. Bruus. *Theoretical microfluidics*, volume 18. Oxford University Press, USA (2008).
- G. Cimatti. How the reynolds equation is related to the stokes equations. *Applied Mathematics & Optimization* **10**, 267–274 (1983).
- R. V. Craster and O. K. Matar. Dynamics and stability of thin liquid films. *Reviews of Modern Physics* **81**, 1131 (2009).
- P. Gilormini and H. Teyssedre. On using the leveling of a polymer free surface to measure viscosity and navier slip length. *To be published* (2012).
- M. Hamdorf and D. Johannsmann. Surface-rheological measurements on glass forming polymers based on the surface tension driven decay of imprinted corrugation gratings. *The Journal of Chemical Physics* **112**, 4262 (2000).
- J. L. Harden, H. Pleiner, and P. A. Pincus. Hydrodynamic surface modes on concentrated polymer solutions and gels. *The Journal of Chemical Physics* **94**, 5208–5221 (1991).
- M. L. Henle and A. J. Levine. Capillary wave dynamics on supported viscoelastic films: Single and double layers. *Physical Review E* **75**, 021604 (2007).
- J. N. Israelachvili. *Intermolecular and Surface Forces*. Academic Press Inc, 2nd revised edition edition (1991).
- J. Jäckle. The spectrum of surface waves on viscoelastic liquids of arbitrary depth. *Journal of Physics Condensed Matter* **10**, 7121–7131 (1998).
- K. Kargupta, A. Sharma, and R. Khanna. Instability, dynamics, and morphology of thin slipping films. *Langmuir* **20**, 244–253 (2003).
- R. Keunings and D. Bousfield. Analysis of surface tension driven leveling in viscoelastic films. *Journal of Non-Newtonian Fluid Mechanics* **22**, 219–233 (1987).
- T. Leveder, S. Landis, N. Chaix, and L. Davoust. Thin polymer films viscosity measurements from nanopatterning method. *Journal of Vacuum Science & Technology B: Microelectronics and Nanometer Structures* **28**, 1251 (2010).
- S. Orchard. On surface levelling in viscous liquids and gels. *Applied Scientific Research* **11**, 451–464 (1963).
- A. Oron, S. H. Davis, and S. G. Bankoff. Long-scale evolution of thin liquid films. *Reviews of Modern Physics* **69**, 931 (1997).
- O. Reynolds. On the theory of lubrication and its application to mr. beauchamp tower’s experiments, including an experimental determination of the viscosity of olive oil. *Proceedings of the Royal Society of London* **40**, 191–203 (1886).
- H. Teyssedre and P. Gilormini. Extension of the natural element method to surface tension and wettability for the simulation of polymer flows at the micro and nano scales. *Journal of Non-Newtonian Fluid Mechanics*, submitted (2012).

Chapter 5

Partial reflow with residual layer for complex shapes manufacturing

5.1 General purposes

Many applications in optics, micro-electro-mechanical devices or microfluidics, require three dimensional (3D) nanostructures that are difficult or expensive to construct with standard nanolithography techniques. Although particular etching processes or numerous lithography steps can be employed for manufacturing 3D nanoimprint molds, other methods are needed to realize fast and cost-effective complex shaping.

Techniques for manufacturing 3D shapes with a reflow step already exist. In the field of optical devices, microlenses have been fabricated using reflow for more than two decades (Popovic *et al.*, 1988; Daly *et al.*, 1990; Audran *et al.*, 2010). Generally, a cylinder or a line of photoresist is created on a substrate and heated until it forms a more or less spherical shape, as depicted on figure 5.1a (for a review of microlenses manufacturing, see O'Neill and Sheridan, 2002; Ottevaere *et al.*, 2006). Various topographies can be created with this technique combined with capillary instabilities, as reported by Chae *et al.* (2011); Schiff *et al.* (2011); Grilli *et al.* (2011). Other example of optical devices are linear optical filters fabricated by Emadi *et al.* (2009) consisting of very small angle tapers. Grooves are developed in a photoresist film, and the density of the grooves varies from one side of the filter to the other. Under annealing, the pattern is smoothed resulting in a small angle slope (Fig. 5.1b). Finally, higher aspect ratio features can be made by grayscale lithography, as demonstrated by Schleunitz and Schiff (2011). In this technique, the local thickness of the developed resist depends on the exposure dose. A final reflow step produces smooth slopes (Fig. 5.1c).

All these techniques have a point in common: the lack of residual layer. In this case the reflow is not only driven by surface tension, but also by triple contact line tension (or contact angle) that strongly depends on the underlying substrate. The aim

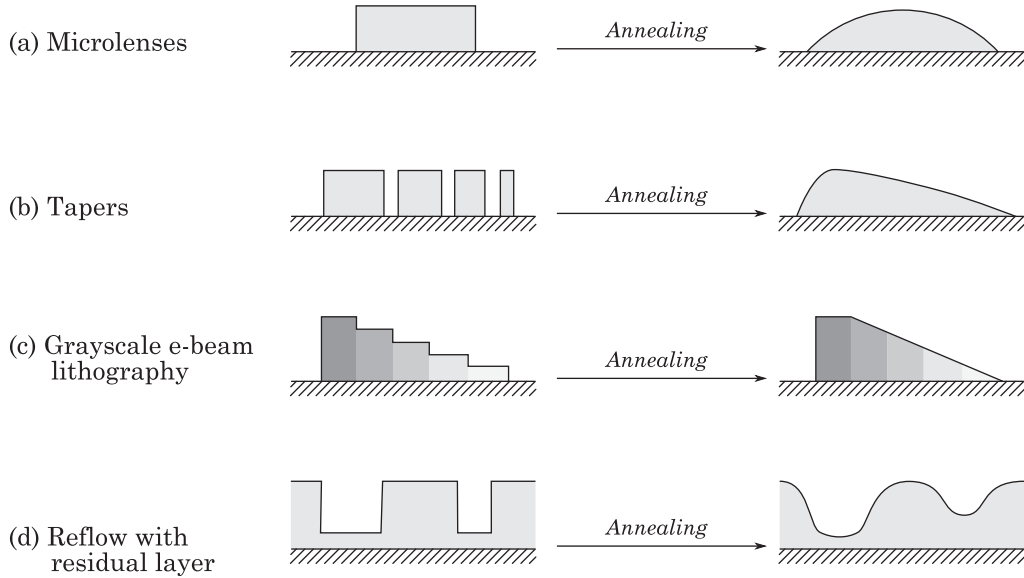


Figure 5.1 – Various manufacturing techniques based on reflow.

of this chapter is to present some concepts of reflow with a non-zero residual layer, in other words when no contact line takes part in the dynamics of the reflow. By doing so, we can apply the theoretical results of chapter 4 where we explored the dynamics of a supported fluid film.

5.2 Reflow with a large residual layer

In this section, we will focus on the reflow of patterns that are imprinted with a large residual layer. The idea is to develop some concepts or methods for designing complex shapes based on the results of capillary wave theory we developed in chapter 4. We saw that this robust asymptotic model is relevant to a 5% precision for pattern depth up to 50% of the mean thickness (isodense patterns and small aspect ratios), in other words, if the residual layer is at least 1.5 times thicker than the imprinted depth.¹

In such cases, the reflow of nanoimprinted films can be described as a low-pass spatial filter that depends on time and physical parameter (surface tension, viscosity or viscoelasticity, mean thickness...). For a time t of reflow, each Fourier component of the profile is damped by a factor $\exp(-t/\tau)$, with τ a characteristic time depending on the wavelength of the component. We saw that there are two characteristic times for the leveling of a wavelength λ depending on how λ compares to the thickness of the film: $\tau \sim 3\eta/\gamma h_0^3 k^4$ if $kh_0 \ll 1$, with η the Newtonian viscosity, γ the surface tension, h_0 the mean thickness, and $k = 2\pi/\lambda$, we called this dynamics the thin film regime;

¹This means that, for this degree of accuracy, if we consider for example 50-nm-deep isodense patterns, the reflow can be modeled by a linear approach for a residual layer greater than 75 nm.

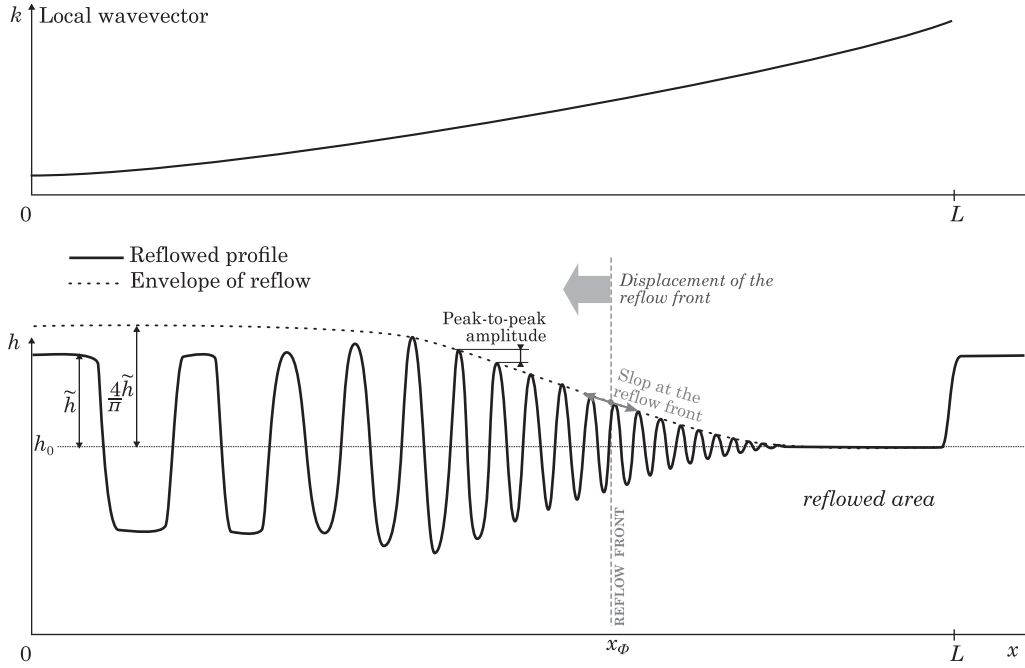


Figure 5.2 – Reflow of a spatially modulated isodense patterns.

and $\tau \sim 2\eta/\gamma k$ if $kh_0 \gg 1$, called the thick film (or bulk) regime. The intermediary dynamics is fully described by the function f defined by equation (4.26) on page 66. If we take the viscoelastic behavior of the polymer into account, the dynamics is again different, but we leave that issue to paragraph 5.2.4.

5.2.1 Reflow of spatially modulated isodense patterns

First, we consider what we call *spatially modulated isodense* patterns. A pattern is isodense if the area of the bottom of the shape (area under the protrusions of the mold) equals, at least locally, the area of the top of the shape (area of the cavities of the mold). For example, a pattern made of 100-nm-width lines with a space of 100 nm between the lines is isodense. Now, if we have a profile combining side by side isodense patterns of different characteristic lengths (or periods), then we talk of spatially modulated patterns.

Envelope of reflow. We can define a pattern shape $m(x)$ of length L , of depth $2\tilde{m}$ by the modulation function:

$$m(x) = \tilde{m} \times \text{sign} \left[\cos \left(\int_0^x k(\xi) d\xi \right) \right] \quad (5.1)$$

where $k(\xi)$ is the local wavevector (see figure 5.2, top graph). Note that if $k(\xi) = k_1$ (the pattern is periodical), then $m(x) = \tilde{m} \times \text{sign}[\cos k_1 x]$. The choice of the function $k(\xi)$ depends on the wished properties of the reflowed profile. First, we can define the

envelope of reflow. If we assume that $k(\xi)$ varies slowly with ξ (we will see in chapter 6 that there is an experimental lower bound though), in other words $\frac{\partial k}{\partial \xi} \ll k^2$, then it is possible to show that the reflow of a local period has the same dynamics as a regular pattern of the same period (see appendix A, section A.3.5 on page 187. The *envelope of reflow* is then the amplitude evolution of the local fundamental of the pattern, $a(x, t)$, defined by:

$$a(x, t) = h_0 + \frac{4\tilde{m}}{\pi} \exp\left(-\frac{t}{\tau(k(x))}\right) \quad (5.2)$$

where $\tau(k)$ is the characteristic time found in capillary wave theory, defined by equation (4.27) on page 66. The factor $4/\pi$ accounts for the ratio of the fundamental mode by the depth of the profile in the Fourier transform of a square pattern.

We can then define the *reflow front*, as the coordinate x_ϕ for which the relative decrease of the envelope is $\exp(-\phi)$. We assume for the whole pattern that $k(x) \times h_0 \ll 1$ (thin film dynamics), then the characteristic leveling time is $\tau \sim 3\eta/\gamma h_0^3 k^4$. In other words, at the reflow front, since the damping factor is $\exp(-t/\tau(x_\phi))$, we have the property:

$$\phi = \frac{t\gamma h_0^3 k(x_\phi)^4}{3\eta} \quad (5.3)$$

We are now able to extract $k(x)$ functions with interesting properties for the reflow.

ENHANCED VISUAL CONTRAST between reflowed areas (high frequencies) and slower dynamics areas (low frequencies) is achieved by keeping constant the growth rate of the envelope at the reflow front, which is the quantity:

$$\frac{\partial a}{\partial x}(x_\phi) = -\frac{16\tilde{h}\phi e^{-\phi}}{\pi} \times \frac{\frac{\partial k}{\partial x}}{k(x_\phi)}. \quad (5.4)$$

This is realized if k follows an exponential variation, for example:

$$k(x) = k_{\max} \left(\frac{k_{\min}}{k_{\max}}\right)^{\frac{x}{L}}. \quad (5.5)$$

CONSTANT SPEED of the reflow front is achieved by a function of the form:

$$k(x) = k_{\max} \left(\frac{x}{L}\right)^{-\frac{1}{4}}. \quad (5.6)$$

Indeed, in that case the reflow front takes the expression:

$$x_\phi = \frac{\gamma h_0^3 k_{\max}^4 L}{3\eta} \times t \quad (5.7)$$

which has a constant time derivative.

CONSTANT PEAK-TO-PEAK DIFFERENCE (see figure 5.2) is to the first order:

$$\lambda(x_\alpha) \frac{\partial a}{\partial x}(x_\alpha) = -32\tilde{h}\phi e^{-\phi} \times \frac{\frac{\partial k}{\partial x}}{k(x_\phi)^2} = \text{Constant}, \quad (5.8)$$

which means that $1/k$ is a linear function of x :

$$\frac{1}{k(x)} = \frac{1}{k_{\max}} + \left(\frac{1}{k_{\min}} - \frac{1}{k_{\max}}\right) \frac{x}{L} \quad (5.9)$$

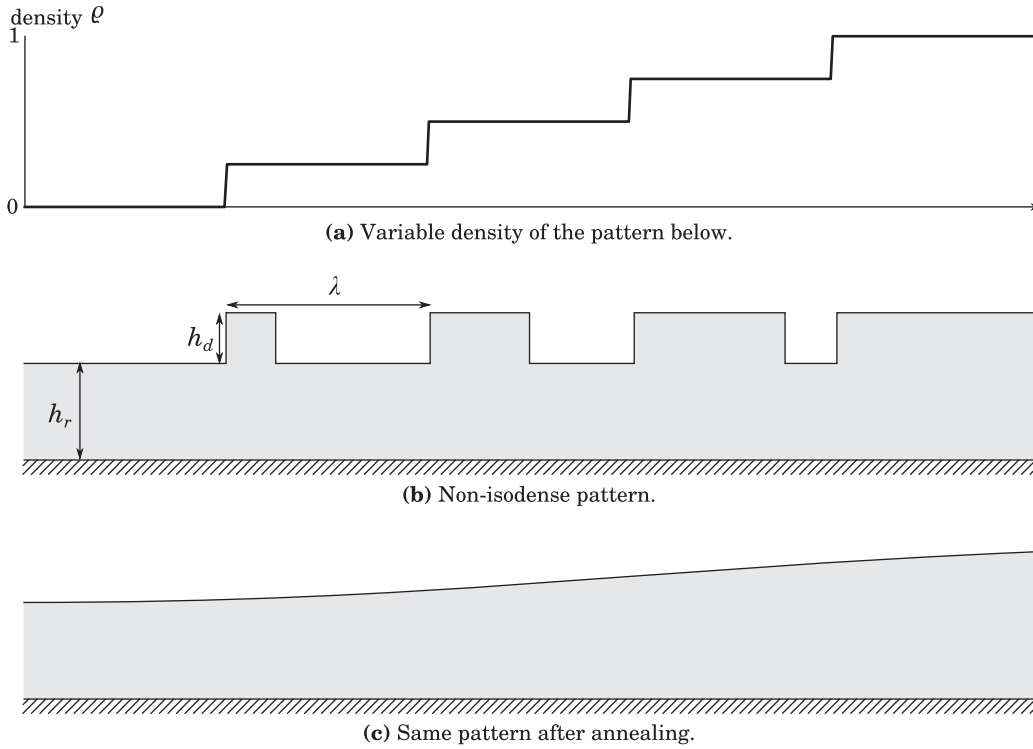


Figure 5.3 – Illustration of a non-isodense pattern.

Examples. An implementation of this kind of reflow for the rheological properties measurements of thin films is presented in chapter 6.

5.2.2 Reflow of non-isodense patterns

The next concept of reflow is the reflow of patterns with opposite properties to the previous section. Here the pattern is periodic (there is a characteristic period λ), but the repeating units can vary in density. Such a pattern is described on figure 5.3. We follow the idea of Emadi *et al.* (2009) presented in figure 5.1c, but in the presence of a residual layer and with specific constraints of nanoimprint.

After annealing, the local thickness should be proportional to the density of the pattern ρ , from h_r for residual layer with no shape (density of zero) to $h_r + h_d$, (density of 1) with h_d the depth of the mold:

$$h(x) \approx h_r + \rho(x)h_d, \quad (5.10)$$

with surface tension smoothing the transitions from one density to the other (Fig. 5.3c). The time of the reflow should be the leveling time of an element (period λ), but smaller than the leveling time of the global targeted shape.

Constraints. Besides the issue of a non-uniform residual layer for imprints with variable density on the same mold, we can find some limitation on the shapes that

could be made with this method of reflow. The minimal non-zero density ρ_{\min} is given by the maximal achievable aspect ratio R , defined by the ratio of the feature height over its width. Indeed, a smaller and smaller density is realized by a more and more narrow line, but at constant mold depth, this line would overtake the maximal achievable aspect ratio. The relation is:

$$\rho_{\min} > \frac{h_d}{R\lambda}. \quad (5.11)$$

Now if we want to create a linear slope of angle α , and say we need N elementary units to make it, an evenly spaced density function would imply $\rho_{\min} = \frac{1}{N}$. For small α , $\alpha \approx \frac{h_d}{N\lambda}$. Combining with the previous criterion, we get:

$$\alpha < \frac{R}{N^2}. \quad (5.12)$$

With realistic values of $R = 2$ and $N = 10$, we get $\alpha < 1^\circ$. Consequently, this method of reflow is unlikely to produce strong slopes or high aspect ratio features with accuracy.

5.2.3 Reflow of 3D shapes

Reflow in the thick film regime. One of the issues of reflow in the thin film regime is that the rate of smoothing strongly depends on the local thickness (factor h_0^3), as depicted on figure 5.4 on the facing page. If the residual layer is not homogeneous, this means that patterns with a smaller residual layer (thus smaller h_0) will not flow as fast as patterns with a larger residual layer (Fig. 5.4a). To circumvent this difficulty, the idea is to perform the reflow in the thick film regime, where the characteristic leveling time does not depend on the thickness (Fig. 5.4b). This is particularly interesting if the topology of the mold makes it difficult to achieve a uniform residual layer, or if the underlying substrate is not planar.

We implemented this concept of reflow both numerically and experimentally on 3D pyramids. The pyramids have a $9 \mu\text{m}$ square base and a height of $15 \mu\text{m}$. The longest characteristic period is thus the diagonal $12.7 \mu\text{m}$. In the experiments, the residual layer ranged from $15 \mu\text{m}$ to $23 \mu\text{m}$, so the product $k \times h_0 > 7$, which ensure that the reflow dynamics is in the thick film regime.

A simulation in capillary wave theory (see appendix C) of the reflow of a pyramid with a $20 \mu\text{m}$ residual layer is presented on figure 5.5 on page 88. The graphs on the left are 3D views of the free interface of the fluid, while the plots on the right are contour lines of the same interface. Under annealing, the initial sharp pyramid (Fig. 5.5a) becomes a smoothed bump (Fig. 5.5d). The leveling of the height can be clearly seen on the 3D views. An interesting point in this example is that we can also see on the contour plots the horizontal smoothing of the pyramid. In other words, the topology goes from a square shape to a more circular shape.

SEM images of reflow experiments are presented on figure 5.6. The pyramids were imprinted in SU-8 resist using a silicon mold. Samples were then heated at 70°C during various times and rapidly cooled down at room temperature.

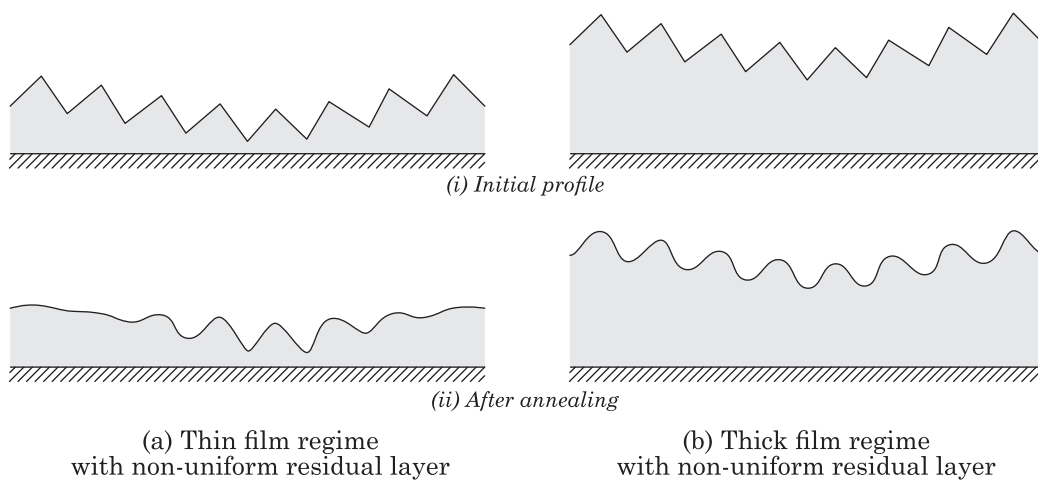
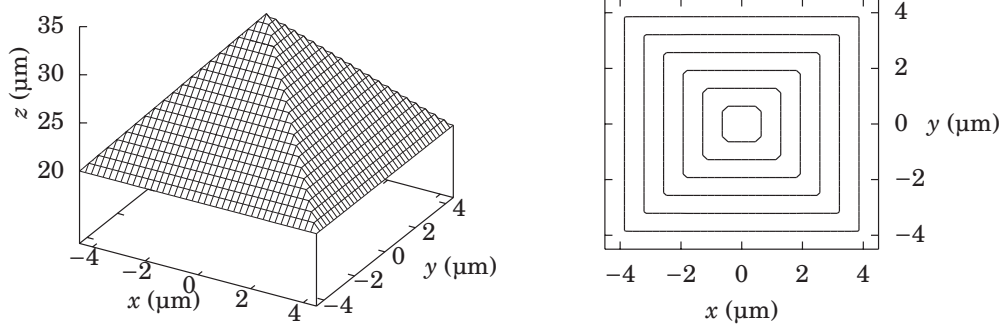
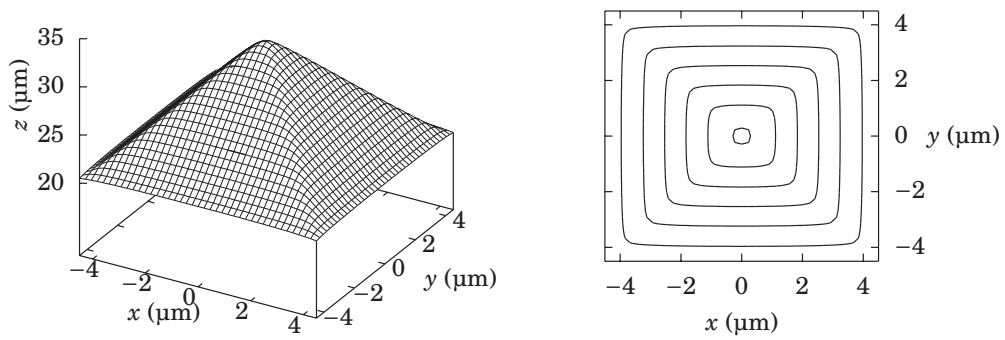


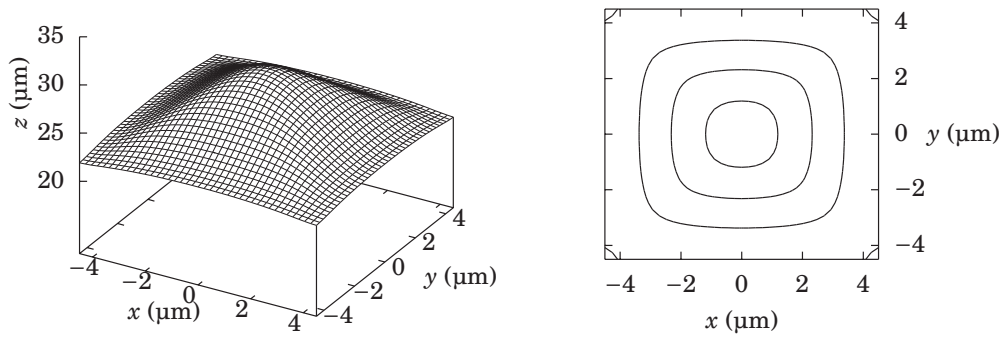
Figure 5.4 – Reflow of a pattern with a non-uniform residual layer in two cases: **(a)** thick film regime where the reflow dynamics depends strongly on the residual layer: the reflow is not homogeneous; **(b)** thin film regime where the reflow dynamics does not depend on the residual layer: the reflow is homogeneous.



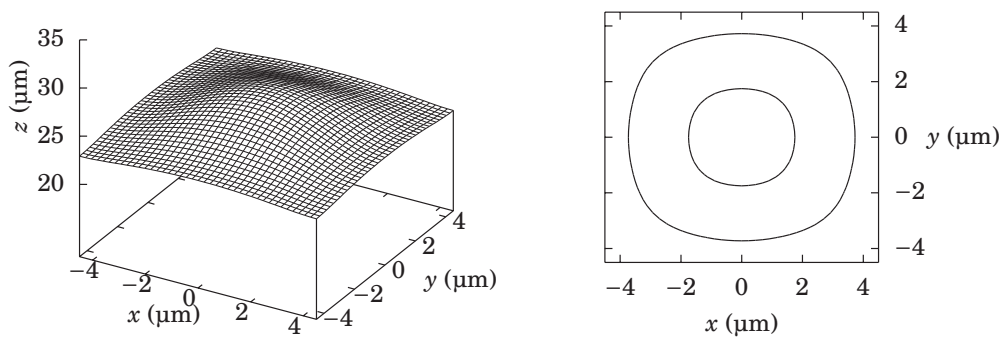
(a) Initial pattern.



(b) After 2 min at 70°C.



(c) After 10 min at 70°C.



(d) After 20 min at 70°C.

Figure 5.5 – Simulated 3D reflow of a pyramid.

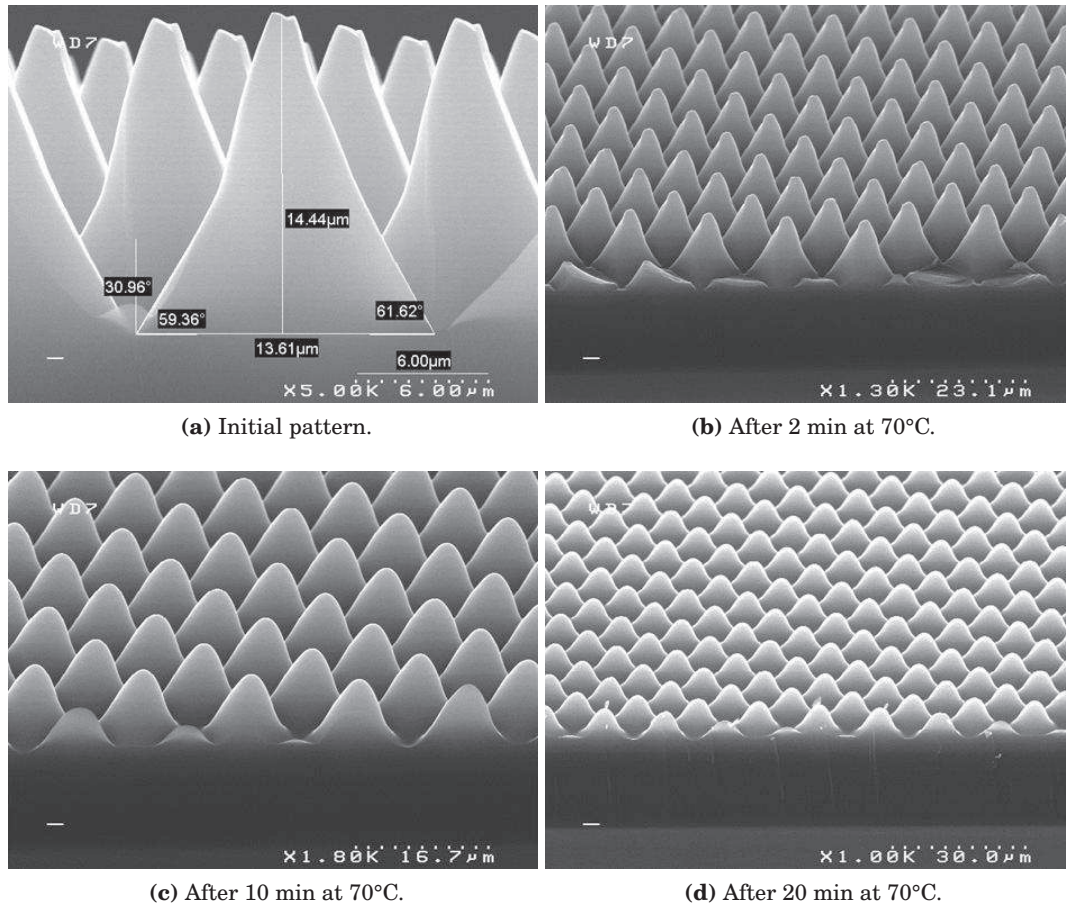


Figure 5.6 – Experimental reflow of nanoimprinted pyramids made of SU-8 resist, with residual layers ranging from to 15 μm to 23 μm.

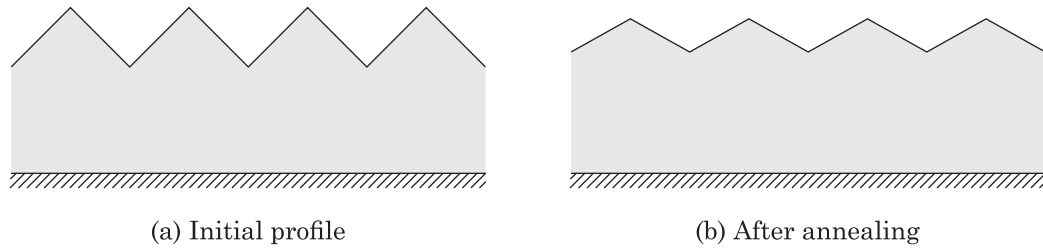


Figure 5.7 – Concept of elastic reflow of a pattern. The profile after annealing (b) is a homothetic reduction of the initial profile (a), provided that the period of the pattern is smaller than the elastic period.

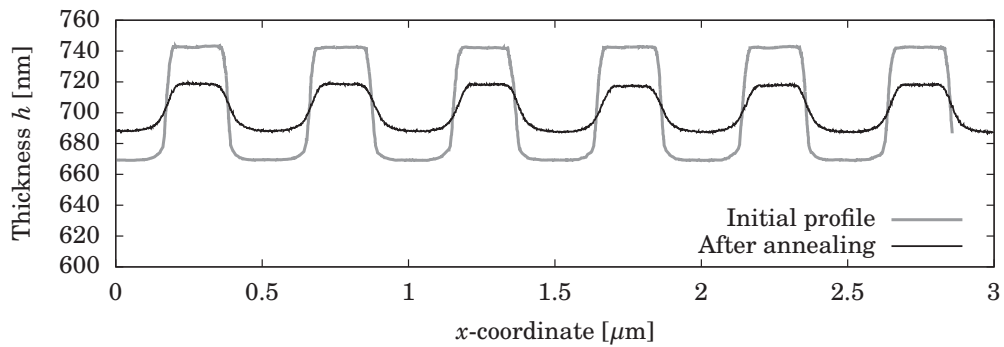


Figure 5.8 – AFM profiles of a nanoimprinted NEB 22 film that was annealed at 100°C during 60 s.

5.2.4 Elastic reflow

The last concept of reflow with a large residual layer we would like to present is what we call in this thesis the *elastic reflow*. Here, we take into account the viscoelastic behavior of the polymer. The reflow time t is of the order of the terminal relaxation time τ_t . In that case, we saw in section 4.3.3 on page 68 of chapter 4 that the modes with a wavelength smaller than a characteristic *elastic wavelength* λ_e (Eq. 4.36) are all damped by approximately the same factor $\exp(-t/\tau_t)$. The consequence of this fact is that high order features of the shape (smaller than λ_e) undergo a homothetic reduction of a factor $\exp(-t/\tau_t)$, as depicted on figure 5.7.

Elastic reflow for cross-linked polymers was qualitatively observed in a previous study carried out in our group. An example can be seen on figure 5.8, where a reflow experiment of a nanoimprinted film is reported. The material used is a commercial e-beam lithography resist named NEB 22. We can see that, after annealing, in spite of a decrease in height, the tops of the lines are still flat, while a Newtonian reflow would have rounded them. Nevertheless, a quantitative analysis is still lacking to validate this concept of reflow.

5.3 Reflow with a thin residual layer

5.3.1 Concept

Let us now focus on the reflow if the residual layer is thin compared to the amplitude of the imprinted shapes. In chapter 4, section 4.2.4, we saw that the fluid moves with more difficulty in thin areas (residual layer) than in thick areas. Consequently protrusions are deformed and flow faster at the top than at the bottom. We illustrated this fact in figure 4.4b on page 61 with the reflow of a square profile: after a certain time of annealing, the top of the square is perfectly rounded while the bottom still has sharp angles. We can benefit from this non-linearity to manufacture interesting objects such as microlenses, as we will see in the next paragraph.

5.3.2 Aspherical lens

We focus on a class of lenses for which the cross section is mathematically described by a conic:

$$h(x) = \frac{\frac{x^2}{r}}{1 + \sqrt{1 - (1 + q)\frac{x^2}{r^2}}} \quad (5.13)$$

with r the curvature at the top of the lens and q the conic parameter: if $q = 0$ the lens is spherical, $q > -1$ it is elliptic, $q = -1$ parabolic, and $q < -1$ hyperbolic. Those latter kinds of lenses ($q \neq 0$) are called *aspherical* lenses.

We simulated the production of aspherical lenses using our 2D code for the numerical resolution of lubrication theory (see appendix B). Two kinds of patterns were reflowed, as presented on figure 5.9 on the following page: rectangular shapes or spaced pyramids, with a fixed period of 15 μm . During annealing, the reflowed shape is fitted to equation (5.13) in order to extract q and r , as well as the correlation coefficient R^2 . Thus, the reflow of one pattern defines a trajectory in the space (q, r, R^2) . The trajectories for various heights, residual layers and densities are presented on figure 5.10 on the next page. Several conclusions can be drawn:

1. The global shape of a trajectory is made of two parts:
 - (a) a first complex curve, generally with increasing r and increasing q . This corresponds to the non-linear stage of the reflow. It strongly depends on the initial pattern.
 - (b) a second nearly linear curve with slowly increasing r and rapidly decreasing q . This correspond to the last stage of reflow when the pattern is a small amplitude sinusoid, for both rectangular and sinusoidal initial patterns.
2. The correlation is much better (R^2 close to 1) at the beginning of reflow in the case of pyramids, but only hyperbolic lenses are likely to be made ($q < -1$). The conic parameters can be tuned by the initial shape of the pyramid (angle) and the reflow time.

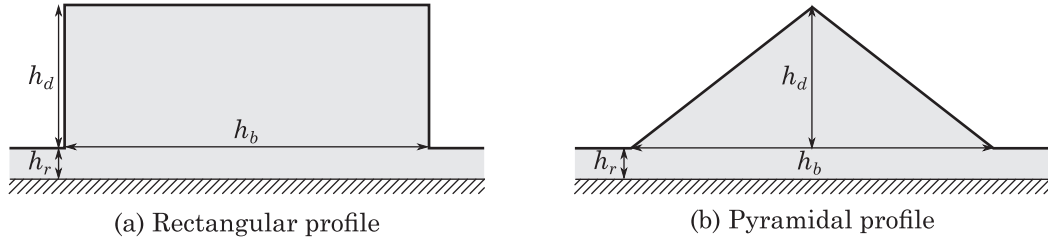


Figure 5.9 – 3-parameter functions: the residual layer h_r , the height of the profile h_d and the length of the base h_b .

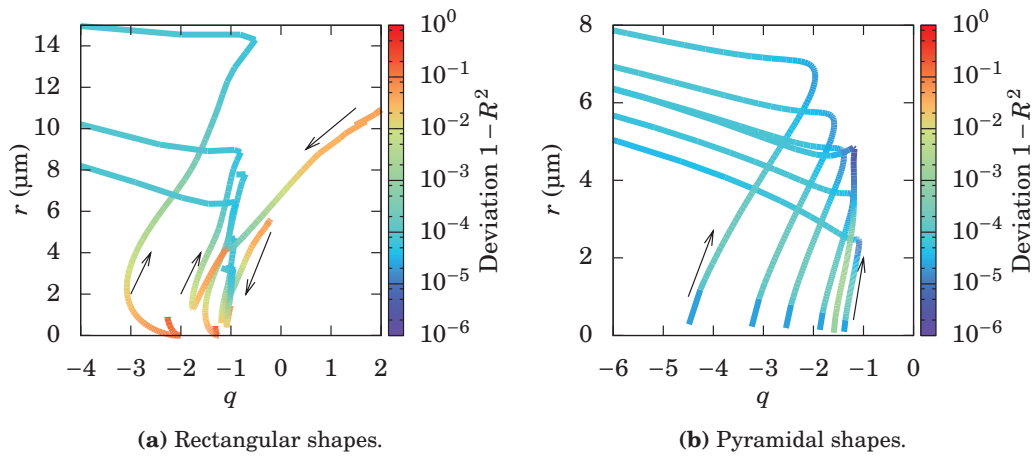


Figure 5.10 – Conic parameters extracted from the simulated reflow of various initial shapes. \rightarrow reflow time

3. The correlation at the beginning of reflow is poorer in the case of the reflow of rectangular shapes, but elliptic lenses could be achieved.

Reflow experiments were carried out on pyramidal shapes with a thin residual layer. The pyramids were imprinted in SU-8 resist using a silicon mold. Samples were then heated at 65°C during various times and rapidly cooled down at room temperature. Figure 5.11 on the facing page presents SEM images of the experiments. The profiles of the reflowed patterns were then extracted and conic parameters q and r were computed. The resulting plot (q, r) is traced on figure 5.12 along with a simulation that uses the same starting shape, as already done above. It turns out that the global bent shape is recovered, but the curvature r is more pronounced in the experimental measurements. We think that this discrepancy is mainly due to the fact that we simulated a 2D flow (x, z) whereas the real flow is clearly in 3D (x, y, z) . Moreover, lubrication theory may fail at describing the reflow of not so small aspect ratio pyramids.

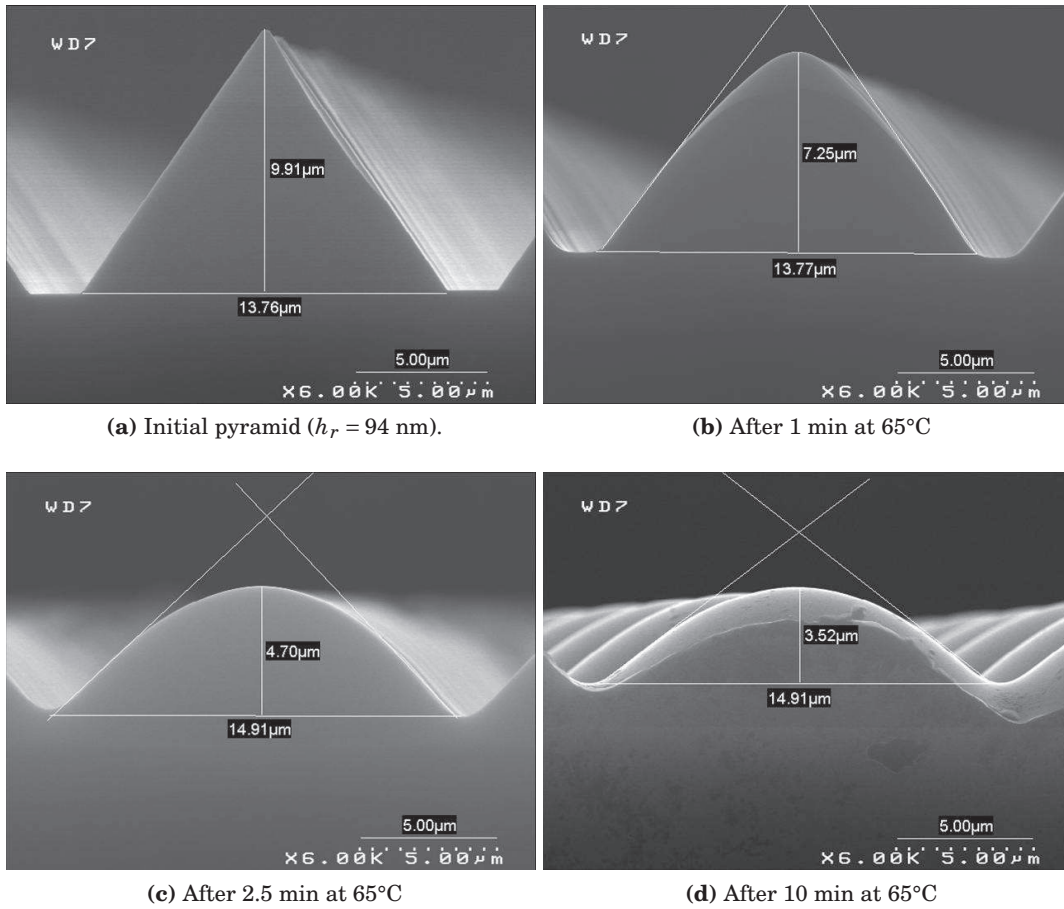


Figure 5.11 – Experimental reflow of nanoimprinted pyramids made of SU-8 resist, with a thin residual layer ($h_r = 94$ nm).

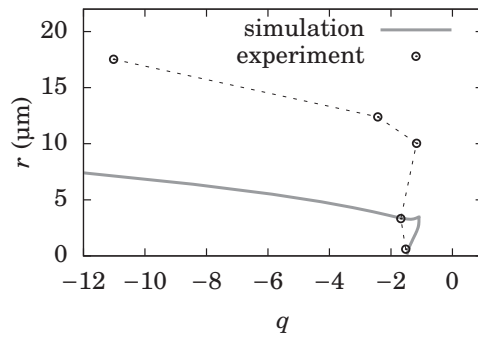


Figure 5.12 – Conic parameters plot from the reflow experiment (3D) compared to simulation (2D).

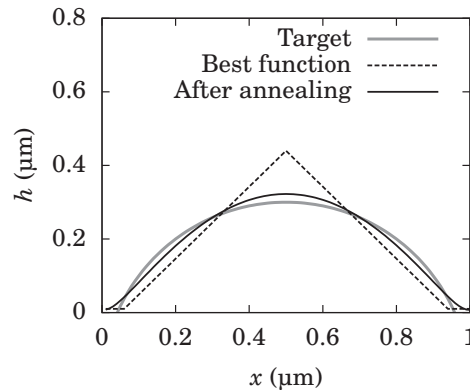


Figure 5.13 – Inverse reflow optimization. The target function (a semi circle) is approached with a pyramidal function.

5.3.3 Inverse reflow programming

The difficulty here is to choose the best initial profile to obtain the desired shape after reflow. We cannot directly process from the final shape and play the reflow backward, because the reflow erase information (high frequencies) as time goes by. So we need to guess what the initial shape may be, and try to optimize it. This is what we call *inverse reflow programming*. An optimization algorithm is of the following kind (for the numerical implementation, see appendix B.3 on page 192):

1. Define a target shape (for example a semi-circle, see figure 5.13)
2. Start with a parametrized shape (for example, a pyramid defined by its height, the length of its base, and the residual layer of the imprint, see figure 5.9)
3. Reflow the test shape until complete leveling, find the reflow duration at which the correlation with the target shape is maximum. The correlation can disregard some part of the profile, for example the extrema (in our example, only the profile between 0.1 μm and 0.9 μm).
4. Optimize parameters with a simplex algorithm.

Because many local minima seem to exist, the initial guess is really important to find a convincing shape. Finding the global minimum of a function is a complex issue beyond the scope of this thesis, and a dedicated software could be worthily employed here.

5.4 Conclusion

In this chapter, we explored several ways of manufacturing complex polymer shapes with use of reflow. We benefited from the theoretical results of chapter 4 to develop

different approaches of reflow, depending on the residual layer and the initially imprinted patterns. These concepts are summarized in table 5.1. We also presented some experimental implementations of reflow. From our point of view, reflow is a promising technique to achieve complex shapes with the help of a robust and predictive model.

Table 5.1 – Summary of concepts of reflow

Name	Description	Implementation
Modulated patterns	With a thick residual layer, high frequency features flow faster than low frequency features.	Rheology (see chap. 6)
Non-isodense patterns	With a thick residual layer, the reflow is performed until individual features are leveled but keeping the general shape that depends on the local density of the initial pattern.	Slopes with small aspect ratios
Thick film reflow	With a thick residual layer, the wavelength of the shapes is smaller than the mean thickness: the reflow is homogeneous even though the residual layer is not uniform.	Reflow on non-planar substrates
Elastic reflow	With a thick residual layer, the wavelength of the shapes is smaller than the elastic wavelength, and the time of reflow is smaller than the elastic relaxation time of the polymer: the reflow is homothetic.	Reduction of aspect ratio
Non-linear reflow	With a thin residual layer, the tops of features are rounded while the bottoms remain sharp.	Microlenses

References

- S. Audran, B. Mortini, B. Faure, and G. Schlatter. Dynamical formation of microlenses by the reflow method: numerical simulation and experimental study of the process fabrication. *Journal of Micromechanics and Microengineering* **20**, 095008 (2010).
- J. J. Chae, S. H. Lee, and K. Y. Suh. Fabrication of multiscale gradient polymer patterns by direct molding and spatially controlled reflow. *Advanced Functional Materials* **21**, 1147–1153 (2011).
- D. Daly, R. F. Stevens, M. C. Hutley, and N. Davies. The manufacture of microlenses by melting photoresist. *Measurement Science and Technology* **1**, 759–766 (1990).
- A. Emadi, H. Wu, S. Grabarnik, G. de Graaf, and R. F. Wolffenbuttel. Vertically tapered layers for optical applications fabricated using resist reflow. *Journal of Micromechanics and Microengineering* **19**, 074014 (2009).
- S. Grilli, S. Coppola, V. Vespini, F. Merola, A. Finizio, and P. Ferraro. 3D lithography by rapid curing of the liquid instabilities at nanoscale. *Proceedings of the National Academy of Sciences* **108**, 15106–15111 (2011).
- F. T. O'Neill and J. T. Sheridan. Photoresist reflow method of microlens production part i: Background and experiments. *Optik - International Journal for Light and Electron Optics* **113**, 391–404 (2002).
- H. Ottevaere, R. Cox, H. P. Herzig, T. Miyashita, K. Naessens, M. Taghizadeh, R. Völkel, H. J. Woo, and H. Thienpont. Comparing glass and plastic refractive microlenses fabricated with different technologies. *Journal of Optics A: Pure and Applied Optics* **8**, S407–S429 (2006).
- Z. D. Popovic, R. A. Sprague, and G. A. N. Connell. Technique for monolithic fabrication of microlens arrays. *Applied Optics* **27**, 1281–1284 (1988).
- H. Schiff, C. Spreu, A. Schleunitz, and J. Lee. Shape control of polymer reflow structures fabricated by nanoimprint lithography. *Microelectronic Engineering* **88**, 87–92 (2011).
- A. Schleunitz and H. Schiff. Fabrication of 3D patterns with vertical and sloped sidewalls by grayscale electron-beam lithography and thermal annealing. *Microelectronic Engineering* **88**, 2736–2739 (2011).

Chapter 6

Characterization of annealed nanoimprinted patterns applied to thin polymer films rheology

Note: This chapter is constructed from previously published articles.¹

6.1 Introduction

6.1.1 State of the art

Nowadays, numerous methods are available to engineers and physicists for characterizing the rheological properties of fluids at the macroscopic scale.² Among others:

ROTATIONAL METHODS consist of a probe such as a cylinder, a cone, a plate, or a sphere, rotating at a definite speed and immersed in the fluid. The rheological properties are computed from the measurement of the torque generated by viscous shear.

VIBRATING METHODS are quite similar to the latter, except that the motion of the probe is oscillating. This method is more relevant for viscoelastic measurements

CAPILLARY METHODS consist of the flow of a fluid from a reservoir through a thin pipe. The fluid viscosity is measured from the time it takes for the reservoir to empty.

¹Etienne Rognin, Stefan Landis, and Laurent Davoust. Viscosity measurements of thin polymer films from reflow of spatially modulated nanoimprinted patterns. *Physical Review E* **84**, 041805 (2011).

Etienne Rognin, Stefan Landis, and Laurent Davoust. Viscoelastic properties measurements of thin polymer films from reflow of nanoimprinted patterns. *Journal of Vacuum Science & Technology B: Microelectronics and Nanometer Structures* **30**, 011602 (2012).

²For example, see

ATS RheoSystems www.atsrheosystems.com,

Malvern Instruments www.malverninstruments.fr.

However, these methods require a rather important amount of fluid, which can be prohibitive in terms of cost. Moreover, it is not possible to perform measurements on films thinner than about ten micrometers. In order to circumvent these limits, other methods have been suggested for measurements at the nanoscale:

DEWETTING METHOD is based on the nucleation and growth rate of holes in a dewetting polymer film (Redon *et al.*, 1991; Masson and Green, 2002; Li *et al.*, 2005; Bodiguel and Fretigny, 2006; Gabriele *et al.*, 2006). Although this approach yields consistent results, it also raises both theoretical and experimental issues. The dynamics of a moving contact line is indeed largely simplified (Ren and E, 2007). Moreover, a limited range of film thickness and substrate material can be used in order to observe the expected dewetting dynamics.

IMMERSED TIP METHOD measures the resistance of the flow around an immersed Atomic Force Microscope (AFM) tip (Mechler *et al.*, 2004; Feibelman, 2006; Major *et al.*, 2006; Svintsov *et al.*, 2007; Papi *et al.*, 2008; Moeller, 2009; Zhang *et al.*, 2010). Conceptually, this method is a scale-down of macroscopic vibrating methods. However, only mechanical properties at high frequency can be measured and the accuracy of the method depends to a large extent on an exact knowledge of the tip shape.

SURFACE DYNAMICS METHODS focus on the relaxation dynamics of a surface topography. In this case, we can distinguish between methods where the topography is induced by thermal fluctuations (Kim *et al.*, 2003; Li *et al.*, 2005; Jiang *et al.*, 2007; Yang *et al.*, 2009; Pottier *et al.*, 2011) or imprinted by a mold, using common nanoimprint techniques (Hamdorf and Johannsmann, 2000; Darhuber *et al.*, 2001; Jones *et al.*, 2006; Ding *et al.*, 2007, 2008). The dynamics is probed using x-ray photon correlation microscopy, or more generally by light scattering techniques. In this approach, attention is given to the time evolution of the fundamental spatial frequency of the shape, and viscoelastic properties are determined from the measured relaxation time. In many cases, neither the exact topology nor the thermal dependence of the optical index of the material are known, and a delicate data processing is needed.

In this chapter, we present a method to measure the viscoelastic properties of a thin polymer film from the reflow of nanoimprinted patterns. We focus our efforts on the accurate spatial determination of the film surface, rather than on its temporal evolution, and we extend the method developed in our group by Leveder *et al.* (2007, 2008, 2010).

6.1.2 Overview of our method

The main steps of our method are drawn in figure 6.1 on the next page. The material (polymer) is spin-coated onto a silicon substrate (a) and the thickness of the film is

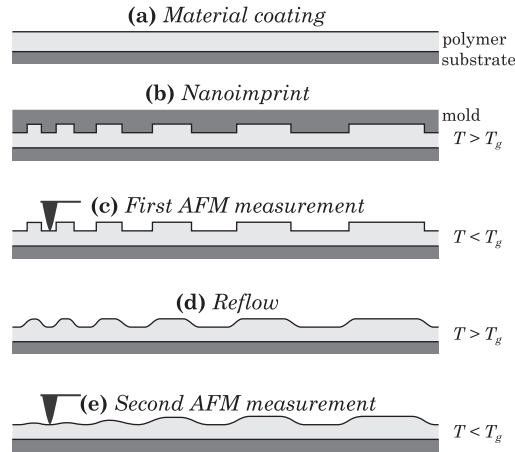


Figure 6.1 – Main steps of the viscosity measurement method.

measured by ellipsometry. We begin with imprinting the film by thermal nanoimprint (b), using a specially designed mold that will be described hereafter. After demolding at room temperature, a first measurement of the imprinted profile is done by AFM³ (c). The film is then heated at a definite temperature above the glass transition temperature (T_g) during a definite time (d). The film is then rapidly cooled down and the reflowed profile is again measured by AFM (e). Spectral densities of the profiles are computed using standard Fourier transform algorithms, and the sought viscosity is a fitting parameter of an evolution model for the spectral density of the topography, described in the next section.

At temperatures above T_g , the film becomes viscous and begins to flow. At the submicron scale and for highly viscous fluids, both gravity and inertia are negligible: the flow is only driven by surface tension and in some cases van der Waals forces (see chapter 2). The film reaches a steady state when the surface energy of the free interface is minimum. In other words, if no dewetting occurs, then the film becomes completely flat. During the reflow process, the shape of the interface evolves with the balance between the surface tension which tends to smooth the bumps and protrusions, and the viscous shear which damps the flow. Locally, the more curved the interface is, the higher the pressure is inside the fluid: short length features of high curvature are the first elements to disappear. Moreover, long length general shapes flatten out more slowly because the fluid must flow over longer distances under high shear and smaller pressure gradient. These local behaviors produce a large scale consequence of the reflow which is a low-pass filtering of the topology of the film. We take advantage precisely of this spatial filtering to extract the viscoelastic properties of the material.

³Other methods to measure the topology of thin films, such as colorimetry (Bodiguel, 2006, p. 215) or confocal microscopy, are not covered in this thesis.

6.2 Reflow of spatially modulated patterns

6.2.1 Model

We assume that the deviation of the free surface, noted \tilde{h} , from the mean thickness value, noted h_0 , is small, in other words that $\tilde{h} \ll h_0$. Under this assumption we can use the results of capillary wave theory for supported thin films, presented in chapter 4. In particular, we recall that each Fourier component $\hat{h}(k)$ of the interface is damped with a wavevector-dependent relaxation time $\tau(k)$:

$$\hat{h}(k, t) = \hat{h}(k, 0) \times \exp\left(-\frac{t}{\tau(k)}\right). \quad (6.1)$$

The relaxation time $\tau = 1/i\omega$ is constrained by the dispersion relation:

$$\frac{i\omega\eta(\omega)h_0}{\gamma} = f(kh_0, \text{Ha}, \beta), \quad (6.2)$$

where $\eta(\omega)$ is the frequency-dependent complex viscosity, γ is the surface tension, and f is a dimensionless function (Eq. 4.26 on page 66) of the normalized wavevector $k \times h_0$, the Hamaker number (Eq. 4.11 on page 59) and the slip length β (Eq. 4.2 on page 56).

Equation (6.1) shows that the reflow of the film is equivalent to a low-pass Fourier spatial filter, for which we gave a physical explanation in the previous section. The *filter kernel* $\exp(-t/\tau(k))$ is given by the physical parameters of the problem. Consequently, there are two ways to measure the kernel function and then extract the viscoelastic properties. The first one, extensively used by previous authors (see the paragraph on SURFACE DYNAMICS METHODS presented in the introducing section), is to follow the amplitude $h(k_1, t)$ of the surface for a given mode k_1 , as a function of time t . This is done with periodical patterns, focusing on the decrease of the fundamental frequency. An exponential decrease is found, and the model is fitted to that data. This is straightforward if there is a real-time analysis, such as scatterometry. Nevertheless, along with the issues raised in the introduction section of this chapter, an additional experimental problem occurs. The steep variation of the decay time with respect to the wavevector and the mean thickness limits the viscosity measurement to a range of a single decade, using a given pattern and thickness, and assuming reasonable experimental times. Multiple patterns are therefore needed to cover a wide range of viscosity and viscoelastic properties. Another issue is the fact that one measurement flattens the topology, hence several samples have to be used in order to perform measurements at different temperatures.

The other way to obtain the kernel function is to measure the decay of all the modes for a given time t_a of annealing, in other words, to measure $h(k, 0)$ and $h(k, t_a)$ as a function of wavevector k . We also recall from chapter 4 that elastic effects will come into play for high spatial frequencies, whereas viscosity drives the low order modes. Thus, if we can measure the kernel function for both low and high wavevectors, then viscous and elastic properties are likely to be derived at the same time. In order to realize this effectively, we need a topology with a rich spectral density but

short enough to be measured by a single AFM or profilometer scan. We present below a patented approach to designing a mold with such a profile.

6.2.2 Pattern design

We can define a pattern shape $m(x)$ of length L , of depth $2\tilde{m}$ by the modulation function:

$$m(x) = \tilde{m} \times \text{sign} \left[\cos \left(\int_0^x k(\xi) d\xi \right) \right], \quad (6.3)$$

where $k(\xi)$ is the local wavevector. Note that if $k(\xi) = k_1$ (the pattern is periodical), then $m(x) = \tilde{m} \times \text{sign}[\cos k_1 x]$. The choice of the function $k(\xi)$ is essential to determine the spectral density. We already studied the reflow of such modulated patterns in chapter 5). Here, we give examples of relevant local wavevector functions.

UNIFORM SPECTRAL DENSITY gives the same weight to low and high frequencies through the Fourier transform. Its expression is given by the linear function:

$$k(\xi) = k_{\max} + (k_{\min} - k_{\max}) \times \frac{\xi}{L}, \quad (6.4)$$

where k_{\min} and k_{\max} are, respectively, the minimum and the maximum local wavevectors. This type of profile is particularly relevant if the measurements are performed by AFM or profilometer.

In case of optical measurement methods, other function $k(\xi)$ can be useful:

ENHANCED VISUAL CONTRAST between reflowed areas (high frequencies) and slower dynamics areas (low frequencies) is achieved by:

$$k(\xi) = k_{\max} \left(\frac{k_{\min}}{k_{\max}} \right)^{\frac{\xi}{L}}. \quad (6.5)$$

CONSTANT SPEED

$$k(\xi) = k_{\max} \left(\frac{\xi}{L} \right)^{-\frac{1}{4}}. \quad (6.6)$$

CONSTANT PEAK-TO-PEAK DIFFERENCE

$$\frac{1}{k(\xi)} = \frac{1}{k_{\max}} + \left(\frac{1}{k_{\min}} - \frac{1}{k_{\max}} \right) \frac{\xi}{L}. \quad (6.7)$$

6.2.3 Mold fabrication

The general method to design a mold is the following (see figure 6.2 for an example of implementation):

1. Setting of the pattern length L , for example $L = 40\mu\text{m}$ (AFM scans).
2. Setting of the function $k(\xi)$, for instance according to equation (6.5).

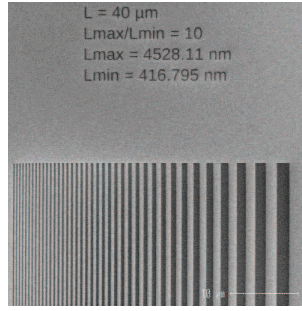


Figure 6.2 – SEM image of a 40 μm pattern of a mold manufactured with e-beam lithography.

3. Setting of k_{\min} and k_{\max} , or equivalently λ_{\min} and λ_{\max} with $\lambda = 2\pi/k$. For this step:

- (a) λ_{\max} as a function of λ_{\min} , for example $\lambda_{\max} = 10\lambda_{\min}$.
- (b) λ_{\min} is imposed by the lithography technique employed to make the mold. Indeed, for a first period $\lambda_1 = \lambda_{\min}$, the difference with the next one λ_2 should be close to λ_{\min} times the growth rate of λ . Whether λ_1 and λ_2 will be different depends on the following criterion:

$$\lambda_{\min} \times \frac{\partial \lambda}{\partial \xi}(\lambda_{\min}) \geq 2\delta, \quad (6.8)$$

with δ the resolution of the lithography ($\delta \sim 5$ nm for e-beam lithography). The factor 2 comes from the fact that the line width is half of the period. For our example, we find: $\lambda_{\min} = 417$ nm.

6.3 Experimental viscosity measurements

6.3.1 Experiments

Experiments were carried out on polystyrene samples. The following paragraphs cover many aspects of the experimental process. The first one is dedicated to the materials properties and preparation. The second and third paragraphs go through the imprint and reflow of the samples. The last one is a comment on the AFM measurements. Results are finally presented in the next subsection.

Materials. Low molecular weights ($M_w = 30$ kg·mol⁻¹ and $M_w = 130$ kg·mol⁻¹) monodisperse ($M_w/M_n < 1.06$) polystyrene (PS 30k and PS 130k) solution was spin-coated onto 8 inch silicon substrates. Prior to coating PS, substrates were rinsed with a hydroxylamine/aminethoxyethanol (60%-40%) bath during 600 s at 343 K, and a O₂/N₂H₂ (2150 sccm/240 sccm) plasma during 180 s at 543 K was performed in order to obtain a homogeneous 4 nm-thick SiO_x layer. Thicknesses of coated polystyrene films

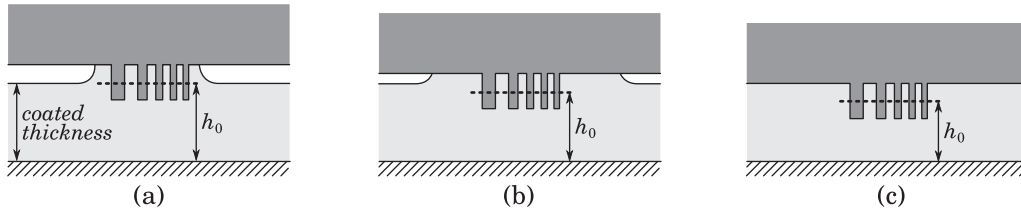


Figure 6.3 – Evolution of the local mean thickness (h_0) during imprint: **(a)** short imprint times, only local flow takes place, the mean thickness equals the coated thickness (the pattern is iso-dense); **(b)** intermediate state; **(c)** long imprint time, long-range flow occurred to spread the material.

were 150 ± 1 nm (measured by ellipsometry). In chapter 3, we reviewed the properties of polystyrene and reported those of PS 30k and PS 130k in table 3.2 on page 39.

Imprint. The imprints of the patterns were made at 13 bars of pressure and at temperature $T_g + 80^\circ\text{C}$ where the elastic stress relaxes quickly (measured by disk rheometry to be less than 1 s) in comparison to the imprint time (which was at least 30 min). The uniformity of the residual layer is ensured because first, the depth of the pattern is small compared with the initial thickness of the film, second, the pattern is locally iso-dense (no large scale flow of mass), and third, the total length of the pattern ($40\mu\text{m}$) is small compared to the thickness of the mold ($750\mu\text{m}$) so that no bending of the mold occurred (Landis *et al.*, 2006). Demolding was performed at room temperature.

The local mean thickness is between the initial coated thickness (150 nm) and the initial thickness minus half of the mold depth (125 nm), as it is sketched on figure 6.3. We assume that long-range flow occurs during the imprint time, so that the local mean thickness is close to the latter case. Keeping a reasonable uncertainty range: $h_0 = 135 \pm 10$ nm.

Heating and quench. The model we previously described requires that the polymer film changes instantaneously from a glassy solid state below T_g to a fluid state at a fixed temperature above T_g . From an experimental point of view, this cannot be strictly achieved because of thermal inertia of the sample. However, we can choose the total reflow duration so that the duration of the unsteady state can be neglected, at the cost of an appropriate error estimate on the final viscosity measurement.

In our experiments, the heating of the sample was done with a hot plate with 1°C precision. The energy is transferred to the sample through the contact surface. The quench, i.e. the rapid cooling, was performed by using a cooling plate thermalized at room temperature. Given that the sample is thin (no significant heat flux at the edges) and that the flux through both sides are homogeneous, this quench is a one-dimensional thermal transfer through the thickness of the sample. In chapter 2, we saw that it was reasonable to assume an homogeneous temperature inside the film (Biot number, Eq. 2.14 on page 26). The cooling (or heating) of the sample is then

driven by the fastest transfer phenomenon.⁴ It turns out to be the thermal contact with the plate, of characteristic time $\tau \sim 1$ s, therefore the sample reaches a steady state within a few seconds at most. According to this scaling analysis, if we choose a reflow duration of at least 5 min, it is reasonable to consider that the transition is instantaneous.

AFM measurements. For the AFM measurements we used Nanosensors™ AR5-NCHR tips in tapping mode. These tips have high aspect ratios (7:1) and low radii (< 15 nm). The typical resonance frequency was 330 kHz.

All AFM measurements are done at room temperature, thus there is essentially no issue of temperature drift. It is however well-known that tip geometry induces a distortion in the measured image (Keller, 1991; Hahlweg *et al.*, 2009). This effect is a non-linear convolution which can have a direct influence on the spectral density, and finally on the viscosity measurement. The mathematical treatment of a nonlinear deconvolution is not straightforward and requires an accurate knowledge of the tip shape. Without special equipment dedicated to this issue it is thus of importance to minimize such convolution. In our case, this is ensured by the low aspect ratio of the imprinted profiles, which means that the tip can fully enter the trenches and that the shadows induced by the steep steps are negligible. It is also possible to perform a brief reflow just after demolding in order to soften the edges of the profile, and thus reduce or suppress the tip convolution. This new state may be therefore used as the initial one.

6.3.2 Results and discussion

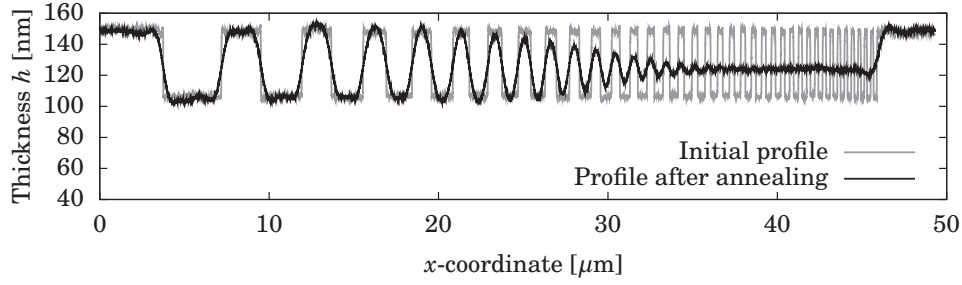
Figure 6.4 on the facing page shows an example of a viscosity measurement done with the method described above. A 150nm-thick PS 30k was annealed at 120°C for 5 min. The AFM measurements reported on figure 6.4a emphasize the low-pass filtering behavior of the reflow, since the high frequency part of the profile completely vanished after annealing, which is confirmed by the Fourier transforms plotted on figure 6.4b. The ratio of Fourier transforms of both profile plotted on figure 6.4c gives the experimental kernel function. The error bars are drawn assuming a 1 nm RMS Gaussian noise for each AFM measurement. The large uncertainty area for the high order modes accounts for the fact that no information can be extracted from features which have completely flowed. From the data points it is then possible to compute the capillary number:

$$\text{Ca} = \frac{\eta h_0}{\gamma t}, \quad (6.9)$$

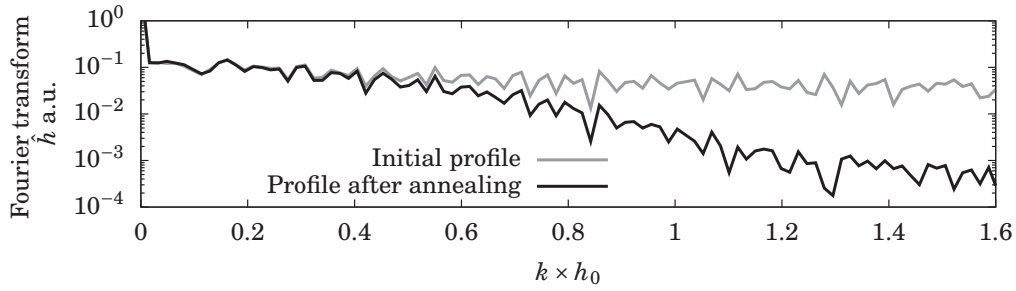
⁴Assuming a linear heat transfer on one side of the sample, an energy balance would give for the silicon substrate (we neglect the thermal inertia of the polymer film):

$$\tau \frac{\partial T}{\partial t} = T_{\text{plate}} - T \quad \text{with } \tau = \frac{\rho c_p \ell}{H}$$

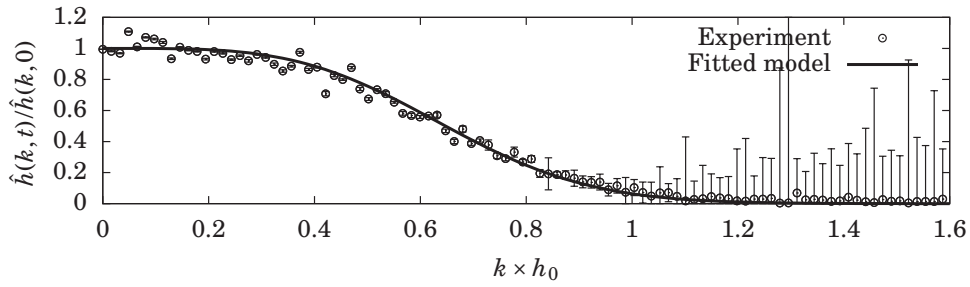
where ρ is the density of the silicon, c_p its specific heat, $\ell = 750 \mu\text{m}$ the wafer thickness and H the coefficient of the linearized heat transfer.



(a) AFM measurements of an imprinted pattern before and after annealing.



(b) Fourier transforms of signals in figure (a).



(c) Kernel function of the reflow, experimental points, and fitted model $\exp(-f(kh_0)/Ca)$ as defined by equation (6.10). The fitted value Ca is 0.062 ± 0.001 .

Figure 6.4 – Viscosity measurement example for PS 30k at 120°C.

(see Eq. 4.30 on page 67) as a fitting parameter of the theoretical kernel function:

$$\frac{\hat{h}(k, t)}{\hat{h}(k, 0)} = \exp\left(-\frac{f(kh_0)}{\text{Ca}}\right). \quad (6.10)$$

Viscosity is readily obtained with the knowledge of the other physical parameters (Tab. 3.2 on page 39).

Accuracy of the method. Let's now make several remarks about the accuracy of the method. The number Ca is given with a relative error $\sigma_{\text{Ca}} = 2\%$ which comes from the residuals of the fitting. The uncertainty of the other parameters is, in our experiments (see previous section), $\sigma_{h_0} = 7\%$ for the mean thickness, $\sigma_\gamma = 9\%$ for the surface tension, $\sigma_t = 1\%$ for the duration of the reflow. The way the uncertainty of the mean thickness influences the final result is not straightforward since it plays a role both in the fitting (through $f(kh_0)$) and in the number Ca . Still, it is possible to estimate an upper bound of this error by recalling the fact that the dynamics of the film is independent of its thickness for high order modes ($kh_0 \gg 1$) and varies as h_0^3 for low order modes (thin film regime). Keeping the most significant dependency, we can finally write:

$$\sigma_\eta = \sqrt{\sigma_{\text{Ca}}^2 + \sigma_\gamma^2 + \sigma_t^2 + (3\sigma_{h_0})^2} = 23\%, \quad (6.11)$$

The uncertainty is mainly due to surface tension and mean thickness estimates. For example, it could be worth using a dedicated equipment to accurately measure surface tension. Although uncertainty seems rather high, our method should fairly give an order of magnitude for viscosity, which is what we are interested in from a process point of view. To conclude on this particular example, the result of the fit for PS 30k at 120°C is $\eta = 1.0 \pm 0.2 \times 10^6 \text{ Pa}\cdot\text{s}$.

Temperature dependence. Finally, the viscosity of polymer melts can be extracted using the previously described technique at various temperatures (Tab. 6.1). Viscosity results for PS 30k and 130k between 120°C and 180°C are reported on figure 6.5 on the next page. The reference curves are obtained from Plazek (1965); Majeste *et al.* (1998); Li *et al.* (2005); Kim *et al.* (2007); Leveder (2009) (see chapter 3, tables 3.4 and 3.5 on page 44). In spite of the large scattering of reference curves,⁵ good agreement can be seen with our viscosity measurements.

The WLF law was fitted to our data and parameters $c_1 = 12.6 \pm 0.1$, $c_2 = 101 \pm 1 \text{ K}$ and $\eta_{s@35\text{kg}\cdot\text{mol}^{-1}} = 1.1 \pm 0.2 \times 10^4 \text{ Pa}\cdot\text{s}$ were found. These results also confirm that the deviation of flow properties encountered for thickness below ten nanometers does not occur here, since we obtained the properties of the bulk materials.

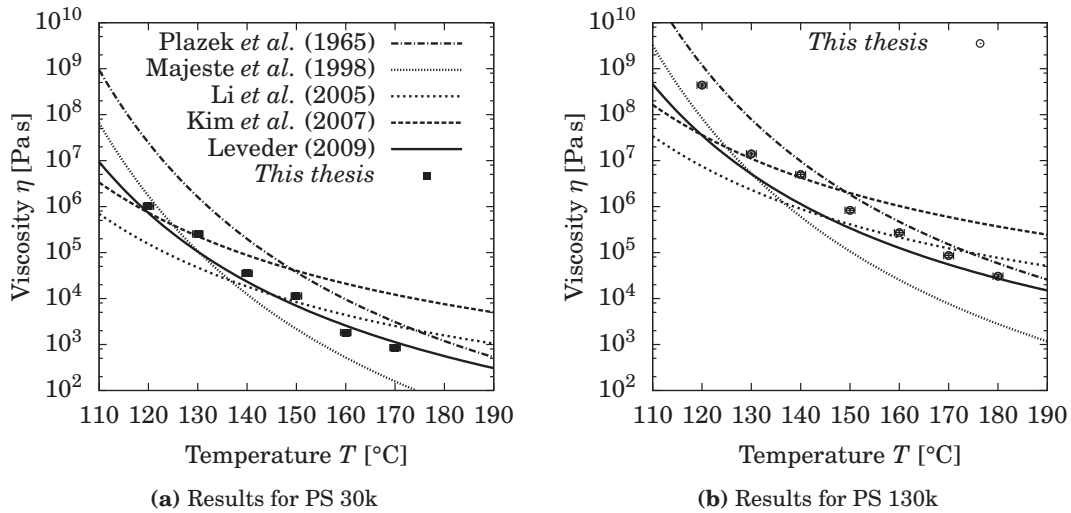
6.4 Experimental viscoelastic measurements

In the previous section, we saw that it is possible to measure the viscosity of polystyrene by looking at how fast low spatial frequencies flow. We will now see that it is also

⁵This is traditionally explained by differences in preparation of samples, rheology methods, or polydispersity index.

Table 6.1 – Reflow time and results for samples of PS 30k and PS 130k

Temperature (°C)	Reflow time (min)		Fitted Ca ($\pm 2\%$)	
	PS 30k	PS 130k	PS 30k	PS 130k
120	10	60	6.6×10^{-3}	4.9×10^{-1}
130	5	60	3.4×10^{-3}	1.5×10^{-2}
140	2	40	1.1×10^{-3}	8.2×10^{-3}
150	1	10	7.5×10^{-4}	5.5×10^{-3}
160	1	10	1.2×10^{-4}	1.8×10^{-3}
170	1	10	5.7×10^{-5}	5.7×10^{-4}
180	-	10	-	2.0×10^{-4}


Figure 6.5 – Viscosity measurements for polystyrene of two molecular weights. The experimental points are plotted along with reference curves.

possible to extract some information about elasticity by looking at high frequencies. However, these high frequencies should not completely flow in order to keep an acceptable signal-to-noise ratio (see error bars in figure 6.4c). That is why viscoelastic measurements require quicker reflow times.

6.4.1 Models

In section 3.3.4 on page 45 of chapter 4, we found that the theoretical kernel function of the reflow was, in the case of a Maxwell fluid:

$$\hat{h}(k, t) = \hat{h}(k, 0) \times \exp\left(-\frac{1}{\frac{\text{Ca}}{f(kh_0)} + \text{De}}\right), \quad (6.12)$$

with Ca the capillary number related to the zero-shear viscosity and

$$\text{De} = \frac{\tau_t}{t}, \quad (6.13)$$

the ratio of the terminal relaxation time over the reflow time, called the *Deborah number*. We also saw that we could use a reptation model that is a kind of Maxwell model with a continuous spectrum, although we cannot in that case find an analytical kernel function (see Eq. 4.37 on page 69). The numbers Ca and De will then be our fitting parameters for the experimental data.

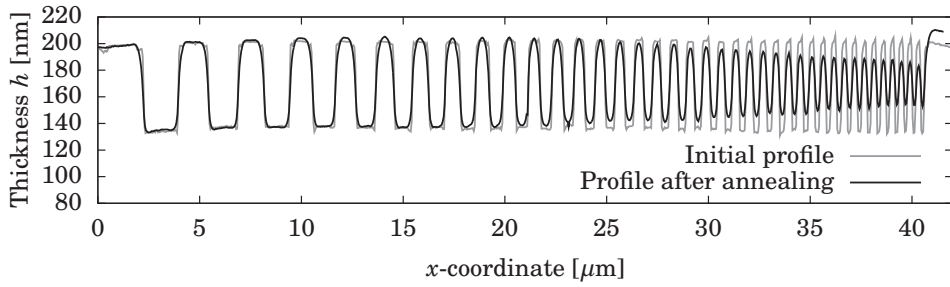
6.4.2 Single temperature example

We used 205 nm-thick PS 130k samples. Figure 6.6 on the next page gives an example of a reflow experiment at 140°C for 30s. The reflow time is quite short in order to prevent the complete flow of high frequencies (Fig. 6.6a). Contrary to viscosity measurements in the previous section, high order modes of the Fourier transforms will be used to extract elastic properties (Fig. 6.6b). High frequencies come from both small pitch lines (below about $kh_0 \approx 6$) but also high orders of the Fourier components of square signals.

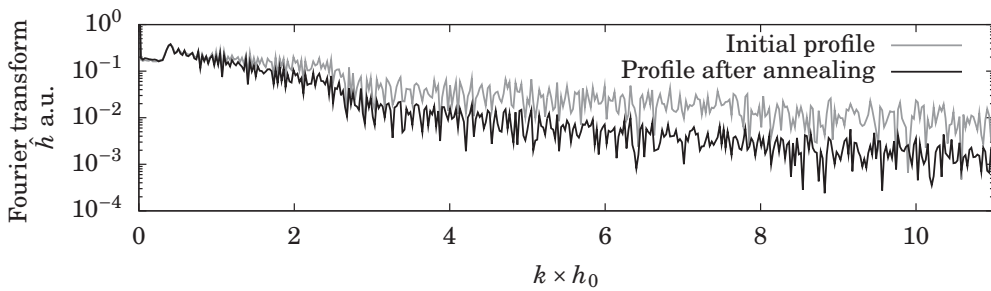
Unfortunately, if we directly compute the experimental kernel, a large scattering is found in the high frequencies, as shown on figure 6.7a. In order to reduce the scattering of data, the Fourier spectra are smoothed with use of a convolution with a blurring vector,⁶ and a smoother kernel is found (Fig. 6.7b).

Now, we can fit our models to the experimental points, as done in figure 6.8 on page 110. From this experiment, we can see that a viscoelastic Maxwell model is more relevant to describe the flow than a purely viscous model. Especially at high spatial frequencies, a viscous kernel is exponentially decreasing (straight line in a semi-log plot), whereas a viscoelastic kernel tends towards a horizontal asymptote. Theoretically, elastic effects should appear for $kh_0 \gtrsim 2.5$ (see equation 4.36 on page 69), and we see that it reflects the experimental data. The result of the fitting is $\text{Ca} = 0.9 \pm 0.2$ and $\text{De} = 0.36 \pm 0.08$. In the next paragraph, we will see the results in terms of viscosity and relaxation time.

⁶This is a very common filtering method in data processing. Here we used a rather narrow blurring vector: [0.05 0.1 0.15 0.4 0.15 0.1 0.05]

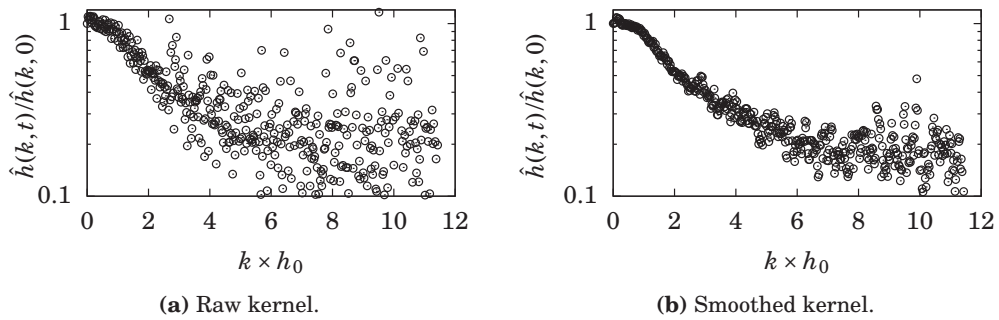


(a) AFM measurements of an imprinted pattern before and after annealing.



(b) Fourier transforms of signal in figure (a).

Figure 6.6 – Viscoelastic reflow experiment with PS 130k at 140°C for 30s. Contrary to viscosity measurements, high order modes (b) will be used to extract elastic properties.



(a) Raw kernel.

(b) Smoothed kernel.

Figure 6.7 – Experimental kernel functions from figure 6.6, (a) without treatment, (b) from smoothed Fourier spectra.

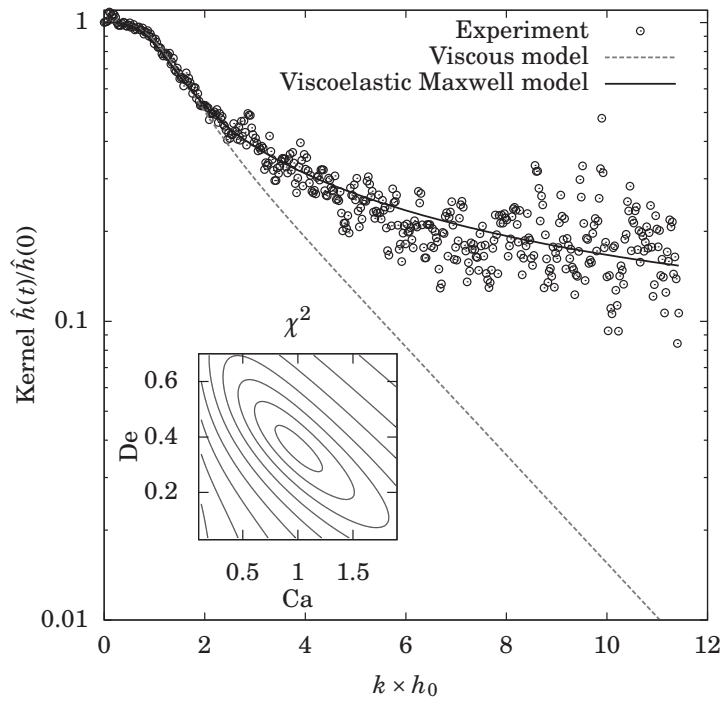


Figure 6.8 – Experimental kernel $\hat{h}(t)/\hat{h}(0)$ as a function of the normalized wavevector. Experimental points are fitted with two models: a purely viscous model (Eq. 6.10) and a viscoelastic single mode Maxwell model (Eq. 6.12). **Inset:** arbitrary levels of the cost function χ^2 (least squares fitting of the Maxwell model) showing a single minimum. The fitted parameters are $Ca = 0.9 \pm 0.2$ and $De = 0.36 \pm 0.08$.

Table 6.2 – Reflow times and viscoelastic fits.

Temp. (°C)	Reflow time (s)	fitted Ca		fitted De	
		Maxwell	Reptation	Maxwell	Reptation
110	600	0.86	1.4	0.30	0.40
120	300	1.3	2.0	0.30	0.41
130	60	1.0	1.8	0.28	0.38
140	30	0.78	0.73	0.42	0.54
150	30	0.076	0.30	0.23	0.27

6.4.3 Temperature dependence

The method was used to measure the viscoelastic properties of PS 130k at various temperatures. Experimental sets and fitting results are reported on table 6.2. Physical parameters are reported on figure 6.9. Zero-shear viscosity (Fig 6.9a) is consistent with the WLF model we found in the previous section, confirming the robustness of the rheology method.

We now focus on the relaxation times of figure 6.9b. In chapter 3, we saw that the terminal relaxation time could be expressed by:

$$\tau_t(T) = \frac{\eta_0(T)}{G_e}, \quad (6.14)$$

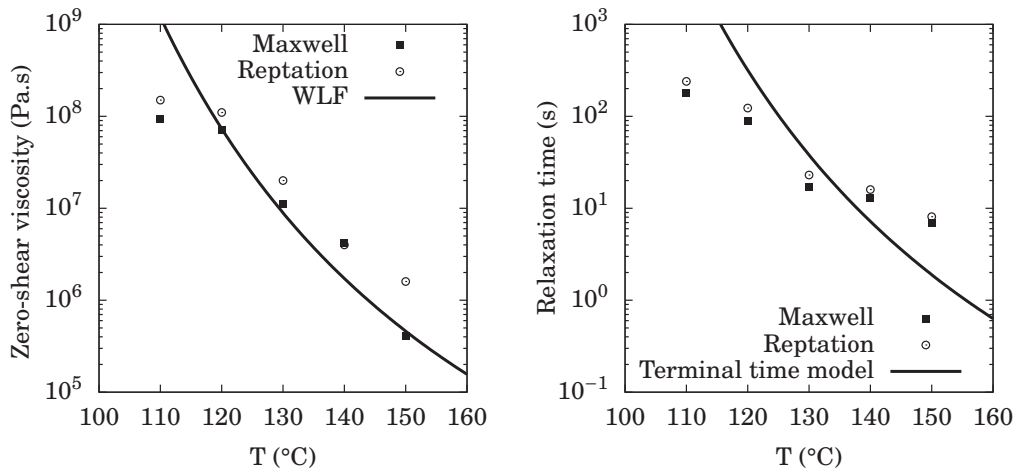
with η_0 the zero-shear viscosity and G_e the elastic plateau modulus given by equation (3.19) on page 45, which has a negligible dependence on temperature with respect to the variations of η_0 . The curve in figure 6.9b is then the zero-shear viscosity model (Fig. 6.9) divided by $G_e \approx 0.2$ MPa. It is remarkable to recover the same order of magnitude, in spite of the scattering of data. The large discrepancy with experimental data for low temperatures suggests that the observed relaxation time at these temperatures may not be the terminal time but a relaxation time (or a combination of times) associated with faster dynamics.

6.4.4 Maxwell versus reptation model

In the previous paragraph, we found that there are no significant difference between the Maxwell model and the reptation model in terms of measured viscosity and relaxation time. However, if we look at figure 6.10 on the next page which is the experimental kernel for the reflow at 150°C, we see that data is more closely fitted with the reptation model, because the latter reaches its asymptote faster, although remaining discrepancy near $kh_0 \sim 2$ suggests that an even more relevant model is required.

6.5 Conclusion and outlooks

In this chapter, we presented a method to measure the viscoelastic properties of polymer thin films from the reflow of nanoimprinted patterns. We made use of a complete



(a) Zero-shear viscosity measurements. (b) Relaxation time measurements.

Figure 6.9 – Viscoelasticity measurements for PS 130k at several temperatures. (a) Experimental viscosity (points) and the WLF model (line) with the parameters found in the previous section. (b) Relaxation time (points) and the theoretical terminal time (line).

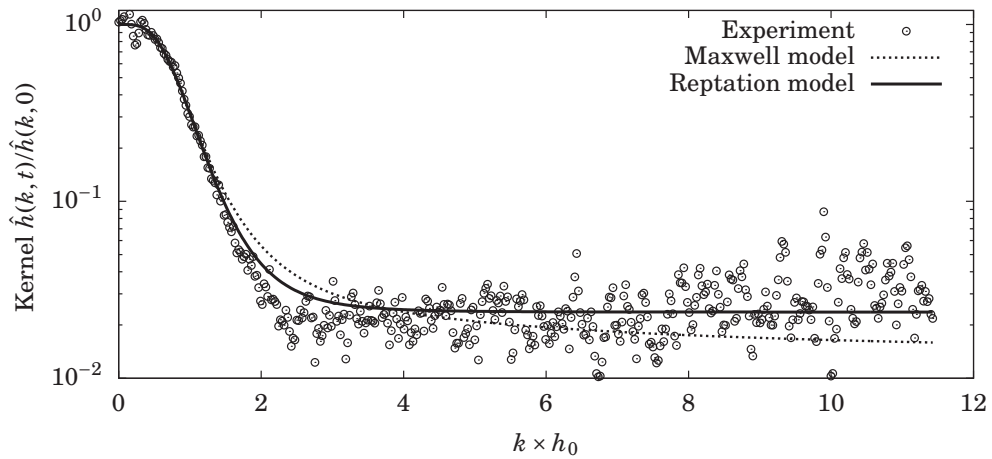


Figure 6.10 – Difference between a Maxwell model and a reptation model for the experimental fit. Reflow at 150°C for 30s.

and accurate model for the spectral density evolution of the topology. Contrary to previous similar approaches, emphasis was put on the spatial description rather than the temporal decay of the patterns. With this model, we could develop relevant stamp designs with spatially modulated patterns to optimize experimental measurements and to ensure fruitful data processing. Our approach was then successfully applied to measure viscosity of PS 30k and PS 130k, and the viscoelastic properties of PS 130k. The measured relaxation time is of practical importance for imprint processes: it is the time needed for internal stresses to relax. Our method does not require dedicated equipment since it makes use of imprint tools and AFM. It is then a fast and cost-effective method to measure the rheological properties of polymer thin films.

The question remaining now, is whether it is possible to measure other physical quantities like slip lengths or disjoining pressures. In the case of periodical patterns leveling, this issue has been partially addressed by Gilormini and Teyssedre (2012) for the former, and Seemann *et al.* (2001); Steiner (2005) for the latter. It is clear that the first step is to decorrelate the slip length and disjoining pressure from the rheological properties. We saw in chapter 4 that high spatial frequencies are not affected by those two quantities (Fig. 4.7 on page 66), whereas slip and van der Waals forces strongly affect the flow of low frequencies. So in theory, it should be possible to measure other physical parameters with the technique presented in this chapter. The experimental implementation is left to future studies.

References

- H. Bodiguel and C. Fretigny. Viscoelastic dewetting of a polymer film on a liquid substrate. *The European Physical Journal E* **19**, 185–193 (2006).
- H. Bodiguel. Propriétés mécaniques de films polymères ultraminces. PhD thesis, Université Paris VI (2006).
- A. A. Darhuber, S. M. Troian, and S. Wagner. Physical mechanisms governing pattern fidelity in microscale offset printing. *Journal of Applied Physics* **90**, 3602 (2001).
- Y. Ding, H. W. Ro, T. A. Germer, J. F. Douglas, B. C. Okerberg, A. Karim, and C. L. Soles. Relaxation behavior of polymer structures fabricated by nanoimprint lithography. *ACS Nano* **1**, 84–92 (2007).
- Y. Ding, H. W. Ro, K. J. Alvine, B. C. Okerberg, J. Zhou, J. F. Douglas, A. Karim, and C. L. Soles. Nanoimprint lithography and the role of viscoelasticity in the generation of residual stress in model polystyrene patterns. *Advanced Functional Materials* **18**, 1854–1862 (2008).
- P. J. Feibelman. Lubrication theory of drag on a scanning probe in structured water, near a hydrophilic surface. *Langmuir* **22**, 2136–2140 (2006).
- S. Gabriele, P. Damman, S. Slavons, S. Desprez, S. Coppée, G. Reiter, M. Hamieh, S. A. Akhrass, T. Vilmin, and E. Raphaël. Viscoelastic dewetting of constrained polymer thin films. *Journal of Polymer Science Part B: Polymer Physics* **44**, 3022–3030 (2006).
- P. Gilormini and H. Teyssedre. On using the leveling of a polymer free surface to measure viscosity and navier slip length. *To be published* (2012).

- C. Hahlweg, M. Gruhlke, and H. Rothe. Nonlinear distortion in atomic force microscopy (AFM) measurements. *Measurement Science and Technology* **20**, 084018 (2009).
- M. Hamdorf and D. Johannsmann. Surface-rheological measurements on glass forming polymers based on the surface tension driven decay of imprinted corrugation gratings. *The Journal of Chemical Physics* **112**, 4262 (2000).
- Z. Jiang, H. Kim, X. Jiao, H. Lee, Y.-J. Lee, Y. Byun, S. Song, D. Eom, C. Li, M. H. Rafailovich, L. B. Lurio, and S. K. Sinha. Evidence for viscoelastic effects in surface capillary waves of molten polymer films. *Physical Review Letters* **98**, 227801 (2007).
- R. L. Jones, T. Hu, C. L. Soles, E. K. Lin, R. M. Reano, S. W. Pang, and D. M. Casa. Real-time shape evolution of nanoimprinted polymer structures during thermal annealing. *Nano Letters* **6**, 1723–1728 (2006).
- D. Keller. Reconstruction of STM and AFM images distorted by finite-size tips. *Surface Science* **253**, 353–364 (1991).
- H. Kim, A. Rühm, L. B. Lurio, J. K. Basu, J. Lal, D. Lumma, S. G. J. Mochrie, and S. K. Sinha. Surface dynamics of polymer films. *Physical Review Letters* **90**, 068302 (2003).
- S. H. Kim, F. Teymour, and J. A. Debling. A unifying approach for melt rheology of linear polystyrene. *Journal of Applied Polymer Science* **103**, 2597–2607 (2007).
- S. Landis, N. Chaix, C. Gourgon, C. Perret, and T. Leveder. Stamp design effect on 100 nm feature size for 8 inch NanoImprint lithography. *Nanotechnology* **17**, 2701–2709 (2006).
- T. Leveder, S. Landis, L. Davoust, and N. Chaix. Flow property measurements for nanoimprint simulation. *Microelectronic Engineering* **84**, 928–931 (2007).
- T. Leveder, S. Landis, and L. Davoust. Reflow dynamics of thin patterned viscous films. *Applied Physics Letters* **92**, 013107 (2008).
- T. Leveder. Etude et caractérisation de films polymère ultra-minces dans le cadre de la lithographie par nanoimpression. PhD thesis, Institut Polytechnique de Grenoble (2009).
- T. Leveder, S. Landis, N. Chaix, and L. Davoust. Thin polymer films viscosity measurements from nanopatterning method. *Journal of Vacuum Science & Technology B: Microelectronics and Nanometer Structures* **28**, 1251 (2010).
- C. Li, T. Koga, C. Li, J. Jiang, S. Sharma, S. Narayanan, L. B. Lurio, X. Hu, X. Jiao, S. K. Sinha, S. Billet, D. Sosnowik, H. Kim, J. C. Sokolov, and M. H. Rafailovich. Viscosity measurements of very thin polymer films. *Macromolecules* **38**, 5144–5151 (2005).
- J.-C. Majeste, J.-P. Montfort, A. Allal, and G. Marin. Viscoelasticity of low molecular weight polymers and the transition to the entangled regime. *Rheologica Acta* **37**, 486–499 (1998).
- R. C. Major, J. E. Houston, M. J. McGrath, J. I. Siepmann, and X.-Y. Zhu. Viscous water meniscus under nanoconfinement. *Physical Review Letters* **96**, 177803 (2006).
- J.-L. Masson and P. F. Green. Viscosity of entangled polystyrene thin film melts: Film thickness dependence. *Physical Review E* **65**, 031806 (2002).

- A. Mechler, B. Piorek, R. Lal, and S. Banerjee. Nanoscale velocity-drag force relationship in thin liquid layers measured by atomic force microscopy. *Applied Physics Letters* **85**, 3881 (2004).
- G. Moeller. AFM nanoindentation of viscoelastic materials with large end-radius probes. *Journal of Polymer Science Part B: Polymer Physics* **47**, 1573–1587 (2009).
- M. Papi, G. Maulucci, G. Arcovito, P. Paoletti, M. Vassalli, and M. De Spirito. Detection of microviscosity by using uncalibrated atomic force microscopy cantilevers. *Applied Physics Letters* **93**, 124102 (2008).
- D. J. Plazek. Temperature dependence of the viscoelastic behavior of polystyrene. *The Journal of Physical Chemistry* **69**, 3480–3487 (1965).
- B. Pottier, G. Ducouret, C. Frétiigny, F. Lequeux, and L. Talini. High bandwidth linear viscoelastic properties of complex fluids from the measurement of their free surface fluctuations. *Soft Matter* **7**, 7843 (2011).
- C. Redon, F. Brochard-Wyart, and F. Rondelez. Dynamics of dewetting. *Physical Review Letters* **66**, 715 (1991).
- W. Ren and W. E. Boundary conditions for the moving contact line problem. *Physics of Fluids* **19**, 022101 (2007).
- R. Seemann, S. Herminghaus, and K. Jacobs. Dewetting patterns and molecular forces: A reconciliation. *Physical Review Letters* **86**, 5534–5537 (2001).
- U. Steiner. Force measurements using capillary instabilities. *Journal of Polymer Science Part B: Polymer Physics* **43**, 3395–3405 (2005).
- A. A. Svintsov, O. V. Trofimov, and S. I. Zaitsev. Viscosity measurement of nanoimprint lithography resists with a rheological nanoindenter. *Journal of Vacuum Science & Technology B: Microelectronics and Nanometer Structures* **25**, 2435 (2007).
- Z. Yang, C.-H. Lam, E. DiMasi, N. Bouet, J. Jordan-Sweet, and O. K. C. Tsui. Method to measure the viscosity of nanometer liquid films from the surface fluctuations. *Applied Physics Letters* **94**, 251906 (2009).
- X. Zhang, X. Zhang, and T. Chen. Investigation on dynamic rheology properties of ultra-thin film using ultra-vacuum non-contact AFM. In *Society of Tribologists and Lubrication Engineers Annual Meeting and Exhibition 2010*, pages 652–654 (2010).

Part III

Tuned instabilities

Chapter 7

Disjoining pressure and the modern theory of van der Waals forces

In the previous parts, we mentioned the existence of a disjoining pressure responsible for the spontaneous rupture of thin films. In the absence of electrostatic forces, the intermolecular driving interactions are forces called long-range *van der Waals forces*, named after the Dutch scientist Johannes Diderik van der Waals. So far we employed a common approximation of the disjoining pressure in $A/6\pi h^3$, with A the Hamaker constant, and h the thickness of the film. In this chapter, we will see that in fact A is a constant only for infinitely thin films, and is rather a function of h for finite films. The modern theory of van der Waals forces gives a practical method to compute the disjoining pressure from the optical properties of the materials in planar multilayer geometries, although its extension to arbitrary geometries is still a challenge today.

The reference book in that field has been for a long time the work by Israelachvili (1991, Chap. 11). A more practical and thorough approach is provided by the recent book of Parsegian (2005), although the present chapter is inspired to a large extent by the work of Mulet (2003, Chap. 6). Finally, the most advanced improvements in long-range forces understanding can be found in the review by French *et al.* (2010).

7.1 Studied geometries

Two configurations are encountered in our experimental setup, as depicted on figure 7.1 on the next page. The first one is called the *supported film*: a polymer film lies on a silicon substrate. We can add layers between the substrate and the film in order to tune the properties of the disjoining pressure. The second configuration is called the *confined film*: the film is sandwiched between the substrate and the mold. Here again we can add intermediate layers on the substrate or on the mold. Usually, there is also an anti-sticking layer covering the mold.

For such geometries, it is clear that in areas far from the edges of the protrusions

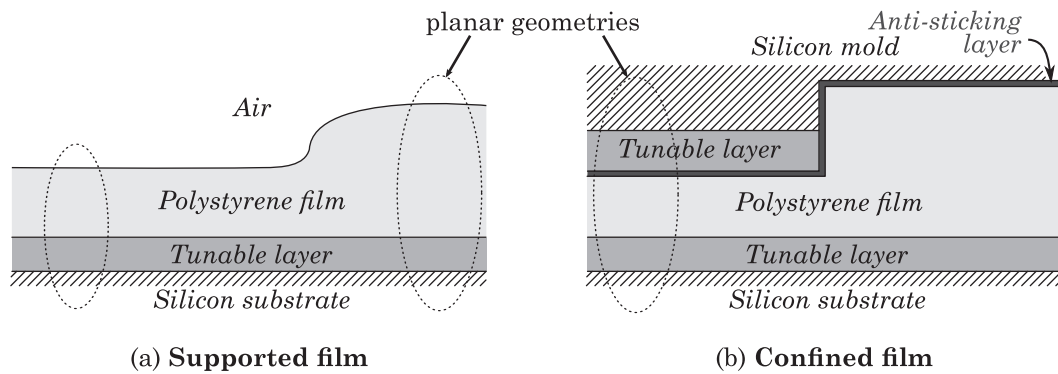


Figure 7.1 – Experimental geometries.

(much farther than the characteristic thickness), the system can be studied as a planar stratified medium, at least at initial times (circles in figure 7.1). We also have to keep in mind that the theory described in this chapter is a macroscopic theory, thus the thickness of layers should be at least of several molecular lengths (Ninham, 1980). Finally, we do not take into account the motion of the interface or the fluid velocity: we consider a quasi-static system.¹

7.2 Long-range van der Waals forces

The ideal gas law (the product of the pressure by the volume of the gas is constant at a given temperature) was already known since the middle of the eighteenth century when, in his PhD thesis of 1873, van der Waals found that the behavior of real gas near the liquefaction point was more accurately described by taking into account an attractive interaction between the molecules of the gas. The nature of this interaction was later determined by London (1930) under the name of *dispersion forces*. Electrically neutral molecules attract each other because of the fluctuations of their electronic cloud, which generates an instantaneous dipole moment at each molecule.

7.2.1 Pair interaction between molecules

We can easily derive the interaction potential between two molecules of type 1 and 2, as depicted on figure 7.2a on the facing page. In this simplified approach,² the first fluctuating dipole P_1 generates an electric field E_1 proportional to $P_1 r^{-3}$ at large distance (we compute *long-range* interactions) and for an infinite speed of light. E_1

¹In fact, the motion of the interacting materials only plays a role when the velocities approach the speed of light. In that case, a dissipative force called *Casimir friction* appears (Kardar and Golestanian, 1999; Zurita-Sánchez *et al.*, 2004; Volokitin and Persson, 2007, 2008).

²A more rigorous computation has to be done in the framework of quantum mechanics. We can have an insight of what happens in a quantum approach in an article by Feynman (1939). Citing his own words, “the negative charge distribution of each atom has its center of gravity moved slightly toward the other. It is not the interaction of these dipoles which leads to van der Waals’ force, but rather the attraction of each nucleus for the distorted charge distribution of its *own* electrons [...]”

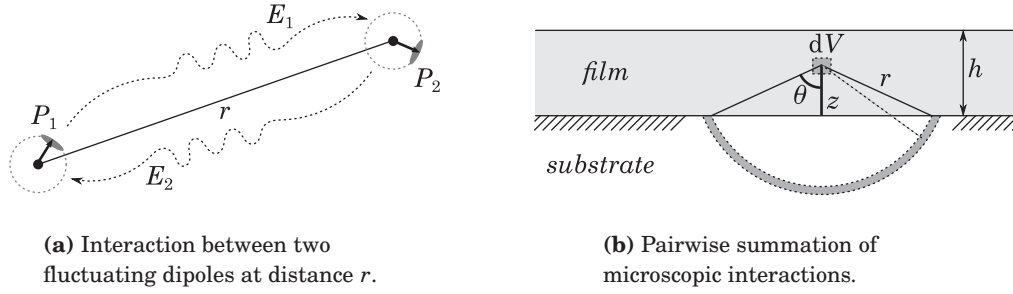


Figure 7.2 – Van der Waals force and Hamaker's theory.

induces a dipole P_2 at a second molecule. This second dipole is proportional to the electric field: $P_2 \propto E_1$, and generates a field E_2 back to the first dipole. This latter field is again proportional to $P_2 r^{-3}$, so eventually $E_2 \propto P_1 r^{-6}$. The interaction energy between the two dipoles is then proportional to $P_1^2 r^{-6}$. Consequently, even if the average of P_1 is zero, the average of P_1^2 is not, and the energy has a finite value of the form:

$$w = -\frac{C}{r^6}, \quad (7.1)$$

where C is a constant related to the polarizability of the interacting molecules.

7.2.2 Hamaker's theory

How can we compute van der Waals forces between macroscopic bodies? Hugo Christiaan Hamaker (1937) gave a first answer based on the concept of *pairwise summation*. The idea is the following.

We try to compute the macroscopic interaction between a flat film of thickness h having a density ρ_1 of molecules #1 per unit of volume, and a semi-infinite substrate of density ρ_2 of molecules #2 (Fig. 7.2b). We will assume that the total interaction is the sum of all pair interactions as describe above, in other words, that two molecules of the same type do not interact, and that many-body interactions (interactions between three or more molecules) are not significant. This assumption is called *pairwise summation*, or *additivity* of van der Waals forces, and will be discussed later. We consider a small volume dV of fluid at distance z from the substrate. The interaction of this volume with the substrate is:

$$\begin{aligned} dW &= -C\rho_1\rho_2 \int_z^\infty 2\pi \frac{r(1-\cos\theta)}{r^6} r dr \\ &= -\frac{\pi C\rho_1\rho_2}{6z^3}. \end{aligned} \quad (7.2)$$

So the total interaction per unit of surface should be found by integrating over the whole thickness:

$$W = \int_0^h -\frac{\pi C\rho_1\rho_2}{6z^3} dz, \quad (7.3)$$

but this expression yields an infinite energy. This is a common issue in dispersion force computation. To extract a finite energy, we have to recall that the interaction should be zero for a bulk film, in other words, when $h \rightarrow \infty$. So we can formally subtract this energy to equation (7.3), and find:

$$W = \int_h^\infty \frac{\pi C \rho_1 \rho_2}{6z^3} dz = \frac{\pi C \rho_1 \rho_2}{12h^2}. \quad (7.4)$$

If the disjoining pressure is defined by

$$\Pi(h) = -\frac{\partial W}{\partial h}, \quad (7.5)$$

then we recover the well-known disjoining pressure of the form:

$$\Pi(h) = -\frac{A}{6\pi h^3}, \quad (7.6)$$

where the Hamaker constant is defined by $A = -\pi^2 C \rho_1 \rho_2$.

Although the h^{-3} dependence of the disjoining pressure, which was experimentally observed, was an important success, Hamaker's theory failed at predicting the constant A , especially for dense phases. The reason is that pairwise summation completely neglects many-body effects (Ninham and Parsegian, 1970a; Podgornik *et al.*, 2006). A more quantitatively robust theory was needed, and it was essentially developed by Evgeny Mikhailovich Lifshitz in the second half of the twentieth century.

7.2.3 Lifshitz' theory and the fluctuating sources

In a quantum approach, Casimir (1948) discovered that two perfectly reflecting metallic plates in vacuum attract each other, a phenomenon later referred as the *Casimir effect*. This force surprisingly arises out of the quantized fluctuating electromagnetic field between the plates. Casimir forces in real materials were later derived in a different framework by Lifshitz and Kosevich (1955); Lifshitz (1956). Lifshitz developed a theory based on classical electrodynamics, where fluctuating sources are introduced in Maxwell equations. At a given frequency and at a given location, the more absorbent the material is, the more significant the fluctuation. This property is an important result of statistical mechanics, called the *fluctuation-dissipation theorem*. Lifshitz employed complex dielectric functions that can represent metals as well as dielectrics, the absorption being related to the imaginary part of the dielectric function. The next step of the theory is that the fluctuating sources interact through an electromagnetic field. The power of Lifshitz theory is that the many-body interactions are all taken into account in the computation of this electromagnetic field. This field can be analytically derived in simple geometries such as planar media. The modern theory of van der Waals forces was finally presented in Dzyaloshinskii *et al.* (1961). Boyer (1968) eventually proved that the quantum approach of Casimir and the classical fluctuating approach of Lifshitz were equivalent.

Lifshitz and his colleagues were able not only to overcome the non-additivity problem of Hamaker's theory, but they provided a very practical way of computing the

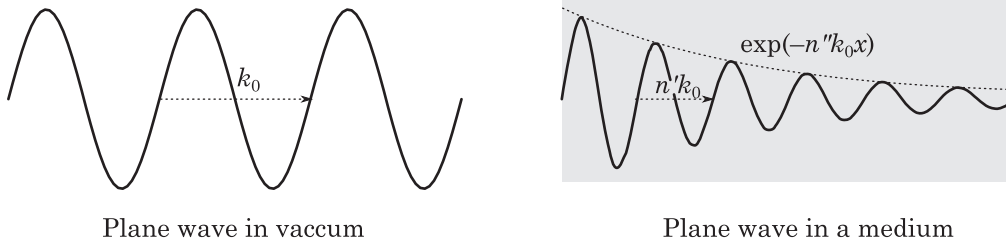


Figure 7.3 – Effect of complex refractive index $n = n' + in''$ on a plane wave.

forces: through the optical properties of materials. Lifshitz theory has been employed to compute the disjoining pressure in various situations (Ninham and Parsegian, 1970b; Ninham *et al.*, 1970; Donners *et al.*, 1977; Correa and Saramago, 2004). Has the modern theory been confirmed by experiment? A review of experimental measurements of Casimir forces can be found in Klimchitskaya *et al.* (2009). In spite of improving results (up to 5% agreement), it seems that the accurate computation of forces in realistic cases—non-planar media, corrugated surfaces (Emig *et al.*, 2003), unknown optical indices—is still a challenge to take up.

7.3 Dielectric functions

7.3.1 Macroscopic optical properties of materials

The accurate description of the optical properties of interacting media is a key factor to the computation of van der Waals forces. At a given angular frequency of light ω , the complex refractive index n of a material is the sum of a real part n' related to the velocity of propagation, and an imaginary part n'' , related to the absorption of light (figure 7.3):

$$n(\omega) = n'(\omega) + in''(\omega). \quad (7.7)$$

In electrodynamics framework, the *dielectric function*, ϵ defined by $\epsilon = n^2$ is more commonly employed:

$$\epsilon = \epsilon' + i\epsilon'' = n'^2 - n''^2 + 2in'n''. \quad (7.8)$$

A standard material presents an absorption spectrum similar to the one sketched on figure 7.4 on the next page. The loss in the infrared part corresponds to interactions with the vibrations of the bonds between molecules, whereas the loss in the ultraviolet part is due to the electronic transitions of the atoms or molecules. It turns out that it is this latter part that mostly account for van der Waals forces.

The imaginary part of the dielectric functions of various materials are reported on figure 7.5. The data is from Palik (1998) regarding silicon, silicon dioxide and water, and from Parsegian (2005) regarding polystyrene. In addition, the ultraviolet spectrum of polystyrene was studied by French *et al.* (2007). According to the authors, the first peak near 6 eV is due to the bounding of the aromatic rings, whereas the second bump above 10 eV is generated by the bounding of the carbon backbone.

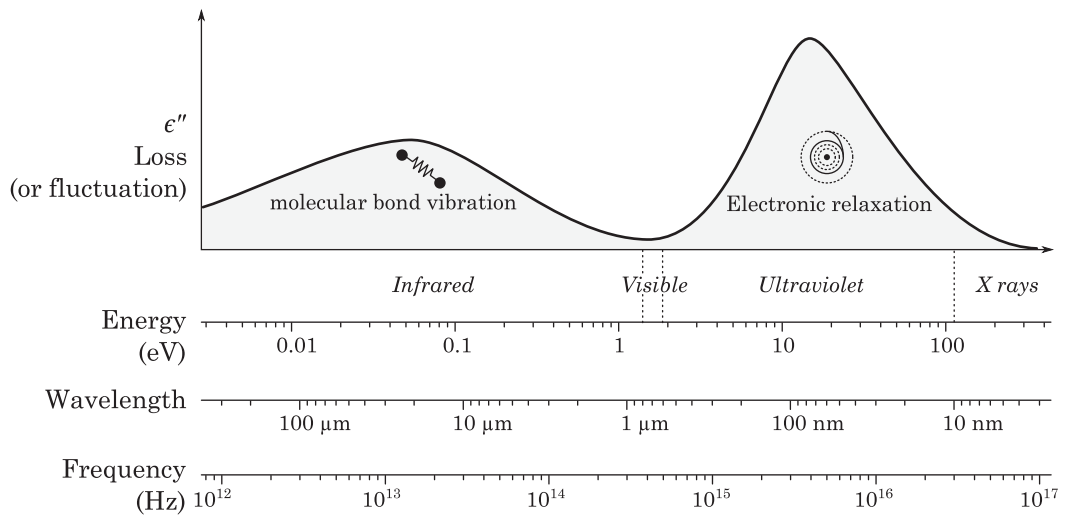


Figure 7.4 – Schema of the imaginary part of the dielectric function $\epsilon''(\omega)$ of common materials, represented with different scales: energy ($\hbar\omega$), wavelength ($2\pi c/\omega$) and frequency ($\omega/2\pi$).

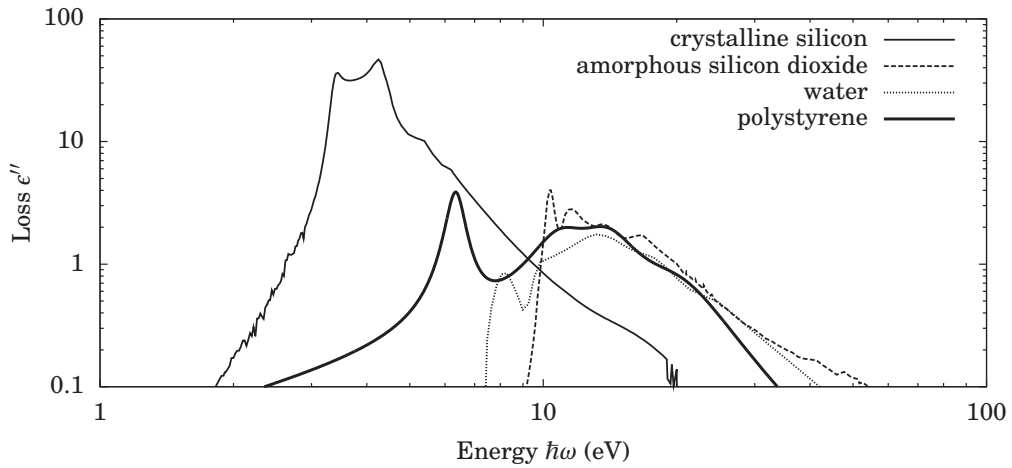
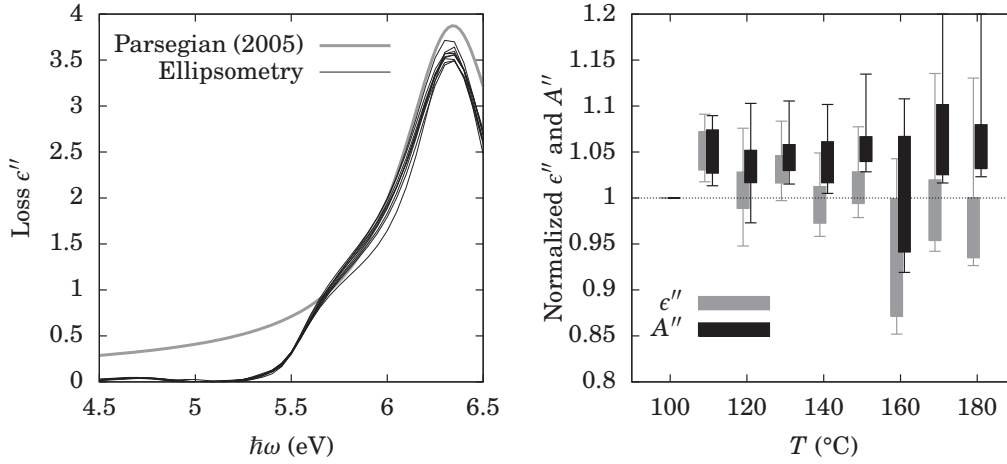


Figure 7.5 – Imaginary part of the dielectric function for various materials in the visible and ultraviolet spectrum. Sources: Si, SiO₂ and water from Palik (1998), polystyrene from Parsegian (2005).



(a) Experimental measurements of the dielectric function of polystyrene between 100°C and 180°C, and reference curve from Parsegian (2005).

(b) Imaginary part of the dielectric function normalized by its value at 100°C; same for $A(\omega)$.

Figure 7.6 – Temperature dependence of the dielectric function for polystyrene and test of the Clausius-Mossotti law.

7.3.2 Experimental measurements and temperature dependence

Using ellipsometry, we measured the optical index of polystyrene (molecular weight 30 kg·mol⁻¹) on the range 1.5 eV to 6.5 eV. Unfortunately, it was not possible to go over 6.5 eV with our equipment. The measurements were made at different temperatures. Results are reported on figure 7.6. Figure 7.6a shows the imaginary part of the dielectric function over the absorption range. The thick line is the reference index from Parsegian (2005). The thin lines are our measurements, each line corresponding to one temperature.

The effect of temperature is analyzed in the second graph 7.6b. At a given frequency ω , the temperature dependence of the dielectric function of a material can be modeled by the Clausius-Mossotti law:

$$\frac{\epsilon(T, \omega) - 1}{\epsilon(T, \omega) + 2} = \rho(T)A(\omega), \quad (7.9)$$

where $\rho(T)$ is the temperature-dependent density and $A(\omega)$ is a complex function related to the polarizability of the material. The meaning of this equation can be seen if density goes to zero: then the dielectric function is 1, as it is for vacuum. ϵ'' and A'' normalized by their value at 100°C are plotted on figure 7.6b. The first noticeable element is that ϵ'' depends weakly on temperature: the mean deviation is roughly 10% over a range of 80°C. We will see in section 7.5.3 if this dependence has a significant impact on van der Waals forces. The second element is that A'' seems to be constant,

at least above 110°C, as suggested by the Clausius-Mossotti law. Nevertheless, we cannot firmly conclude because of the large scattering of data.

7.4 Computation of van der Waals forces

Now that we have seen the optical properties of materials, we can proceed to the computation of the van der Waals forces. There are actually several equivalent methods to derive the forces. In this thesis, we used the same framework as in Henkel *et al.* (2000, 2002, 2004); Mulet (2003); Joulain *et al.* (2005). The method can be summarized as:

1. The instantaneous force is expressed in terms of the squared amplitude of the local electromagnetic field (Eq. 7.11).
2. The net force is assumed to be an ensemble average of the fluctuating force. The average fluctuating electromagnetic field can be expressed in terms of correlations of the field in the frequency space (Eq. 7.14).
3. The fluctuation-dissipation theorem gives the spectrum of the correlations in terms of imaginary parts of Green functions (Eq. 7.15).
4. The force is obtained by integrating the found distribution over the whole spectrum (Eq. 7.23).
5. The integration on the ω axis is found to be difficult numerically because of strong oscillations of the force distribution for thick films. The force distribution is expanded to the complex plane $\omega + i\xi$ and the integral over ω reduces to the sum of rapidly decreasing terms by use of the Cauchy's residue theorem (Eq. 7.29).

7.4.1 Maxwell stress tensor

From Maxwell's equations, it is possible to express the instantaneous electromagnetic force per unit of volume $\mathbf{f}(t)$, also known as the *Lorentz force*, as the divergence of a tensor minus a term proportional to the time derivative of the Poynting vector (Jackson, 1998; Ninham and Daicic, 1998; Pitaevskii, 2005, 2009; Raabe and Welsch, 2005, 2006a,b):

$$\mathbf{f}(t) = \nabla \cdot \mathbb{M} - \epsilon_0 \frac{\partial}{\partial t} (\mathbf{E} \times \mathbf{B}), \quad (7.10)$$

where ϵ_0 is the vacuum permittivity, \mathbf{E} the electric field, \mathbf{B} the magnetic field, and \mathbb{M} the *Maxwell stress tensor*, defined by:

$$\mathbb{M} = \epsilon_0 \mathbf{E}\mathbf{E} + \mu_0^{-1} \mathbf{B}\mathbf{B} - \frac{1}{2} (\epsilon_0 \mathbf{E}^2 + \mu_0^{-1} \mathbf{B}^2) \mathbb{1}, \quad (7.11)$$

with μ_0 the vacuum permeability. We also recall the useful relation:

$$\epsilon_0 \mu_0 = \frac{1}{c^2}, \quad (7.12)$$

with c the speed of light.

We see that the local stress is defined by the local electromagnetic field. The tensor product $\mathbf{E}\mathbf{E}$ can be expressed as the convolution of the Fourier transforms of the electric field:³

$$\begin{aligned}\mathbf{E}(t)\mathbf{E}(t) &= \frac{1}{4\pi^2} \int_{\omega} \int_{\omega'} \mathbf{E}(\omega)\mathbf{E}(\omega') e^{-i(\omega+\omega')t} d\omega d\omega' \\ &= \frac{1}{4\pi^2} \int_{\omega} \int_{\omega'} \mathbf{E}(\omega)\mathbf{E}^*(\omega') e^{-i(\omega-\omega')t} d\omega d\omega'.\end{aligned}\quad (7.13)$$

Under the assumption of ergodicity, we can express the average force as the ensemble average of the fluctuations:

$$\langle \mathbf{E}(t)\mathbf{E}(t) \rangle = \frac{1}{4\pi^2} \int_{\omega} \int_{\omega'} \langle \mathbf{E}(\omega)\mathbf{E}^*(\omega') \rangle e^{-i(\omega-\omega')t} d\omega d\omega'. \quad (7.14)$$

In statistical mechanics, the fluctuation-dissipation theorem can give the cross spectral correlation $\langle \mathbf{E}(\omega)\mathbf{E}^*(\omega') \rangle$ for a medium at homogeneous temperature T (See for example Joulain *et al.*, 2005):

$$\begin{aligned}\langle \epsilon_0 \mathbf{E}(t)\mathbf{E}(t) \rangle &= \frac{\epsilon_0}{4\pi^2} \int_{\omega} \int_{\omega'} 2\pi\delta(\omega-\omega')\mu_0\hbar\omega^2 \coth\left(\frac{\hbar\omega}{2k_B T}\right) \mathbb{G}''(\mathbf{r}, \mathbf{r}, \omega) e^{-i(\omega-\omega')t} d\omega d\omega' \\ &= \frac{1}{\pi c^2} \int_{-\infty}^{+\infty} \omega \Theta(\omega, T) \mathbb{G}''(\mathbf{r}, \mathbf{r}, \omega) d\omega,\end{aligned}\quad (7.15)$$

with δ the Dirac delta function, \mathbb{G}'' the imaginary part of the electric Green tensor defined below and $\Theta(\omega, T)$ the energy function derived from quantum mechanics:

$$\Theta(\omega) = \frac{\hbar\omega}{2} \coth\left(\frac{\hbar\omega}{2k_B T}\right), \quad (7.16)$$

with \hbar the reduced Plank constant and k_B the Boltzmann constant. The electric Green's tensor $\mathbb{G}(\mathbf{r}, \mathbf{r}')$ is the solution of the wave equation with a point source located at \mathbf{r}' :

$$\nabla \times \nabla \times \mathbb{G}(\mathbf{r}, \mathbf{r}') - k_0^2 \epsilon(\mathbf{r}) \mathbb{G}(\mathbf{r}, \mathbf{r}') = \delta(\mathbf{r} - \mathbf{r}') \mathbb{1}, \quad (7.17)$$

so that the electric field at \mathbf{r} is given by the current distribution $\mathbf{j}(\mathbf{r}')$:

$$\mathbf{E}(\mathbf{r}) = i\omega\mu_0 \iiint \mathbb{G}(\mathbf{r}, \mathbf{r}') \mathbf{j}(\mathbf{r}') d^3\mathbf{r}'. \quad (7.18)$$

The notation $\mathbb{G}''(\mathbf{r}, \mathbf{r}, \omega)$ is only formal, since in general the Green function has a singularity in $\mathbf{r}' \rightarrow \mathbf{r}$. It is often stated that this issue is solved by removing the contribution of the homogeneous Green tensor—the Green tensor of an infinite homogeneous medium—to the full Green tensor. However, in the case of a thin film, the singularity remains near the interfaces. In fact, exactly as in the pairwise summation (Eq. 7.3),

³With use of the property $f(-\omega) = f^*(\omega)$ if $f(t)$ is a real function, where $*$ denotes the complex conjugate.

we must remove the contribution of the infinite thickness case. Removing the diverging terms is the main issue in computing the van der Waals forces in arbitrary geometries, since there is no standard normalization method (we will come back to this in the conclusion of this chapter). Moreover, the physical meaning of infinite terms in Casimir-Lifshitz theory is the subject of controversies still living today.

Returning to the computation of the stress, for the fluctuations of the magnetic field, we have:

$$\langle \mu_0^{-1} \mathbf{B}(t) \mathbf{B}(t) \rangle = -\frac{1}{\pi} \int_{-\infty}^{+\infty} \omega^{-1} \Theta(\omega) \mathbb{H}''(\mathbf{r}, \mathbf{r}, \omega) d\omega, \quad (7.19)$$

where \mathbb{H} is the double curl of \mathbb{G} , such that for a constant vector \mathbf{x} , $\nabla_{\mathbf{r}} \times (\nabla_{\mathbf{r}'} \times (\mathbb{G}^T(\mathbf{r}, \mathbf{r}') \mathbf{x}))^T = \mathbb{H} \mathbf{x}$. Finally, let us consider the term $\frac{\partial}{\partial t} (\mathbf{E} \times \mathbf{B})$ in the Lorentz force (7.10). Because of the time derivative, this term introduces a $(\omega - \omega') \delta(\omega - \omega')$ factor that is always zero.

The final expression of the Maxwell stress tensor is:

$$\mathbb{M}(\mathbf{r}) = \int_{-\infty}^{+\infty} \frac{\Theta(\omega, T)}{\pi \omega} \mathbb{L}(\mathbf{r}, \omega) d\omega, \quad (7.20)$$

where

$$\mathbb{L} = \mathbb{K}'' - \frac{\text{Tr} \mathbb{K}''}{2} \mathbb{1}, \quad (7.21)$$

and

$$\mathbb{K}(\mathbf{r}, \omega) = \frac{\omega^2}{c^2} \mathbb{G}(\mathbf{r}, \mathbf{r}, \omega) - \mathbb{H}(\mathbf{r}, \mathbf{r}, \omega). \quad (7.22)$$

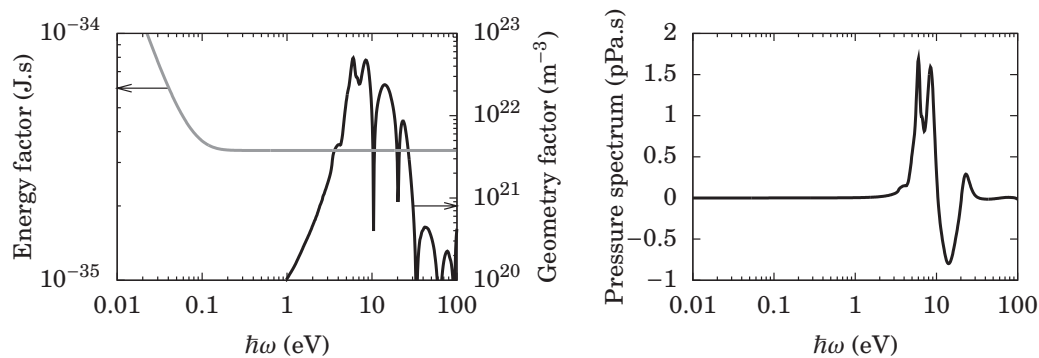
Or equivalently, the stress tensor is the integral over positive frequencies of the product of two terms:

$$\mathbb{M}(\mathbf{r}) = \int_0^{+\infty} \underbrace{\mathbb{L}(\mathbf{r}, \omega)}_{\text{geometry factor}} \underbrace{\coth\left(\frac{\hbar \omega}{2k_B T}\right) \frac{\hbar d\omega}{\pi}}_{\text{energy factor}}. \quad (7.23)$$

7.4.2 The issue of oscillating distribution

Formally, we could stop here and use equation (7.23) to compute the force. This was done by several authors (Henkel *et al.*, 2000, 2002, 2004; Mulet, 2003; Joulain *et al.*, 2005) who interpret the interaction ω -distribution in terms of attractive or repulsive modes. Following their example, we computed the disjoining pressure distribution in a 10 nm-thick polystyrene film on a silicon substrate at 100°C (see appendix D). Results are reported on figure 7.7 on the facing page. The geometry factor $\mathbb{L}(\omega)$ is the strongest in the ultraviolet range, in fact where the absorption of the media is significant (Fig. 7.7a). The energy factor $\frac{\hbar}{\pi} \coth\left(\frac{\hbar \omega}{2k_B T}\right)$ is almost constant above 1 eV. If we consider the final pressure distribution (Fig. 7.7b), we see indeed that some part of the distribution below 10 eV is positive, whereas some other part is negative between 10 eV and 20 eV.

Unfortunately, for thicker films, the distribution becomes strongly oscillating, as reported on figure 7.8. Because of these oscillations, the distribution becomes increasingly hard to integrate numerically. That is why a mathematical method has to be applied to compute the total force efficiently.



(a) Contributions from the energy factor $\frac{\hbar}{\pi} \coth\left(\frac{\hbar\omega}{2k_B T}\right)$ (left axis) and norm of the geometry factor $|\mathbb{L}(\omega)|$ (right axis).

(b) Pressure distribution.

Figure 7.7 – Disjoining pressure distribution in a supported 10 nm-thick polystyrene film, at 100°C.

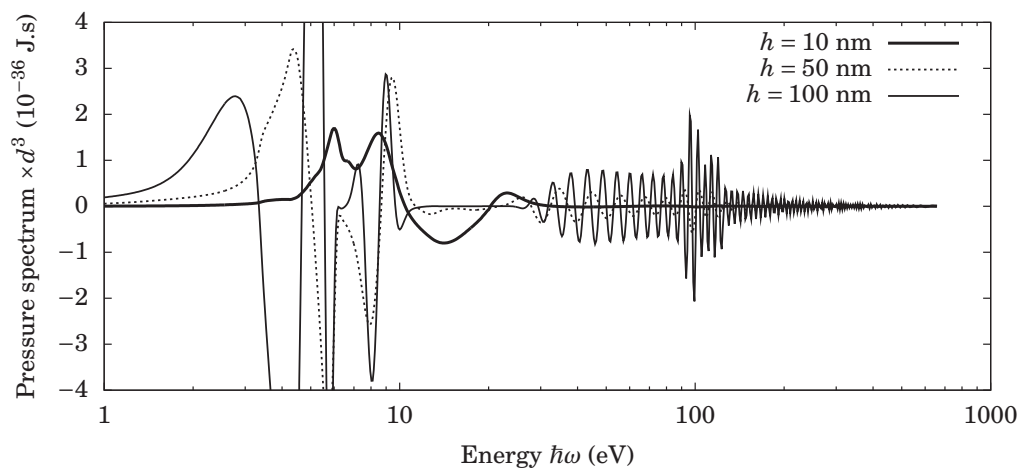


Figure 7.8 – Disjoining pressure distribution at 100°C in a supported polystyrene film of various thickness.

7.4.3 Integration in the complex plane

This method consists of expanding the pressure distribution in the complex plane and computing the integral over the ω frequencies as the sum of the residues of the distribution. Dielectric functions are given (and measured) in the positive and real axis ω , but for computation purpose, it is possible to expand these functions on the upper half complex plane of the variable $s = \omega + i\xi$. In references, $i\xi$ is called *imaginary frequency*, although it is rather a characteristic decay time than a frequency. This transformation is possible given the *Kramers-Kronig relations*: we assume that ϵ is a function of the complex variable s , and has no singularity on the upper half plane.⁴ Let $s_0 = \omega_0 + i\xi_0$ be a complex number with $\xi_0 > 0$. The function $\epsilon(s) - 1/s - s_0$ has a pole in s_0 , so the *Cauchy's residue theorem* gives:⁵

$$\oint \frac{\epsilon(s) - 1}{s - s_0} = 2\pi i (\epsilon(s_0) - 1), \quad (7.24)$$

with an appropriate path integration. For the integration, we choose the real axis because we can have experimental access to these values:

$$\epsilon(s_0) = 1 + \frac{1}{\pi} \mathcal{P} \int_0^{+\infty} \frac{\omega \epsilon''(\omega) - i s_0 (\epsilon'(\omega) - 1)}{\omega^2 - s_0^2} d\omega, \quad (7.25)$$

with the property $\epsilon(-\omega) = \epsilon^*(\omega)$. We will see that the dielectric function will have to be evaluated on the imaginary axis. In that case it takes the simple form:

$$\epsilon(i\xi_0) = 1 + \frac{2}{\pi} \int_0^{+\infty} \frac{\omega \epsilon''(\omega)}{\omega^2 + \xi_0^2} d\omega. \quad (7.26)$$

It turns out that $\epsilon(i\xi)$ is a smooth decreasing function taking real values, as we can see on figure 7.9 on the next page.

Now, what are the poles of the pressure distribution? If we consider the energy factor of equation 7.23, on the imaginary axis, we see that:

$$\coth\left(\frac{\hbar i \xi}{2k_B T}\right) = -i \cot\left(\frac{\hbar \xi}{2k_B T}\right), \quad (7.27)$$

which has poles at evenly spaced frequencies called the *Matsubara frequencies*:

$$\xi_n = \frac{2\pi k_B T}{\hbar} \times n, \quad n = 1 \dots \infty. \quad (7.28)$$

The residue of each pole is $2k_B T/\hbar$.⁶ By integration around all the upper half complex plane, as presented on figure 7.10, the Cauchy's residue theorem for the pressure distribution yields:

$$\mathbb{M}(\mathbf{r}) = \int_{-\infty}^{+\infty} \frac{\hbar}{2\pi} \coth\left(\frac{\hbar i \xi}{2k_B T}\right) \mathbb{L}(\mathbf{r}, \omega) d\omega = \sum' 2k_B T \mathbb{L}(\mathbf{r}, i\xi_n), \quad (7.29)$$

⁴This property is a consequence of causality, see Jackson (1998) or any reference book about electrodynamics.

⁵Cauchy's residue theorem only applies to functions that vanish at infinity, which is not the case for the dielectric function, ϵ , but which is the case for the *susceptibility*, $\epsilon - 1$.

⁶It can be recovered from the asymptotic development of the cotangent function: $\cot x = x^{-1} - x/3 - x^3/45 - \dots$

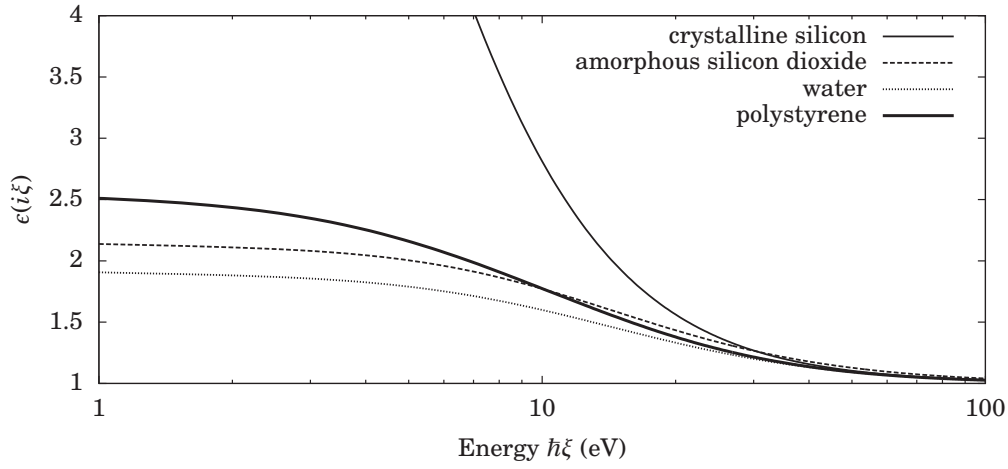
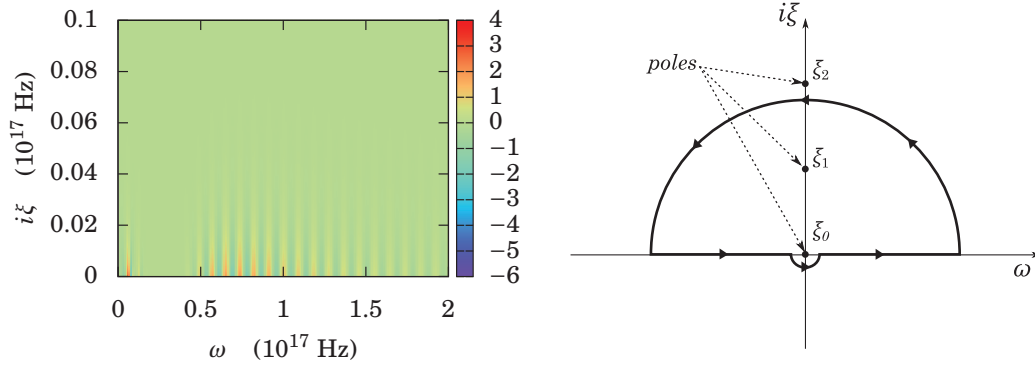


Figure 7.9 – Dielectric function on the imaginary axis for various materials (same source as in Fig. 7.5)



(a) Real part of the disjoining pressure distribution (arbitrary units) represented in the upper-right quarter complex plane. The function is oscillating near the ω axis, whereas it is a smooth function elsewhere.

(b) Integration path for the residue theorem. The disjoining pressure has poles at Matsubara frequencies (ξ_n).

Figure 7.10 – Integration of the disjoining pressure in the complex plane.

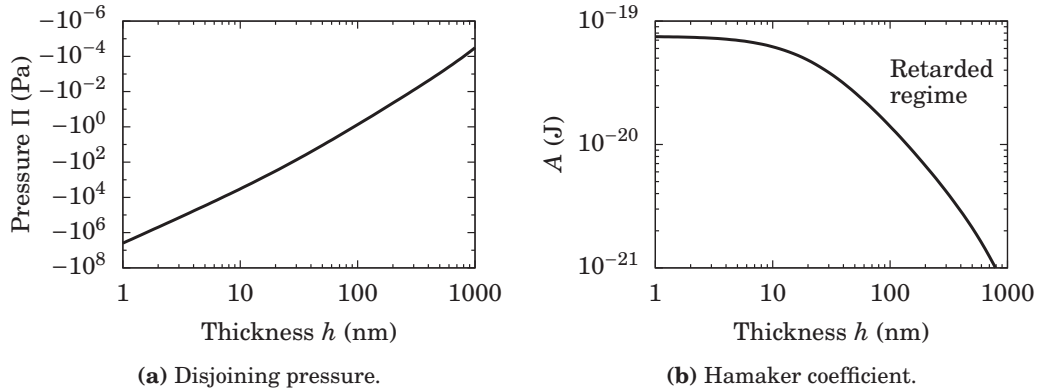


Figure 7.11 – Disjoining pressure and corresponding Hamaker coefficient as a function of thickness in a polystyrene film supported on a silicon substrate.

with the usual writing convention $\sum' x_n = \frac{x_0}{2} + \sum_1^\infty x_n$. The first pole ($n = 0$) is taken half-value because it lays on the integration axis. Instead of integrating along $\hbar d\omega$ energies (oscillating function), we sum $k_B T$ energies (smooth and rapidly decreasing terms).

7.5 Exact solution for planar geometry

The last step is to compute the Green functions in \mathbb{L} . This is a common problem of classical electrodynamics. For planar geometries it can be done analytically (Paulus *et al.*, 2000; Mulet, 2003) with use of the mathematical tools developed by Sipe (1987). The result is reported in appendix D.

7.5.1 Retarded regime

Keeping the same example system, we computed the disjoining pressure in a supported polystyrene film with thickness ranging from 1 nm to 1 μm . Results are reported on figure 7.11. In addition, we can plot the Hamaker *coefficient* (it is no longer a *constant*) defined by:

$$A(h) = -6\pi h^3 \Pi(h), \quad (7.30)$$

as done on figure 7.11b. We can see that even for this simple geometry, the Hamaker coefficient is not a constant nor a simple power law, but strongly decreases above 10 nm. This phenomenon is called *retardation*. The physical explanation is that, due to the finite speed of light, the interaction between media at a large distance is weakened. However, the Hamaker constant can be defined as the asymptotic limit for infinitely thin films. This limit value is called the *non-retarded Hamaker constant*.

Table 7.1 – Computation of the non-retarded Hamaker constant and comparison with literature values.

System	Non-retarded Hamaker constant ($ A $, 10^{-21} J)		
	This thesis	Israelachvili (1991)	Parsegian (2005)
PS vacuum PS	81	66	79
PS water PS	4.1	9.5 – 14	13
water vacuum water	53	37	55.1
SiC vacuum SiC	242	440	-
quartz vacuum quartz	78	65	66
quartz water quartz	3.0	8.3	1.6
gold vacuum gold	361	300 – 500	200 – 400
gold water gold	194	400	90 – 300

7.5.2 Comparison with literature values

We computed the non-retarded Hamaker constant in various systems, using optical indices from our own database. Results are reported on table 7.1 along with values from Israelachvili (1991) and Parsegian (2005). A good agreement with reference values was found.

7.5.3 Anisothermal force and temperature dependence

If the temperature is not homogeneous in the system, but assuming a local thermodynamic equilibrium (we can define a local temperature), then the fluctuation-dissipation theorem does not take the form of equation (7.15) any more. Instead, the fluctuations of the field at a location \mathbf{r} depend on the temperature distribution $T(\mathbf{r}')$ of the whole system. The fluctuation-dissipation theorem yields (Mulet, 2003):

$$\langle \epsilon_0 \mathbf{E}(\mathbf{r}, t) \mathbf{E}(\mathbf{r}, t) \rangle = \frac{1}{\pi c^4} \int d\omega \iiint d^3 \mathbf{r}' \omega^3 \Theta(\omega, T(\mathbf{r}')) |\mathbb{G}(\mathbf{r}, \mathbf{r}', \omega)|^2 \epsilon''(\mathbf{r}', T(\mathbf{r}'), \omega). \quad (7.31)$$

In particular, the fluctuation is stronger in areas of higher temperature, due to the factor $\Theta(T)$. However, the effect is significant only if temperature varies within the range of the force itself, which is less than a micrometer. Such high temperature gradients are not encountered in our case, as we saw in chapter 2.

We can still analyze the temperature dependence of the disjoining pressure in a film of homogeneous temperature. From equation (7.29), the temperature appears explicitly in the $k_B T$ factor and in the frequencies ξ_n of summation. We also saw in a previous section that the dielectric functions depend on temperature, so the Green functions may also implicitly depend on temperature. If we first consider the explicit dependence for increasing temperature, we can take the example of a 10 nm polystyrene film coated in a silicon wafer. Computation results at 100°C and 200°C are reported on figure 7.12 on page 135. Assuming that optical properties do not depend on temperature (we take the value at room temperature), we can see that there

is a competition between the $k_B T$ factor which increases pressure, and the ξ_n which realize a sparser sampling of the Green functions (Fig. 7.12a). However, it seems that these effects tend to cancel each other out when the total disjoining pressure is computed (Fig. 7.12b). The final difference between the two pressures is less than 0.5%.

Let us assume now that the dielectric function of polystyrene follows a Clausius-Mossotti relation (Eq. 7.9). When we compare the spectrum at 200°C computed with the dielectric function at room temperature to the spectrum at 200°C computed with the dielectric function corrected with the appropriate Clausius-Mossotti factor, then again the difference is barely visible (Fig. 7.12c and 7.12d). The total pressure difference is less than 2%, which is clearly negligible compared to the dramatic variation of viscosity over this range of temperature.

In conclusion, we can reasonably assume that van der Waals forces do not depend on temperature, for a given geometry. Temperature may affect van der Waals forces indirectly, for example by modifying the geometry through thermal expansion.

7.6 Approximation for long-wave topology

What happens for film with a deformed interface? If the wavelength of the deformation is large compared to the range of the force, then a zero-order approximation is to assume that the disjoining pressure at a given thickness $h(x)$ is the same as the pressure for an infinite planar film of thickness $h(x)$. This is called the *Derjaguin approximation*, or *proximity force theorem*, after Derjaguin (1936) (see figure 7.13). Note that the amplitude of the perturbation can be large. This approximation is the equivalent of the lubrication theory we saw in previous chapters.

Using pairwise summation, Dai *et al.* (2008) derived a second order term as a function of the first and second derivatives of the thickness, but the zero-order Derjaguin approximation is already enough for practical applications.

7.7 Conclusion and open problems

In this chapter, we presented a method to compute the long-range van der Waals forces in a thin film. The modern theory makes use of the optical properties of the interacting materials and the Green functions for the propagation of the electromagnetic waves. Since the theory was first presented by Lifshitz more than fifty years ago, many challenging issues still remain.

For instance, the problem of computing van der Waals forces in arbitrary geometries is still unsolved. Mostly this is done within the Derjaguin approximation (see the numerous examples in Parsegian, 2005). Still, at first sight, the approach seems quite straightforward: we could use one of the already existing software to compute numerically the Green functions, since this is a classical problem in electrodynamics. The problem comes from the infinite terms that appear in the calculation. Remember that in the case of a thin film, we had to remove the infinite contribution for an infinitely thick film—in other words, the disjoining pressure is zero in a bulk

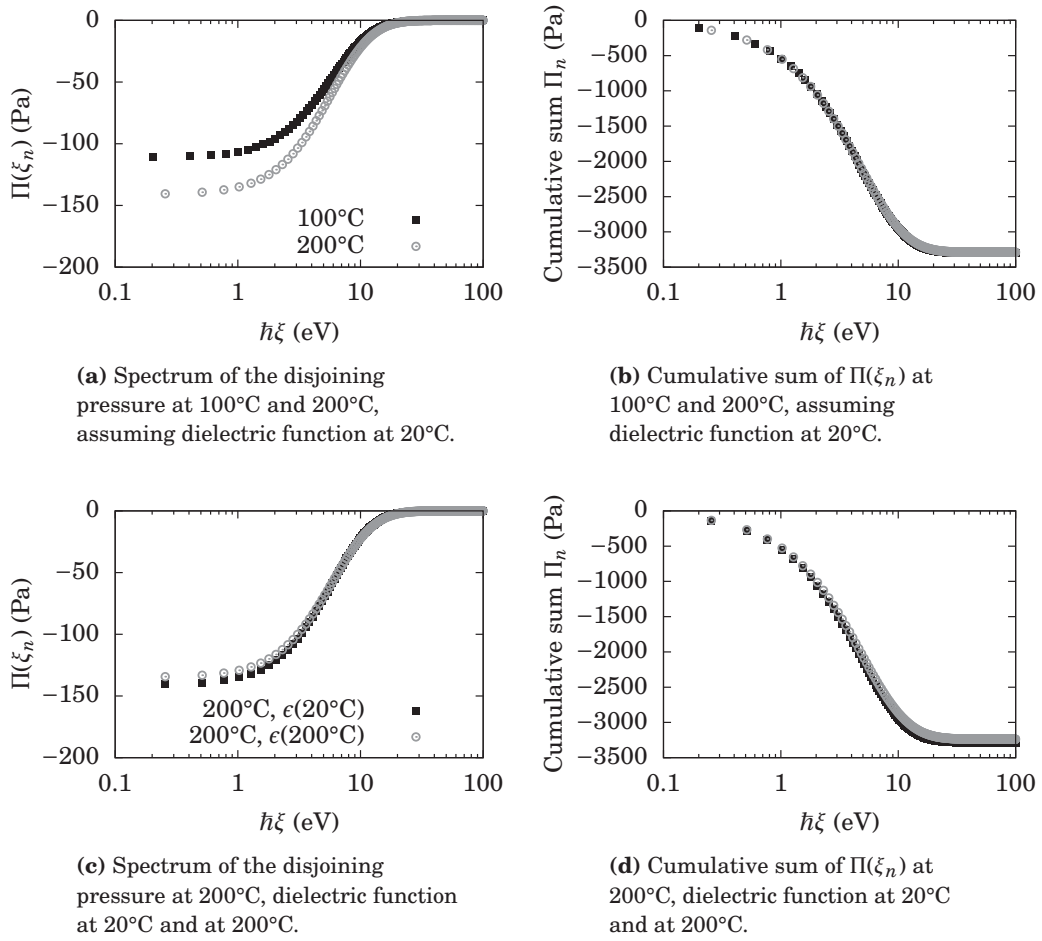


Figure 7.12 – Computation of the disjoining pressure in a 10 nm supported polystyrene film at 100°C and 200°C. The final difference is less than 2%.

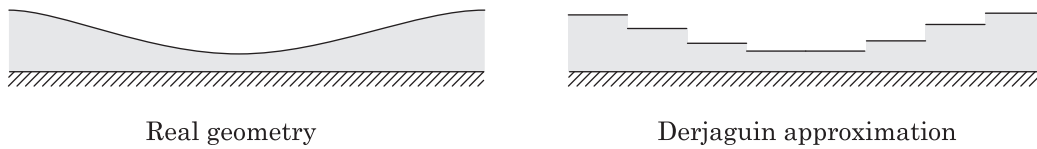


Figure 7.13 – Derjaguin approximation.

fluid. We can do it formally inside the analytical calculation. But in the case of a numerical computation, no standard normalization method has been proposed yet. Some authors recently published numerical methods to compute the Casimir force between objects of arbitrary shape (Golestanian, 2005; Rodriguez *et al.*, 2007, 2011; Veble and Podgornik, 2007; Xiong *et al.*, 2010; Johnson, 2010). Nevertheless, in their approaches, the force is integrated over the full objects which have to be at a finite distance from one another. For instance, it is not possible to compute the interaction of a fluid particle (localized point) with its complete environment, including its very neighbors.

A numerical method to compute the disjoining pressure in arbitrary geometries would be of great interest. For instance, it could be used to compute the disjoining pressure inside a capillary bridge, or near a triple line contact, not to mention the applications in chemistry or biology.

References

- T. H. Boyer. Quantum electromagnetic zero-point energy of a conducting spherical shell and the casimir model for a charged particle. *Physical Review* **174**, 1764–1776 (1968).
- H. Casimir. On the attraction between two perfectly conducting plates. In *Proc. K. Ned. Akad. Wet.*, volume 51, page 793 (1948).
- R. Correa and B. Saramago. On the calculation of disjoining pressure isotherms for nonaqueous films. *Journal of Colloid and Interface Science* **270**, 426–435 (2004).
- B. Dai, L. G. Leal, and A. Redondo. Disjoining pressure for nonuniform thin films. *Physical Review E* **78**, 061602 (2008).
- B. Derjaguin. Range of action of surface forces. *Nature* **138**, 330–331 (1936).
- W. A. B. Donners, J. B. Rijnbout, and A. Vrij. Calculations of van der waals forces in thin liquid films using lifshitz' theory. *Journal of Colloid and Interface Science* **60**, 540–547 (1977).
- I. E. Dzyaloshinskii, E. M. Lifshitz, and L. P. Pitaevskii. General theory of van der waals' forces. *Soviet Physics Uspekhi* **4**, 153–176 (1961).
- T. Emig, A. Hanke, R. Golestanian, and M. Kardar. Normal and lateral casimir forces between deformed plates. *Physical Review A* **67**, 022114 (2003).
- R. P. Feynman. Forces in molecules. *Physical Review* **56**, 340 (1939).
- R. H. French, K. I. Winey, M. K. Yang, and W. Qiu. Optical properties and van der waals-london dispersion interactions of polystyrene determined by vacuum ultraviolet spectroscopy and spectroscopic ellipsometry. *Aust. J. Chem.* **60**, 251–263 (2007).
- R. H. French, V. A. Parsegian, R. Podgornik, R. F. Rajter, A. Jagota, J. Luo, D. Asthagiri, M. K. Chaudhury, Y.-m. Chiang, S. Granick, S. Kalinin, M. Kardar, R. Kjellander, D. C. Langreth, J. Lewis, S. Lustig, D. Wesolowski, J. S. Wettlaufer, W.-Y. Ching, M. Finnis, F. Houlihan, O. A. von Lilienfeld, C. J. van Oss, and T. Zemb. Long range interactions in nanoscale science. *Reviews of Modern Physics* **82**, 1887 (2010).

- R. Golestanian. Lifshitz interaction between dielectric bodies of arbitrary geometry. *Physical Review Letters* **95**, 230601 (2005).
- H. Hamaker. The london-van der waals attraction between spherical particles. *Physica* **4**, 1058–1072 (1937).
- C. Henkel, K. Joulain, R. Carminati, and J. J. Greffet. Spatial coherence of thermal near fields. *Optics Communications* **186**, 57–67 (2000).
- C. Henkel, K. Joulain, J.-P. Mulet, and J.-J. Greffet. Radiation forces on small particles in thermal near fields. *Journal of Optics A: Pure and Applied Optics* **4**, S109–S114 (2002).
- C. Henkel, K. Joulain, J.-P. Mulet, and J.-J. Greffet. Coupled surface polaritons and the casimir force. *Physical Review A* **69**, 023808 (2004).
- J. N. Israelachvili. *Intermolecular and Surface Forces*. Academic Press Inc, 2nd revised edition edition (1991).
- J. D. Jackson. *Classical Electrodynamics*. John Wiley & Sons (1998).
- S. G. Johnson. Numerical methods for computing casimir interactions. *1007.0966* (2010).
- K. Joulain, J.-P. Mulet, F. Marquier, R. Carminati, and J.-J. Greffet. Surface electromagnetic waves thermally excited: Radiative heat transfer, coherence properties and casimir forces revisited in the near field. *Surface Science Reports* **57**, 59–112 (2005).
- M. Kardar and R. Golestanian. The "friction" of vacuum, and other fluctuation-induced forces. *Reviews of Modern Physics* **71**, 1233 (1999).
- G. L. Klimchitskaya, U. Mohideen, and V. M. Mostepanenko. The casimir force between real materials: Experiment and theory. *Reviews of Modern Physics* **81**, 1827 (2009).
- E. M. Lifshitz and A. Kosevich. Dan sssr 96, 963 (1954). *Zh. eksp. teor. fiz* **29**, 730 (1955).
- E. Lifshitz. The theory of molecular attractive forces between solids. *Sov. Phys. JETP* **2**, 73–83 (1956).
- F. London. Zur theorie und systematik der molekularkräfte. *Zeitschrift für Physik* **63**, 245–279 (1930).
- J.-P. Mulet. Modélisation du rayonnement thermique par une approche électromagnétique. rôle des ondes de surface dans le transfert d'énergie aux courtes échelles et dans les forces de casimir. PhD thesis, Université Paris XI Orsay (2003).
- B. W. Ninham. Long-range vs. short-range forces. the present state of play. *The Journal of Physical Chemistry* **84**, 1423–1430 (1980).
- B. W. Ninham and J. Daicic. Lifshitz theory of casimir forces at finite temperature. *Physical Review A* **57**, 1870 (1998).
- B. W. Ninham and V. A. Parsegian. van der waals interactions in multilayer systems. *The Journal of Chemical Physics* **53**, 3398–3402 (1970)a.
- B. W. Ninham, V. A. Parsegian, and G. H. Weiss. On the macroscopic theory of temperature-dependent van der waals forces. *Journal of Statistical Physics* **2**, 323–328 (1970).

- B. Ninham and V. Parsegian. van der waals forces: Special characteristics in lipid-water systems and a general method of calculation based on the lifshitz theory. *Biophysical Journal* **10**, 646–663 (1970)b.
- E. D. Palik. *Handbook of Optical Constants of Solids*. Academic Press (1998).
- V. A. Parsegian. *Van der Waals Forces: A Handbook for Biologists, Chemists, Engineers, and Physicists*. Cambridge University Press (2005).
- M. Paulus, P. Gay-Balmaz, and O. J. F. Martin. Accurate and efficient computation of the green's tensor for stratified media. *Physical Review E* **62**, 5797 (2000).
- L. P. Pitaevskii. Why and when the minkowski's stress tensor can be used in the problem of casimir force acting on bodies embedded in media. *arXiv:cond-mat/0505754* (2005).
- L. P. Pitaevskii. Van der waals forces and spatial dispersion. *Laser Physics* **19**, 632–635 (2009).
- R. Podgornik, R. H. French, and V. A. Parsegian. Nonadditivity in van der waals interactions within multilayers. *The Journal of Chemical Physics* **124**, 044709 (2006).
- C. Raabe and D.-G. Welsch. Casimir force acting on magnetodielectric bodies embedded in media. *Physical Review A* **71**, 013814 (2005).
- C. Raabe and D.-G. Welsch. Dispersive forces on bodies and atoms: A unified approach. *Physical Review A* **73**, 063822 (2006)a.
- C. Raabe and D.-G. Welsch. Lorentz-force approach to the casimir force. *Journal of Physics: Conference Series* **36**, 159–163 (2006)b.
- A. Rodriguez, M. Ibanescu, D. Iannuzzi, J. D. Joannopoulos, and S. G. Johnson. Virtual photons in imaginary time: Computing exact casimir forces via standard numerical electromagnetism techniques. *Physical Review A* **76**, 032106 (2007).
- A. W. Rodriguez, F. Capasso, and S. G. Johnson. The casimir effect in microstructured geometries. *Nat Photon* **5**, 211–221 (2011).
- J. E. Sipe. New green-function formalism for surface optics. *Journal of the Optical Society of America B* **4**, 481–489 (1987).
- G. Veble and R. Podgornik. The boundary element approach to van der waals interactions. *The European Physical Journal E: Soft Matter and Biological Physics* **23**, 275–279 (2007).
- A. I. Volokitin and B. N. J. Persson. Near-field radiative heat transfer and noncontact friction. *Reviews of Modern Physics* **79**, 1291 (2007).
- A. I. Volokitin and B. N. J. Persson. Theory of the interaction forces and the radiative heat transfer between moving bodies. *Physical Review B* **78**, 155437 (2008).
- J. L. Xiong, M. S. Tong, P. Atkins, and W. C. Chew. Efficient evaluation of casimir force in arbitrary three-dimensional geometries by integral equation methods. *Physics Letters A* **374**, 2517–2520 (2010).
- J. R. Zurita-Sánchez, J.-J. Greffet, and L. Novotny. Friction forces arising from fluctuating thermal fields. *Physical Review A* **69**, 022902 (2004).

Chapter 8

Dewetting dynamics

If one tries to spread a film of water onto a clean glass plate (or on the surface of glasses for instance), the result will not be a uniform film, unless it is thick enough¹ to be stabilized by gravity. The film beaks up instead, and water gathers into more or less numerous droplets. The rupture of the fluid film is called *dewetting*. In fact, we should talk about the rupture of the macroscopic film, because a thin molecular layer can remain on the substrate, as we will see below.

The stability of fluid films has been an active field of research regarding fundamental issues, such as intermolecular forces, as well as applications, such as industrial coatings processes, thin film patterning, or even the study of tear films between the eye and a contact lens. Extensive reports on dewetting can be found in the reviews by Bonn *et al.* (2009); Xue and Han (2011). In this chapter, we briefly present the main concepts of the dewetting of a thin film and discuss some particular aspects related to nanoimprint.

8.1 Main concepts

Spreading coefficient. As in the previous chapter, we consider the two configurations depicted in figure 8.1 on the next page: a film laying on a substrate, and a film confined between a substrate and a nanoimprint mold, the latter being often coated with an anti-sticking layer. In the case of a supported film, the *spreading coefficient*, S , is defined by:

$$S = \gamma_{\text{Sub}} - (\gamma_{\text{Sub-PS}} + \gamma_{\text{PS}}), \quad (8.1)$$

where γ_{Sub} , γ_{PS} and $\gamma_{\text{Sub-PS}}$ are the interfacial energies² of, respectively, the substrate with air, PS with air and the substrate with PS. If $S < 0$, then the substrate covered by a macroscopic PS film (Fig. 8.1a i) is in a higher state of energy than the dry substrate (Fig. 8.1a iii), and dewetting can occur. In the opposite case $S > 0$, the PS film is in a stable configuration. In the case of a film confined between the mold and a substrate,

¹Thicker than the capillary length we introduced in chapter 2: about 3 mm in this case.

²We saw in chapter 2 that the higher state of energy of molecules at interfaces is responsible for an energy per unit of surface or equivalently a tension (force) per unit of length.

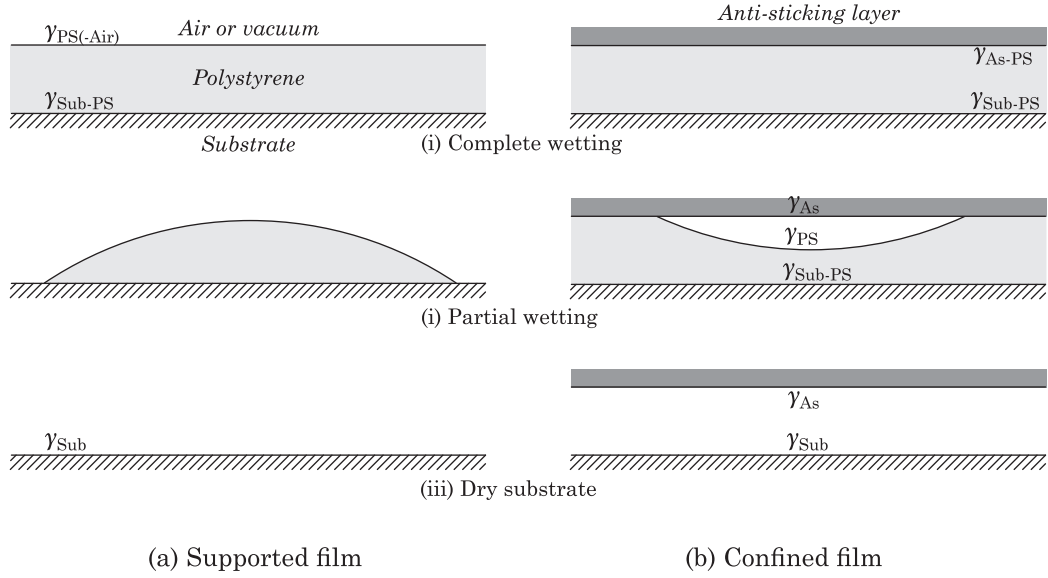


Figure 8.1 – Interfaces in two kinds of situations: (a) a supported film; (b) a confined film.

the spreading coefficient would be:

$$S = \gamma_{\text{Sub}} + \gamma_{\text{AS}} - (\gamma_{\text{Sub-PS}} + \gamma_{\text{AS-PS}}), \quad (8.2)$$

where γ_{AS} and $\gamma_{\text{AS-PS}}$ are the interfacial energies of, respectively, the anti-sticking (mold) with air, and the anti-sticking with PS.

Spinodal dewetting. Still, for sub-micrometer thin films, discussing the sign of the spreading coefficient appears to be incomplete. Indeed, in the previous chapter, we saw the role of long-range intermolecular interactions for the presence of a disjoining pressure. Assuming a thickness h of the film smaller than the capillary length, the free energy G of the film per unit of surface should write:

$$G(h) = W(h) + \gamma_{\text{Sub-PS}} + \gamma_{\text{PS}}, \quad (8.3)$$

with W the contribution of the intermolecular interactions (both short-range and long-range) vanishing for thick films ($W(\infty) = 0$). In order to realize $G(0) = \gamma_{\text{Sub}}$ and $G(\infty) = \gamma_{\text{Sub-PS}} + \gamma_{\text{PS}}$, the intermolecular energy should have the property $W(0) = S$.

We also mentioned in chapter 4 that the film is unstable if the disjoining pressure is a decreasing function of thickness, or, when the Hamaker approximation is employed, if the Hamaker constant A is negative. In the latter case, for a thickness that is large compared to the molecular length, the free energy of the film takes the form:

$$G(h) = \frac{A}{12\pi h^2} + \gamma_{\text{Sub-PS}} + \gamma_{\text{PS}}. \quad (8.4)$$

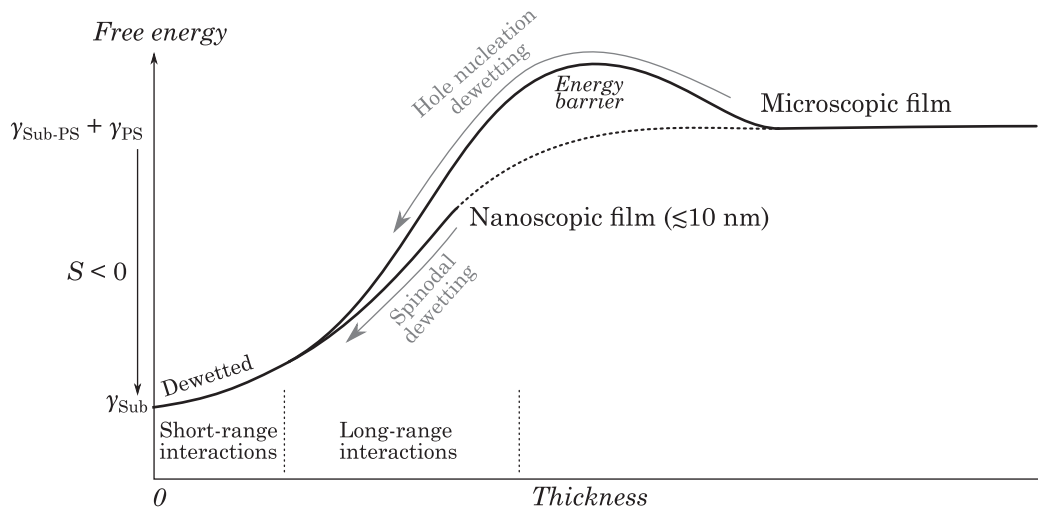


Figure 8.2 – Free energy of a supported polystyrene film, assuming a negative spreading coefficient ($S < 0$) and a negative Hamaker constant ($A < 0$), for thicknesses small enough to neglect gravity.

Now, let us consider the diagram plotted on figure 8.2. The dotted line corresponds to equation (8.4), which does not hold in short-range interactions area. Two processes of dewetting are represented:

1. If the film is thin enough, the free energy will be lowered by a spontaneous rupture due to long-range forces. This process is called *spinodal dewetting* (Vrij and Overbeek, 1968).
2. If the film is thicker, long-range force may be extremely weak and spinodal dewetting, although possible, extremely slow. But dewetting can still occur by the nucleation of holes in the film. However, nucleation phenomena require excess energy corresponding to the creation of additional free interface during the film deformation. Consequently, the film has to gain some energy in order to jump this energy barrier (Herminghaus and Brochard, 2006). This excess energy can be provided by thermal fluctuations or by defects such as dust, particles, or heterogeneous density.

We see that there are several situations that can exist, depending on the sign of the spreading coefficient and the shape of the W function. Some of them are reported on figure 8.3 on the next page, assuming a monotonic shape for the long-range forces:

- (a) $S < 0$ and $A < 0$ is the situation described above: spinodal dewetting can occur, leading to *partial wetting* of the substrate.
- (b) $S > 0$ and $A < 0$ Dewetting of the macroscopic film can occur, but a molecular film will remain.

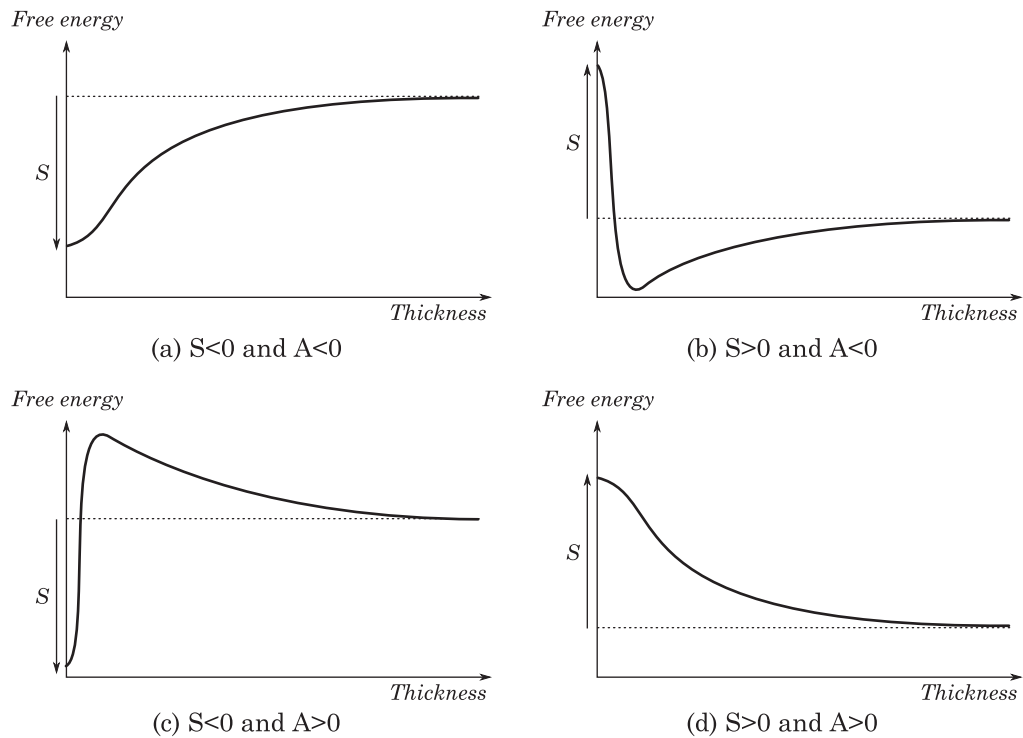


Figure 8.3 – Forms of the free energy of the film, assuming negligible gravity. (a) Partial wetting with dry areas; (b) Partial wetting with microscopic precursor film (c) Frustrated wetting (d) Complete wetting.

(c) $S < 0$ and $A > 0$ Dewetting can occur but only through nucleation. This situation is called frustrated wetting (Thiele *et al.*, 2001).

(d) $S > 0$ and $A > 0$ The film is stable and spreads completely on the substrate. This is called *complete wetting*.

Of course, many other situations are possible because the form of $W(h)$ can be more complicated, for example if the substrate is stratified.

8.2 Supported dewetting

8.2.1 Morphology

The dewetting of a polystyrene film on various substrates has been an experimental test case, probably because technologies for coating nanometric polymer films on wafers and characterization means have reached a mature state (Redon *et al.*, 1991; Reiter, 1993, 1992, 1998; Reiter *et al.*, 1999; Stange *et al.*, 1997; Karapanagiotis *et al.*, 2001). Using a statistical characterization of dewetting experiments, Meredith *et al.* (2000) identified three regimes for the dewetting of polystyrene on a silicon substrate, as depicted on figure 8.4 on the facing page:

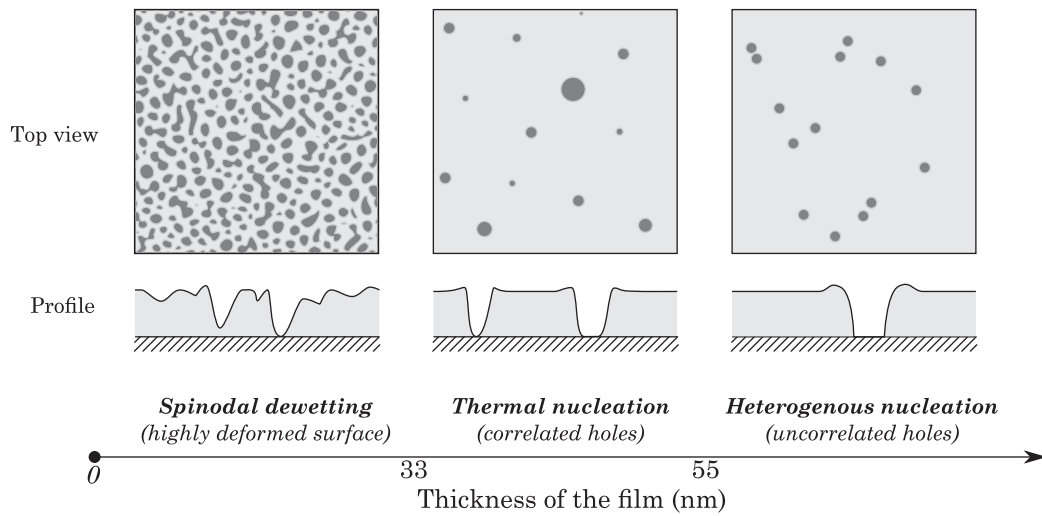


Figure 8.4 – Schematic view of the three regimes of dewetting polystyrene. **Left:** spinodal dewetting, the interface is highly deformed. **Middle:** thermal nucleation, the holes appear regularly and their positions are correlated. **Right:** heterogeneous nucleation, the holes are all present at the beginning of the dewetting process, and their position are uncorrelated.

1. For thin films ($h < 33$ nm), the interface is highly deformed, this is the spinodal regime.
2. For intermediate films ($33 \text{ nm} < h < 55$ nm), holes appear regularly in the film and their positions are correlated: this is the thermal nucleation regime. The thermal fluctuation of the interface creates local depressions that promote the rupture of the film. It can be viewed as a localized spinodal dewetting.
3. For thicker films ($h > 55$ nm), holes are all formed at the beginning of the dewetting process, and their positions are uncorrelated: this is the heterogeneous nucleation regime. Their presence is explained by defects in the film.

Complementary theoretical and experimental studies brought a finer understanding of the processes, regarding viscoelastic behavior (Saulnier *et al.*, 2002; Gabriele *et al.*, 2006) or hole forming (Thiele, 2003; Tsui *et al.*, 2003; Bertrand *et al.*, 2009, 2010).

In addition, Seemann *et al.* (2001a,b, 2005) were able to reconstruct the free energy as a function of thickness on the base of the morphology of the dewetting film. Steiner (2005) also proposed to use the morphology of dewetting patterns as a general thickness-dependent force³ measurement method. To see what role physical parameters play in the dynamics of dewetting, a stability analysis is done in the following subsection.

³Such as long-range intermolecular or electrostatic forces.

8.2.2 Growth rate in capillary wave theory

Using capillary wave theory, it is possible to extract the driving growth rate of supported dewetting (Oron *et al.*, 1997; Craster and Matar, 2009, p. 1165). Let us go back to the characteristic leveling time of a capillary wave of wavevector k (Eq. 4.27 on page 66), for a film of thickness h_0 :

$$\tau(k) = \frac{\eta h_0}{\gamma f(kh_0, \text{Ha}, \beta)}. \quad (8.5)$$

We already mentioned in chapter 55 that a negative Hamaker number can cause instability in the film (a negative leveling time being a growth rate). Features whose wavevectors are smaller than $k_c = \sqrt{|\text{Ha}|}/h_0$ tend to grow exponentially, leading to the rupture of the film, while high frequency features are leveled (exponentially) by surface tension.⁴ However, in the destabilizing process, the wavevector for which the growth rate is the fastest will dominate, yielding a characteristic length in the dewetted patterns. The characteristic time has a minimum in:

$$k_d = \frac{1}{h_0} \sqrt{\frac{|\text{Ha}|}{2}}, \quad (8.6)$$

yielding a characteristic length:

$$\lambda_d = h_0 \sqrt{\frac{8\pi^2}{|\text{Ha}|}}. \quad (8.7)$$

Assuming a thin film dynamics ($k_d h_0 \ll 1$),⁵ the fastest growing time is then:

$$\tau_d = \frac{12\eta h_0}{\gamma \left(1 + 3\frac{\beta}{h_0}\right) \text{Ha}^2}, \quad (8.8)$$

or, in terms of the Hamaker constant,⁶ assuming a no-slip condition ($\beta = 0$):

$$\tau_d = \frac{48\pi^2 h_0^5 \gamma \eta}{A^2} \quad (8.9)$$

The dewetting time τ_d has to be compared to the time of the experiment. Although a system could be unstable (negative Hamaker number), if τ_d is much larger than the experimental time, no spinodal dewetting can be observed. We recover in equation (8.9) the physical parameters driving the instability: the Hamaker constant lowers the dewetting time whereas the thickness, surface tension and viscosity hinder

⁴We recall that the Hamaker number quantifies the competition between the long-range van der Waals forces and surface tension.

⁵In practice, the thin film dynamics assumption is fairly reasonable ($k_d h_0 \ll 0.1$), mainly because $\text{Ha} \ll 1$.

⁶See Eq. (4.14) on page 60:

$$\text{Ha} = \frac{A}{2\pi h_0^2 \gamma}.$$

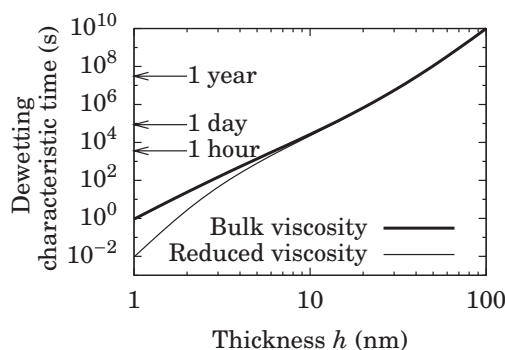


Figure 8.5 – Characteristic time of spinodal dewetting for PS 30k at 180°C coated on a silicon dioxide substrate.

the dynamics. In particular, we see the dramatic increase of the term h_0^5 as the thickness increases: that is why spinodal dewetting is observed only for very thin films, whereas the nucleation of holes is the prevailing dynamics for thicker films.

Figure 8.5 is an illustration of this property. The plot of the characteristic time of spinodal dewetting for polystyrene 30 kg·mol⁻¹ at 180°C supported on a silicon dioxide substrate shows that although the characteristic time is of the order of the minute for nanometric films, it blows up for thicker films. Fetzer *et al.* (2007) reported a dewetting dynamics faster than expected, which was explained by the influence of thermal fluctuation in the flow. We can also take into account the reduction of viscosity for very thin supported films we saw in chapter 3, as reported by equation (3.33) on page 48. This reduction also leads to a shorter dewetting characteristic time, and could contribute to accelerate the dynamics. However, accurate quantitative experimental studies are still needed to draw a conclusion on that subject.

8.2.3 Dewetting structured film

Until here, we focused only on the dewetting of planar films on planar homogeneous substrates. Although the patterns produced by the spinodal dewetting of a planar film can exhibit a characteristic length (Eq. 8.7), the position of the final droplets is not controlled. Still, the dynamics of dewetting is largely influenced by the initial shape of the polymer sample as well as of the substrate.

For example, a line of fluid on a non-wetting substrate undergoes a Plateau-Rayleigh instability that breaks the line into droplets. Recent experiments have been done at nanoscale by Schiff *et al.* (2011); Schleunitz *et al.* (2010) and it was shown that the resulting droplets can be organized by an initial modulation of the line. In another experiment, Luo *et al.* (2004) patterned a PS film using soft nanoimprint with a PDMS mold consisting in arrays of squares and rectangles (5 μm by 5 μm for the smallest). During annealing, they observed that the film dewets in a regular array of droplets of various dimensions governed by the imprinted pattern. Dewetting experiments on chemically or topologically patterned substrate were done by Kao *et al.* (2006); Kargupta and Sharma (2002); Mukherjee *et al.* (2008).

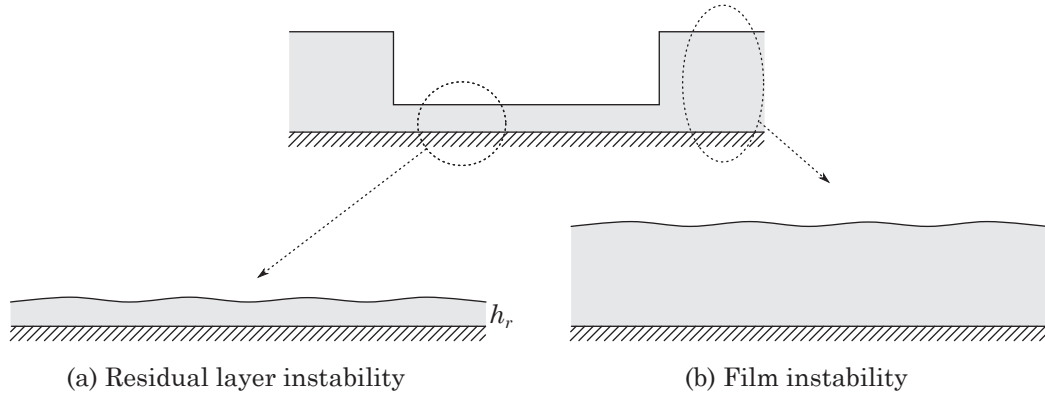


Figure 8.6 – Instability of a residual layer.

Let us turn our attention to the case of an imprinted pattern with a residual layer h_r . If the residual layer is thin, the global stability analysis of the previous subsection is not relevant any more. We can still make a local stability analysis considering a planar film of thickness h_r , as depicted on figure 8.6. This approach is valid only if the resulting characteristic instability wavelength λ_d is smaller than the extension of the residual layer area. In the case of a 5 nm PS film on a glass substrate (negative Hamaker number), we find⁷ $\lambda_d = 1.7 \mu\text{m}$. If the extension of the residual layer is smaller than λ_d , a full non-linear stability analysis has to be performed.

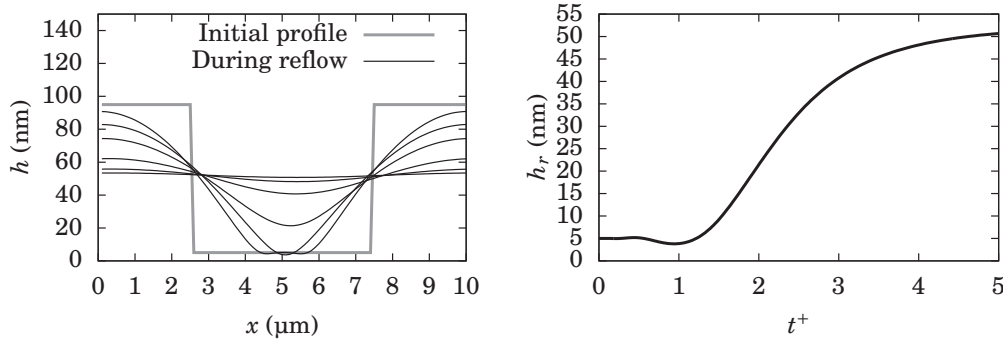
Now, because of the leveling of the global topology due to surface tension, the residual layer increases if no dewetting occurs in time. Reflow simulations⁸ of square profiles with a small residual layer, reported on figure 8.7 on the facing page, show that the value of the residual layer is almost constant within a duration of about τ , τ being the characteristic reflow time of the global shape (Eq. 8.5). For dewetting to take place, the characteristic time of local dewetting (related to the thickness h_r) has to be smaller than the characteristic time of leveling of the global structure (of fundamental wavevector k , related to the mean thickness h_0), in other words:

$$\frac{\tau_d}{\tau} = 4 \frac{h_r h_0^3 k^4}{\text{Ha}(h_r)^2} \approx 16\pi^2 \frac{\gamma^2 h_r^5 h_0^3 k^4}{A^2} < 1. \quad (8.10)$$

In this particular example, we find $\tau_d/\tau = 0.9$, which is a borderline case. However, this ratio decreases strongly if the residual layer is lowered a little or the size of the profile widened (decreasing k).

⁷With $\text{Ha} = -6.6 \times 10^{-4}$, figure 4.3 on page 60.

⁸See appendix B on page 189.



(a) Simulation of the reflow of a 10- μm -long square profile with a residual layer of 5 nm (assuming no dewetting).

(b) Residual layer h_r as a function of the normalized time $t^+ = t/\tau$.

Figure 8.7 – Simulation of the evolution of the residual layer in a flowing film not subject to dewetting.

8.3 Confined dewetting

8.3.1 State of the art

Although many studies have been published on the dewetting of supported films, few authors have reported observations on confined dewetting of nanometric films. In the next chapter, we will see that several methods have been presented to achieve nanoimprints with negligible residual layers, but the way the polymer clears under the protrusions is still unknown to a large extent. Kim and Lee (2003) presented an experimental method to dewet locally a polystyrene film (thickness around 100 nm) by indenting the film with PDMS tips. Nevertheless, this setup is different from the one investigated in this thesis: first, a tip is a sharp object while we use planar molds, and second, PDMS is soft compared to silicon, and the tip may crush into the film, changing the flow dynamics as we will see in the next chapter.

Other interesting results were obtained by Chou *et al.* (1999); Harkema *et al.* (2003); Landis *et al.* (2008). They observed that a plate approaching a fluid polymer film can attract the material to form pillars. This phenomenon named *capillary bridge*, appears only under definite circumstances (thickness of the polymer film, distance between the polymer and the top plate...). Verma *et al.* (2006) simulated the instability dynamics and showed that numerous patterns can be obtained depending on the ratio of the polymer thickness and the interstitial gap, and long-range intermolecular interactions. However, what happens in the absence of an interstitial gap, in other words, when the space between the two plates is filled by the polymer, as shown on picture 8.1b (i), remains unclear.

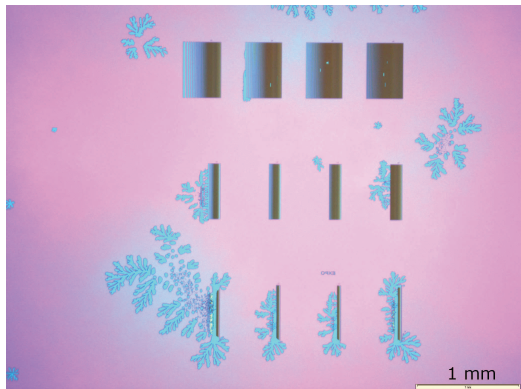
8.3.2 Evolution of the dewetted area.

Although we do not exactly know what mechanism allows the initial formation of dewetting areas under confinement, we can put forth hypotheses on how the dry areas grow. Schiff *et al.* (2001) reported that if some air is trapped between the polymer and the mold during nanoimprint, and if the imprint pressure is suddenly released, the dramatically expanding air bubbles form finger-like fractals, as those we can see in figure 8.8b on the next page. This phenomenon, referred to as Saffman-Taylor instability (Bensimon *et al.*, 1986; Sharon *et al.*, 2003), happens when a low viscosity fluid pushes against a more viscous fluid. The driving parameters are the ratio of viscosities, surface tension and the fluid velocity. Depending on these parameters, the fingers will be more or less narrow, and more or less ramified. In the case of an exploding air bubble, the fingering is due to the high velocity of the gas. However, we believe that a similar behavior can be obtained with low velocity but high viscosity, because velocity and viscosity act in the same way (Bensimon *et al.*, 1986, Eq. 1.7). In our case, it is not air that pushes against the polymer (imprints are made under vacuum), but it is rather the polymer that clears the confined area under capillary and long-range pressure. This could happen in a similar way to how fingers appear on holes in dewetting supported films which reach a critical radius (Thiele, 2003).

Images in figure 8.8 report such dewetting finger-like patterns. Image 8.8a shows an imprinted pattern in a PS film on a silicon substrate covered by silicon oxide. Millimetric Saffman-Taylor shapes formed during the nanoimprint process. Image 8.8b is a magnification of one of these shapes. More interesting are images 8.8c–f: we could observe Saffman-Taylor instability occurring in the residual layer. The shapes are much smaller than the instability outside the imprinted patterns. Surprisingly, they are bigger where the residual layer extends in a large area, and get smaller and denser as the period of the imprinted pattern decreases. No Saffman-Taylor instability was observed for residual trenches narrower than about 5 μm .

8.3.3 Conclusion

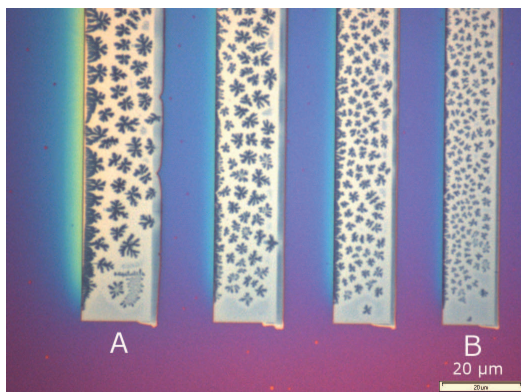
In this chapter, we reviewed the mechanisms of the dewetting of a thin polymer film. We made connections with the previous chapters to extract a characteristic of spinodal dewetting when surface tension tends to level the patterns. The next chapter concludes this part with attempts to tune the dewetting of residual layers in nanoimprint lithography. Indeed, new residual-layer-free nanoimprint processes can be considered with controlled dewetting.



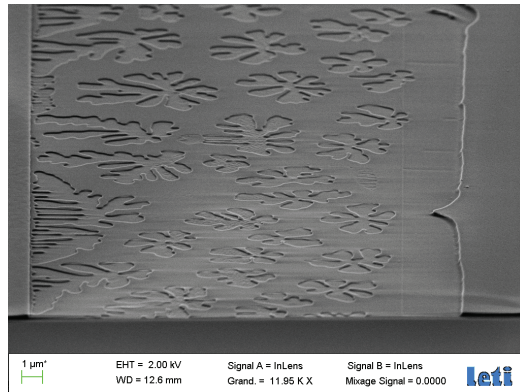
(a) Imprinted patterns in polystyrene.



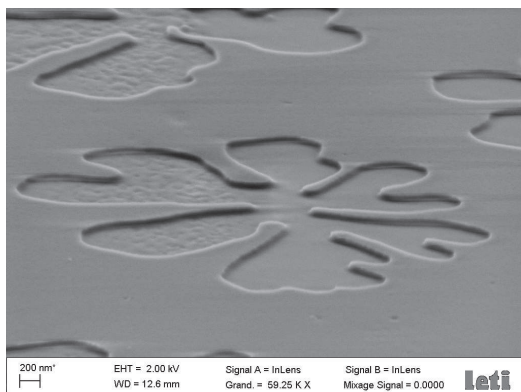
(b) Magnification of an instability outside the patterns.



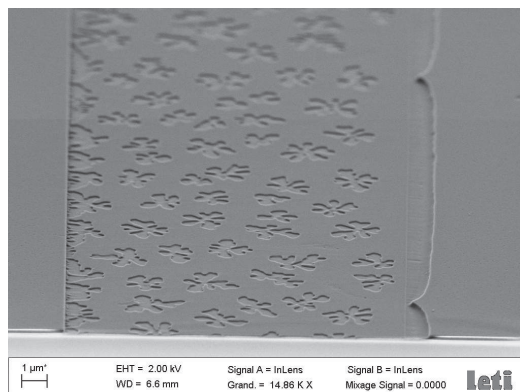
(c) Fingers formed in the residual layer.



(d) Magnification (SEM) of the residual layer (trench A).



(e) Magnification on fingers formed in the residual layer.



(f) Magnification (SEM) of the residual layer (trench B).

Figure 8.8 – Saffman-Taylor instability in a confined polystyrene film. Imprint conditions were: temperature 180°C, pressure 13 bar.

References

- D. Bensimon, L. P. Kadanoff, S. Liang, B. I. Shraiman, and C. Tang. Viscous flows in two dimensions. *Reviews of Modern Physics* **58**, 977–999 (1986).
- E. Bertrand, T. D. Blake, and J. De Coninck. Dynamics of dewetting at the nanoscale. *The European Physical Journal Special Topics* **166**, 173–176 (2009).
- E. Bertrand, T. Blake, and J. De Coninck. Dynamics of dewetting. *Colloids and Surfaces A: Physicochemical and Engineering Aspects* **369**, 141–147 (2010).
- D. Bonn, J. Eggers, J. Indekeu, J. Meunier, and E. Rolley. Wetting and spreading. *Reviews of Modern Physics* **81**, 739 (2009).
- S. Y. Chou, L. Zhuang, and L. Guo. Lithographically induced self-construction of polymer microstructures for resistless patterning. *Applied Physics Letters* **75**, 1004–1006 (1999).
- R. V. Craster and O. K. Matar. Dynamics and stability of thin liquid films. *Reviews of Modern Physics* **81**, 1131 (2009).
- R. Fetzer, M. Rauscher, R. Seemann, K. Jacobs, and K. Mecke. Thermal noise influences fluid flow in thin films during spinodal dewetting. *Physical Review Letters* **99**, 114503 (2007).
- S. Gabriele, P. Damman, S. Slavovs, S. Desprez, S. Coppée, G. Reiter, M. Hamieh, S. A. Akhrass, T. Vilmin, and E. Raphaël. Viscoelastic dewetting of constrained polymer thin films. *Journal of Polymer Science Part B: Polymer Physics* **44**, 3022–3030 (2006).
- S. Harkema, E. Schäffer, M. D. Morariu, and U. Steiner. Pattern replication by confined dewetting. *Langmuir* **19**, 9714–9718 (2003).
- S. Herminghaus and F. Brochard. Dewetting through nucleation. *Comptes Rendus Physique* **7**, 1073–1081 (2006).
- J. C.-T. Kao, A. A. Golovin, and S. H. Davis. Rupture of thin films with resonant substrate patterning. *Journal of Colloid and Interface Science* **303**, 532–545 (2006).
- I. Karapanagiotis, D. F. Evans, and W. W. Gerberich. Nucleation processes for dewetting initiation of thin polymer films. *Langmuir* **17**, 3266–3272 (2001).
- K. Kargupta and A. Sharma. Creation of ordered patterns by dewetting of thin films on homogeneous and heterogeneous substrates. *Journal of Colloid and Interface Science* **245**, 99–115 (2002).
- Y. Kim and H. Lee. Selective dewetting for general purpose patterning. *Advanced Materials* **15**, 332–334 (2003).
- S. Landis, N. Chaix, C. Gourgon, and T. Leveder. Quantitative characterizations of a nanopatterned bonded wafer: force determination for nanoimprint lithography stamp removal. *Nanotechnology* **19**, 125305 (2008).
- C. Luo, R. Xing, Z. Zhang, J. Fu, and Y. Han. Ordered droplet formation by thin polymer film dewetting on a stripe-patterned substrate. *Journal of Colloid and Interface Science* **269**, 158–163 (2004).

- J. C. Meredith, A. P. Smith, A. Karim, and E. J. Amis. Combinatorial materials science for polymer thin-film dewetting. *Macromolecules* **33**, 9747–9756 (2000).
- R. Mukherjee, D. Bandyopadhyay, and A. Sharma. Control of morphology in pattern directed dewetting of thin polymer films. *Soft Matter* **4**, 2086 (2008).
- A. Oron, S. H. Davis, and S. G. Bankoff. Long-scale evolution of thin liquid films. *Reviews of Modern Physics* **69**, 931 (1997).
- C. Redon, F. Brochard-Wyart, and F. Rondelez. Dynamics of dewetting. *Physical Review Letters* **66**, 715 (1991).
- G. Reiter. Unstable thin polymer films: rupture and dewetting processes. *Langmuir* **9**, 1344–1351 (1993).
- G. Reiter. Dewetting of thin polymer films. *Physical Review Letters* **68**, 75–78 (1992).
- G. Reiter. The artistic side of intermolecular forces. *Science* **282**, 888–889 (1998).
- G. Reiter, A. Sharma, A. Casoli, M.-O. David, R. Khanna, and P. Auroy. Thin film instability induced by long-range forces. *Langmuir* **15**, 2551–2558 (1999).
- F. Saulnier, E. Raphaël, and P.-G. de Gennes. Dewetting of thin polymer films near the glass transition. *Physical Review Letters* **88**, 196101 (2002).
- H. Schift, L. J. Heyderman, M. A. d. Maur, and J. Gobrecht. Pattern formation in hot embossing of thin polymer films. *Nanotechnology* **12**, 173–177 (2001).
- H. Schift, C. Spreu, A. Schleunitz, and J. Lee. Shape control of polymer reflow structures fabricated by nanoimprint lithography. *Microelectronic Engineering* **88**, 87–92 (2011).
- A. Schleunitz, C. Spreu, J. Lee, and H. Schift. Fabrication of ordered nanospheres using a combination of nanoimprint lithography and controlled dewetting. *Journal of Vacuum Science & Technology B: Microelectronics and Nanometer Structures* **28**, C6M41 (2010).
- R. Seemann, S. Herminghaus, and K. Jacobs. Dewetting patterns and molecular forces: A reconciliation. *Physical Review Letters* **86**, 5534–5537 (2001)a.
- R. Seemann, S. Herminghaus, and K. Jacobs. Gaining control of pattern formation of dewetting liquid films. *Journal of Physics: Condensed Matter* **13**, 4925–4938 (2001)b.
- R. Seemann, S. Herminghaus, C. Neto, S. Schlagowski, D. Podzimek, R. Konrad, H. Mantz, and K. Jacobs. Dynamics and structure formation in thin polymer melt films. *Journal of Physics: Condensed Matter* **17**, S267–S290 (2005).
- E. Sharon, M. G. Moore, W. D. McCormick, and H. L. Swinney. Coarsening of fractal viscous fingering patterns. *Physical Review Letters* **91**, 205504 (2003).
- T. G. Stange, D. F. Evans, and W. A. Hendrickson. Nucleation and growth of defects leading to dewetting of thin polymer films. *Langmuir* **13**, 4459–4465 (1997).
- U. Steiner. Force measurements using capillary instabilities. *Journal of Polymer Science Part B: Polymer Physics* **43**, 3395–3405 (2005).
- U. Thiele. Open questions and promising new fields in dewetting. *The European Physical Journal E - Soft Matter* **12**, 409–416 (2003).

- U. Thiele, M. G. Velarde, and K. Neuffer. Dewetting: Film rupture by nucleation in the spinodal regime. *Physical Review Letters* **87**, 016104 (2001).
- O. K. C. Tsui, Y. J. Wang, H. Zhao, and B. Du. Some views about the controversial dewetting morphology of polystyrene films. *The European Physical Journal E - Soft Matter* **12**, 417–425 (2003).
- R. Verma, A. Sharma, I. Banerjee, and K. Kargupta. Spinodal instability and pattern formation in thin liquid films confined between two plates. *Journal of Colloid and Interface Science* **296**, 220–232 (2006).
- A. Vrij and J. T. G. Overbeek. Rupture of thin liquid films due to spontaneous fluctuations in thickness. *Journal of the American Chemical Society* **90**, 3074–3078 (1968).
- L. Xue and Y. Han. Pattern formation by dewetting of polymer thin film. *Progress in Polymer Science* **36**, 269–293 (2011).

Chapter 9

Towards tuned dewetting for residual-layer-free nanoimprint

As stated in the introduction of this thesis, the presence of a residual layer in the NanoImprint Lithography (NIL) process is at the root of many issues when nanoimprint is used to manufacture lithographic masks. An additional step (usually reactive ion etching) is required to remove the residual layer, jeopardizing the cost-effectiveness and throughput of NIL technology. Several attempts have been made to develop imprint processes without residual layer. In this chapter, we explore new residual-layer-free processes based on the dewetting of the residual layer.

We saw in the previous chapter that for very thin films, disjoining pressure becomes the driving force, and can lead to the breakup of the residual layer and the growth of dry areas on the substrate, a phenomenon referred to as spinodal dewetting. In this chapter, we will see how the disjoining pressure can be tuned by changing the materials of the substrate or of the mold.

9.1 Disjoining pressure engineering

9.1.1 Disjoining pressure in stratified media

It is rather straightforward to compute the disjoining pressure in a planar stratified medium based on expression (D.2) in appendix D. In this expression, the disjoining pressure is given as a function of the Fresnel equations of the interfaces, in other words, as a function of the reflective property of the interfaces. If we add some layers, we just need to modify these coefficients in order to take into account the new interfaces.¹ In optics, it is known that the influence of a coating layer on reflection is negligible when the thickness of this layer vanishes. On the contrary, if the coating layer is thick enough, the reflection properties are those of the coating material in a bulk form.

The disjoining pressure in a stratified medium behaves in a similar way, as sketched on figure 9.1. We imagine a layer between the polymer film and the silicon

¹Such coefficients are sometimes called *Fabry-Perot* coefficients

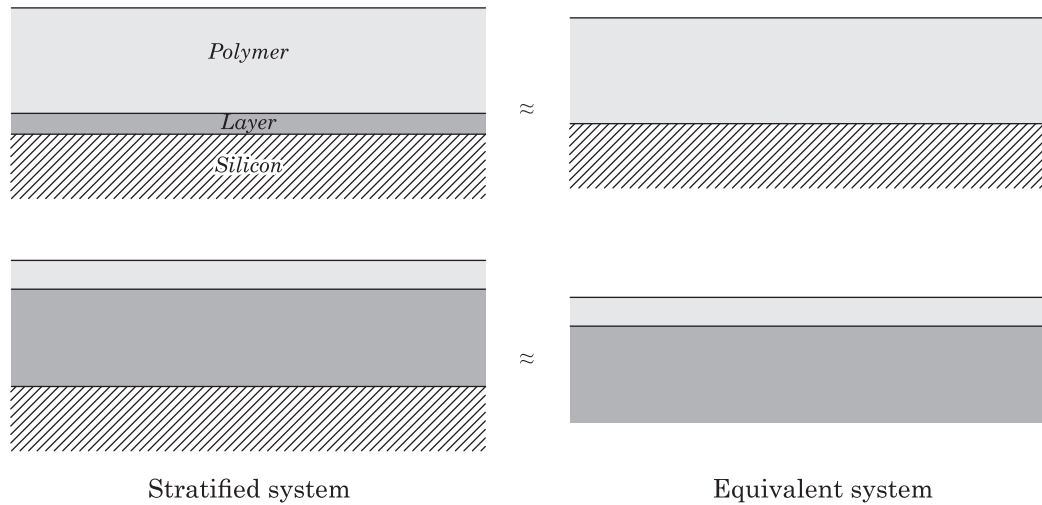


Figure 9.1 – Effect of a coating layer on the disjoining pressure, depending on its relative thickness. **Top:** if the polymer layer is much thicker than the coating layer, then the latter is negligible. **Bottom:** if the coating layer is much thicker than the polymer layer, then the effect of the underlying substrate is negligible.

substrate. If the polymer layer is much thicker than the coating layer, then the latter is negligible. On the contrary, if the coating layer is much thicker than the polymer layer, then the effect of the underlying substrate is negligible, and the polymer interacts only with the coating layer.

The idea is then to tune the disjoining pressure by choosing appropriate coating layers. In this chapter, we focus on the effect of a silicon oxide layer.

9.1.2 Role of silicon oxide

A native oxide layer forms on the surface of a silicon wafer in air. Its thickness is around 2 nm. Thicker oxide layers can be obtained through a reaction with an oxygen plasma. The role of a silicon oxide layer on the dewetting of a supported polystyrene film has already been emphasized by Seemann *et al.* (2001, 2005); Zhao *et al.* (2005). The authors observed that a thicker oxide layer enhances the spinodal dewetting of the film. Here, we computed the disjoining pressure using our own dielectric data for silicon, silicon dioxide and anti-sticking, and data from Parsegian (2005) for polystyrene (see chapter 7 and appendix D). The molecular weight of the polystyrene for viscosity data is assumed to be $M_w = 30 \text{ kg}\cdot\text{mol}^{-1}$.

Supported dewetting. Figure 9.2 on the facing page presents the effects of a silicon oxide layer covering a silicon substrate on the disjoining pressure in a supported polystyrene film, as sketched in figure 9.2a. The disjoining pressure is plotted on figure 9.2b. The pressure is negative and increases for a silicon substrate without oxide (stable polystyrene film), and strictly positive and decreasing for thick oxide layers

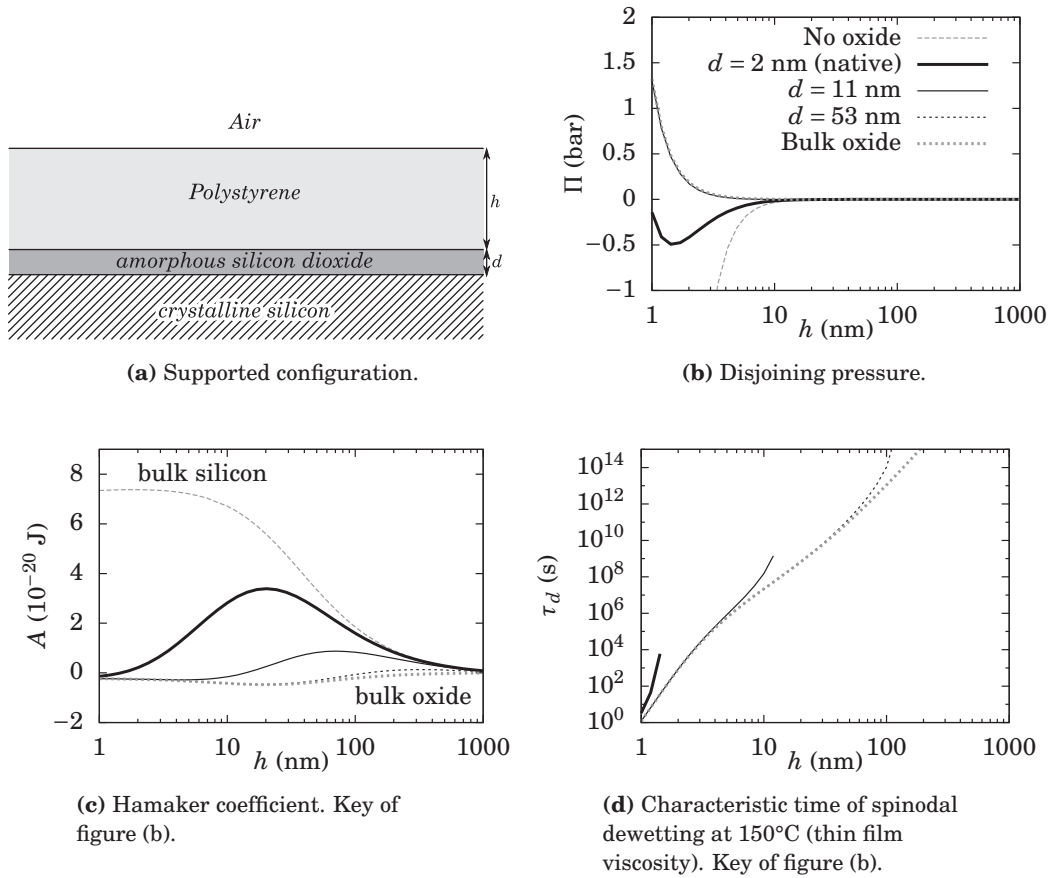


Figure 9.2 – Effects of a silicon dioxide layer covering a silicon substrate on the disjoining pressure in a polystyrene film ($M_w = 30 \text{ kg}\cdot\text{mol}^{-1}$) computed from the Lifshitz theory.

(unstable polystyrene film). Layers of thicknesses 11 nm and 53 nm can hardly be distinguished from the bulk oxide substrate. Silicon substrate with a native oxide layer has an intermediary shape: the disjoining pressure is first decreasing and then increasing, which should lead to an unstable film for a thickness lower than about 1.5 nm, and stability for thicker films. Here we already encounter a limit of our model. Indeed, we saw in chapter 8 that spinodal dewetting could be observed for thicknesses up to about 30 nm in various published research, and at least for 5-nm films in our experiments. This inaccuracy may come from inappropriate dielectric data for polystyrene, as we saw for example in figure 7.6a on page 125 of chapter 7, where the dielectric data of Parsegian (2005) mismatch our own measurements below 5.5 eV.

The Hamaker coefficient is plotted on figure 9.2c for reference, but the relevant information here is the characteristic time of spinodal dewetting² plotted on figure 9.2c. In this graph, we can see around 1.5 nm that thick oxide layers can accelerate dewetting by a factor 10 to 100, as it was qualitatively observed by Seemann *et al.* (2001, 2005); Zhao *et al.* (2005).

Confined dewetting. Figure 9.3 on the facing page presents the same previously discussed functions but in a confined configuration. The thicknesses of the anti-sticking layer and the underlying oxide layer was measured by ellipsometry. We must emphasize a strong assumption in our model: we were not able to measure the optical properties of the anti-sticking layer above 6.5 eV. Still, absorption peaks above 6.5 eV can play an important role in the disjoining pressure (Fig 7.5 on page 124 in chapter 7). That is why theoretical results presented here should be interpreted with care.

Let us focus directly on figure 9.3d. Here, the characteristic time of spinodal dewetting dramatically increases with decreasing thickness below 2 nm: this is the effect of increasing viscosity in confined configuration. Now, we see that there are two groups of curves: for bulk silicon substrate and native oxide, the film might be stable below about 20 nm, whereas for thicker oxide layers, the film might be unstable. It is also remarkable that no difference can be really made between those thick oxide layers below 10 nm. These computations suggest that a thick oxide layer could promote the dewetting of the residual layer during the imprint process.

The next two sections present experiments of both supported and confined dewetting of the residual layer.

²It is computed from the disjoining pressure using equations (8.8) on page 144 (characteristic time) and (3.33) on page 48 (thickness-dependent viscosity).

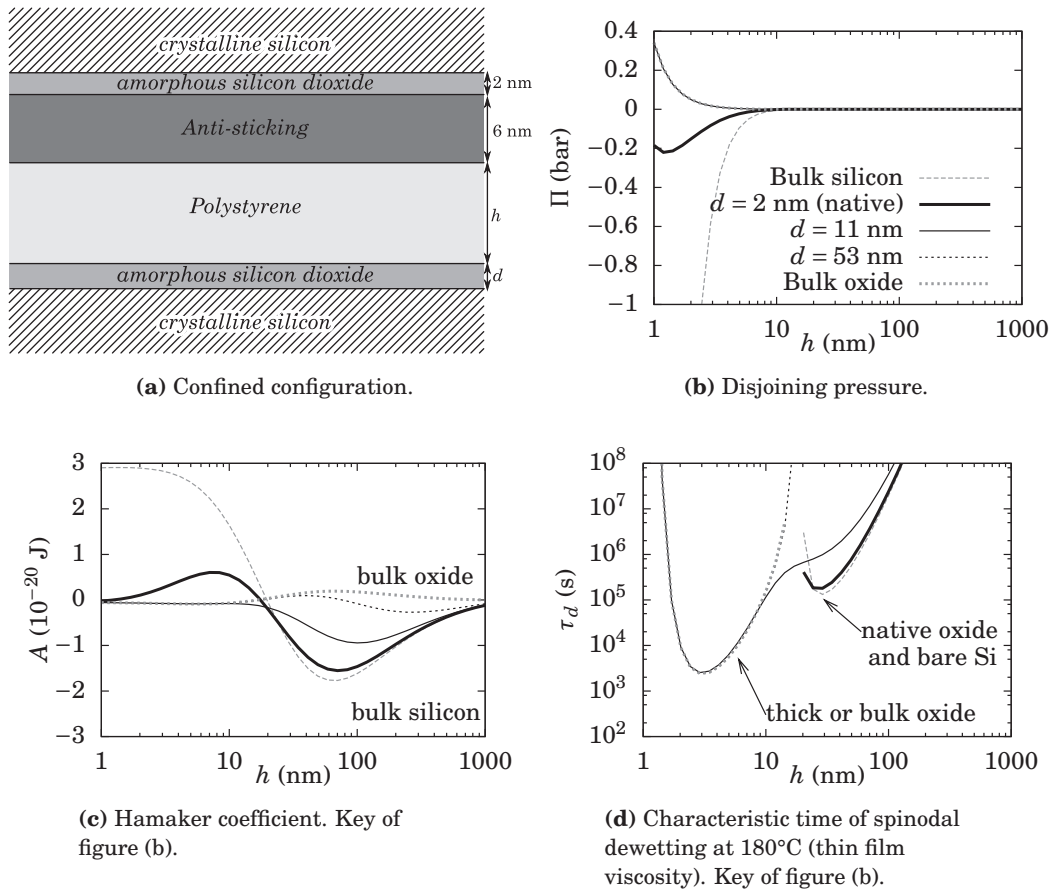


Figure 9.3 – Effects of a silicon dioxide layer covering a silicon substrate on the disjoining pressure in a confined polystyrene film ($M_w = 30 \text{ kg}\cdot\text{mol}^{-1}$) computed from the Lifshitz theory.

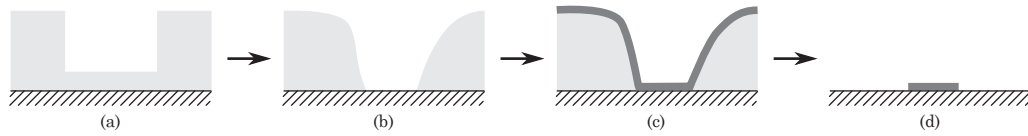


Figure 9.4 – Manufacturing process of metallic nanostructures: (a) Nanoimprinted polymer pattern; (b) Dewetting under annealing; (c) Metal deposition; (d) Lift-off of the polymer.

9.2 Supported dewetting experiments of the residual layer

9.2.1 Concept

In the previous chapter, section 8.2.3 on the dewetting of structured film, we saw that a nanoimprinted film can level or dewet depending on its initial topography. The idea here is to trigger the dewetting of the residual layer, while preventing the pattern from a complete reflow.

Regarding the disjoining pressure, it needs to be destabilizing for the residual layer, but stabilizing for the rest of the pattern. As a matter of fact, this latter property is not really important, because dewetting vanishes (as h^5) for thicker films. The contrast is even stronger if we take into account the reduction of viscosity, since the polymer in the residual layer will flow more rapidly (low viscosity) than in the rest of the pattern (high viscosity). We saw in the previous section that a native oxide layer is already a good promoter for dewetting, and the following experiments were carried out on that kind of substrate.

9.2.2 Manufacturing of metallic nanostructures

To implement this approach, we manufactured metallic nanostructures on silicon substrates with a native oxide layer. The process is the following (figure 9.4):

- (a) A pattern is nanoimprinted in polymer layer (here polystyrene 30 kg/mol) with a small residual layer. We used a 45-nm-deep mold with lines of pitches ranging from 100 nm to 30 μm . The residual layer was assessed to be of 5 nm.
- (b) The wafer is then heated above the glass transition temperature of the polymer. The thinnest parts of the polymer breakup, leading to the formation of a mask.
- (c) A metallic layer is coated on the wafer (here an Al-Ti alloy).
- (d) The polymer is dissolved in a solvent, leaving only metal in dewetted surfaces. This step is called *lift-off*.

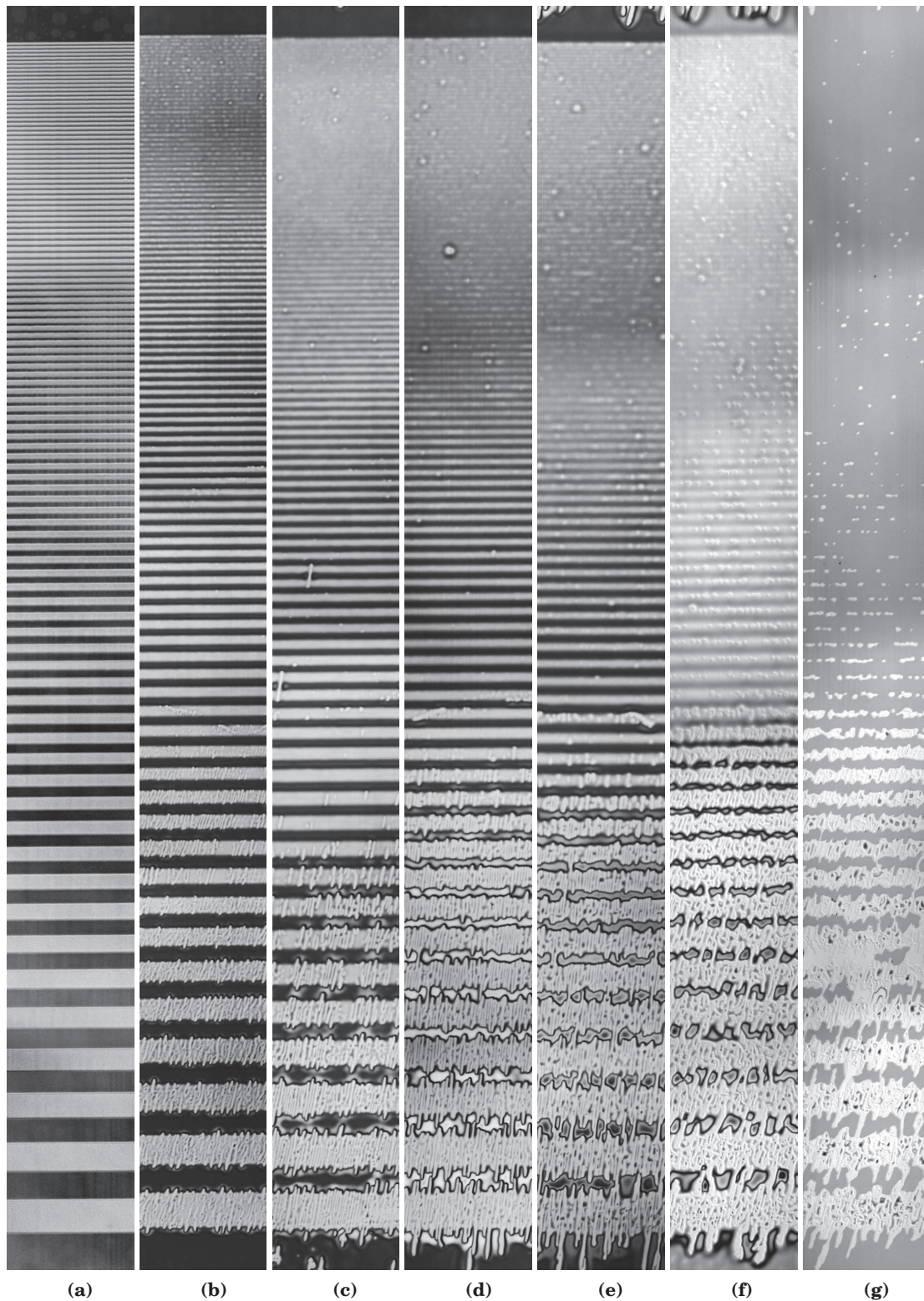


Figure 9.5 – Steps in the manufacturing of metallic lines, optical microscopy (scale bar — 15 μm). (a) Initial polymer pattern; (b) after annealing at 150°C during 4 min; (c) 8 min; (d) 16 min; (e) 32 min; (f) After metal deposition (Al-Ti); (g) After lift-off in toluene.

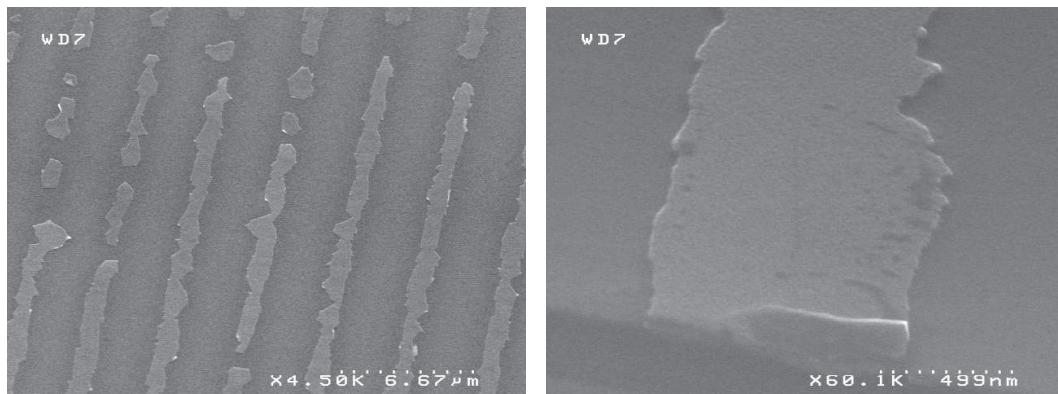


Figure 9.6 – Metallic lines after lift-off.

Optical images of the manufacturing process are collected in figure 9.5 on the previous page. Image (b)–(e) are pictures of the dewetting process. For the wider lines (bottom), dewetting occurred. The triple contact lines (edge of the dewetted areas) have a sharp contrast. We can also see that strong scratches appear as the dewetting time increases. The triple contact line follows those scratches, severely damaging the imprinted pattern, even causing its breakup. The dewetting dynamics is different for smaller lines. Surface tension overcomes dewetting and smooth the pattern, as we can see by the blurring effect of the annealing. However, some localized dewetted holes have formed, and are visible as metallic dots on picture (g).

Scanning Electron Beam (SEM) images of the metallic lines are presented on figure 9.6. The smallest regular lines have a width of about 1 μm . Note that this is close to the value of the critical dewetting wavelength found in section 8.2.3 of the previous chapter, which was of 1.7 μm on a glass substrate. Other smaller lines could be observed but the defectivity dramatically increases.

9.2.3 Conclusion and outlooks

The simple experiments presented above show that it is possible to manufacture metallic nanostructures by making use of the dewetting of the residual layer, in spite of many remaining issues. Surface roughness and surface properties influence the dewetting dynamics to a large extent. The smoothing effect of surface tension makes it difficult to form the thinnest features. Residual layer thickness homogeneity is also a key factor, as areas with a thicker residual layer will smooth more rapidly. Finally, for the evolution and coalescence of dry areas, it is important to have an accurate nanoscale description of the triple contact line, which is still a delicate issue today.

9.3 Dewetting experiments of the residual layer during imprint

9.3.1 Residual-layer-free nanoimprint: state of the art

Several attempts have been made to develop imprint processes without residual layer. The most straightforward one is probably to imprint the polymer and keep the pressure in order to expel the excess of fluid, until the residual layer vanishes. Although this method can be relevant in the case of very low viscosity resists, such as in UV-NIL (Lee, 2005; Lee and Jung, 2005), the time for the polymer to escape from the wafer is prohibitive in a common thermal NIL setup.

Other approaches are presented in figure 9.7a–c on the following page. In figure 9.7a, a process called *reversal imprint* (or inking) consists in filling the cavities of the mold, pressing the mold to the substrate and then demolding (Kao and Hong, 2011; Park and Cheng, 2009; Finn *et al.*, 2012). Another process presented in figure 9.7b, mainly developed by Bogdanski *et al.* (2006); Yang *et al.* (2009); Mayer *et al.* (2010) is called *partial cavity filling*. In this approach, the polymer is not coated thick enough to completely fill the cavities of the mold. During the process, a high pressure is thus continuously applied on the residual layer which reduces to a negligible thickness. Nevertheless, imprinted patterns are often damaged by capillary defects and unwanted dewetted areas can appear. A last concept is sketched in figure 9.7c. In this approach, a soft mold is used to imprint the polymer and clear the residual layer (Yoon *et al.*, 2004; Choi *et al.*, 2009). The mold has to have sharp (Kim and Lee, 2003) or rounded (Yoon *et al.*, 2011) protrusions in order to push the polymer away as the mold crushes against the substrate. Theoretical studies of the dewetting of a thin polymer film in this configuration (a hard substrate and a bendable mold) were also reported by Martin and Brochard-Wyart (1998); Martin *et al.* (2001). An example of this promising technique carried out in our group can be found in figure 9.8 on the next page. Here, SU-8 resist was imprinted by soft mold made of PDMS pyramids.

In this thesis, we investigated the concept presented in figure 9.7d. The amount of coated polymer is just enough to fill the mold, while targeting the smallest residual layer, as in classical NIL. The novelty of our approach is based on the addition of a layer covering the substrate. The overlaying material is chosen in order to promote the dewetting of the residual layer during the imprint process.

9.3.2 Complete filling with silicone oxide layers: experiments

To implement this approach, 142 nm of polystyrene (molecular weight 30 kg/mol) was coated on various 8-inch silicon substrates covered by a silicon oxide layer ranging from 2 nm (native oxide) to 532 nm. Table 9.1 reports the five different types of substrates, named from A to E. We used a 147-nm-deep mold with lines of pitches ranging from 100 nm to 30 μm . Imprints were made at 13 bars and 180°C during 15 min.

An overview of imprint results is given by figure 9.9. For each wafer, a series of images were taken in order to assess roughly the quality of the imprint. Surprisingly,

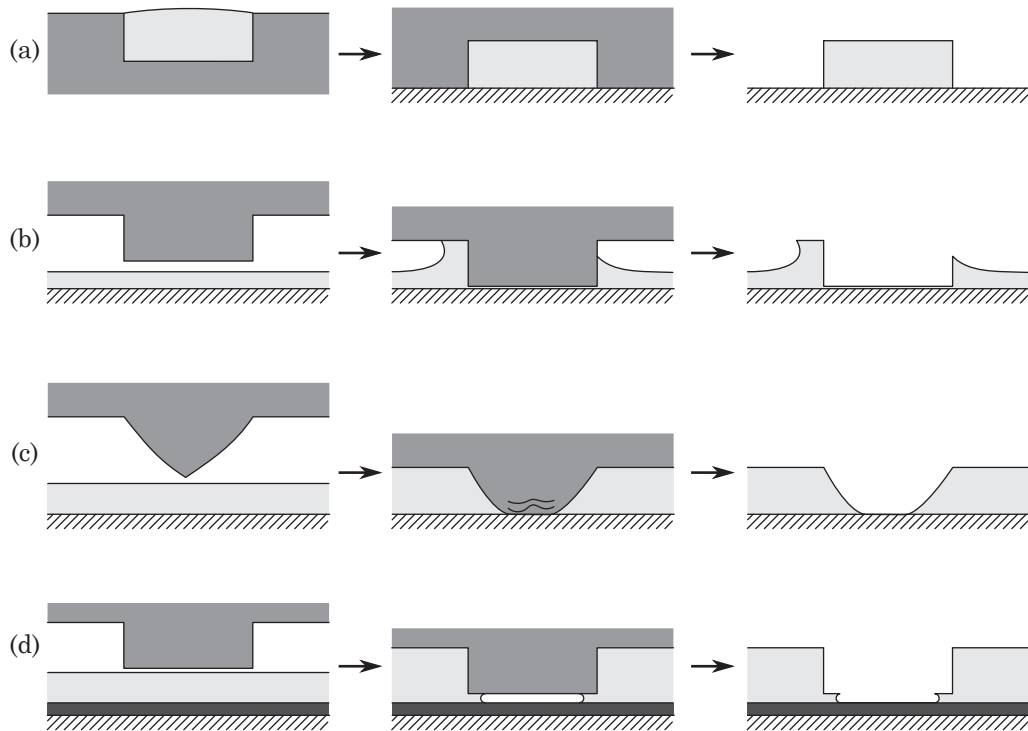


Figure 9.7 – Strategies for residual-layer-free nanoimprint processes: **(a)** Reversal imprinting; **(b)** Partial cavity filling; **(c)** Sharp soft mold; **(d)** Promoted dewetting.

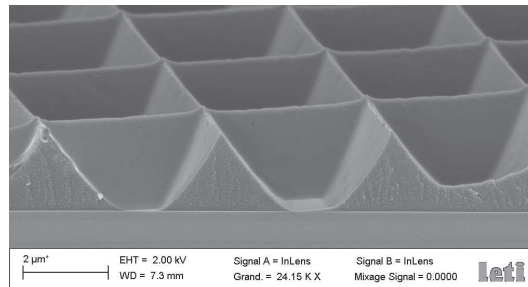


Figure 9.8 – Cross-sectional SEM image of a residual-layer-free nanoimprint of SU-8 resist. The mold is made of a soft PDMS pyramids.

Table 9.1 – Different types of silicon substrates covered by a silicon oxide layer.

Substrate type	Oxide layer thickness
A	2 nm (native)
B	11 nm
C	53 nm
D	105 nm
E	532 nm

wafers D and E (thickest oxide layers) exhibit strong capillary instabilities, whereas the computation of the disjoining pressure (Fig. 9.3d) showed no difference between bulk oxide and thicknesses of 11 nm and 53 nm.

Magnified optical images, such as those reported on figure 9.10 on page 165 for wafer E, present some patterns where no difference can be made between areas where we should have some residual layer and areas that dewetted by capillary defects. Indeed, a difference in thickness should imply a difference in color, and yet those areas have the same purple color. Fine characterization with SEM (figure 9.11 on page 165) tends to confirm that dewetting indeed occurred under the protrusions of the mold. In these top-view images, the same topography is found at the residual layer and at the bottom of dewetting finger-like patterns. However, the roughness of dewetted areas suggests that specks of polymer (probably of molecular size) still remain on the substrate.

Other SEM characterizations were performed and figures from 9.12 to 9.16 show tilted cross-section views of imprinted patterns. For each wafer, two images are presented: at the left side is a topographical image (secondary electrons) and at the right side is a chemical contrast image (selective back-scattered electrons, not sensitive to charging). On the latter images, each shade of gray represents a material (depending on the atomic numbers of its components). For example, we can clearly see on figure 9.16 the oxide layer in a darker gray than the silicon underneath. This property is interesting to localize the dewetted areas. Polystyrene is indeed pictured in very dark gray. On figure 9.12 (wafer with native oxide), we can see that the residual layer is still present, but display some holes, which might be a kind of dewetting through hole nucleation. On the contrary, on figures 9.13 to 9.16, the residual layer is captured in a lighter gray, which suggest that the polymer dewetted. However, the quantity of the remaining polymer could not be precisely assessed.

If we go back to section 9.1.2 where we presented numerical computations of the disjoining pressure. We found in figure 9.3d that a native oxide layer was not enough to promote the spinodal dewetting of a confined film. Moreover, an oxide layer of only 11 nm could make possible such dewetting. It is quite remarkable that these experiments tend to confirm the theoretical results .

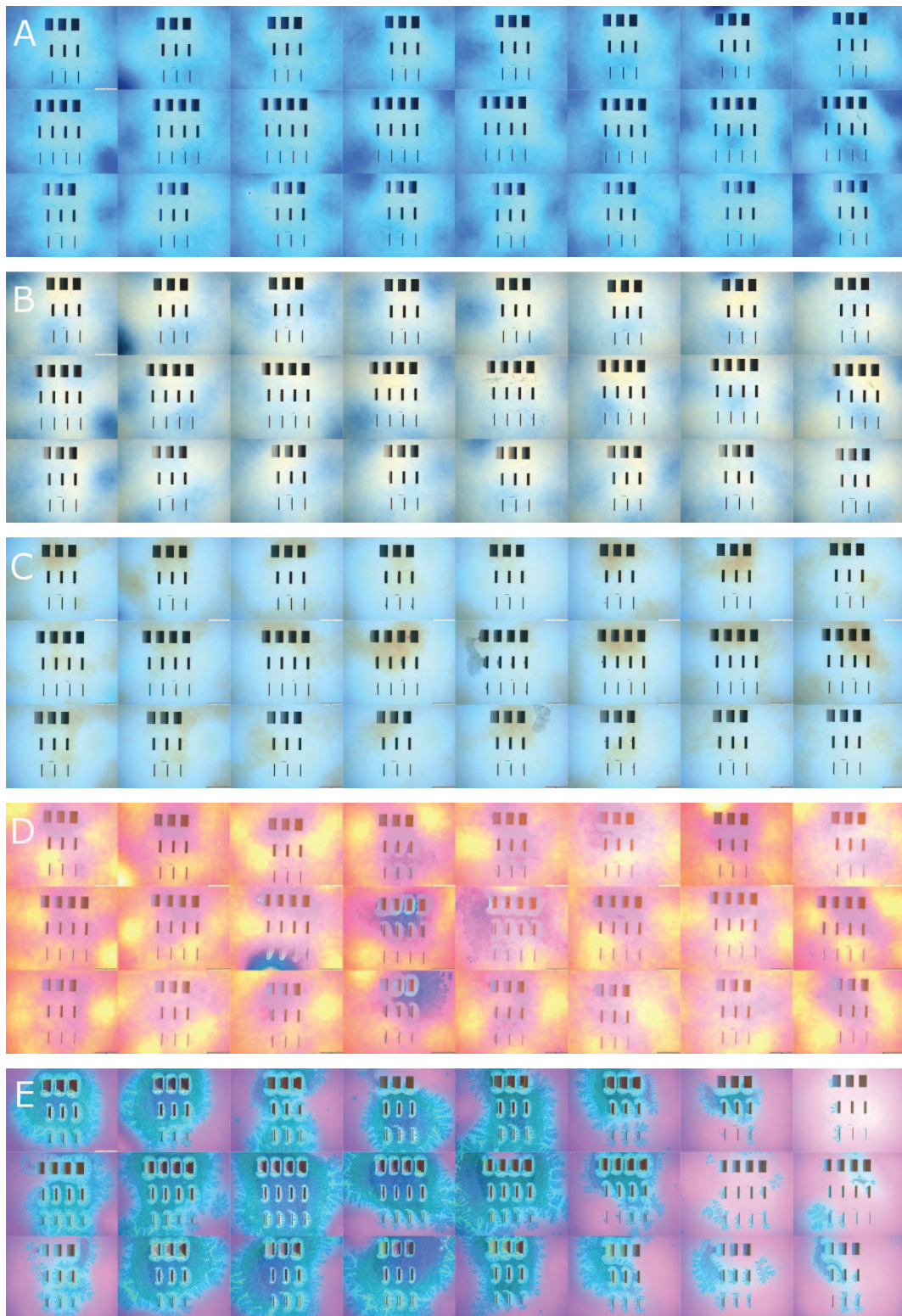


Figure 9.9 – Images (optical microscopy, scale bar — 5 mm) of nanoimprinted patterns on substrates A to E. Images are all taken on the same wafer for each type of substrate.

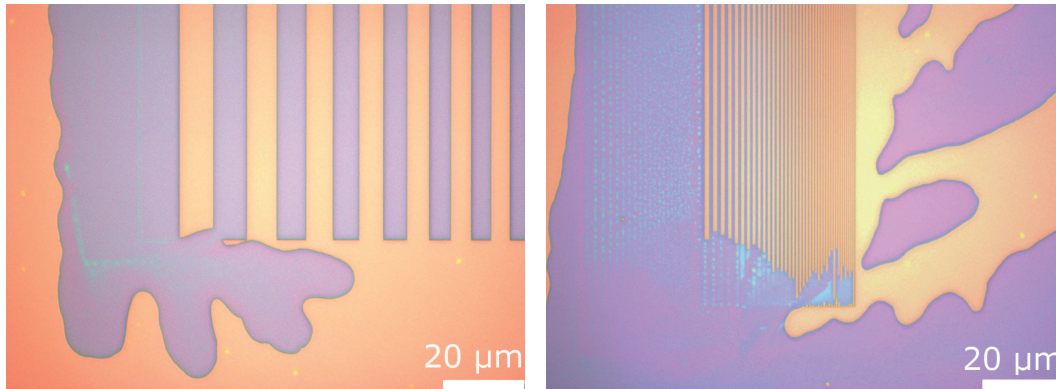


Figure 9.10 – Optical images of imprinted patterns and capillary defects, substrate E (532 nm). The same color is found for the residual layer and the dewetted areas.

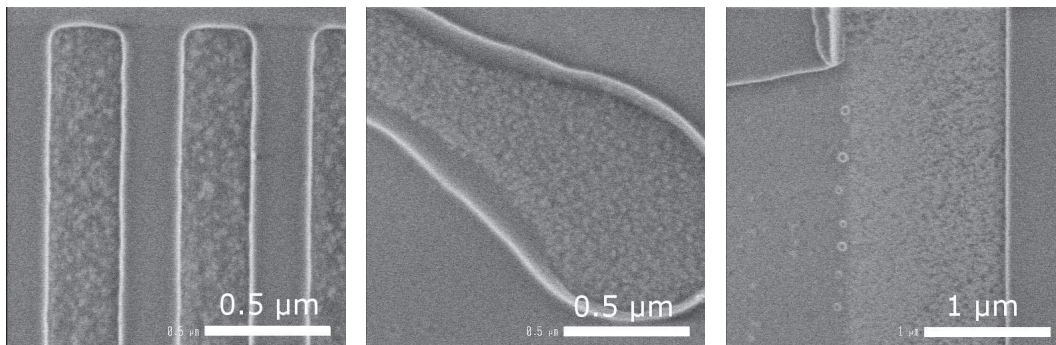


Figure 9.11 – SEM top views of imprinted lines (left) and capillary defects (middle and right), substrate D (105 nm). A high surface roughness is found at both the bottom of the lines and of the dewetted fingers

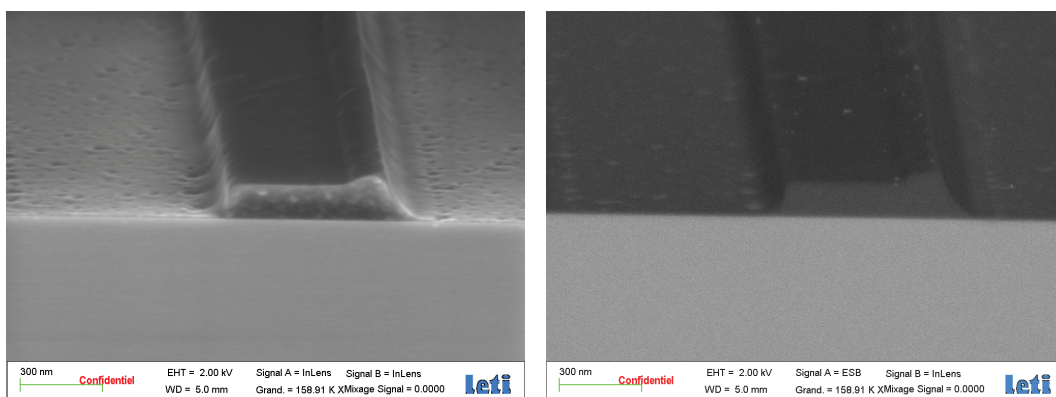


Figure 9.12 – SEM tilted views of an imprinted line on substrate A (native oxide). **Left**: topographical contrast; **right**: chemical contrast.

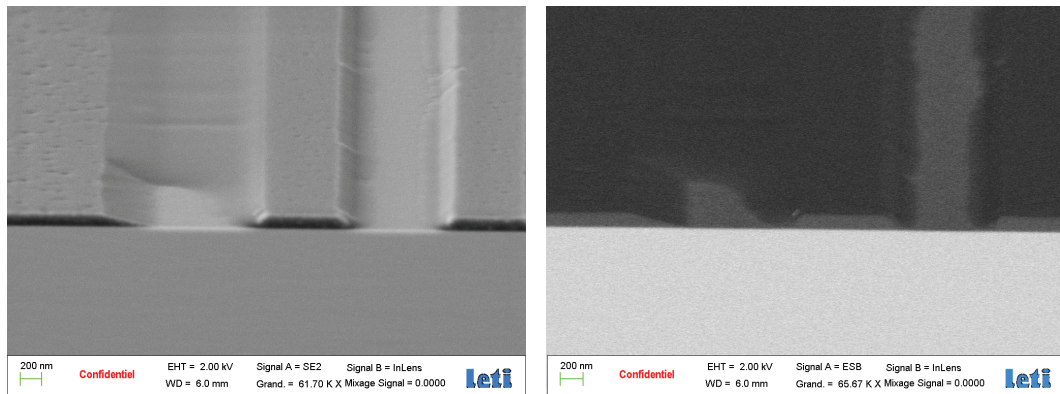


Figure 9.13 – SEM tilted views of an imprinted line on substrate B (11 nm).
Left: topographical contrast; **right:** chemical contrast.

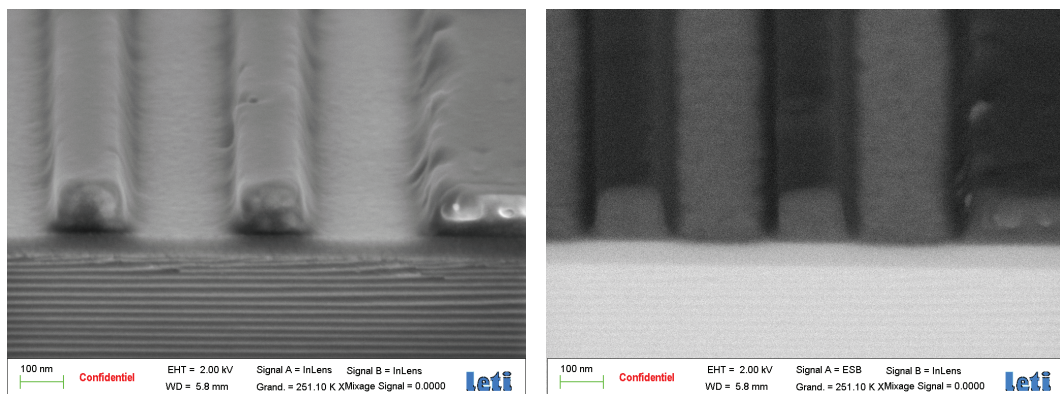


Figure 9.14 – SEM tilted views of an imprinted line on substrate C (53 nm).
Left: topographical contrast; **right:** chemical contrast.

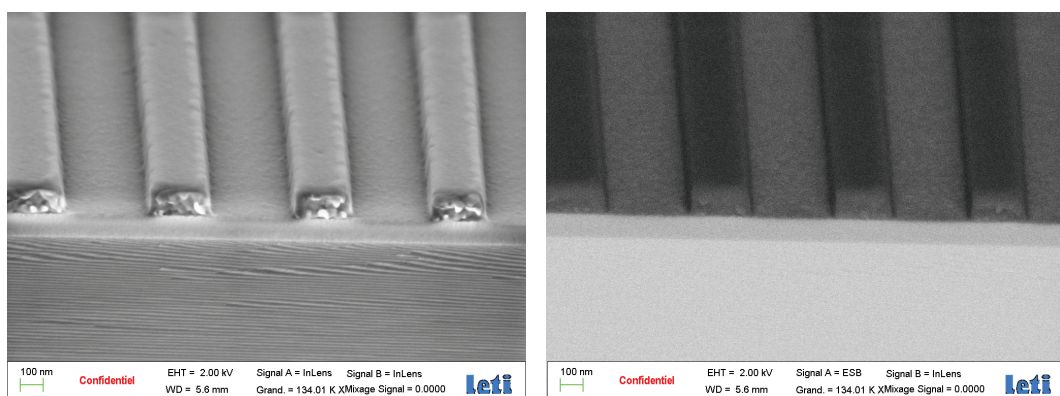


Figure 9.15 – SEM tilted views of an imprinted line on substrate D (105 nm).
Left: topographical contrast; **right:** chemical contrast.

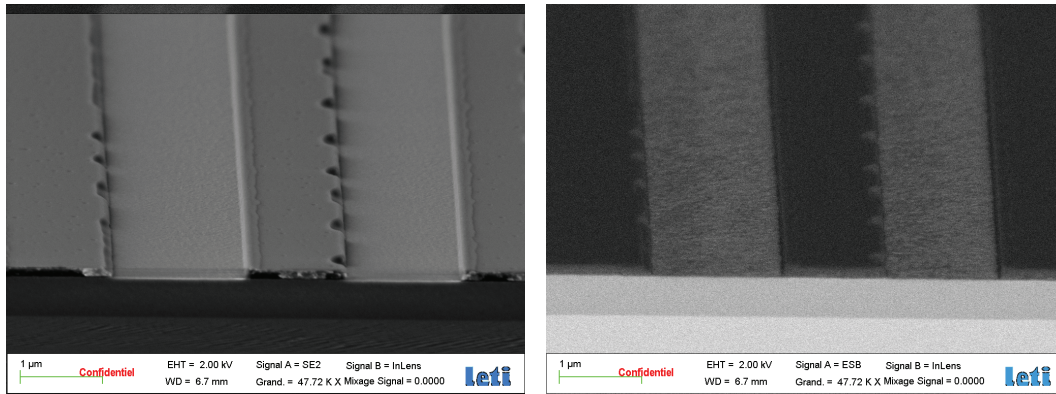


Figure 9.16 – SEM tilted views of an imprinted line on substrate E (532 nm).
Left: topographical contrast; **right:** chemical contrast.

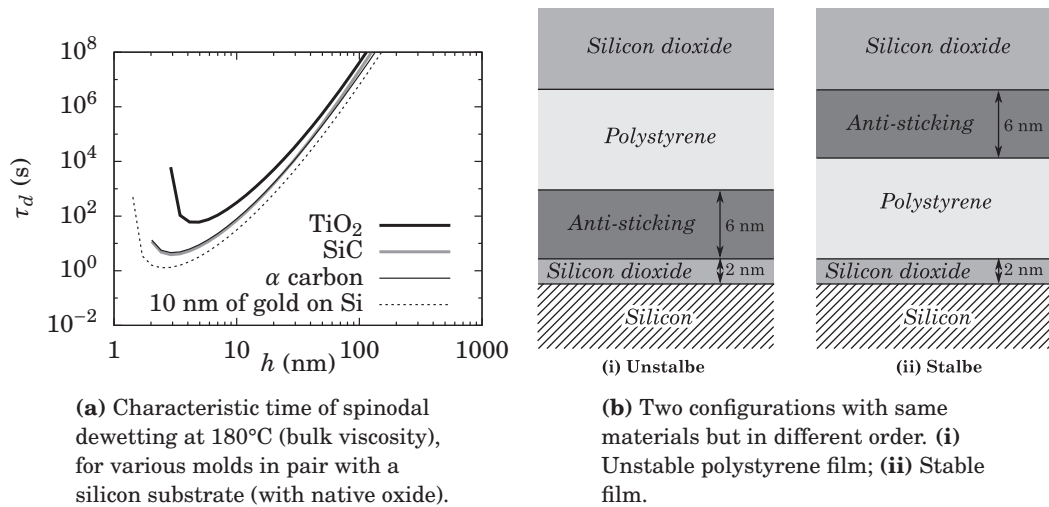


Figure 9.17 – Effects of various materials on the disjoining pressure in a confined polystyrene film.

9.3.3 Other materials: simulations

In order to see if other material could be relevant in this study, we computed the disjoining pressure in various cases. We tried several materials such as amorphous carbon (α C) on silicon, silicon on silicon oxide (SOI), gold (Au) on silicon, titanium dioxide (TiO_2) and silicon carbide (SiC). Each material was used either as a substrate with a silicon mold (with anti-sticking layer), or as the material of the mold itself (without anti-sticking layer) in pair with a silicon substrate (with native oxide).

It turned out that according to the theory, none of the above material yields a dewetting substrate when used with a silicon mold. On the other hand, if they are used as a mold without anti-sticking layer, dewetting can occur (except for SOI), as reported on figure 9.17a. Dewetting is even faster than in the case we explored before, since the lower characteristic time is found to be about 1 s for a silicon mold covered with a 10-nm gold film, while it was 1 hour in the previous cases (figure 9.3).

However, it should be stressed that the anti-sticking layer seems to play a decisive role. Indeed, we saw above that a silicon oxide substrate with a silicon mold promotes dewetting (figure 9.17b-i). But we calculated that an oxide mold with a silicon substrate yields a stable polystyrene film (figure 9.17b-ii). Experiments are needed to confirm this property. In the end, without any accurate data about the anti-sticking layer, the computation of the disjoining pressure should be interpreted with care.

9.3.4 Conclusion and outlooks

We carried out dewetting experiments of confined films during a nanoimprint process. In good agreement with theoretical calculations, the experiments revealed that a thick silicon oxide layer is a good promoting material for the dewetting of the resid-

ual layer. However, the thickest layers produced large capillary instabilities, damaging the imprint quality. From a theoretical point of view, a better dielectric model of the anti-sticking layer, for example by use of ultraviolet synchrotron spectroscopy measurements, could strengthen the computation of the disjoining pressure. Other issues remain unclear, such as the confined dewetting dynamics, the influence of short range forces, and the dynamics of molecular-thick films.

On the other hand, the concepts developed in this chapter can be used to prevent unwanted dewetting by choosing appropriate materials.

References

- N. Bogdanski, M. Wissen, S. Mošllenbeck, and H.-C. Scheer. Thermal imprint with negligibly low residual layer. *Journal of Vacuum Science & Technology B: Microelectronics and Nanometer Structures* **24**, 2998 (2006).
- S.-J. Choi, D. Tahk, and H. Yoon. Spontaneous dewetting-induced residue-free patterning at room temperature. *Journal of Colloid and Interface Science* **340**, 74–81 (2009).
- A. Finn, R. Hensel, F. Hagemann, R. Kirchner, A. Jahn, and W.-J. Fischer. Geometrical properties of multilayer nano-imprint-lithography molds for optical applications. *Microelectronic Engineering* **98**, 284–287 (2012).
- Y.-C. Kao and F. C.-N. Hong. Residual-layer-free direct printing by selective filling of a mould. *Journal of Micromechanics and Microengineering* **21**, 025026 (2011).
- Y. Kim and H. Lee. Selective dewetting for general purpose patterning. *Advanced Materials* **15**, 332–334 (2003).
- H. Lee. Effect of imprinting pressure on residual layer thickness in ultraviolet nanoimprint lithography. *Journal of Vacuum Science & Technology B: Microelectronics and Nanometer Structures* **23**, 1102–1106 (2005).
- H. Lee and G.-Y. Jung. Full wafer scale near zero residual nano-imprinting lithography using UV curable monomer solution. *Microelectronic Engineering* **77**, 42–47 (2005).
- A. Martin, A. Buguin, and F. Brochard-Wyart. Dewetting nucleation centers at soft interfaces. *Langmuir* **17**, 6553–6559 (2001).
- P. Martin and F. Brochard-Wyart. Dewetting at soft interfaces. *Physical Review Letters* **80**, 3296–3299 (1998).
- A. Mayer, N. Bogdanski, S. Möllenbeck, and H.-C. Scheer. Pattern definition through guided self-assembly in thermal nanoimprint. *Microelectronic Engineering* **87**, 907–909 (2010).
- H. Park and X. Cheng. Thermoplastic polymer patterning without residual layer by advanced nanoimprinting schemes. *Nanotechnology* **20**, 245308 (2009).
- V. A. Parsegian. *Van der Waals Forces: A Handbook for Biologists, Chemists, Engineers, and Physicists*. Cambridge University Press (2005).
- R. Seemann, S. Herminghaus, and K. Jacobs. Gaining control of pattern formation of dewetting liquid films. *Journal of Physics: Condensed Matter* **13**, 4925–4938 (2001).

- R. Seemann, S. Herminghaus, C. Neto, S. Schlagowski, D. Podzimek, R. Konrad, H. Mantz, and K. Jacobs. Dynamics and structure formation in thin polymer melt films. *Journal of Physics: Condensed Matter* **17**, S267–S290 (2005).
- K.-Y. Yang, K.-M. Yoon, J.-W. Kim, J.-H. Lee, and H. Lee. Low temperature fabrication of residue-free polymer patterns on flexible polymer substrate. *Japanese Journal of Applied Physics* **48**, 095003 (2009).
- H. Yoon, K. M. Lee, D.-Y. Khang, H. H. Lee, and S.-J. Choi. Rapid flash patterning of nanostructures. *Applied Physics Letters* **85**, 1793–1795 (2004).
- H. Yoon, S. H. Lee, S. H. Sung, K. Y. Suh, and K. Char. Mold design rules for residual layer-free patterning in thermal imprint lithography. *Langmuir* **27**, 7944–7948 (2011).
- H. Zhao, Y. J. Wang, and O. K. C. Tsui. Dewetting induced by complete versus nonretarded van der waals forces. *Langmuir* **21**, 5817–5824 (2005).

Part IV

Conclusion and appendices

Chapter 10

Conclusion

Nanoimprint lithography may be one of the few industrial processes where flows at the nano—or at least submicron—scale play a decisive role. New tools have to be developed for engineers to design molds, find new materials and optimize processes. In this thesis, we tried to contribute to a better understanding of various aspects of such nanoscale flows.

Reflow of a nanoimprinted pattern. For describing flows of nanoimprinted patterns with a thick residual layer and small aspect ratios, we implemented a versatile analytical model called capillary wave theory. With this model, we are able to correctly depict the leveling of an arbitrary (injective) shape, and in particular high spatial frequencies that are overlooked in lubrication models. The other major advantage of capillary wave theory is that any linear behavior law for the material can be used. Not only Newtonian behavior, but also linear viscoelastic laws, from the simple Maxwell model to integral reptation theory, can be an input of the model.

On the other hand, when the residual layer is thin compared to the amplitude of the patterns, or for large aspect ratios, lubrication theory or complete simulation is needed. We analyzed some aspects of non-linearity involved, and in particular the effect of residual layer thickness. From our analysis we could determine several key factors to accurately manufacture shapes with an annealing step. For large aspect ratios though, a complete numerical simulation is required, but few cases were addressed in the present work. It should also be interesting to make use of other features such as highly viscoelastic materials or new driving (acoustic, electrostatic, etc.) forces for the flow. Complementary studies with both numerical approaches and experiments would certainly enrich our know-how about reflow processes.

Nanoscale polymer characterization. We also implemented capillary wave theory to develop a polymer characterization method based on the reflow of spatially modulated patterns. The Newtonian viscosity and the terminal relaxation time of thin polymer films could be measured in a standard NIL environment. Although there is always room for improvement, we can reasonably state that we developed a robust method to characterize several hundred nanometers polymer films *in situ*.

However, characterization of sub-hundred-nanometer films is very delicate with this technique, for two reasons. First, when decreasing the film thickness, one has to decrease the pattern amplitude in order to keep the linear behavior of the reflow. Patterns of several nanometers then have to be used, and signal-to-noise ratio, roughness, or imprint defects begins to seriously interfere in the method. Second, ultra-thin polymer films are transparent. Most work is done blind, and for example it is then practically very difficult to place an AFM cantilever on the right pattern. To what extent is the WLF law still relevant for ultra-thin films? Could surface tension be a function of thickness, too? Can we measure the disjoining pressure inside the film? It is clear that the experimental extension of our method to ultra-thin films is necessary to tackle these fundamental issues.

Dewetting of ultra-thin films. In order to compute the disjoining pressure in our polymer films, we implemented the modern theory of Lifshitz that describes long-range van der Waals forces in continuous matter. This theory makes use of the optical properties of the interacting materials and the Green functions for the propagation of electromagnetic waves. In that matter, we could benefit from the resources of our optronics department and develop a state-of-the-art multilayer code. With this numerical tool, disjoining pressure engineering can be achieved, that is, the disjoining pressure tuning as a function of the material stack.

According to simulations, the spinodal dewetting of a polystyrene film can be enhanced by adding a silicon oxide layer on the silicon substrate. This property was known for supported thin films, but had never been reported for confined geometries. Confined dewetting experiments were also carried out and indeed tend to support this result. Nevertheless, a complete model for the dewetting mechanism in this confined geometry is required if we want to go further and answer fundamental questions, such as where and how free surface is created, or whether finger-like patterns always appear.

From a numerical point of view, a real breakthrough would be to develop a numerical method to compute the disjoining pressure in arbitrary geometries. No doubt that future efforts will be put in this cross-disciplinary subject, where fluctuating electrodynamics meets fluid mechanics. At least it is necessary in order to keep continuum mechanics relevant at these scales.

As a conclusion, we would like to present in the following table, a synthesis of the various achievements presented in this thesis. For each item, the state of the art or starting point, then the results achieved in our particular conditions, and finally some opportunity for prospective work, are presented.

Reflow of a nanoimprinted pattern

Before	Achieved	Prospective work
Analytical model: lubrication theory only	Capillary wave theory implemented. Small and high spatial frequencies correctly described. Simulation tools for both lubrication theory and capillary wave theory.	Integration of other forces, such as acoustic waves or electrostatic forces.
Linearized lubrication theory	Non-linear effects studied	Reflow of very high aspect ratio features
Newtonian case	Viscoelastic case, shear thinning criteria	Implementation of a thickness-dependent viscosity in numerical methods.
Empirical applications of reflow with triple contact lines	Several concepts of reflow with residual layer, depending on the relative thickness of this residual layer. Inverse reflow programming	Viscoelastic reflow experiments. Reflow of various 3D shapes.

Nanoscale polymer characterization

Before	Achieved	Prospective work
Rheological measurements with periodic patterns.	Relevant spatially modulated patterns.	Use of 3D patterns.
Newtonian viscosity	Viscoelasticity	Slip length, disjoining pressure measurement. Ultra-thin films characterization to confirm the applicability of WLF law.
AFM characterization	(No particular change)	optical characterization such as confocal microscopy

Dewetting of ultra-thin films

Before	Achieved	Prospective work
Non-retarded Hamaker theory	Lifshitz theory based on optical properties implemented. State-of-the-art simulation tool for stratified media.	Numerical tool for arbitrary geometries. Optical properties measurements in UV with synchrotronic light (for polymers and anti-sticking layers).
Temperature not discussed.	Disjoining pressure theoretically weakly dependent on temperature for a system in thermal equilibrium. Optical properties at room temperature can be used.	Investigate the disjoining pressure gradient due to high temperature gradients.
Stability discussed in terms of the sign of the Hamaker constant.	Stability discussed in term of the characteristic dewetting time (more practical).	Computation of the characteristic time for the nucleation of holes
Experimental supported dewetting.	Experimental confined dewetting. Sub-micron Saffman-Taylor instabilities observed.	Quantitative characterization of microscopic Saffman-Taylor instabilities
Theoretical effect of silicon oxide layer for supported dewetting.	Theoretical effect of silicon oxide layer and other materials for both confined and supported dewetting.	Measurements and integration of surface energies and short-range forces.
Experimental effect of silicon oxide layer for supported dewetting.	Experimental effect of silicon oxide layer films.	Experimental effects of other materials.

Appendix A

Mathematical treatments for the supported thin film equations of creeping flow

This appendix gathers the mathematical developments of chapter 4. We consider the flow depicted in figure 4.1 on page 56, with the notations and boundary conditions of section 4.1 on page 55.

A.1 Fourier transform

A.1.1 Fourier transform of an integrable function

In this thesis, we use the following definitions for the direct and inverse Fourier transforms of an integrable function:

$$\hat{s}(\mathbf{k}, \omega) = \iint_{-\infty}^{+\infty} d^2\mathbf{x} \int_{-\infty}^{+\infty} dt s(\mathbf{x}, t) \exp(-i\mathbf{k} \cdot \mathbf{x} + i\omega t), \quad (\text{A.1})$$

$$s(\mathbf{x}, t) = \iint_{-\infty}^{+\infty} \frac{d^2\mathbf{k}}{4\pi^2} \int_{-\infty}^{+\infty} \frac{d\omega}{2\pi} \hat{s}(\mathbf{k}, \omega) \exp(i\mathbf{k} \cdot \mathbf{x} - i\omega t). \quad (\text{A.2})$$

Consequently, the time derivative writes:

$$\left[\frac{\partial \hat{s}}{\partial t} \right] = -i\omega \hat{s},$$

And for spatial gradients:

$$[\nabla_{\mathbf{x}} \hat{s}] = i\mathbf{k} \hat{s}.$$

A.2 Lubrication theory

A.2.1 Derivation of the Reynolds equation

The Reynolds equation gives the evolution of the thickness h as a function of the pressure gradient. The growth rate of the thickness, $\frac{\partial h}{\partial t}$, is simply the instantaneous vertical velocity at the free surface, $v_z(h)$. So we need to solve the velocity field of the flow. The following derivation of the Reynolds equation with basic assumptions can be found in numerous books (see for example Bruus, 2008), but here we will derive an expression for non-homogeneous viscosity and Navier slip boundary condition.

We begin with the Stokes equation of flow for incompressible Newtonian fluids:

$$\nabla p = \eta \nabla^2 \mathbf{v} + 2\mathbb{D}\nabla\eta, \quad (\text{A.3})$$

where \mathbb{D} is the strain rate tensor:

$$\mathbb{D}_{ij} = \frac{1}{2} \left(\frac{\partial v_i}{\partial x_j} + \frac{\partial v_j}{\partial x_i} \right).$$

Note that if viscosity η is a constant, then $\nabla\eta = 0$ and equation (2.5) on page 24 is recovered. We assume that η is a known function of z (and possibly x) only (Newtonian fluid). For writing simplicity, we will consider a 2D flow in the plane (x, z) , although the extension to the 3D case entails no additional difficulty. With $x^+ = x/L$ and $z^+ = z/h_0$, the Stokes equation can be recast in the form:

$$\begin{aligned} \varepsilon^2 L \frac{\partial p}{\partial x^+} &= \eta \varepsilon^2 \frac{\partial^2 v_x}{\partial x^{+2}} + 4\pi^2 \eta \frac{\partial^2 v_x}{\partial z^{+2}} + 2\varepsilon^2 \frac{\partial \eta}{\partial x^+} \times \frac{\partial v_x}{\partial x^+} + 2\pi \varepsilon \frac{\partial \eta}{\partial z^+} \times \frac{\partial v_z}{\partial x^+} + 4\pi^2 \frac{\partial \eta}{\partial z^+} \times \frac{\partial v_x}{\partial z^+}, \\ \varepsilon 2\pi L \frac{\partial p}{\partial z^+} &= \eta \varepsilon^2 \frac{\partial^2 v_z}{\partial x^{+2}} + 4\pi^2 \eta \frac{\partial^2 v_z}{\partial z^{+2}} + \varepsilon^2 \frac{\partial \eta}{\partial x^+} \times \frac{\partial v_z}{\partial x^+} + 2\pi \varepsilon \frac{\partial \eta}{\partial x^+} \times \frac{\partial v_x}{\partial z^+} + 8\pi^2 \frac{\partial \eta}{\partial z^+} \times \frac{\partial v_z}{\partial z^+}, \end{aligned} \quad (\text{A.4})$$

where we defined the lubrication ratio ε by $\varepsilon = 2\pi h_0/L$. By writing the pressure and velocity as asymptotic expansions:

$$\begin{aligned} p &= \frac{1}{\varepsilon^2} p_{-2} + \frac{1}{\varepsilon} p_{-1} + p_0 + \dots, \\ \mathbf{v} &= \mathbf{v}_0 + \varepsilon \mathbf{v}_1 + \varepsilon^2 \mathbf{v}_2 + \dots, \end{aligned} \quad (\text{A.5})$$

we get the first order equations in ε :

$$\begin{aligned} L \frac{\partial p_{-2}}{\partial x^+} &= 4\pi^2 \left(\eta \frac{\partial^2 v_{x0}}{\partial z^{+2}} + \frac{\partial \eta}{\partial z^+} \times \frac{\partial v_{x0}}{\partial z^+} \right), \\ \frac{\partial p_{-2}}{\partial z^+} &= 0, \end{aligned} \quad (\text{A.6})$$

and the following order equations, for example the second order, but which are not used here:

$$\begin{aligned} L \frac{\partial p_{-1}}{\partial x^+} &= 4\pi^2 \left(\eta \frac{\partial^2 v_{x1}}{\partial z^{+2}} + \frac{\partial \eta}{\partial z^+} \times \frac{\partial v_{x1}}{\partial z^+} \right) + 2\pi \frac{\partial \eta}{\partial z^+} \times \frac{\partial v_{z0}}{\partial x^+}, \\ L \frac{\partial p_{-1}}{\partial z^+} &= 2\pi \left(\eta \frac{\partial^2 v_{z1}}{\partial z^{+2}} + 2 \frac{\partial \eta}{\partial z^+} \times \frac{\partial v_{z1}}{\partial z^+} \right) \end{aligned} \quad (\text{A.7})$$

...

If we bring the first order equation back to the real coordinates (x, z) , we finally get:

$$\frac{\partial p}{\partial x} = \frac{\partial}{\partial z} \left(\eta \frac{\partial v_x}{\partial z} \right), \quad (\text{A.8})$$

$$\frac{\partial p}{\partial z} = 0. \quad (\text{A.9})$$

The first interesting result is that pressure does not depend on z . It is thus possible to integrate equation (A.8) along the z -coordinate:

$$\eta(z)v'_x(z) = z \frac{\partial p}{\partial x} + C. \quad (\text{A.10})$$

The no tangential stress condition at the free interface implies $v'_x(h) = 0$, which leads to:

$$v'_x(z) = \frac{\partial p}{\partial x} \times \frac{z-h}{\eta(z)}. \quad (\text{A.11})$$

Integrating a second time yields:

$$v_x(z) = v_x(0) + \frac{\partial p}{\partial x} \int_0^z \frac{\zeta-h}{\eta(\zeta)} d\zeta. \quad (\text{A.12})$$

The Navier slip condition at the bottom interface sets $v_x(0) = \beta v'_x(0)$ ($\beta = 0$ corresponds to a non-slip condition):

$$v_x(z) = -\frac{\partial p}{\partial x} \left(\beta \frac{h}{\eta(z=0)} + \int_0^z \frac{h-\zeta}{\eta(\zeta)} d\zeta \right). \quad (\text{A.13})$$

Now that we have an expression for v_x , we can get $v_z(h)$ by integrating the mass balance:

$$v_z(h) = \frac{dh}{dt} = \frac{\partial h}{\partial t} + \frac{\partial h}{\partial x} v_x(h) = - \int_0^h \frac{\partial v_x}{\partial x} dz. \quad (\text{A.14})$$

Formally, the equation above is enough to describe the evolution of h . However, it is preferred to switch the derivative and the sum sign, in other words, to express the growth rate of h as the derivative of a total flux:

$$\frac{\partial h}{\partial t} = -\frac{\partial h}{\partial x} v_x(h) - \frac{\partial}{\partial x} \int_0^h v_x dz + \frac{\partial h}{\partial x} v_x(h). \quad (\text{A.15})$$

The last term appears because the upper bound of the integral along z depends on x . Nevertheless, we see that it cancels out with the first term. Finally we get:

$$\frac{\partial h}{\partial t} = \frac{\partial}{\partial x} \left[\left(\beta \frac{h^2}{\eta(z=0)} + \int_0^h \int_0^z \frac{h-\zeta}{\eta(\zeta)} d\zeta dz \right) \times \frac{\partial p}{\partial x} \right]. \quad (\text{A.16})$$

If the viscosity is constant, or depends only on the local thickness h , this equation reduces to:

$$\frac{\partial h}{\partial t} = \frac{\partial}{\partial x} \left(\frac{h^2(h+3\beta)}{3\eta(h)} \times \frac{\partial p}{\partial x} \right). \quad (\text{A.17})$$

A.2.2 Harmonics generation in lubrication theory

We consider the non-linear dimensionless lubrication equation:

$$\frac{\partial h^+}{\partial t^+} + \frac{1}{(2\pi)^4} \times \frac{\partial}{\partial x^+} \left(h^{+3} \frac{\partial^3 h^+}{\partial x^{+3}} \right) = 0, \quad (\text{A.18})$$

and assume that a solution is given by:

$$h^+(x^+, t^+) = 1 + f_1(t^+) \cos 2\pi x^+ + f_2(t^+) \cos 4\pi x^+, \quad (\text{A.19})$$

with $f_1(0) = a_0 > 0$ and $f_2(0) = 0$: the shape is sinusoidal at $t^+ = 0$. The aim of this paragraph is to extract some information about $f_2(t^+)$, in other words to see what happens to the first harmonics of the shape. By trigonometric linearization,¹ we get:

$$\begin{aligned} \frac{h^{+3}}{(2\pi)^3} \times \frac{\partial^3 h^+}{\partial x^{+3}} = & \left[f_1 \left(1 + \frac{3}{4} f_1^2 + \frac{9}{8} f_2^2 - \frac{3}{2} f_2 \right) + 8f_2 \left(\frac{1}{4} f_1^3 + \frac{3}{2} f_1 + \frac{3}{8} f_1 f_2^2 \right) \right] \sin 2\pi x^+ \\ & + \left[f_1 \left(\frac{1}{4} f_1^3 + \frac{3}{2} f_1 + \frac{3}{8} f_1 f_2^2 \right) + 8f_2 \left(1 + \frac{3}{8} f_1^2 f_2 + \frac{3}{2} f_1^2 + \frac{3}{4} f_2^2 \right) \right] \sin 4\pi x^+ \\ & + \dots \end{aligned} \quad (\text{A.20})$$

Neglecting higher modes, the lubrication equation gives coupled evolution equations for f_1 and f_2 :

$$f_1' + f_1 + \frac{3}{4} f_1^3 + \frac{21}{2} f_1 f_2 + \frac{3}{2} f_1 f_2^2 + 2f_1^3 f_2 + \frac{21}{8} f_1 f_2^3 = 0, \quad (\text{A.21})$$

$$f_2' + 16f_2 + 12f_2^3 + \frac{1}{2} f_1^4 + 3f_1^2 + \frac{27}{4} f_1^2 f_2^2 + 24f_2 f_1^2 = 0. \quad (\text{A.22})$$

When f_2 is not too big, the governing equation for f_1 is then:

$$f_1' + f_1 + \frac{3}{4} f_1^3 = 0, \quad (\text{A.23})$$

and again if we neglect the f_1^3 term (we are interested in the weakly non-linear problem), then:

$$f_1(t^+) = a_0 e^{-t^+}. \quad (\text{A.24})$$

The equation for f_2 with a source term (the increase of f_2 is fed by f_1) is:

$$f_2' + 16f_2 + 3f_1^2 = 0, \quad (\text{A.25})$$

which is solved in:

$$f_2(t^+) = e^{-16t^+} \left[f_2(0) + \frac{3a_0^2}{14} (1 - e^{14t^+}) \right]. \quad (\text{A.26})$$

¹The open source software *Maxima* was used. See <http://maxima.sourceforge.net/>.

This is the first order evolution of the second mode. We will assume that $f_2(0) = 0$ (as it is the case for a square signal or a sinusoid). We see that f_2 is of order 2 in a_0 . We can write the order of the terms of equation (A.21):

$$\underbrace{f_1'}_1 + \underbrace{f_1}_1 + \underbrace{\frac{3}{4}f_1^3}_3 + \underbrace{\frac{21}{2}f_1f_2}_3 + \underbrace{\frac{9}{8}f_1f_2^2}_5 + \underbrace{2f_1^3f_2}_5 + \underbrace{3f_1f_2^3}_7 = 0. \quad (\text{A.27})$$

So the third order evolution equation for f_1 is:

$$f_1' + f_1 + \frac{3}{4}f_1^3 + f_1\frac{9}{4}a_0^2e^{-16t^+} (1 - e^{14t^+}) = 0. \quad (\text{A.28})$$

In order to keep the equation linear, we assume: $f_1^3 = f_1 \times a_0^2 e^{-2t^+}$. The solution of equation (A.28) is:

$$f_1(t^+) = a_0 \exp \left[-t^+ + a_0^2 \frac{3}{4} (1 - e^{-2t^+}) - a_0^2 \frac{9}{64} (1 - e^{-16t^+}) \right]. \quad (\text{A.29})$$

The first mode f_1 decreases with a characteristic speed t^+ , but this decrease is delayed by a source arriving as $2t^+$ and vanishing as $16t^+$ (like the second mode where it comes from). For $t^+ \rightarrow \infty$, if we note θ the shift between f_1 and its linear decrease ($a_0 e^{-t^+}$):

$$\theta = \frac{57}{64} a_0^2. \quad (\text{A.30})$$

This function is plotted on figure 4.6b on page 63.

A.3 Capillary wave theory

A.3.1 Derivation of the dispersion relation

The goal of this paragraph is to derive the dispersion relation of a leveling supported film (Eq. 4.25 on page 66). We first compute (4.19)' - $i\mathbf{k}$ (4.19) and get:

$$-k^2 \hat{\mathbf{u}}' + \hat{\mathbf{u}}''' + ik^2 \hat{v}_z \mathbf{k} - i\hat{v}_z'' \mathbf{k} = \mathbf{0}. \quad (\text{A.31})$$

We take the scalar product by \mathbf{k} and then mass conservation yields:

$$\hat{v}_z'''' - 2k^2 \hat{v}_z'' + k^4 \hat{v}_z = 0. \quad (\text{A.32})$$

This equation is directly solved in:

$$\hat{v}_z(z) = P_1(z) \cosh kz + P_2(z) \sinh kz, \quad (\text{A.33})$$

where P_1 and P_2 are unknown polynomials of degree one (ie. linear functions):

$$P_1(z) \equiv A_1 + B_1 z \quad \text{and} \quad P_2(z) \equiv A_2 + B_2 z, \quad (\text{A.34})$$

and where we have four unknown constants A_1 , B_1 , A_2 and B_2 . We use the property $P_1'' = P_2'' = 0$ to write:

$$\hat{v}'_z = (B_1 + kP_2) \cosh kz + (B_2 + kP_1) \sinh kz, \quad (\text{A.35})$$

$$\hat{v}''_z = (2kB_2 + k^2P_1) \cosh kz + (2kB_1 + k^2P_2) \sinh kz, \quad (\text{A.36})$$

$$\hat{v}'''_z = (3k^2B_1 + k^3P_2) \cosh kz + (3k^2B_2 + k^3P_1) \sinh kz. \quad (\text{A.37})$$

Constants A_1 , B_1 , A_2 and B_2 are found with the boundary conditions. The impermeability and Navier slip conditions at the bottom interface ($z = 0$) implies $\hat{v}_z(0) = 0$ and $\hat{v}'_z(0) = \beta\hat{v}''_z(0)$ (from a mass balance), so that:

$$A_1 = 0 \quad \text{and} \quad A_2 = 2\beta B_2 - \frac{B_1}{k}. \quad (\text{A.38})$$

We use this result to rewrite P_1 and P_2 at $z = h_0$:

$$P_1(h_0) = B_1 h_0 \quad \text{and} \quad P_2(h_0) = -\frac{B_1}{k} + B_2(h_0 + 2\beta). \quad (\text{A.39})$$

The tangential stress (proportional to $\hat{\mathbf{u}}' + i\mathbf{k}\hat{v}_z$, and consequently to $\hat{v}''_z + k^2\hat{v}_z$, mass balance again) must vanish at the interface:

$$(kh_0B_1 + B_2) \cosh kh_0 + (kh_0 + 2k\beta) B_2 \sinh kh_0 = 0. \quad (\text{A.40})$$

We are now able to write B_2 as a function of B_1 :

$$B_2 = -\frac{kh_0 \cosh kh_0}{\cosh kh_0 + (kh_0 + 2k\beta) \sinh kh_0} B_1. \quad (\text{A.41})$$

We now use the normal stress balance at the interface:

$$\hat{p}(h_0) - 2\eta(\omega)\hat{v}'_z(h_0) = \left(\gamma k^2 + \frac{\partial \Pi}{\partial h}(h_0) \right) \hat{h}(\mathbf{k}, \omega), \quad (\text{A.42})$$

and get

$$B_1 = \frac{(\gamma k^2 + \frac{\partial \Pi}{\partial h}(h_0)) \hat{h}}{2\eta} \times \frac{\cosh kh_0 + (kh_0 + 2k\beta) \sinh kh_0}{\cosh^2 kh_0 + k^2 h_0^2 + 2k\beta(kh_0 + \sinh \cosh kh_0)}, \quad (\text{A.43})$$

and

$$B_2 = \frac{(\gamma k^2 + \frac{\partial \Pi}{\partial h}(h_0)) \hat{h}}{2\eta} \times \frac{-kh_0 \cosh kh_0}{\cosh^2 kh_0 + k^2 h_0^2 + 2k\beta(kh_0 + \sinh \cosh kh_0)}. \quad (\text{A.44})$$

Since constants A_1 , B_1 , A_2 and B_2 are now known, it is possible to express the pressure or velocity field as functions of the physical parameters. The final step is to recall that the growth rate of h is the vertical velocity near h_0 :

$$-i\omega \hat{h} = \hat{v}_z(h_0), \quad (\text{A.45})$$

which directly leads to the dispersion relation we were looking for:

$$\frac{i\omega\eta(\omega)h_0}{\gamma} = f(kh_0, \text{Ha}, \beta), \quad (\text{A.46})$$

with:

$$f(kh_0, \text{Ha}, \beta) = \frac{kh_0 \sinh \cosh kh_0 - k^2 h_0^2 + 2kh_0 k \beta \sinh^2 kh_0}{2 \cosh^2 kh_0 + 2k^2 h_0^2 + 4k\beta(kh_0 + \sinh \cosh kh_0)} \left(1 + \frac{\text{Ha}}{k^2 h_0^2}\right), \quad (\text{A.47})$$

and

$$\text{Ha} = \frac{h_0^2 \frac{\partial \Pi}{\partial h}(h_0)}{\gamma}. \quad (\text{A.48})$$

For computation purpose, this function is numerically more efficient in the form:

$$f(kh_0, \text{Ha}, \beta) = \frac{kh_0 \tanh kh_0 - \left(\frac{kh_0}{\cosh kh_0}\right)^2 + 2\frac{\beta}{h_0} (kh_0 \tanh kh_0)^2}{2 + 2\left(\frac{kh_0}{\cosh kh_0}\right)^2 + 4\frac{\beta}{h_0} \left(\frac{kh_0}{\cosh kh_0}\right)^2 + 4\frac{\beta}{h_0} kh_0 \tanh kh_0} \left(1 + \frac{\text{Ha}}{k^2 h_0^2}\right). \quad (\text{A.49})$$

A.3.2 Solving integral dispersion relation

Let ϕ be the progress of the flow:

$$\phi = \frac{t}{\tau} = -\ln \left(\frac{\hat{h}(\mathbf{k}, t)}{\hat{h}(\mathbf{k}, 0)} \right). \quad (\text{A.50})$$

In the case of a pure reptation model, the dispersion relation gives:

$$\int_0^1 \frac{3x^2}{\frac{1}{\phi} - \text{De}x^2} dx = \frac{f(kh_0)}{\text{Ca}}. \quad (\text{A.51})$$

The issue is to find ϕ as a function of the physical parameters Ca and De, and the mode kh_0 . If we differentiate the relation dispersion with respect to $k^+ = kh_0$, we get a non-linear differential equation for ϕ :²

$$\frac{\partial \phi}{\partial k^+} \mathcal{X}(\phi) = \frac{1}{\text{Ca}} \times \frac{\partial f}{\partial k^+}, \quad (\text{A.52})$$

where \mathcal{X} is a function of ϕ derived from integration by parts:

$$\mathcal{X}(\phi) = \frac{6}{\phi^2} \left(\frac{\text{De}}{\frac{1}{\phi} - \text{De}} - \sqrt{\phi \text{De}} \times \text{arctanh} \left(\sqrt{\phi \text{De}} \right) \right). \quad (\text{A.53})$$

If we now try to numerically solve the latter differential equation, we may define:

$$\frac{\partial \phi}{\partial k^+} \equiv \frac{\phi_{n+1} - \phi_n}{\delta k^+}, \quad (\text{A.54})$$

²Richard Feynman would say: "Try to differentiate under the integral sign".

and

$$\frac{\partial f}{\partial k^+} \equiv \frac{f_{n+1} - f_n}{\delta k^+}. \quad (\text{A.55})$$

In a direct numerical integration scheme, we have an expression of ϕ_{n+1} as a function of ϕ_n :

$$\phi_{n+1} = \phi_n + \frac{f_{n+1} - f_n}{\text{Ca} \mathcal{X}(\phi_n)}, \quad (\text{A.56})$$

where both δk^+ cancel out. Now, we must find ϕ_0 . From mass conservation, we know that the mean thickness h_0 does not depend on time, and thus the progress of the flow for $k = 0$ is zero: $\phi_0 = 0$. However, the function $\mathcal{X}(\phi)$ is ill-defined in 0. An asymptotic expansion of $\mathcal{X}(\phi)$ in the limit $\phi \rightarrow 0$ (which means at very small times) gives $\mathcal{X}(0) = 4\text{De}^2$. We can now compute an expression of ϕ as a function of the wavevector. An implementation of this method is found in figure 6.10 on page 112. See also the numerical implementation in section C.5.2 on page 202.

A.3.3 Streamlines

At a given time, streamlines are curves that are always parallel to the velocity field. They give the direction of the flow. One way to compute streamlines is to plot them as contour lines of a potential function, noted $\Phi(x, z)$. This function should have the following properties:

1. $\nabla\Phi$ should be perpendicular to \mathbf{v} , and for example $\nabla\Phi \propto (v_z, -v_x)$.
2. The flow between two contour lines should be constant: the narrower the lines, the steeper the flow.

If we define Φ as a primitive in z of v_x :

$$\Phi(x, z) = \int_0^z v_x(x, \zeta) d\zeta, \quad (\text{A.57})$$

then mass balance and no-slip boundary condition give $\nabla\Phi = (-v_z, v_x)$. So the streamlines are indeed parallel to the flow. The second condition is also true, and the proof is the following. We want to compute the flux through a curve drawn from one contour line of value Φ_1 to another one of value Φ_2 . First, since the divergence of the velocity is zero, the divergence theorem allows us to chose any curve between those two contour lines (the flux is constant along a tube). Let us chose a parametric curve $\mathbf{L}(t)$ parallel to $\nabla\Phi$, going from $\mathbf{L}(t_1) = (x_1, z_1)$ to $\mathbf{L}(t_2) = (x_2, z_2)$. The normal vector along the curve is $\mathbf{n} = (-\frac{\partial z}{\partial t}, \frac{\partial x}{\partial t})/|\mathbf{L}'|$, the value of $\nabla\Phi$ in terms of \mathbf{v} gives:

$$\int_{t_1}^{t_2} \mathbf{v} \cdot \mathbf{n} dt = \int_{t_1}^{t_2} -\nabla\Phi \cdot \frac{\mathbf{L}'}{|\mathbf{L}'|} dt = \Phi_1 - \Phi_2. \quad (\text{A.58})$$

That is why for equally spaced contour lines (constant $\Phi_n - \Phi_{n+1}$), the total flow is constant between two contour lines.

Lubrication case. If we know the thickness $h(x)$ at a given time, then we can compute the velocity $v_x(x, z)$ from equation (A.13) on page 179. This can be done analytically for simple profiles h , or at least numerically with no specific difficulty.

Small perturbations case. In Fourier space (k, z) , we can express $\hat{\Phi}$ in terms of \hat{v}_z with use of the mass balance and no-slip boundary condition:

$$\hat{\Phi}(k, z) = \int_0^z i \frac{\hat{v}_z'}{k}(k, \zeta) d\zeta = i \frac{\hat{v}_z}{k}, \quad (\text{A.59})$$

and then:

$$\hat{\Phi}(k, z) = i \frac{\gamma \hat{h}}{2\eta} \times \frac{(kz + kzkh_0 \tanh kh_0) \frac{\cosh kz}{\cosh kh_0} - (1 + kzkh_0 + kh_0 \tanh kh_0) \frac{\sinh kz}{\cosh kh_0}}{1 + \left(\frac{kh_0}{\cosh kh_0} \right)^2}. \quad (\text{A.60})$$

Consequently we can directly compute streamlines for any thickness function \hat{h} . Streamlines are computed in the rectangle domain of length L and height h_0 , but for presentation purpose, they are stretched to the physical fluid domain $\{L, h(x)\}$.

A.3.4 Shear rate

In this subsection, we compute the shear rate $\dot{\gamma} = \frac{\partial v_x}{\partial z} + \frac{\partial v_z}{\partial x}$ inside a flowing film (no van der Waals forces and no slip condition) in order to extract the maximum shear rate and thus a criterion for the Newtonian behavior validity.

Lubrication case. For a sinusoidal profile: $h(x) = h_0 + \tilde{h} \cos kx$ with $kh_0 \ll 1$. We can compute:

$$\frac{\partial v_x}{\partial z} = -\frac{\gamma}{\eta} k^3 \tilde{h} \sin kx (z - h_0 - \tilde{h} \cos kx). \quad (\text{A.61})$$

By integrating the mass balance, we get:

$$v_z = \frac{\gamma}{\eta} k^4 \tilde{h} \left[\frac{z^3}{6} \cos kx + \frac{z^2}{2} (\tilde{h} \sin^2 - \tilde{h} \cos^2 - h_0) \right]. \quad (\text{A.62})$$

So:

$$\frac{\partial v_z}{\partial x} = \frac{\gamma}{\eta} k^5 \tilde{h} \left[-\frac{z^3}{6} \sin kx + 2z^2 \tilde{h} \sin \cos kx \right], \quad (\text{A.63})$$

and finally:

$$\dot{\gamma}(x, z) = \frac{\gamma}{\eta} k^3 \tilde{h} \left[\left(h_0 - z - \frac{z^3}{6} k^2 \right) \sin kx + (2z^2 \tilde{h} k^2 + \tilde{h}) \sin \cos kx \right]. \quad (\text{A.64})$$

If we write the latter expression in terms of dimensionless quantities $x^+ = kx$, $z^+ = z/h_0$, $k^+ = kh_0$:

$$\dot{\gamma}(x^+, z^+) = \frac{\gamma}{\eta} k^3 \tilde{h} h_0 \left[\left(1 - z^+ - \frac{z^{+3}}{6} k^{+2} \right) \sin x^+ + (2z^{+2} k^{+2} + 1) \frac{\tilde{h}}{2h_0} \sin 2x^+ \right]. \quad (\text{A.65})$$

with making use of $\cos = \sqrt{1 - \sin^2}$, it is possible to show that the maximum is at the bottom boundary ($z^+ = 0$), in:

$$x_{\max}^+ = \arccos \left[\frac{\sqrt{1 + 8 \left(\frac{\tilde{h}}{h_0} \right)^2 - 1}}{4 \frac{\tilde{h}}{h_0}} \right]. \quad (\text{A.66})$$

Although the expression of x_{\max}^+ seems rather complicated, the maximum shear rate is surprisingly weakly non-linear in \tilde{h} . In fact it is bounded by:

$$\frac{\gamma h_0 \tilde{h} k^3}{\eta} < \dot{\gamma}_{\max} < \frac{\gamma h_0 \tilde{h} k^3}{\eta} \times \underbrace{\frac{3^{\frac{3}{2}}}{4}}_{1.3}. \quad (\text{A.67})$$

Hence the criterion for a sinus profile in lubrication theory:

$$\dot{\gamma}_0 > 1.3 \frac{\gamma h_0 \tilde{h} k^3}{\eta}. \quad (\text{A.68})$$

Small perturbations case. In capillary wave theory, the result is straightforward. In Fourier space:

$$\hat{\gamma} = \hat{v}'_x + ik \hat{v}_z = i \frac{\hat{v}''_z}{k} + ik \hat{v}_z, \quad (\text{A.69})$$

which leads to:

$$\hat{\gamma}(k, z) = \frac{\gamma \hat{h}}{\eta} i k^2 \frac{((kz - kh_0) + kzkh_0 \tanh kh_0) \frac{\cosh kz}{\cosh kh_0} - kh_0 kz \frac{\sinh kz}{\cosh kh_0}}{1 + \left(\frac{kh_0}{\cosh kh_0} \right)^2}. \quad (\text{A.70})$$

So the shear rate spectrum is expressed as a function of the Fourier components of h . For a sinusoidal shape (single wavevector k), the maximum shear rate can be expressed by:

$$\dot{\gamma}_{\max} = \frac{\gamma}{\eta} \tilde{h} k^2 \tilde{\Gamma}(kh_0), \quad (\text{A.71})$$

where $\tilde{\Gamma}(kh_0)$ is:

$$\tilde{\Gamma}(kh_0) = \max_{0 \leq z \leq h_0} \left[k^2 \frac{((kz - kh_0) + kzkh_0 \tanh kh_0) \frac{\cosh kz}{\cosh kh_0} - kh_0 kz \frac{\sinh kz}{\cosh kh_0}}{1 + \left(\frac{kh_0}{\cosh kh_0} \right)^2} \right]. \quad (\text{A.72})$$

Generally, it is impossible to compute the maximum shear rate on the base of the Fourier components, but we rather need to compute the inverse transform first. This is how it is done for arbitrary geometries (figure 4.11 on page 74).

A.3.5 Reflow of spatially modulated patterns

We consider an imprinted film $h(x, t)$ of length L , of pattern depth $2\tilde{m}$ described by the initial modulation function:

$$h(x, 0) = h_0 + \tilde{m} \times \text{sign} \left[\cos \left(\int_0^x k(\xi) d\xi \right) \right] \quad (\text{A.73})$$

where $k(\xi)$ is the local wavevector. Assuming that the flow occurs in the thin film regime, the thickness follows the equation:

$$\frac{\partial h}{\partial t} + \frac{\gamma h_0^3}{3\eta} \times \frac{\partial^4 h}{\partial x^4} = 0. \quad (\text{A.74})$$

In the case of a periodic pattern of wavevector k_1 , the solution, after all high order frequencies have vanished, would be an exponentially decreasing sinusoid:

$$h(x, t) = h_0 + \frac{4\tilde{m}}{\pi} \cos(k_1 x) \exp\left(-\frac{t}{\tau_1}\right), \quad (\text{A.75})$$

where the factor $4/\pi$ accounts for the ratio of the fundamental mode by the depth of the profile in the Fourier transform of a square pattern, and with the characteristic leveling time:

$$\tau_1 = \frac{3\eta}{\gamma h_0^3 k_1^4}. \quad (\text{A.76})$$

Now, let us assume that in the case of a spatially modulated pattern, the reflow of a local period could have the same dynamics as a regular pattern of the same period, in other words, that the pattern evolution could be:

$$h(x, 0) = h_0 + \frac{4\tilde{m}}{\pi} \times \cos \left(\int_0^x k(\xi) d\xi \right) \times \exp\left(-\frac{t}{\tau(x)}\right), \quad (\text{A.77})$$

with the local characteristic time:

$$\tau(x) = \frac{3\eta}{\gamma h_0^3 k(x)^4}. \quad (\text{A.78})$$

The function defined in equation (A.77) does not necessarily follows equation (A.74). In fact, extra terms appear due to the modulation of the pattern. For the first spatial derivative, one gets:

$$\frac{\partial h}{\partial x} = \frac{4\tilde{m}}{\pi} \exp\left(-\frac{t}{\tau(x)}\right) \times \left[-k(x) \sin \left(\int_0^x k(\xi) d\xi \right) + \underbrace{\frac{t}{\tau^2} \frac{\partial \tau}{\partial x} \cos \left(\int_0^x k(\xi) d\xi \right)}_{\text{additional term}} \right]. \quad (\text{A.79})$$

If we assume:

$$\frac{t \left| \frac{\partial \tau}{\partial x} \right|}{\tau^2} \ll k, \quad (\text{A.80})$$

then the additional term can be neglected, and the second derivative yields:

$$\frac{\partial h}{\partial x} = \frac{4\tilde{m}}{\pi} \exp\left(-\frac{t}{\tau(x)}\right) \times \left[-k(x)^2 \cos\left(\int_0^x k(\xi)d\xi\right) - \underbrace{\left(\frac{\partial k}{\partial x} + k \frac{t \frac{\partial \tau}{\partial x}}{\tau^2}\right) \sin\left(\int_0^x k(\xi)d\xi\right)}_{\text{additional term}} \right]. \quad (\text{A.81})$$

Again, in order to neglect the additional term, we assume:

$$\left| \frac{\partial k}{\partial x} \right| \ll k^2. \quad (\text{A.82})$$

If we proceed the same way up to the fourth derivative, we obtain again conditions (A.80) and (A.82) so that the reflow equation (A.74) is valid.

Assumption (A.82) is easy to identify: it depends only on the topography of the pattern. In practical application, we can get without difficulty $|\frac{\partial k}{\partial x}|/k^2 < 10^{-3}$. Regarding assumption (A.80), it can be recast in:

$$\frac{t}{\tau} \times \frac{\left| \frac{\partial k}{\partial x} \right|}{k^2} \ll 1. \quad (\text{A.83})$$

For a given pattern, it is then an assumption on the time of reflow. Indeed, considering a local point of the pattern, if the reflow time is too long, fluid from neighbor parts can flow up to this point and influence its dynamics. However, if the time of interest is near $t \sim \tau$, then this assumption is fulfilled whenever assumption (A.82) is true.

References

See chapter 4.

Appendix B

Numerical integration of the lubrication equation

In this appendix, we present a numerical method to solve the lubrication equation.

B.1 Numerical scheme

We consider a 2D flowing film described by the non-linear lubrication equation:

$$\frac{\partial h}{\partial t} + \frac{\partial}{\partial x} \left(\frac{\gamma}{3\eta} h^3 \frac{\partial^3 h}{\partial x^3} \right) = 0 \quad (\text{B.1})$$

with t the time, $h(x, t)$ the local instantaneous thickness, γ the surface tension and η the (homogeneous) viscosity. This equation is a continuity equation of fourth order. The stability criterion in the case of a direct integration scheme requires a time increment of:

$$\delta t \lesssim \frac{3\eta}{\gamma} \delta x^4 \quad (\text{B.2})$$

where δx is the space increment. If we need a resolution of $\delta x \sim 10$ nm, with $\eta \sim 10^6$ Pa·s and $\gamma \sim 30$ mN·m⁻¹ we get:

$$\delta t \sim 10^{-24} \text{ s}, \quad (\text{B.3})$$

which makes a direct integration scheme inappropriate in our case, since the reflow durations are typically of several minutes. This is why the numerical integration is done with an implicit scheme.

We used the scheme of Ha *et al.* (2008). In this scheme, the free interface is meshed with a constant and uniform mesh of N points. We assume that the function h is periodic over a length $L = N \delta x$. We define (see figure B.1 on the following page):

$$U_j^n = \frac{1}{\delta x} \int_{x_{j-\frac{1}{2}}}^{x_{j+\frac{1}{2}}} h(x, n \delta t) dx. \quad (\text{B.4})$$

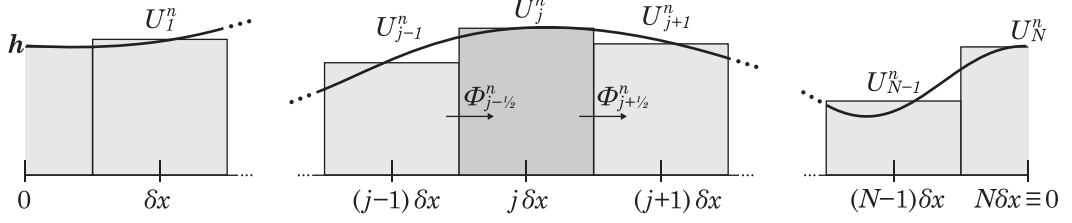


Figure B.1 – Quantization of the interface with periodic boundary condition.

Given the structure of the lubrication equation (B.1), we define a mass flux:

$$\phi(h) = \frac{\gamma}{3\eta} h^3 \frac{\partial^3 h}{\partial x^3}, \quad (\text{B.5})$$

so that equation (B.1) becomes:

$$\frac{\partial h}{\partial t} = -\frac{\partial \phi}{\partial x}. \quad (\text{B.6})$$

Now, if $u_{j+\frac{1}{2}}^{n+1}$ is the temporal average of $h(x_{j+\frac{1}{2}})$ over $[n\delta t, (n+1)\delta t]$:

$$u_{j+\frac{1}{2}}^{n+1} = \frac{1}{\delta t} \int_{n\delta t}^{(n+1)\delta t} h(x_{j+\frac{1}{2}}, t) dt, \quad (\text{B.7})$$

integration equation (B.6) over $[x_{j-\frac{1}{2}}, x_{j+\frac{1}{2}}] \times [n\delta t, (n+1)\delta t]$, the spatial averages U_j have the following relation:

$$U_j^{n+1} = U_j^n - \frac{\delta t}{\delta x} \left(\phi(u_{j+\frac{1}{2}}^{n+1}) - \phi(u_{j-\frac{1}{2}}^{n+1}) \right). \quad (\text{B.8})$$

The final step is to choose a finite difference approximation for ϕ . following Ha *et al.* (2008):

$$\Phi_{j+\frac{1}{2}}^n = \delta x^3 \phi(u_{j+\frac{1}{2}}^n) = \frac{\gamma}{3\eta} \cdot \left(\frac{U_{j+1}^n + U_j^n}{2} \right)^3 \left(U_{j+2}^n - 3U_{j+1}^n + 3U_j^n - U_{j-1}^n \right) \quad (\text{B.9})$$

Hence the implicit numerical scheme:

$$U_j^{n+1} = U_j^n - \frac{\delta t}{\delta x^4} \left(\Phi_{j+\frac{1}{2}}^{n+1} - \Phi_{j-\frac{1}{2}}^{n+1} \right) \quad (\text{B.10})$$

B.2 Octave/Matlab Script

```

1 %% Initializing
2
3 % Matlab terminal initialization
    
```

```

4 clear all
5 close all
6 clc
7 tic
8
9 % Parameters
10 dx = 2E-9;           % (m) x pace
11 Nx = 1000;          % Number of points
12 L = dx*Nx;           % (m) Total length
13 x = dx*(0:Nx-1)';   % x vector
14 Nt = 1000;           % Number of time iteration
15 tmin = 1E-10;        % Minimal dimensionless time
16 tmax = 1E-5;         % Duration of flow (dimensionless time)
17 t_constr = tmin * (tmax/tmin).^((0:Nt)' / Nt);
18 dt = diff(t_constr); % Vector of durations (logscale)
19 t = cumsum(dt);      % Dimensionless time vector
20
21 % Starting shape
22 h0 = 40E-9;          % (m) Mean thickness
23 eps = 0.8;           % Perturbation ratio
24 h = h0*( 1 + eps*cos(2*pi/L*x) );
25
26 %% Main loop
27
28 % Conditioning coefficients
29
30 coef = -dt *L^4 /(2*pi)^4 /8 /dx^4 /h0^3;
31
32 % Time loop
33 for n=[1:Nt]
34     U0 = h;
35     F0 = ones(size(U0));
36
37     % Non-linear solver (Newton-Raphson method)
38     while sum(F0.^2)>10^-8
39         % Jacobian matrix
40         Jacobien = spalloc (Nx, Nx);
41
42         for j=[1:Nx]
43             Umm = h(mod(j-3,Nx)+1);
44             Um = h(mod(j-2,Nx)+1);
45             U = h(j);
46             Up = h(mod(j,Nx)+1);
47             Upp = h(mod(j+1,Nx)+1);
48
49             Jacobien(j, mod(j-3,Nx)+1) = coef(n)*(U+Um)^3;
50             Jacobien(j, mod(j-2,Nx)+1) = coef(n)*(- (Up+U)^3 -3*(U+Um)^2 *(←
51                 Up-3*U+3*Um-Umm) -3*(U+Um)^3 );
52             Jacobien(j, j) = -1+coef(n)*3*( (Up+U)^2 *(Upp-3*Up+3*U-Um) -(U+←
53                 Um)^2 *(Up-3*U+3*Um-Umm) +(Up+U)^3 +(U+Um)^3 );
54             Jacobien(j, mod(j,Nx)+1) = coef(n)*(- (U+Um)^3 -3*(Up+U)^2 *(Upp←
55                 -3*Up+3*U-Um) -3*(Up+U)^3 );
56             Jacobien(j, mod(j+1,Nx)+1) = coef(n)*(U+Up)^3;
57
58         % Second term

```



```

56         F0(j,1) = U0(j)-U + coef(n) * ( (Up+U)^3 *(Upp-3*Up+3*U-Um) -(U+Um-
          )^3 *(Up-3*U+3*Um-Umm) );
57     end
58
59     % System solving. The inverse of the Jacobian is automatically ←
        computed by Octave/Matlab.
60     Hr = - Jacobien \ F0 ;
61
62     % Increment
63     h = h + Hr;
64
65     end
66 end
67
68 %% Output
69
70 out = horzcat(x,h);
71 save "x_h.txt" out
72
73 toc

```

B.3 Inverse reflow programing

In this section, we will see an example of code that uses the non-linear solver presented above in order to optimize some parameters.

B.3.1 Cost function

This function computes the complete reflow of the input shape, finds the time when the annealed shape is the closest to the target, and returns this optimal distance.

```

1 function distance = lubricationflow(x,h_init,h_target,spread,Nt)
2
3     Nx = numel(x);           % -
4     % temps min et max (ajust to stability)
5     tmin = 1E-8;
6     tmax = 5;
7     % vecteur temps de construction , échelle log
8     t_constr = tmin * (tmax/tmin).^((0:Nt)' /Nt);
9     dt = diff(t_constr);
10    % vecteur temps
11    t = cumsum(dt);
12
13    mdistance = zeros(size(t));
14
15    % Conditioning coefficients
16
17    coef = -dt *L^4 /(2*pi)^4 /8 /dx^4 /h0^3;
18
19    % Time loop
20    for n=[1:Nt]

```

```

21 U0 = h;
22 F0 = ones(size(U0));
23
24 % Non-linear solver (Newton-Raphson method)
25 while sum(F0.^2)>10^-8
26 % Jacobian matrix
27     Jacobien = spalloc (Nx, Nx);
28
29     for j=[1:Nx]
30         Umm = h(mod(j-3,Nx)+1);
31         Um = h(mod(j-2,Nx)+1);
32         U = h(j);
33         Up = h(mod(j,Nx)+1);
34         Upp = h(mod(j+1,Nx)+1);
35
36         Jacobien(j, mod(j-3,Nx)+1) = coef(n)*(U+Um)^3;
37         Jacobien(j, mod(j-2,Nx)+1) = coef(n)*(- (Up+U)^3 -3*(U+Um)^2*
38             *(Up-3*U+3*Um-Umm) -3*(U+Um)^3 );
39         Jacobien(j, j) = -1+coef(n)*3*( (Up+U)^2 *(Upp-3*Up+3*U-Um) -
40             (U+Um)^2 *(Up-3*U+3*Um-Umm) +(Up+U)^3 +(U+Um)^3 );
41         Jacobien(j, mod(j,Nx)+1) = coef(n)*(- (U+Um)^3 -3*(Up+U)^2 *(
42             Upp-3*Up+3*U-Um) -3*(Up+U)^3 );
43         Jacobien(j, mod(j+1,Nx)+1) = coef(n)*(U+Up)^3;
44
45         % Second term
46         F0(j,1) = U0(j)-U + coef(n) * ( (Up+U)^3 *(Upp-3*Up+3*U-Um) -
47             (U+Um)^3 *(Up-3*U+3*Um-Umm) );
48     end
49
50 % System solving. The inverse of the Jacobian is automatically
51 % computed by Octave/Matlab.
52 Hr = - Jacobien \ F0 ;
53
54 % Increment
55 h = h + Hr;
56
57 % Computation of the cost
58 dh = diff(h(floor(Nx*(1-spread)/2)+1:floor(Nx*(1+spread)/2)));
59 dh = diff(h_target(floor(Nx*(1-spread)/2)+1:floor(Nx*(1+spread)/2)));
60
61 %mdistance(n) = norm(dh-dhta)^2/norm(dh)/norm(dhta);
62 mdistance(n) = norm(dh-dhta)/norm(dhta);
63
64 end
65
66 % Return
67 [distance, i_reflow] = min(mdistance);
68 t_reflow = t(i_reflow);
69 %disp(t_reflow)

```

B.3.2 Main script

```

1 %% Initializing
2 clear all
3 close all
4 clc
5 tic
6
7 %% Paramters
8 % x pace
9 dx = 10E-9;           % [m]
10 % total length
11 L = 1E-6;           % [m]
12 % vecteur x
13 x = (dx:dx:L)';
14 % number of points
15 Nx = numel(x);      % -
16
17 %% Target shape (sphere)
18 hr_target = 0E-9;
19 h_target = hr_target + sqrt(L^2/4 - (L/2-x).^2);
20
21 %% Parameters to fit
22
23 % Density of the profile
24 density = 0.6;
25 % Depth of the mold
26 ht = 724E-9;
27 % Residual layer
28 hr = 10E-9;
29 % Minimum residual layer (prevents singularity)
30 hrmin = 10E-9;
31
32 % Dual unconstrained parameters (Matlab can only fit unconstrained parameters ←
    , and our parameters are constrained)
33 ud = atanh(2*density-1);
34 uht = sqrt(ht);
35 uhr = sqrt(hr-hrmin);
36
37 %% Starting shape
38
39 % Cost function
40 cost = @(vex) lubricationflow(x,init_spacedpyramid(x,[(1+tanh(vex(1)))/2;vex←
    (2)^2;vex(3)^2+hrmin]),h_target,0.8,1000);
41 res = fminsearch(cost,[ud;uht;uhr],optimset('Display','iter','FunValCheck','←
    on','TolFun',1E-14,'TolX',1E-6));
42
43 %% Result display
44
45 disp((1+tanh(res(1)))/2)
46 disp(res(2)^2)
47 disp(res(3)^2+hrmin)
48

```

```
49 h_init = init_spacedpyramid(x,[(1+tanh(res(1)))/2;res(2)^2;res(3)^2+hrmin]);
50 t_reflow = t_lubricationflow(x,h_init,h_target,0.9,1000);
51 h_reflow = duration_lubricationflow(x,h_init,t_reflow);
52
53 figure(2)
54 plot(x,h_target,'r');
55 hold on
56 plot(x,h_init,'k');
57 hold on
58 plot(x,h_reflow,'b');
59 hold off
60 axis equal
61
62 out = [x h_target h_init h_reflow];
63 save distribution.txt out -ASCII
64 toc
```

References

- Y. Ha, Y.-J. Kim, and T. G. Myers. On the numerical solution of a driven thin film equation. *Journal of Computational Physics* **227**, 7246–7263 (2008).

Appendix C

Flow simulation and rheological properties fitting in capillary wave theory

C.1 Main concept

We saw in chapter 4 that the reflow in capillary wave theory is equivalent to a linear low-pass filtering of the topography. The main concept for the simulation of such flow is then a simple signal processing based on Fourier transforms:

1. Acquisition or definition of the initial shape;
2. Fourier transform of the initial shape;
3. Computation of the kernel of reflow, based of material properties and physical paramters (time, thickness...);
4. Multiplication of the Fourier transform of the shape by the kernel;
5. Computation of the inverse Fourier transform to get the shape after reflow.

C.2 Preliminary functions

C.2.1 Assumptions on geometry signals

The Fourier transforms require to work on evenly spaced, non-redundant signals. The following function loads a profile from a text file named `filename`, in which x -coordinates are of unit `x_unit`, and z , `z_unit` all in SI unit. The profile is interpolated on the base of an x -vector of pace `dx`.

```
1 function [x, z] = load_from_file(filename, x_unit, z_unit, dx)
2     val = load(filename);
3     N_tmp = length(val(:,1));
```

```

4   x = x_unit*val(1,1):dx:x_unit*val(N_tmp,1);
5   N = length(x);
6   % Interpolation (suppress redundancy and adds missing points)
7   z_tmp = interp1 (x_unit * val(:,1), z_unit * val(:,2), x, 'linear');
8   % Security
9   z_tmp(N) = z_unit * val(N_tmp,2);
10  z = z_tmp';

```

C.2.2 rfft: Fast Fourier transform of a real signal

The following function computes the fast Fourier transform (FFT) of the real input z of length N . The output is a complex vector of length $\text{ceil}((N+1)/2)$. Note: When the DFT is computed for purely real input, the output is Hermite-symmetric, i.e. the negative frequency terms are just the complex conjugates of the corresponding positive-frequency terms ($\hat{z}(-k) = \hat{z}(k)^*$), and the negative-frequency terms are therefore redundant.

```

1 function z_rfft = rfft(z)
2     z_fft = fft(z);
3     z_rfft = z_fft(1:ceil((numel(z_fft)+1)/2));

```

C.2.3 irfft: inverse of rfft

The following function computes the inverse Fourier transform of a signal z_rfft , so that $\text{irfft}(\text{rfft}(z))=z$. The output is a vector of length N . The real function is here to prevent non-zero imaginary part due to computation noise.

```

1 function z = irfft(z_rfft,N)
2     z_rfft_p = flipud(z_rfft);
3     z_fft = vertcat(z_rfft,conj(z_rfft_p(mod(N+1,2)+1:length(z_rfft)-1)));
4     z = real( ifft(z_fft));

```

C.2.4 wavevector

The following function computes the normalized wavevectors $k \times h_0$, where k is the vector of wavevectors associated to the FFT of z , and h_0 is the mean of z .

```

1 function kh = wavevector(x, z)
2     h0 = mean(z);
3     ke = 2*pi/dx;
4     dk = ke/numel(x);
5     kh = h0*dk*[0:ceil((numel(x)+1)/2)-1]';

```

C.2.5 f

The following function computes the dispersion function $f(kh_0, Ha, \frac{\beta}{h_0})$ in the dispersion relation, where kh_0 is the normalized wavevector, Ha the Hamaker number and β/h_0 the normalized Navier slip length. The formula is written in order to avoid infinite numbers (NaN) when $kh \rightarrow \infty$.

$$f\left(kh_0, Ha, \frac{\beta}{h_0}\right) = \frac{kh_0 \tanh kh_0 - \left(\frac{kh_0}{\cosh kh_0}\right)^2 + 2\frac{\beta}{h_0} (kh_0 \tanh kh_0)^2}{2 + 2\left(\frac{kh_0}{\cosh kh_0}\right)^2 + 4\frac{\beta}{h_0} \left(\frac{kh_0}{\cosh kh_0}\right)^2 + 4\frac{\beta}{h_0} kh_0 \tanh kh_0} \left(1 + \frac{Ha}{k^2 h_0^2}\right) \quad (\text{C.1})$$

```

1 function rel = f(kh, hamaker, slip)
2     rel = (kh*tanh(kh) - (kh./cosh(kh)).^2 + 2*slip*(kh*tanh(kh))) ./ (2 + 2*(←
3     kh./cosh(kh)).^2 + 4*slip*(kh./cosh(kh)).^2 + 4*slip*kh*tanh(kh)) ←
4     .* (1 + hamaker./kh.^2);
5     rel(1) = 0;

```

C.3 Simulating a 2D flow

As an example, we will simulate the viscous reflow of a square profile.

```

1 %% Initializing
2 clear all
3 close all
4 clc
5 tic
6
7 %% Initial geometry
8 dx = 10E-9;
9 L = 1E-6;
10 x = (0:dx:L)';
11 h0 = 100E-9;
12 h_init = h0 * (1 + 20E-9*sign(cos(2*pi*x/L)));
13
14 %% Flow simulation
15
16 % Capillary number desired
17 Ca = 1;
18
19 % Fourier transform
20 h_init_fft = rfft(h_init);
21 % Wavevector
22 kh0 = wavevector(x, h_init);
23 % Kernel for a Newtonian reflow
24 Ker = exp(-f(kh0,0,0)/Ca);
25 % Reflow
26 h_fl_fft = h_init_fft.*Ker;
27 % Back in real space
28 h_fl = irfft(h_fl_fft, numel(x));

```



```

29
30 %% Result display
31
32 figure(1)
33 plot(x,h_init)
34 hold on
35 plot(x,h_hl,'k')
36 hold off
37
38 toc

```

C.4 Simulating a 3D flow

As an example, we will simulate the viscous reflow of a pyramid.

```

1 clear all
2 close all
3 clc
4 tic
5
6 % Capillary number of the flow (progress of the flow)
7 Ca = 10;
8
9 % Geometry z
10 % ht{      /\
11 % {_____/  \____
12 % hr{    | -b- |
13 % {_____
14 % |----- L -----|
15
16 L = 9E-6;
17 ht = 14E-6;
18 b = 9E-6;
19 hr = 20E-6;
20 dx = 40E-9;
21 x = (-L/2:dx:L/2)';
22 N = numel(x);
23
24 [X,Y] = meshgrid(x,x);
25 slop1 = ht+hr - 2*ht/b * abs(X);
26 slop2 = ht+hr - 2*ht/b * abs(Y);
27 z = min(slop1,slop2);
28 z = max(hr*ones(N,N),z);
29
30 % Wavectors array
31 kh = wavevector(x, mean(mean(z)))
32 [KX,KY] = meshgrid(kh,kh);
33 KN = sqrt(KX.^2+KY.^2); % Norm
34
35 % 2D FFT transform
36 z_fft = fft2(z);
37

```

```

38 % 2D dispersion factor
39 rel = KN/2.*(tanh(KN)-KN./cosh(KN).^2)./(1+KN.^2./cosh(KN).^2);
40 rel(1,1) = 0;
41 reltot = min( rel,circshift(flipud(rel),[1 0]) );
42 reltot = min( reltot,circshift(rot90(rel,2),[1 1]) );
43 reltot = min( reltot,circshift(fliplr(rel),[0 1]) );
44
45 % Simulation of the flow
46 z_fft_fl = z_fft .* exp(-reltot/Ca);
47 z_fl = abs(iff2(z_fft_fl));
48
49 toc

```

C.5 Fitting rheological properties

C.5.1 Viscoelastic single mode Maxwell model

The following function fits the rheological parameters Ca (capillary number) and De (Deborah number) to experimental profiles. (x_0, z_0) is the initial profile, (x_1, z_1) is the profile after annealing.

```

1 function [Ca, De] = extract_capillary_tau_smooth(x0, z0, x1, z1)
2     % Spectral analysis
3     z0_rfft = abs(rfft(z0));
4     h0 = mean(z0);
5     kh0 = wavevector(x0, h0);
6     z1_rfft = abs(rfft(z1));
7     h1 = mean(z1);
8     kh1 = wavevector(x1, h1);
9     z1_rfft_tp = interp1(kh1, z1_rfft, kh0, 'linear', 0);
10    % Smooth the spectra
11    fac_conv = conv(z1_rfft_tp, [0.05 0.1 0.15 0.4 0.15 0.1 0.05], 'same') ./ ←
12        conv(z0_rfft, [0.05 0.1 0.15 0.4 0.15 0.1 0.05], 'same');
13
14    % Fit
15    res = fminsearch(@(vex) cost(vex, dispersion, fac_conv), [1, 1]);
16    Ca = res(1);
17    De = res(2);
18
19    function c = cost(vex, dispersion, fac_conv)
20        % Progression of the flow
21        filter = exp(-dispersion./(vex(1)+dispersion*vex(2)));
22        c = sum((filter - fac_conv).^2);

```

C.5.2 Cost function for a reptation model

See section A.3.2 on page 183.

```

1  function c = cost(vex, dispersion, fac_conv)
2      Ca = vex(1);
3      De = vex(2);
4
5      % Progress of flow
6      phi = zeros(size(dispersion));
7      X0 = 4*De^2;
8
9      % Integration
10     for n = 2:numel(dispersion)
11         % precursor
12         phip = phi(n-1);
13         if n==2
14             X = X0;
15         else
16             X = 6/phip^2*(De/(1/phip-De)-sqrt(De*phip)*atanh(sqrt(De*phip-
17             )));
18         end
19         phi(n) = phip + (dispersion(n)-dispersion(n-1))/X/Ca;
20     end
21     filter = exp(-phi);
22     c = sum((filter - fac_conv).^2);

```

Appendix D

Numerical computation of the disjoining pressure

D.1 Optical data

For the computation of the disjoining pressure in Lifshitz theory, we used optical data from our own database regarding silicon, silicon oxide and metals. For polystyrene, we use data from Parsegian (2005). In this model, Lorentz resonant-damped oscillators are used. The dielectric function takes the form:

$$\epsilon(\omega) = 1 + \sum_j \frac{f_j \omega_{0j}^2}{\omega^2 - \omega_{0j}^2 - i\gamma_j \omega}, \quad (\text{D.1})$$

where f_j , ω_{0j} , and γ_j are fitting parameters, reported in table D.1.

D.2 Disjoining pressure formula

We consider a planar film of thickness h (medium #3, dielectric function ϵ_3), sandwiched between two semi-infinite media (#1 and #2, dielectric function ϵ_1 and ϵ_2). The disjoining pressure Π , in this film is Mulet (2003, Chap. 6):

Table D.1 – Dielectric data. Polystyrene data from Parsegian (2005), anti-sticking data from ellipsometry measurements.

$f_j \omega_{0j}^2$	ω_{0j} (eV)	γ_j (eV)
Polystyrene		
14.6	6.35	0.65
96.9	14.0	5.0
44.4	11.0	3.5
136.9	20.1	11.5
Anti-sticking		
117.8	12.2	2.5

$$\Pi(h) = \sum_{n=1}^{\infty} \frac{k_B T \xi_n^3}{\pi c^3} \int_1^{\infty} \kappa \gamma_3 (R^s + R^p) d\kappa \quad (\text{D.2})$$

with k_B the Boltzmann constant, T the temperature, ξ_n the Matsubara frequency of order n (Eq. 7.28 on page 130), c the speed of light, R^s and R^p given by:

$$R^{s,p} = \frac{r_{32}^{s,p} r_{31}^{s,p} \exp(-2h\kappa_0\gamma_3)}{1 - r_{32}^{s,p} r_{31}^{s,p} \exp(-2h\kappa_0\gamma_3)}, \quad (\text{D.3})$$

where

$$\kappa_0 = \frac{\xi_n}{c}, \quad (\text{D.4})$$

and

$$r_{ij}^s = \frac{\gamma_i - \gamma_j}{\gamma_i + \gamma_j}, \quad r_{ij}^p = \frac{\epsilon_j \gamma_i - \epsilon_i \gamma_j}{\epsilon_j \gamma_i + \epsilon_i \gamma_j}, \quad (\text{D.5})$$

are the Fresnel equations for polarization s and p, functions of the normalized wavevectors

$$\gamma_i = \sqrt{\epsilon_i - 1 + \kappa^2}. \quad (\text{D.6})$$

Note that the term for $n = 0$ is zero.

D.3 Matlab/Octave scripts

D.3.1 Dielectric functions from spectroscopic data

Example of file (data for silicon):

```
%nm      n      k
9.998000  0.997730  0.020600
10.250000  0.998500  0.021200
10.510000  0.999580  0.021900
11.070000  1.002400  0.023300
11.590000  1.007000  0.002470
11.920000  1.013200  0.002560
12.160000  1.024100  0.002600
12.400000  1.032000  0.001540
12.600000  1.034000  0.001020
...
```

```
1 function epsilon = xi_epsilon_from_file(xi,filepath)
2 % converts a lambda-n-k file into epsilon at Matsubara imaginary frequencies
3 % Speed of light [m/s]
4 c = 299792458;
5 %
6 L = load(filepath);
7 [Com, m, n] = unique(2*pi*c ./L(:,1) *10^9);
```

```

8  epsilon = ones(size(xi));
9  for i=1:length(xi)
10     Ceps = Com.*2.*L(m,2).*L(m,3) ./ (Com.^2 + xi(i).^2);
11     epsilon(i) = 1 + 2/pi * trapz(Com,Ceps);
12 end

```

D.3.2 Green function for a simple set of 3 media

```

1  function G = xi_green_2interfaces_joulain_quad(xi,epsilon1,epsilon2,epsilon3,←
    d)
2  % Normalized Casimir stress as found in Joulain et al.
3  % Uses an adaptive Gauss-Kronrod quadrature
4
5  % Integrate with adaptive Gauss-Kronrod quadrature
6  G = quadgk(@k) integr(k,xi,epsilon1,epsilon2,epsilon3,d),1,10^5);
7  function Gk = integr(Mkappa,xi,epsilon1,epsilon2,epsilon3,d)
8  % Function to integrate
9  % Speed of light [m/s]
10     c = 299792458;
11     k0 = xi/c;
12     % Normalized gammas
13     gamma1 = sqrt(epsilon1 - 1 + Mkappa.^2);
14     gamma3 = sqrt(epsilon3 - 1 + Mkappa.^2);
15     gamma2 = sqrt(epsilon2 - 1 + Mkappa.^2);
16     % reflexion factors
17     r31s = (gamma3 - gamma1) ./ (gamma3 + gamma1);
18     r31p = (epsilon1.*gamma3 - epsilon3.*gamma1) ...
19           ./ (epsilon1.*gamma3 + epsilon3.*gamma1);
20     r32s = (gamma3 - gamma2) ./ (gamma3 + gamma2);
21     r32p = (epsilon2.*gamma3 - epsilon3.*gamma2) ...
22           ./ (epsilon2.*gamma3 + epsilon3.*gamma2);
23     % Symetrized Fabry-Perot's factors
24     Rs = r32s.*r31s.*exp(-2*d*k0.*gamma3) ./ (1 - r31s.*r32s.*exp(-2*d*k0*←
    .*gamma3));
25     Rp = r32p.*r31p.*exp(-2*d*k0.*gamma3) ./ (1 - r31p.*r32p.*exp(-2*d*k0*←
    .*gamma3));
26     % Final result
27     Gk = Mkappa .* gamma3 .* (Rs + Rp);

```

D.3.3 Green function for 5 media

```

1  function G = xi_green_5interfaces_joulain_quad(xi,epsilon1,epsilon2,epsilon3,←
    epsilon4,epsilon5,epsilon6,d,e,f,g)
2  % Normalized Casimir stress as found in Joulain et al.
3  % Uses an adaptive Gauss-Kronrod quadrature
4  % Case with
5  % 1
6  % --z=d+f
7  % 5

```

```

8 % --z=d
9 % 3 Thin film
10 % --z=0
11 % 6
12 % --z=-g
13 % 4
14 % --z=-g-e
15 % 2
16
17 G = quadgk(@(k)integr(k,xi,epsilon1,epsilon2,epsilon3,epsilon4,epsilon5,←
epsilon6,d,e,f,g),1,10^5);
18 function Gk = integr(Mkappa,xi,epsilon1,epsilon2,epsilon3,epsilon4,←
epsilon5,epsilon6,d,e,f,g)
19 % Speed of light [m/s]
20 c = 299792458;
21 k0 = xi/c;
22 % Normalized gammas
23 gamma1 = sqrt(epsilon1 -1 + Mkappa.^2);
24 gamma5 = sqrt(epsilon5 -1 + Mkappa.^2);
25 gamma3 = sqrt(epsilon3 -1 + Mkappa.^2);
26 gamma2 = sqrt(epsilon2 -1 + Mkappa.^2);
27 gamma4 = sqrt(epsilon4 -1 + Mkappa.^2);
28 gamma6 = sqrt(epsilon6 -1 + Mkappa.^2);
29 % local reflexion factors
30 r36s = (gamma3 - gamma6)/(gamma3 + gamma6);
31 r36p = (epsilon6*gamma3 - epsilon3*gamma6) ...
32 ./ (epsilon6.*gamma3 + epsilon3.*gamma6);
33 r64s = (gamma6 - gamma4)/(gamma6 + gamma4);
34 r64p = (epsilon4*gamma6 - epsilon6*gamma4) ...
35 ./ (epsilon4.*gamma6 + epsilon6.*gamma4);
36 r42s = (gamma4 - gamma2)/(gamma4 + gamma2);
37 r42p = (epsilon2*gamma4 - epsilon4*gamma2) ...
38 ./ (epsilon2.*gamma4 + epsilon4.*gamma2);
39 r35s = (gamma3 - gamma5)/(gamma3 + gamma5);
40 r35p = (epsilon5.*gamma3 - epsilon3.*gamma5) ...
41 ./ (epsilon5.*gamma3 + epsilon3.*gamma5);
42 r51s = (gamma5 - gamma1)/(gamma5 + gamma1);
43 r51p = (epsilon1.*gamma5 - epsilon5.*gamma1) ...
44 ./ (epsilon1.*gamma5 + epsilon5.*gamma1);
45 % equivalent reflexion factors
46 r62s = (r64s + r42s.*exp(-2*gamma4.*k0*e))./(1+r64s.*r42s.*exp(-2*←
gamma4.*k0*e));
47 r62p = (r64p + r42p.*exp(-2*gamma4.*k0*e))./(1+r64p.*r42p.*exp(-2*←
gamma4.*k0*e));
48 r32s = (r36s + r62s.*exp(-2*gamma4.*k0*g))./(1+r36s.*r62s.*exp(-2*←
gamma4.*k0*g));
49 r32p = (r36p + r62p.*exp(-2*gamma4.*k0*g))./(1+r36p.*r62p.*exp(-2*←
gamma4.*k0*g));
50 r31s = (r35s + r51s.*exp(-2*gamma5.*k0*f))./(1+r35s.*r51s.*exp(-2*←
gamma5.*k0*f));
51 r31p = (r35p + r51p.*exp(-2*gamma5.*k0*f))./(1+r35p.*r51p.*exp(-2*←
gamma5.*k0*f));
52 % Symetrized Fabry-Perot's factors
53 Rs = r32s.*r31s.*exp(-2*d*k0.*gamma3) ./ (1 - r31s.*r32s.*exp(-2*d*k0←
.*gamma3));

```

```

54 Rp = r32p.*r31p.*exp(-2*d*k0.*gamma3) ./(1 - r31p.*r32p.*exp(-2*d*k0←
    .*gamma3));
55 % final result
56 Gk = Mkappa .*gamma3.*( Rs + Rp );

```

D.3.4 Main function

```

1 clear all
2 close all
3 clc
4 tic
5 %% Fundamental constants
6 % -----
7 %
8 % Speed of light [m/s]
9 c = 299792458;
10 % Normalized Planck's constant [m2.kg/s]
11 hbar = 1.054571628E-34;
12 % Boltzmann constant [m2.kg/s2/K]
13 kB = 1.3806504E-23;
14 % Temperature [K]
15 T = 453;
16
17 %% External functions
18 % -----
19 % Media :
20 % 1
21 % --z=d+f
22 % 5
23 % --z=d
24 % 3 Thin film ---> Computation of Hamaker Constant
25 % --z=0
26 % 6
27 % --z=-g
28 % 4
29 % --z=-g-e
30 % 2
31 %
32 % Dielectric function for medium 1 (top medium, =ones(size(omega)) for ←
    vacuum)
33 eps1 = @(xi) xi_epsilon_from_file(xi, '../indices/Si_Palik_Esrf.txt');
34 % Dielectric function for medium 5 (coating)
35 eps5 = @(xi) xi_epsilon_from_file(xi, '../indices/SiO2(amorphe)_palik.txt');
36 % Thickness of medium 5
37 f = 8.2E-9;
38 % Dielectric function for medium 3 (thin film)
39 eps3 = @(xi) xi_epsilon_oscillator(xi, 'PS');
40 % Dielectric function for medium 6 (coating)
41 eps6 = @(xi) xi_epsilon_from_file(xi, '../indices/Au_palik.txt');
42 % Thickness of the coating
43 g = 2E-9;
44 % Dielectric function for medium 4 (coating)

```



```

45 eps4 = @(xi) xi_epsilon_from_file(xi, '../indices/SiO2(amorphe)_palik.txt');
46 % Thickness of the coating
47 e = 1.6E-9;
48 % Dielectric function for medium 2 (substrate)
49 eps2 = @(xi) xi_epsilon_from_file(xi, '../indices/Si_Palik_Esrf.txt');
50
51 %% Computation parameters
52 % -----
53 %
54 % Number of Matsubara frequencies
55 n_xi = 2*10^3;
56 % Vector of xis
57 Mxi = 2*pi*kB*T/hbar *(0:n_xi-1)';
58 %=Thickness of the film=
59 % number of computations for d
60 n_d = 40;
61 % minimal distance from the interfaces
62 d_min = 1E-9;
63 d_max = 1E-6;
64 Md = (d_min*(d_max/d_min).^((0:n_d-1)/(n_d-1)));
65
66 % Differential parameter
67 dd = 1E-11;
68
69 %% Epsilon matrices
70 epsilon1 = eps1(Mxi);
71 epsilon5 = eps5(Mxi);
72 epsilon3 = eps3(Mxi);
73 epsilon6 = eps6(Mxi);
74 epsilon4 = eps4(Mxi);
75 epsilon2 = eps2(Mxi);
76 figure(1)
77 semilogx(Mxi,epsilon1,'b.')
78 hold on
79 semilogx(Mxi,epsilon5,'m.')
80 hold on
81 semilogx(Mxi,epsilon3,'r.')
82 hold on
83 semilogx(Mxi,epsilon6,'b.')
84 hold on
85 semilogx(Mxi,epsilon4,'k.')
86 hold on
87 semilogx(Mxi,epsilon2,'g.')
88 hold off
89
90 %% Declaration of outputs
91 TJoulain = zeros(n_d,n_xi);
92 TJoulain1 = zeros(n_d,n_xi);
93 TJoulainInt = zeros(n_d,1);
94 TJoulainInt1 = zeros(n_d,1);
95
96 EnergyFact = kB*T.*Mxi.^3/(pi*c^3);
97
98 %% Main loop
99 % -----

```

```

100 %
101 for m = 1:n_d
102     disp(m)
103     for n = 1:n_xi
104         S = xi_green_5interfaces_joulain_quad(Mxi(n),...
105             epsilon1(n),epsilon2(n),epsilon3(n),epsilon4(n),epsilon5(n),←
106             epsilon6(n),Md(m),e,f,g);
107         TJoulain(m,n) = S .* EnergyFact(n);
108         S1 = xi_green_5interfaces_joulain_quad(Mxi(n),...
109             epsilon1(n),epsilon2(n),epsilon3(n),epsilon4(n),epsilon5(n),←
110             epsilon6(n),Md(m)+dd,e,f,g);
111         TJoulain1(m,n) = S1 .* EnergyFact(n);
112     end
113     TJoulainInt(m) = sum(TJoulain(m,:)) - 1/2* TJoulain(m,1);
114     TJoulainInt1(m) = sum(TJoulain1(m,:)) - 1/2* TJoulain1(m,1);
115 end
116 % Casimir stress as a function of d
117 figure(2)
118 loglog(Md*1E9,TJoulainInt)
119 % Casimir stress distribution
120 figure(3)
121 surface(Mxi/1.5193E15,Md,log10(abs(TJoulain)+1E-9),'LineStyle','none')
122 xlabel({'Xi (eV)'});
123 ylabel({'d (m)'});
124
125 % Hamaker constant
126 A = -TJoulainInt*6*pi.*Md.^3;
127 % Differential Hamaker constant
128 PiP = (TJoulainInt1 - TJoulainInt)/dd;
129 AD = PiP.*Md.^4*2*pi;
130
131 figure(5)
132 semilogx(Md,A,'LineWidth',2,'Color',[0.8 0.8 0.8]),...
133     'DisplayName','Direct');
134 hold on
135 semilogx(Md,AD,'Marker','.', 'LineWidth',1,...
136     'Color',[0.0784313725490196 0.168627450980392 0.549019607843137],...
137     'DisplayName','Differential');
138 hold off
139 % Create xlabel
140 xlabel({'d (m)'});
141 % Create ylabel
142 ylabel({'A (J)'});
143 % Create title
144 title({'Hamaker coefficient'});
145
146 toc

```

References

See chapter 7.

Index

- anti-sticking, 138
- Biot number, 26
- body force, 24
- Bond number, 29
- Brinkman number, 25
- capillary
 - bridge, 145
 - length, 29, 138
- capillary wave theory, 141
- Cauchy number, 24
- Cauchy's residue theorem, 128
- Clausius-Mossotti law, 123
- continuity equation, 23
- continuum
 - fluid dynamics, 20
 - hypothesis, 17
- degree of polymerization, 34
- density, 24, 36
- dewetting, 137
 - characteristic length/mode, 142
 - characteristic time, 142
 - confined, 144
 - spinodal, 30, 139, 140
 - supported, 140
- disjoining pressure, 30
- end-to-end distance, 34
- Fluctuation-dissipation theorem, 125
- fluid, 18
 - particle, 19
- Fox-Flory correction, 36
- free energy, 138
- glass transition temperature, 35
- Green's tensor, 125
- Hamaker
 - constant, 30, 138
 - number, 30, 142
- heat
 - capacity, 25
 - characteristic time of heat transfer, 26
 - conduction, 25
 - convection, 25
 - diffusion, 26
 - equation, 25
- imaginary frequency, *see also* Matsubara frequencies
- instability
 - Plateau-Rayleigh, 143
 - Saffman-Taylor, 145
 - spinodal, 142
- interfacial energy, *see* surface tension
- intermolecular forces, 18
- isothermal hypothesis, 27
- Knudsen number, 20
- Kramers-Kronig relations, 128
- Lattice Boltzmann Method, 19
- Lorentz force, 124
- Marangoni effect, 27
- Matsubara frequencies, 128
- Maxwell
 - model, 38
- Maxwell stress tensor, 124
- mean free path, 20
- mean time between collisions, 20
- molecular

- aspect of matter, 19
- weight, 33
- Molecular Dynamics, 18
- monodisperse, 34
- nanoimprint, 17
- Navier-Stokes equation, 24
- Newtonian fluid, 24, 38
- nucleation
 - heterogeneous, 141
 - hole, 139
 - thermal, 140
- Péclet number, 25
- partial cavity filling, 159
- phonon, 20
- plateau modulus, 43
- polydispersity index, 34
- polymer, 33
- polystyrene, 33
- pressure
 - field, 24
- radius of gyration, 35
- random walk, 34
- reptation (theory of), 41
- residual layer
 - dewetting, 143
- reversal imprint, 159
- Reynolds number, 24
- rheology, 37
- shear
 - modulus, 37
- spreading coefficient, 137
- Stokes equation, *see also* momentum equation
 - time dependent, 24
- surface
 - roughness, 28
 - tension, 37, 137
- temperature, 25
- terminal relaxation time, 43
- thermal conductivity, 25
- van der Waals forces, 30
- velocity
 - field, 23
- viscoelasticity, 40
- viscosity, 24, 38
 - complex, 38
 - thickness-dependent, 45
 - zero-shear, 40
- viscous
 - dissipation, 25
 - stress tensor, 24, 37
- Vogel-Fulcher model, 41
- wetting, 139
- WLF model, 42
 - extended, 46